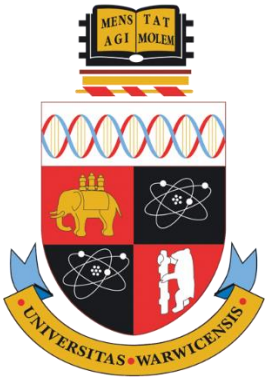

The Application of Scanning Ion Conductance Microscopy to Dental Erosion and Complex Biological Systems

by

Bryn Alan Jones

Thesis

Submitted to the University of Warwick

For the Degree of

Doctor of Philosophy

Supervisor: Prof. Patrick R. Unwin

Department of Chemistry

September 2019

For my parents who instilled in me a love for learning

And for Liz, who made it worthwhile

"*Like most modern people, I don't believe in prophecy or magic and then spend half my time practicing it.*"

- John Steinbeck

Contents

List of Figures

List of Tables

Acknowledgments

First and foremost, I would like to thank my supervisor Prof. Pat Unwin for his guidance throughout my PhD, his time and input was always appreciated. I would also like to thank Dr David Perry, Dr Cameron Bentley, Dr Minkyung Kang, Dr Gabriel Meloni and Dr Ian Macpherson for their postdoctoral skills and valuable advice day to day. I would also like to acknowledge Dr Ashley Page for his mentoring and teaching skills.

I would like to thank my collaborator, fellow PhD student and ‘maths guy’ James Teahan for providing models and insights found down his many rabbit holes. This work is a much higher standard thanks to his efforts and contributions.

I would like to thank my master’s student, turned PhD student, turned life organiser, Kelsey Cremin who worked tirelessly on the bacterial project and gave 100% into everything she did. Again, this work would be much the lesser without her contribution.

I would also like to thank Marlene Hill for her efforts and commitment to the SICM-PCAD project, providing useful data and acting as my second pair of hands during the closing stages of my PhD.

I would like to give thanks to my colleagues at Unilever, particularly Dr Andrew Joiner, Dr Gareth Owens, Dr Alex Ashcroft, Carole Phillpotts and Dr Alison Green for their help, support and feedback during my 4 year PhD and for giving me the confidence to start it in the first place!

I would like to thank my family and friends, particularly my Mum and Dad, my brothers Gwilym and Huw. I also need to mention my friends back home in Wales, especially Adam, Stefan, Christian and Kitch for providing much needed breaks from the work and keeping me sane.

And last of all, to Liz for believing in me.

Declaration

The work contained within this thesis is entirely original and carried out by me apart from where stated. I confirm that this thesis has not been submitted for a degree at another university.

The data set for the aligned enamel samples and dentine in Chapter 3 were collected by Marlene Hill under my supervision as was the dentine surface charge mapping in Chapter 3. Some of the results detailed were submitted as part of her Master's thesis at the University of Warwick.

The FEM modelling in Chapters 3, 4 and 5 was undertaken in collaboration with James Teahan. The models detailed are also used as part of his PhD thesis submission to the University of Warwick. We also collaborated on the statistical analysis in chapter 3.

The bacterial samples were cultured by Kelsey Cremin and the SICM imaging work carried out in Chapter 5 was a joint effort between her and me. The data collected is jointly owned and she has my explicit permission to use any of this data for her PhD thesis or any other work or publication going forward.

Dr Gabriel Meloni took the cryo-TEM images in Chapter 5 and the SEM images in Chapter 3.

The work presented in Chapters 3 and 5 are being prepared for publication.

I am first author on the paper being prepared on Chapter 3 and joint first author with James Teahan and Kelsey Cremin on the paper being prepared on Chapter 5. We expect both manuscripts to be submitted for review in 2020.

Abstract

This thesis catalogues further advancement of scanning ion conductance microscopy (SICM) as a multi-functional imaging technique. Through manipulation of the bias applied and interpretation of the modulated feedback the SICM nanopipette is utilised to measure the susceptibility of dental hard tissues to acid dissolution. By delivering protons to enamel surfaces and measuring the depth of the etch pits created in real time, a platform is developed for assessing the resistance of a surface to acid attack. The technique is then utilised to assess the erosive and protective properties of enamel supplements and antagonists. The work cumulates in a multi-step, multi-sample study to investigate sample variance, repeatability and to draw conclusions on the erosive potential of citric acid and the protective benefits of fluoride.

Work is also done on the expansion of SICM surface charge mapping. This technique, developed at Warwick, uses the SICM probe to measure the local ion concentration at surface interfaces. Here, it is validated on more complex systems and its potential for quantifying surface heterogeneities is explored. First, dental enamel and dentine are studied and surface charge anomalies in their microstructures explored and quantified. Secondly the surface charge is explored as an indicator of erosive damage to enamel surfaces. Surface charge changes are observed from mild dietary acid exposure and areas of increased susceptibility are identified on the enamel surface. Finally, the surface charge is examined as a novel indicator of repair through remineralisation of dental enamel.

Surface charge mapping is then used to investigate the charge discrepancies between the cell wall structures of live bacteria. The differences between gram-negative and gram-positive bacterial strains are assessed. To achieve this, novel bacterial adherence techniques were developed to immobilize but not denature the living cells. Advancements are made in the mathematical modelling of the system to explain the unexpectedly large charge values obtained for gram-positive bacteria.

The work sets out to further establish SICM as a premier technique for surface characterisation and multifunctional imaging of biological substrates.

Abbreviations

AC – Alternating Current

AFM – Atomic Force Microscopy

Ag/AgCl – Silver / Silver Chloride Reference Electrode

ASWm – Artificial Seawater Media

CPP – Current Potential Plot

DC – Direct Current

DNA - Deoxyribonucleic Acid

EDL – Electric Double Layer

EFM – Electrostatic Force Microscopy

EOF – Electroosmotic Flow

EPS – Extra Polymeric Substance

FAP – Fluorapatite

FEM – Finite Element Method

HAP – Hydroxyapatite

ICR – Ion Current Rectification

ITO – Indium Tin Oxide

i-t curve – Current Time Curve

KCl – Potassium Chloride

KPFM – Kelvin Probe Force Microscopy

LHS – Left Hand Side

PCAD – Potential Controlled Acid Delivery

PEIS – Photo-Electrochemical Imaging System

PLL – Poly-L-Lysine

QRCE – Quasi Reference Counter Electrode

RDE – Rotating Disc Electrode

RHS – Right Hand Side

SAM – Self Assembled Monolayer

SCM – Surface Charge Mapping

SECCM – Scanning Electrochemical Cell Microscopy

SECM – Scanning Electrochemical Microscopy

SEM – Scanning Electron Microscope

SEPM – Scanning Electrochemical Probe Microscopies

SICM – Scanning Ion Conductance Microscopy

SICM-SCM – Scanning Ion Conductance Microscopy – Surface Charge Mapping

SMH – Surface Micro Hardness

SPM – Scanning Probe Microscopy

STM – Scanning Tunnelling Microscopy

UME – Ultra Micro Electrode

1 Introduction

1.1 Thesis Summary

This thesis details further work in the expansion of scanning ion conductance microscopy (SICM) as an analytical technique. SICM was introduced by Hansma et al. in 1989.[1] It is a scanning probe microscopy (SPM) that utilises the flow of ions through a glass or quartz nanopipette and is capable of nanometre resolution imaging. Whilst typically a topographical imaging technique, this work focuses on secondary modes of SICM, namely surface charge mapping (SCM) and potential driven acid delivery. In chapter 3, by carefully controlling currents and voltages applied to an acid filled nanopipette, surface dissolution is induced on dental substrates. Through repeated measurements and detailed real time tracking of the resulting etch pits, information on acid resistance is obtained for a variety of samples and conditions.

Chapters 4 and 5 focus on SCM on new substrates with SICM. Here the techniques sensitivity to local ion concentrations is exploited to build detailed ion concentration maps of challenging substrates. Chapter 4 looks at analysing the surface charge heterogeneities on dental enamel and dentine, before expanding onto using SCM to quantify early stage acid erosion and subsequent repair on enamel.

Chapter 5 expands the technique into the field of live bacterial imaging. Here overcoming the challenges of working with live substrates is documented and finite element method (FEM) modelling is used to quantify the surface charge on gram-negative and gram-positive bacteria.

1.2 Scanning Probe Microscopy Overview

Traditional light microscopes obtain an image of a surface by focusing light with a series of lenses. The diffraction limit for a light microscope is around 250 nm, half the wavelength of green light. This means objects (or nanoscale features) smaller than this wavelength cannot be clearly resolved with a light microscope. One method of overcoming this limitation is to sense the surface without the use of natural light. UV and X-ray microscopes offer higher resolution due to the shorter wavelength of the respective waves but are expensive, often lack contrast with biological samples and

may be destructive to the substrate. SPM is a branch of microscopy techniques that utilise a solid probe to overcome the diffraction limit of natural light. All SPMs require a probe-substrate interaction to generate feedback, for example in the case scanning tunnelling microscopy (STM) this is the current generated by tunnelling electrons when the biased probe is in close proximity to a biased, conducting substrate and for scanning electrochemical microscopy (SECM) this is a change in the steady state current generated by redox couples at the electrode when approaching a conducting or insulating surface.[2]

1.2.1 Scanning Tunnelling Microscope

The first scanning probe technique introduced was scanning tunnelling microscopy (STM) which was developed by Binnig and Rohrer in 1981.[3] This technique uses a tungsten, platinum-iridium or gold tip mounted on sub-angstrom precision piezo electric positioners **(**Figure 1.1). Feedback is generated by a tunnelling current that develops between the probe and conducting substrate in a vacuum when a bias is applied between the two at close separation distances. Quantum tunnelling only occurs at very close approach distances (0.4 – 0.7 nm). By adjusting the height of the probe to maintain a constant tunnelling current detailed maps of electron density are possible. These give a visual of atomic scale structures. The probe can also be biased to interact with the substrate. Famously, manipulation of atoms is possible at ultra-low temperatures in ultra-high vacuum.[4,5]

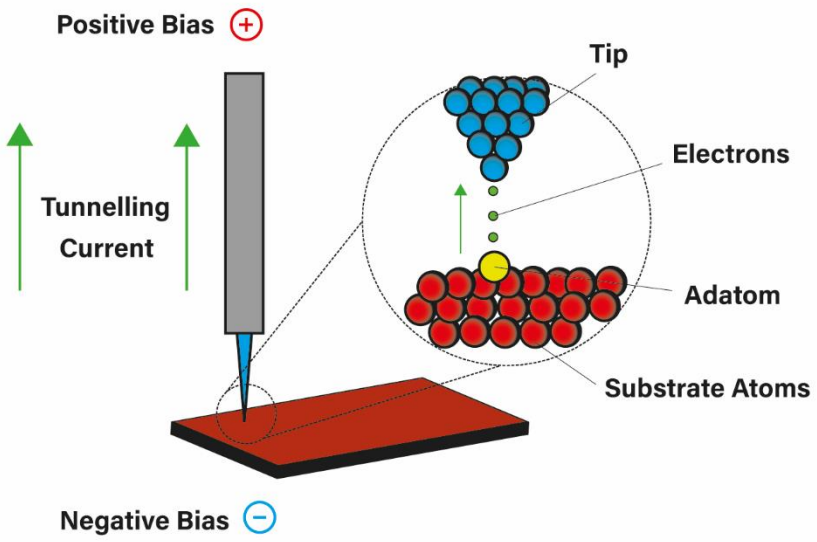

Figure 1.1 Scanning Tunnelling Microscope

A conducting tungsten tip with an atomically sharp point is brought into close proximity to a substrate. A current is generated between tip and substrate by electrons tunnelling across the vacuum gap between tip and substrate. Quantum tunnelling only occurs at sub nm approach distances allowing for high resolution mapping of the electron density of conducting substrates.

1.2.2 Atomic Force Microscopy

AFM (Figure 1.2), or the scanning force microscope, was also developed by Binnig, along with Quate and Gerber in 1986.[6] The AFM consists of a cantilever with a sharp tip (or probe) at its end that is used to scan a target specimen. The cantilever is typically made of silicon or silicon nitride and has a known Young's modulus. The tip is brought into close proximity of the sample surface and the forces between them causes the cantilever to deflect, obeying Hooke's law. The nature of the force in question is variable and depends on the sample, with the instrument being sensitive to van der Waals forces, capillary forces, electrostatic forces, the mechanical contact force, magnetic forces and multiple others.[7,8] The small deflections of the cantilever are measured by a laser that is angled so that its beam hits the end of the cantilever and is reflected into a photodiode array.[9] Through this method small movements of the cantilever cause the reflected laser beam to wobble and this is translated into an electrical signal by the photodiode which can be used to calculate the proportional

displacement of the cantilever away from the surface. This results in a faithful reproduction of sample topography as the tip is rastered across its surface. As well as topographical measurements, force measurements are possible.[10] More recently specialised tips have been developed to make estimates of surface charges and other interfacial properties.[11,12]

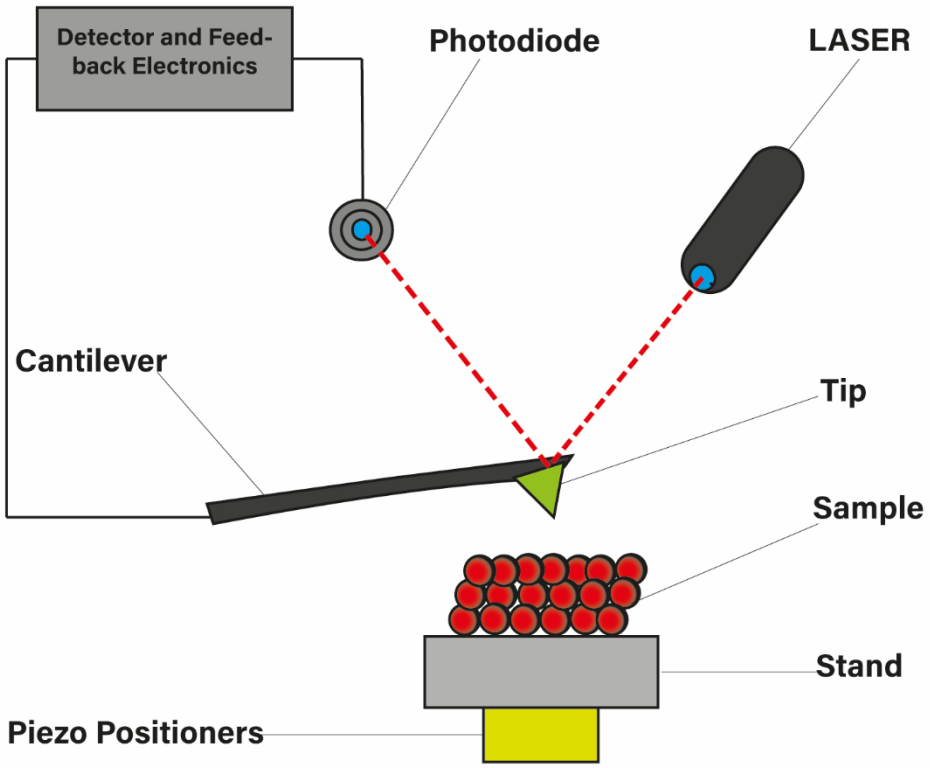

Figure 1.2 Atomic Force Microscope

Infographic showing the laser beam reflecting off the cantilever and into the photodiode. The sample stage can be moved independently in the *x* and *y* directions. The cantilever can be oscillated depending on the feedback mode chosen for the AFM, described *infra*.

The AFM has multiple modes of operation for imaging. The three most common are contact mode, tapping mode and non-contact mode. In contact mode, as the name suggests, the tip is in direct contact with the surface. The tip is dragged across the sample surface and the topography is reproduced from the feedback signal used to keep the tip at a constant distance as it follows the surface contours. Low stiffness

(more flexible) cantilevers are used to give a large enough deflection of the laser light and minimising surface interaction forces. Contact mode is always done at a depth where the overall force is repulsive, to avoid the tip 'snapping in' due to attractive forces at very close distances.

Tapping mode, also known as dynamic contact mode, intermittent contact mode or alternating current (AC) mode overcomes the 'snapping in' problem mentioned above by oscillating the cantilever so that the tip can sense short-range forces but avoids sticking to the surface. The most frequent method of oscillating the cantilever is by applying a harmonic with a piezoelectric positioner in the cantilever holder. The oscillation amplitude is small and variable, from a few nanometres to 200 nm.[13] The frequency and amplitude of the oscillation are constant until the tip comes into close proximity of the surface, where the contribution of Van der Waals forces, dipole-dipole interactions and electrostatics (amongst others) impart their effect, usually reducing the amplitude and frequency. The servo adjusts the cantilever approach distance to maintain a constant oscillation. Therefore an AFM tapping mode image is produced by imaging the force of the intermittent contacts of the tip with the sample surface as the oscillating probe is rastered across it, fleetingly in contact.[14]

Non-contact mode requires a resonant frequency oscillation. In this case the oscillation is much smaller, typically a few nanometres and as low as a few picometres. This mode relies on Van der Waals forces, strongest 1-10 nm above the surface, to dampen the oscillation. More precise piezos and anti-vibration strategies are needed to image in this mode. The resulting images are sensitive to the presence of any water layer on the sample and are sensitive enough to image membranes and biofilms. It is in this mode, in ultra-high vacuum conditions that the first true atomic resolution images were made with AFM.[8]

AFM and STM excel at nanometre resolution imaging. However, they can be found lacking when it comes to electrochemical surface analysis. Capitalising on this, scanning electrochemical probe microscopies (SEPMs) are a sub section of SPMs that map a surface through manipulation of an electrochemical signal that may increase or decrease as a probe approaches a surface. SICM, the focus technique of this thesis, falls into this catergory.[1,15,16]

1.2.3 Scanning Electrochemical Microscopy

The original SEPM is SECM (Figure 1.3). Invented by Bard et al. in 1989 it utilises a conducting wire encased in a non-conducting sheath with a small exposed face that acts as a working electrode.[17] The wire is often fabricated from traditional electrode noble metal substrates: gold, silver and platinum (can also be mercury or carbon fibre) and encased in borosilicate or quartz glass.[18] The glass is polished back to reveal a cross-section (often a disc) of the wire with calculable area (based on the wire diameter.) This probe is known as an ultra-micro electrode (UME).

The UME is connected to a potentiostat and operates as a working electrode. It is placed in an electrolyte bath containing a redox mediator and usually, background electrolyte. A counter (or auxiliary) electrode is used to balance the current generated at the working electrode, usually *via* a redox reaction with the supporting electrolyte. Voltage is measured with regard to the well-defined reduction potential of a reference electrode, often a silver- silver chloride couple, this electrode passes no current. When a bias is applied to the UME the redox mediator is turned over at the electrode, generating a steady-state current limited by the hemispherical diffusion at the electrode.[17,19] As the probe is translated towards a surface, changes in the current correspond to changes in the abundance and diffusion profile of the redox mediator. A drop in current occurs over an insulator as the diffusion of ions to the electrode is disrupted, *i.e.* at close proximity to a surface the mediators flow over the disc is sterically inhibited by the surface. Over a conductor (biased to turn over mediator) the mediator reduced at the UME will be rapidly re-oxidised by the surface, increasing the tip current close to the surface. This change in current can be utilised as a robust feedback mechanism as the approach can be halted when the UME current deviates from the steady state in bulk solution. The technique can be used to generate simple topographical maps based on this feedback response and functionalised images measuring the redox activity of species, for example measuring the flow of mediator in and out of pores.[20–22]

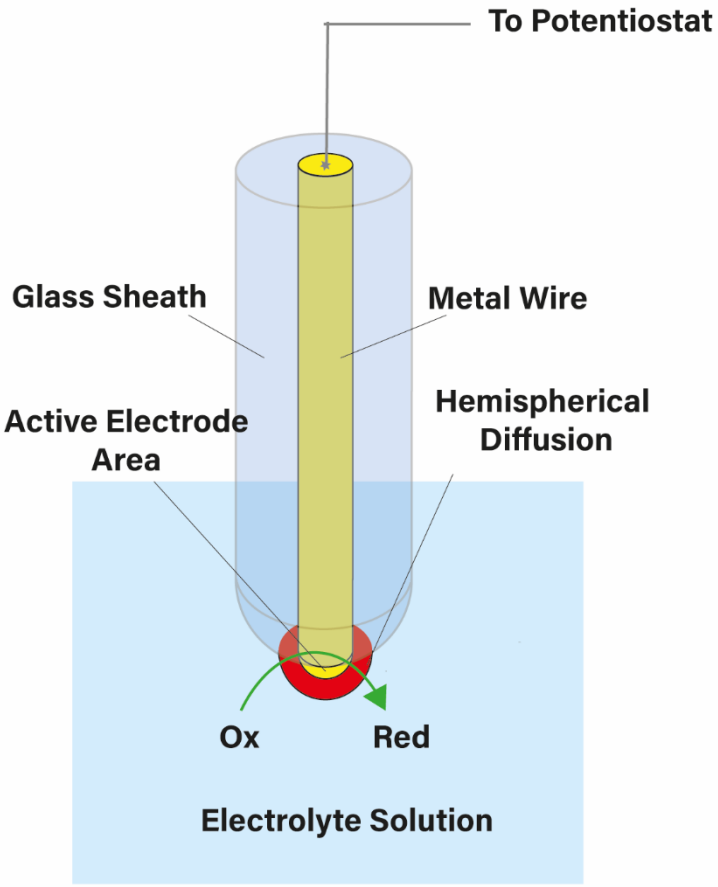

Figure 1.3 Scanning Electrochemical Microscope

A glass sealed metal wire with a disc-shaped face exposed to the electrolyte solution. The redox mediator in the electrolyte is reduced at the electrode generating a steady state current dependant on the mediator concentration and diffusion kinetics at the interface. The UME is sensitive to the local concentration of electroactive species.

The UME is often the working electrode in a simple 3 electrode system, as described above. The rate of reaction can be measured by monitoring the current i that passes between these two electrodes, as given by equation (1):

$$i = nAFj \tag{1}$$

where A is the area of the electrode, and j is the flux. The current recorded depends on the processes occurring at the electrode surface. It means if the process is known and

the area of the surface is known, the measured current can be used to calculate the flux.

SICM falls into the category of open channel SEPMs. These utilise an open channel and flow of ion current between two reference electrodes. A recent addition to the open channel SEPM family is scanning electrochemical cell microscopy (SECCM Figure 1.4). This novel technique pioneered at Warwick by Unwin et al. in 2013 employs a droplet cell to localise and confine electrochemical measurements.[23–25] Useful for high resolution localised electrochemical studies, the technique has found a niche investigating heterogeneities on metal surfaces,[26] probing sites of increased electrochemical activities such as semiconductor step edges.[27] Electro-activity discrepancies can also be detected between otherwise similar structures, for example inter particle differences are clearly observed when analysing catalytic $LiMn_2O_4$ nanoparticles.[28] This technique brings electrochemistry to the single entity level. Another use, of particular interest to this work, is the ability to measure dissolution rates in a controlled manner on acid erosion susceptible surfaces such as dental enamel.[29]

1.2.4 Scanning Electrochemical Cell Microscopy

Like SICM, SECCM does employ an ion current (a flow of ions through the meniscus between the two barrels of the pipette) but the feedback mechanism for surface sensing differs. A sinusoidal oscillation is applied to the nanopipette in the z direction as it approaches a surface. When the meniscus (droplet cell in Figure 1.4) contacts the surface the ion current across the meniscus acquires a modulated AC component at the same frequency as the sinusoidal oscillation, due to the reversible deformation of the droplet.[30] The emergence of the AC signal upon landing is utilised as a feedback mechanism (AC is effectively zero away from the surface). The drawback here is that the approach speed needs to be much slower (sub 1 μms^{-1}) to avoid breaking the probe as it contacts the surface. Once upon the surface, electrochemical measurements such as cyclic voltammetry can be performed on a local area of the substrate, defined by the droplet cell.

As with most glass nanopipette techniques, the fragile probe never contacts the surface but when the meniscus forms it will be within a probe diameter of the surface, allowing for interfacial measurements. SECCM is a versatile technique, if the substrate being

analysed is an electrode or metal surface, a bias can also be applied to the substrate. This allows for analysis of electrochemically catalysed reactions such as electro-polymerisation.[31] The substrate can also be utilised as a working electrode in this mode, allowing for smaller probes (~30 nm) by eliminating the need for the second barrel, as demonstrated by Bentley et al.[32]

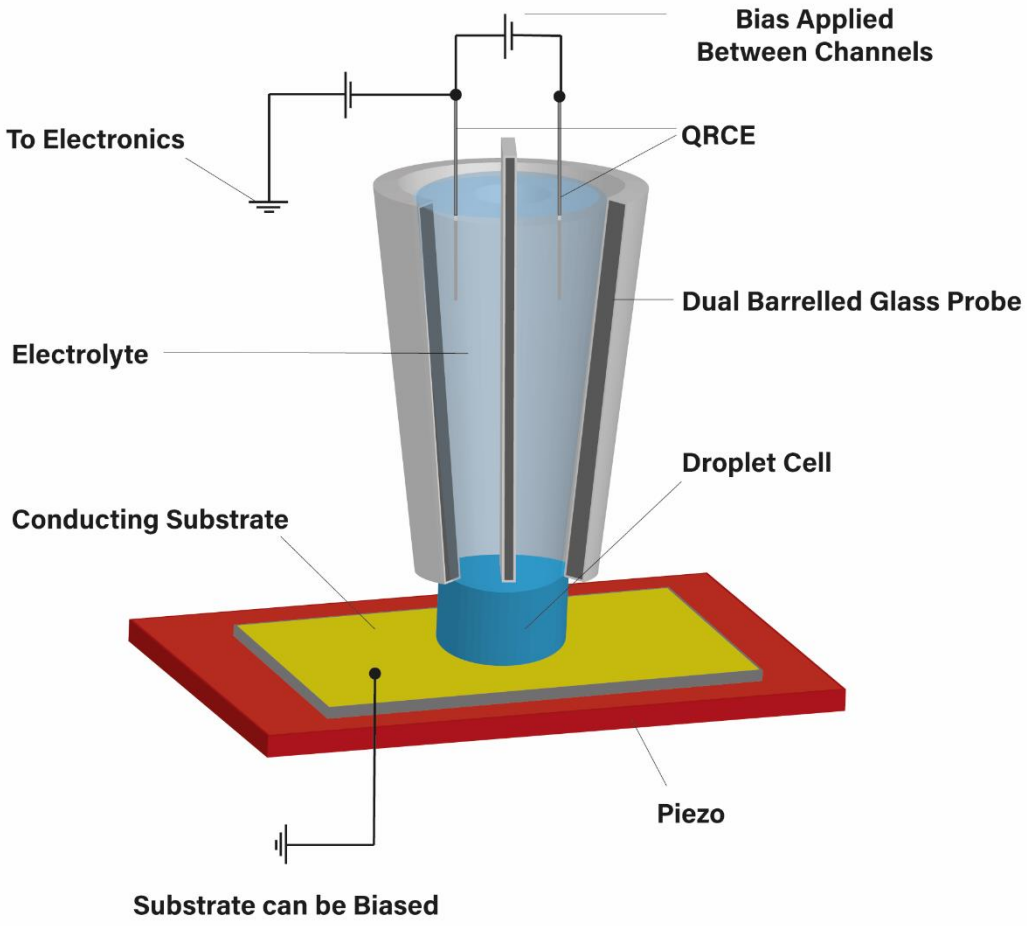

Figure 1.4 Scanning Electrochemical Cell Microscopy

QCREs are placed in both barrels of a theta pipette. The meniscus at the bottom of the probe forms a droplet cell when in contact with the surface. A small oscillation is applied in the z direction and the AC current that arises from the droplet deformation is used for feedback. Localised electrochemical experiments can be performed in the droplet cell.

By their nature the wide array of SPM techniques come with a host of advantages and disadvantages. Conditional and experimental restraints may mean one SPM is favoured over another. For example, STM offers the highest resolution of all SPMs but requires a carefully prepared substrate that is often gold sputtered. STM operates optimally in ultra-high vacuum, these conditions are challenging for biological samples and rule out true live sample imaging. AFM does not have these limitations (although it can be improved with ultra-high vacuum in certain cases[8]) making it useful for non-conducting substrates. However, the contact dependant scanning mechanism can make it challenging for analysis of biological substrates and thin films, antagonising living substrates and imparting contact forces to fragile structures such as membranes. Non-contact AFM does subvert these issues but the instrumentation required is costly. SICM attempts to achieve the same benefits by utilising the ion current in an electrolyte bath as feedback, which provides a stronger signal than the slight perturbation from Van der Waals forces detected in non-contact AFM. SICM can also operate without oscillating the probe opening up the possibility of mapping the local ion concentration at the substrate-electrolyte interface.

SEPMs attempt to avert these issues by maintaining a close working distance to the sample without contact. SECM has been used widely for live cell studies of larger substrates but true nanoscale imaging remains an ongoing challenge in the field.[33–35] For SECM the limitations in probe size, electrode fouling from biological substrates and diffusion complications incurred due to the glass sheath surrounding the electrode frustrate its use for bio-imaging at the nanoscale.[36] Recent advances have attempted to reduce the size of SECM probes, however difficulty of fabrication and inconsistency of probes still plague the field.[37–39]

SECCM employs its unique droplet cell, which has made it useful for electrochemical measurements on well-defined planar surfaces but topographically challenging substrates such as cells are not suitable. As SECCM does not function in an electrolyte bath live cell imaging is not possible. Also, the porosity of a surface and its wettability are factors that may inhibit SECCMs usefulness. In the next section SICM is introduced and its merits and pitfalls discussed in detail.

1.3 Scanning Ion Conductance Microscopy

1.3.1 Standard Set-up

SICM is a non-contact SPM that is preferentially used for topography measurements of soft matter samples such as cells or biological tissues[16,40]. The non-invasive nature of the technique aids it in the analysis of such fragile samples. SICM utilises a quartz or glass nanopipette with an opening (pore) of known size, typically around 150 nm but smaller diameters, around 30 nm, are possible. The nanopipette is filled with electrolyte solution of known concentration and used to analyse substrates submerged in identical electrolyte (Figure 1.5 A). The requirement of electrolyte means biological samples such as cells can be placed in media that will sustain them, extending the operating time for live cell imaging, the media being an important factor for the viability of most cells, along with temperature and pH which can be controlled through experimental modification. A quasi-reference counter electrode (QRCE), fabricated from silver chloride coated silver wire is inserted into the nanopipette and another into the bulk solution. This system is used as it functions as a redox electrode, with an equilibrium existing between the silver metal and its salt, silver chloride. The reaction is characterised by fast electrode kinetics, meaning that a sufficiently high current can be passed through the electrode with 100% efficiency of the redox reaction (dissolution of the metal or cathodic deposition of the silver-ions). The stability makes it a suitable reference electrode.

Applying a bias between the two QRCEs causes ions to flow through the bulk solution and up the nanopipette, generating an ion current[1]. The ion current is limited by the electrolyte concentration, bias applied and by the resistance due to the size of the nanopipette pore[41]. In bulk solution (with the probe many pore diameters away from a surface) the ion current is constant, and its magnitude depends only on those factors. When the probe is translated to within a pore diameter of a surface the ion flow is inhibited resulting in a drop in the ion current (Figure 1.5 B) [16]. This drop in current, as it is a predictable, calculable decrease, is utilised as a feedback mechanism for approaching the nanopipette to within nanometres of the surface.[42] There are multiple factors that control exactly how close to the surface the nanopipette approaches. The size of the nanopipette opening, the concentration of the electrolyte and the feedback threshold elected being the most impactful. For most of the work in this thesis a

feedback threshold of 2% is used, and a threshold of 1-2% is common throughout the literature with most groups reporting an approach distance of roughly a tip diameter at the point of closest approach.[15,43,44] At such distance topography can be faithfully reproduced and interfacial properties of the substrate, such as local ion concentration, analysed.[41,45]

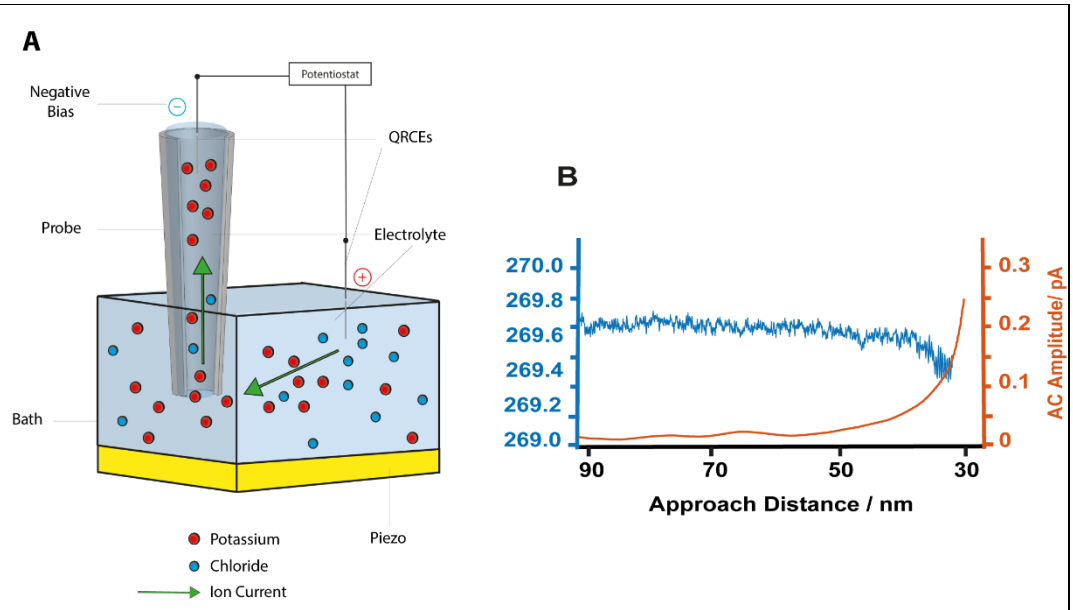

Figure 1.5 Scanning Ion Conductance Microscopy

The image depicts a SICM probe negatively biased at the working QCRE (top of the nanopipette) in bulk solution (**A**). The flow of potassium ions through the bulk solution and up the nanopipette generates an ion current, governed by the access resistance, described *infra*. Vertical movement of the probe is controlled with a Z piezo and the sample can be moved laterally relative to the probe by use of an X-Y piezo. The graph details an experimental approach curve, showing the direct current (DC) and AC response in the current as the probe approaches a surface (**B**).

Nanopipette resistance can be calculated as the sum of the pipette resistance R_p (equation 2) and access resistance R_{ac} (equation 3).

$$R_p = \frac{h}{\kappa \pi r_p r_i} \quad (2)$$

where, h is the tip length, κ is the conductivity of the electrolyte and r_p and r_i are the radii of the pipette opening and pipette base, respectively.

$$R_{ac} = \frac{\frac{3}{2}\ln\left(\frac{r_o}{r_i}\right)}{\kappa\,\pi\,d} \tag{3}$$

where, r_o and r_i are the outer and inner radius of the tip opening and d is the distance between the tip and the sample. These equations show the relationship the tip-substrate separation distance d and the size of the nanopipette pore have on the overall ion current.

The resolution of an SICM experiment is considered to be around 2/3s of the diameter of the nanopipette opening.[46] Thus a typical 150 nm probe would provide a maximum resolution of around 100 nm, being able to resolve features at this length scale. At the limit of technology some groups report nanopipette diameters of around 20 nm, putting the current limit on SICM resolution sub 15 nm.[47,48] Whilst this does not compare to the sub nm imaging of AFM or STM, given the ability to routinely image soft samples and the increasing possibility of live biological imaging SICM maintains its niche advantages.

1.3.2 SICM Feedback Modes

Once an ion current is established through a nanopipette, the user has multiple options in feedback control. DC feedback was described previously, with the nanopipette approach stopping when the measured ion current drops below a defined threshold. (Figure 1.6**A**.) For example, if a bulk current of 200 pA is observed when applying a 50 mV bias through a 50 nm pipette using a 50 mM potassium chloride (KCl) electrolyte, the approach could be halted when the current drops below 196 pA due to the increased access resistance. The values used in this example are arbitrary, but it is often helpful to define the value based on the magnitude of the bulk current.[1]

Some variation in the bulk current over the duration of an SICM experiment is expected due to minor drift of the QRCEs and changes in the conductivity due to small temperature variations. A percentage value is typically used to set the threshold to

account for any small deviations in the bulk current. This gives a more consistent tip-substrate separation distance than using a set value, meaning the probe is more likely to approach to the same distance above the surface. Theoretically, when approaching, a 2% drop in a 200 pA bulk current should achieve close to the same tip-substrate separation distance as a 2% drop in a 300 pA bulk current.[43] In the experiments performed in this thesis a 2% threshold is used unless otherwise stated. Values from half a percent to around 5% are common in the literature.[48] Smaller values risk triggering false approaches (when the probe registers a feedback signal before the surface is actually reached, giving a false, larger topography value) and higher thresholds decrease the sensitivity of the probe and risk approaching too close, leading to breakages. The value of 2% is a compromise that has been shown to give consistent data and minimizing breakages and false approaches.

In its early years SICM users favoured a distance modulated feedback, utilising an induced AC component as a feedback signal. This is robust and reproducible and produces a steady AC current whenever the probe is within a tips diameter of the surface.[16] The AC component arises by applying a physical oscillation to the probe in the z direction, typically this is at several hundred Hz with an amplitude comparable to roughly 15% of the nanopipette diameter. The close proximity to the surface causes a change in the ion current over the course of an oscillation. In essence, when measured in bulk solution there is negligible change in the current from peak to trough (*i.e.*, AC signal is zero), however, when the oscillating probe is within a tip diameter of the surface, there **is** an appreciable change in the AC component as the tip-surface distance is modulated (Figure 1.5**B**). This is due to a drop off in the ion current over the course of a peak to trough oscillation, attributed to the restricted ion flow (resulting from the access resistance increasing the overall resistance of the system) close to the substrate surface.

Whilst robust, this feedback mechanism has fallen out of favour in recent years for several reasons. The physical motion of the probe required to generate an AC signal is not desirable in all applications.[49] Live cell imaging in particular is enhanced by removing the oscillation as the measurements of live substrates are often time critical and shorter experimental times are achievable without the need for an AC signal.[16,50] The requirement of an oscillation for feedback means the measurement is limited by the time-constraint of the lock in amplifier applying the harmonic.[51] In the pursuit of

faster scanning and sampling times the removal of this restraint has been a large benefit.[43]

For other applications that are sensitive to local ionic environments such as SCM, the physical oscillation can reportedly distort the ion composition as the motion causes some local mixing, hindering imaging attempts.[52] The removal of the oscillation keeps the distance between the end of the nanopipette and the substrate constant, this simplifies the process of modelling and analysing experimental SICM data.

A third feedback type developed by Unwin et al. at Warwick utilises bias modulation to achieve a feedback mechanism. By oscillating the bias applied between the two QCREs an oscillating ion current is generated, both its amplitude and phase can be utilised for feedback.[51] Whilst the technique shows promise for resolving convolution in SCM,[53] improvements in DC SICM and its lack of need of a lock-in amplifier make it the favourable technique for high speed charge mapping.[43]

Figure 1.6 shows a representation of SICM being used in constant height mode (**C**) and a hopping mode regime (**D**). Constant height mode utilises a feedback mode, typically distance modulated AC feedback, to maintain a constant tip substrate separation whilst translating across a surface. DC SICM can struggle when used for constant height scanning due to drift in the ion current, for that reason distance modulated AC mode is preferred. This is usually achieved by keeping the AC current constant through small movements in the Z direction, therefore maintaining the separation distance over any topographical features.

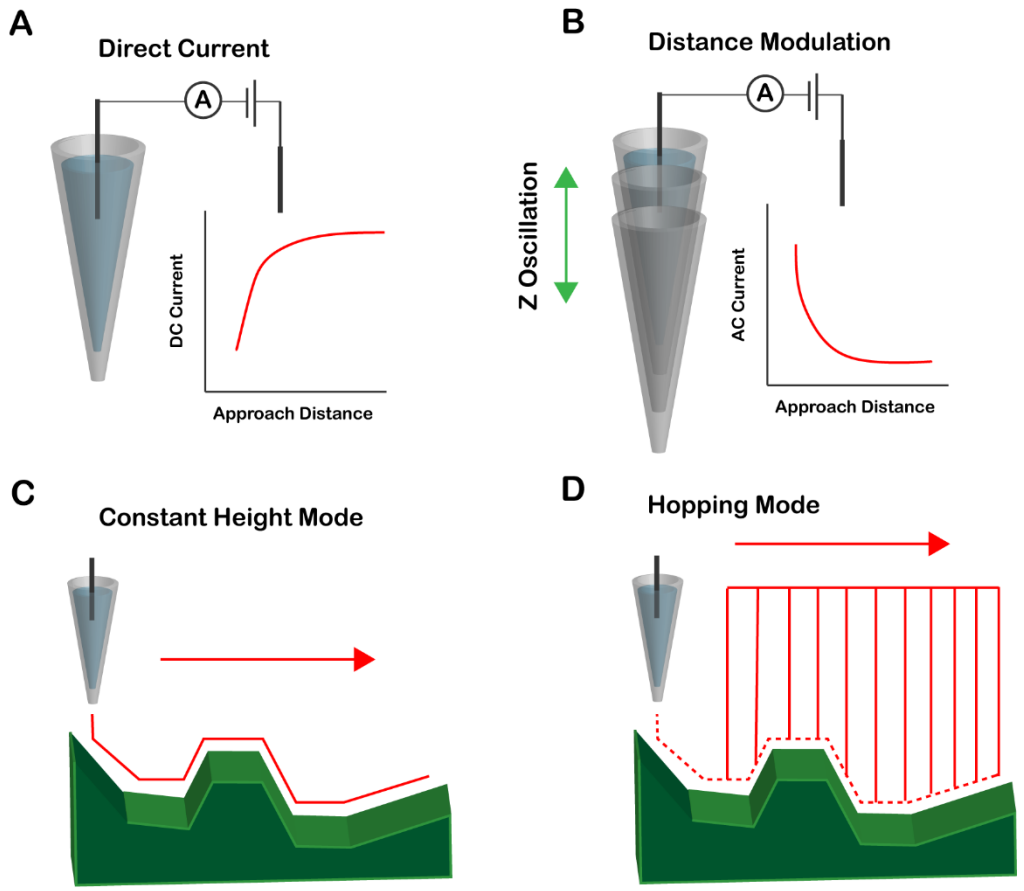

Figure 1.6 SICM Feedback Modes

An SICM infographic depicts standard DC feedback (**A**). A small voltage is applied to the probe and the DC current decreases as the probe is approached to the surface. No oscillation is required. Distance modulated feedback (**B**). The probe is oscillated in the Z direction during the approach. This gives rise to an AC current that drastically increases at close separation distances. Constant height mode (**C**). This shows the probe maintaining a constant separation distance by the electronics holding a steady AC current. This mode also utilises a Z oscillation. Hopping mode (**D**). This image depicts the path a probe may take scanning the topography of a surface with a hopping regime.

The disadvantage of this method of surface tracking is that any particularly sharp changes in sample topography run the risk of breaking the nanopipette. It copes well with gradual surface changes, but prominent features are problematic. Hopping mode overcomes this issue by implementing a retract distance, to safely clear any potential obstacles. By retracting into the bulk solution, self-referencing regimes can be

implemented. For example, with SCM, the ion conductivity is measured in the bulk solution and at the surface, the bulk measurement allowing each surface measurement to be normalized against the bulk helping to mitigate the effect of current drift. Each approach happens after a translation in the *x* or *y* direction. Following a traditional raster pattern (completing a row of *x* measurements from left to right, followed by a translation in the *y* direction, before a second row of *x* measurements from right to left, then repeat) an image of a surface can be built up pixel by pixel. At each pixel an electrochemical measurement, such as a cyclic voltammogram or current-time (*I-t*) curve, can be made. This allows for a functionalised map of the sample to be made to complement the topography. Such regimes are discussed in depth in section 1.3.3.

1.3.3 Principals of SICM Surface Charge Mapping

Two chapters of this thesis are concerned with investigating surface charge on complex substrates. Chapter 4 details the expansion of SICM-SCM on dental surfaces where it is used to visualise the surface heterogeneities in the crystal structures of enamel and dentine. Additionally, experiments to quantify acid erosion and remineralisation processes through a change in the observed surface charge of those materials are undertaken. Chapter 5 is concerned with the quantification of the surface charges of gram-positive and gram-negative bacterial strains and the adaptions to standard methods required for live bacteria imaging with SICM. Therefore, it is necessary to discuss the detail of how surface charge is quantified with SICM-SCM. The nature of charged interfaces and the scientific models that underpin the phenomena are discussed in section 1.4, here the onus is on the experimental methodology.

As mentioned previously, with hopping mode SICM the opportunity to conduct self-referenced electrochemical measurements presents itself. At each pixel of the topographical map a measurement in close proximity to the surface and a corresponding measurement in bulk solution can be made. If the measurement made is an *I-t* curve, a self-referenced, or bulk normalized current map is generated.[50]

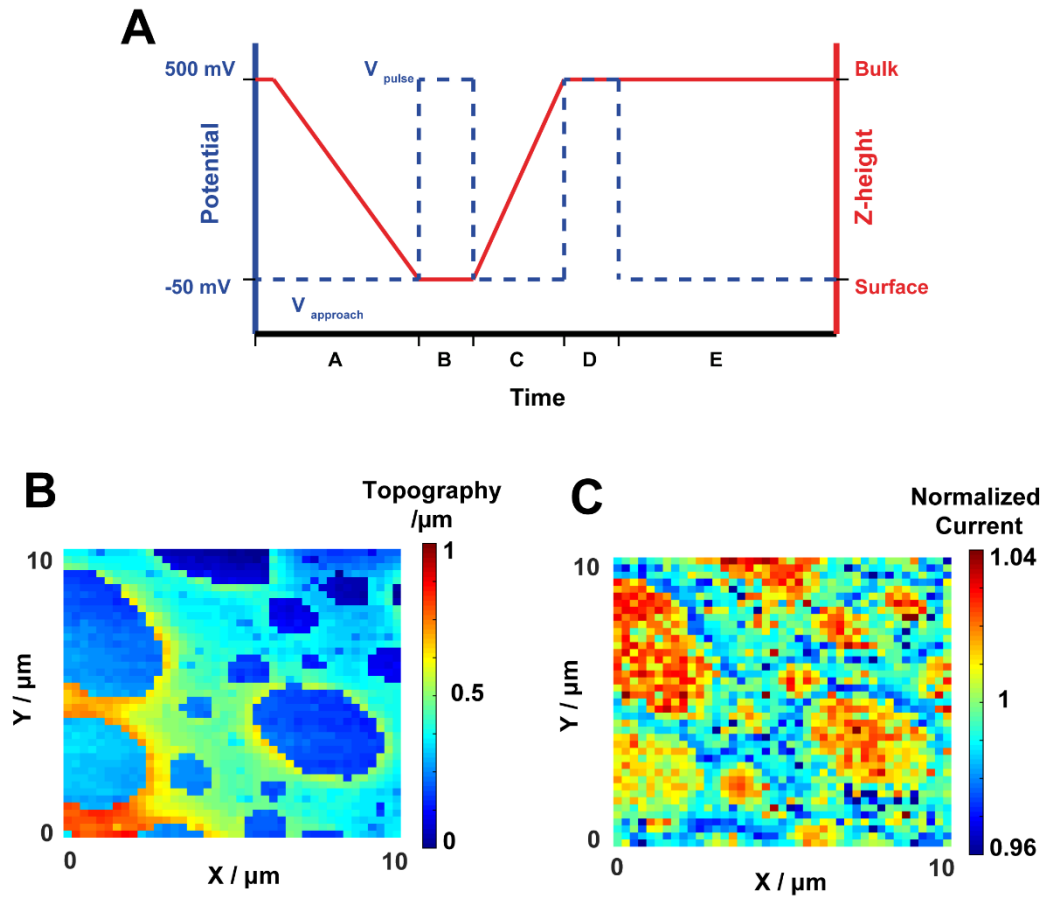

Figure 1.7 Surface Charge Mapping Protocol and Example

A plot of the voltage and Z height during a typical charge mapping approach detailed *infra* (**A**). A typical SICM topography image of an interrupted polystyrene film (**B**) and its corresponding bulk normalized surface current (**C**).

Figure 1.7**A** is a diagrammatic representation of the probe vertical motion and changing potential for a typical pixel in a normalized current map. Each section of the *x* axis is explained. (A) The nanopipette probe is moved toward the surface at 2 µm/s with the QRCE in the probe biased at -50 mV *vs.* the QRCE in bulk solution ($V_{approach}$). When the ionic current between the two electrodes has reduced by a chosen threshold value, nominally 2%, the approach is halted before (B) the potential at the working electrode is increased to 500 mV, (V_{pulse}) for a short duration of time (usually 100 ms). After this pulse (C), the probe potential is returned to -50 mV and the probe retracted into the bulk solution. The retract distance is large enough that the following pulse is characteristic of the bulk solution (5 times the dimensions of the nanopipette

opening away from the surface.) (D) A second 100 ms pulse in the bulk solution; (E) the probe is then translated laterally to the next pixel. The $I-t$ curve at the surface and the $I-t$ curve in bulk are analyzed to extract the normalized current at each pixel. The analysis is carried out using a MATLAB script provided in Appendix section 7.4.

Figure 1.7 **B** and **C** show respective topographical and normalized current maps of a broken polystyrene film surface. Made by dissolving a polystyrene bead in acetone and then dipping a glass slide in the solution and air drying, a patchwork polymer film with areas of exposed glass is created. The intricate yet relatively flat topography is a good control sample for SICM. Between the two images a clear correlation can be seen with the normalized current in good agreement with the topographical features. There may be some enhancement of the signal due to topographic effects but the modelling of the system attempts to account for this and this phenomenon has been discussed in depth by previous studies in the Unwin group.[42,54,55] In the above example there is a manifestation of this which is seen as regions of low (blue) normalized current at the edges of the circular structures. The polystyrene produces a neutrally charged film contrasting with patches of the negatively charged glass showing through. In these conditions an increased value of normalized current corresponds to the negatively charged glass and values around 1 correspond to the neutral film.

1.3.4 Nanopipette Fabrication and Characterization

Nanopipettes are made from a quartz or glass capillary (diameter 0.5 – 1 mm) by using an automated laser puller, such as the Sutter instruments P2000. The capillary is clamped and mounted between two pulling arms in the path of a CO_2 laser beam. A firm constant pressure can be applied for set time increments whilst the laser heats the capillary for controlled melting. As the two halves of the capillary are pulled apart, they narrow to a fine point. If correctly aligned the systematic melting and pulling process results in two nanopipettes of repeatable, small pore size. Consistency is very good with pore sizes typically having a sub 10% error between capillaries and the two halves considered identical. The methods used in house to measure the consistency and acquire the geometry of nanopipettes is discussed in depth here.[56] SICM probes are frequently checked in house with Scanning Electron Microscopy (SEM) in transmission mode to assure these standards do not slide and that nanopipette pore dimensions do not vary. Figure 1.8 shows one such image.

By taking multiple images of a nanopipette from different angles it is possible to gain a measure of the probe's geometry. These images form the framework for the simulated nanopipettes used in the FEM modelling in this work. Although only ever an estimate, particular care is taken to measure the pore opening size, the thickness of the inner and outer radius of the probe (and therefore the pipette wall thickness) and the cone angle. An accurate estimate of these parameters aids the FEM modelling, which is discussed in depth in section 1.3.6.

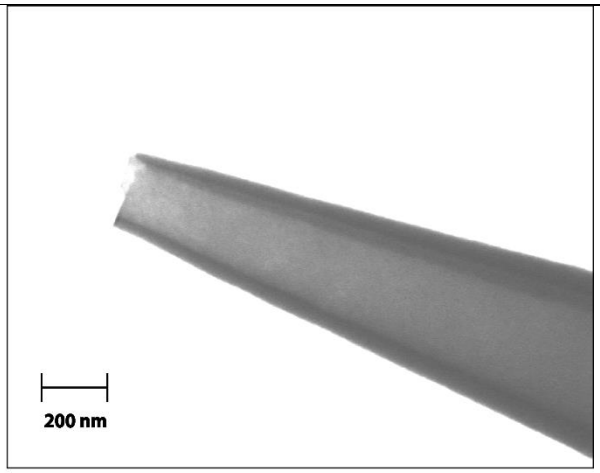

Figure 1.8 SEM Image of a Nanopipette

A SEM image of a nanopipette taken in transmission mode. The pore size, inner and outer radii of the probe and cone angle can be calculated from this image.

1.3.5 Interpreting the Ion Current Response

The charge mapping experiments presented in this thesis rely on the interpretation and quantification of subtle changes in the observed ion current. To understand this information, it is useful to explore and define the contributing factors. When a bias is applied between two Ag/AgCl QRCEs in bulk solution, unconstrained by a nanopipette, the current response is ohmic and linear. The current is directly proportional to the potential applied and the electrolyte concentration. When one of those QRCEs is placed in a nanopipette this relationship changes. The charge on the nanopipette walls can have a large effect on the current passed, where instead of a linear relationship a rectified current response is seen. This ion current rectification (ICR) does not occur in micropipettes and is believed to be a specific property of

nanopipettes.[57] ICR arises due to the similarity in size of the nanopipette pore and the thickness of the double layer on the nanopipette walls in low electrolyte conditions (<100 mM.)[58–60] Due to the chemistry of the nanopipette surface, specifically the presence of silanol groups on the quartz or glass, the composition of the double layer becomes pH dependent. In other words, the surface charge on the nanopipette walls due to the silanol groups is directly correlated with the pH of the system. In typical SICM conditions of 50 mM KCl at pH 7 this results in a net negative charge on the nanopipette walls.[61]

Figure 1.9**A** shows FEM modelled *i*-*V* curves for different surface charges on the walls of a 150 nm diameter nanopipette. 10 mM KCl was used as electrolyte. The bowing (rectification) in each *i*-*V* curve can be seen and corresponds to the magnitude of charge on the glass, larger charges increasing the rectification. This phenomenon is due to the larger double layer in low electrolyte conditions, which is sizable compared to the nanopipette opening radius, affecting the magnitude of the current passed enhancing or subtracting the ion current depending on the magnitude of the charge.[62] This is due to the preferential transport of anions or cations and is reversed if the charge polarity is reversed.

When an SICM probe is biased at a higher potential, above 100 mV for the systems studied (i.e. sub 200 nm nanopipettes in sub 100 mM electrolyte conditions) an interaction with the approached surface occurs. If the surface carries a negative charge, such as glass, the normalized current increases if the bias applied is negative and decreases if the bias is positive. When approaching a positive surface, this is inversed. This phenomenon is detailed in Figure 1.9**B** and **C** which show the normalized current responses when approaching charged surfaces with positive and negative biases applied. This sensitivity to the surfaces charge at different potentials is the foundation for SCM.

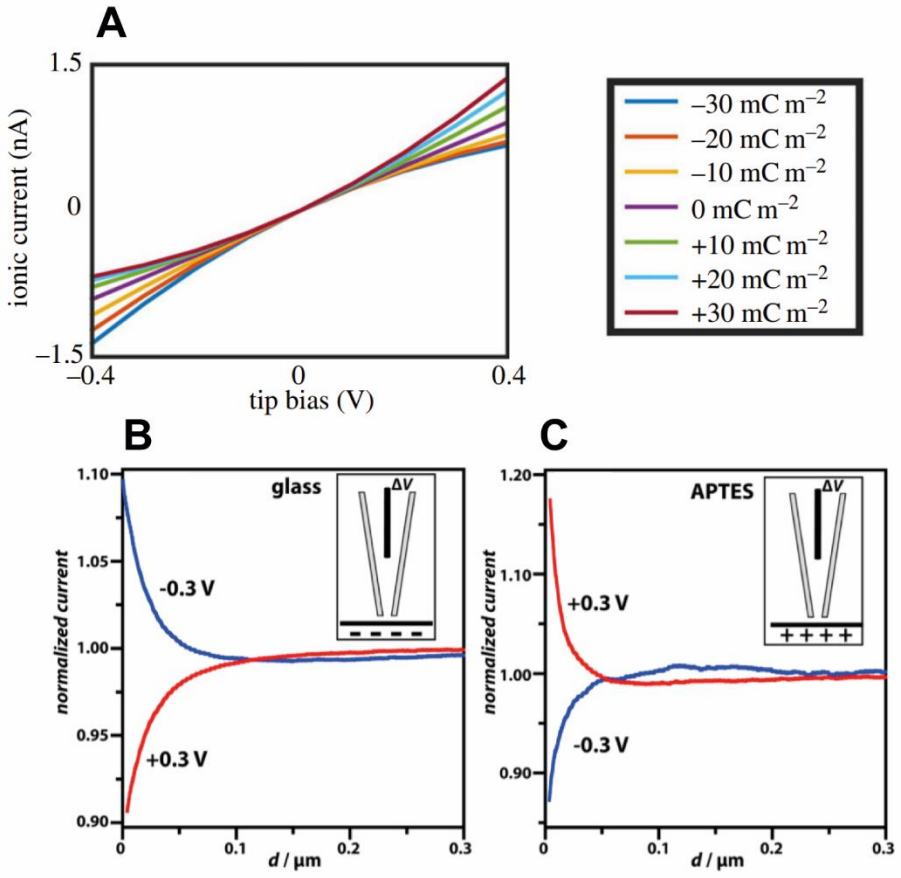

Figure 1.9 Nanopipette Rectification and Charged Surface Approaches

FEM modelled ICR dependence with nanopipette surface charge (**A** Adapted from Page et al.[62]) Simulation conducted in 10 mM KCl for a 150 nm diameter nanopipette. Experimental approach curves depicting normalized DC ion current (**B** and **C**) as a function of the probe-to-substrate distance, d, recorded with ca. 75 nm radius nanopipette over negatively charged glass and positively charged APTES substrates at 0.3 V (red lines), -0.3 V (blue lines.) Schematic illustrations, as insets, depict the nanopipette approaching variously charged substrates for the corresponding plots. The DC ionic currents are normalized to the respective values at solution bulk. (Adapted from Perry et al.[53])

At lower applied tip biases (as can be seen in the ICR plot, Figure 1.9**A**) the nanopipette is insensitive to the charge of the approached surface. Therefore, a low bias of around ±50 mV is typically utilised during an approach. At this potential an ion current is driven which generates a feedback current but is insensitive to the surface charge. At the point of closest approach, the bias is increased to a value that is surface charge sensitive. Originally the bias was swept through a range of voltages, taking a cyclic voltammogram (CV), but for the sake of speed a short pulse to a higher potential of around 500 mV is employed.[43] This sudden change in the applied potential causes a change in the local electric field in the footprint of the nanopipette. As described in Figure 1.10 the change in local flux causes some of the ions in the double layer to be stripped away from the surface leading to an increase in the local ionic concentration which in turn leads to an increase in the measured current during the pulse when it is directly compared to the pulse in bulk solution.

A common misconception about SICM-SCM is that the double layer is being probed directly. With a KCl electrolyte concentration of 50 mM a double layer of around 10 nm is expected. With a 150 nm probe an approach distance of around 50 nm at the point of closest approach is typical. This means the nanopipette does not directly probe the double layer. What is observed is an increase in local ion concentration in the nanopipettes footprint due to the aforementioned change in flux during the pulse, the magnitude of which is related to the ion concentration within the double layer.

Figure 1.10 shows a COMSOL simulated nanopipette 50 nm away from a charged surface. At approach bias the double layer is unperturbed but at the considerably higher pulse bias cations stripped from the surface fill the footprint and opening of the nanopipette. This results in a large change in local ion concentration which is measured by the SICM as an increased current. The magnitude of the increase in the current measured is directly linked to the ion density of the target substrate.

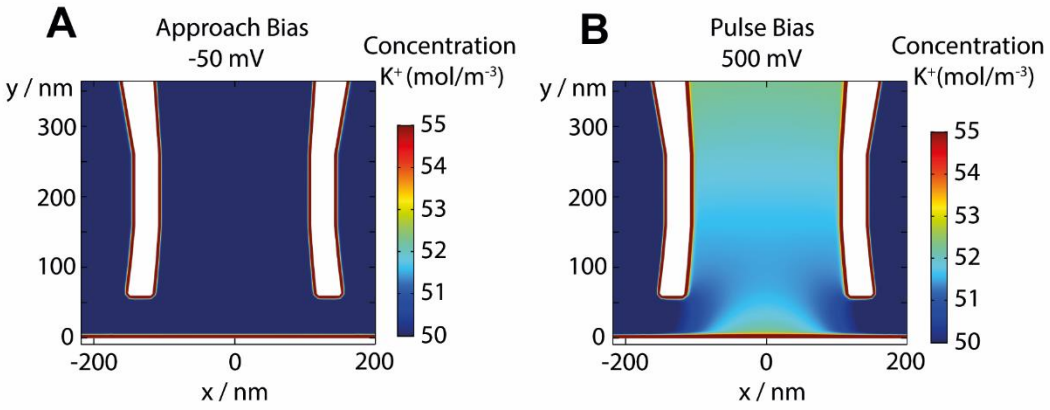

Figure 1.10 Cation Concentration at Approach and Pulse Bias

FEM modelled concentration profiles showing the cation concentration in 50 mM KCl solution at a negatively charged surface (- 80 mCm^{-2}) and on the walls of a nanopipette at – 50 mV approach bias (**A**) and at 500 mV pulse bias (**B**). The extent of the perturbation of the double layer can be seen in **B**, depicting the mechanism through which surface charge sensitivity arises. It is noted that the concentration of ions at the surface and at the tip walls greatly exceeds 55 mol/m^{-3} (dark red regions, note the unit is metre cubed) due to the tight packing of ions in the double layer, thus the potassium concentration is capped at 55 mol/m^{-3} to allow the double layer perturbation to be visualised.

Understanding ICR is essential to being able to interpret any data inferred from changes in ion current in a given SICM experiment. The framework for interpreting this information and implementing it into a functioning FEM model of the system has been covered in depth by the SICM imaging group at Warwick.[43,50,56] The work in this thesis attempts to expand the uses of SCM to practical applications on more challenging substrates and does not need to delve further into the intricacies of the underpinning theory in this introduction. Each modelled system is covered in depth in their corresponding chapter. An overview of the FEM COMSOL simulations is given in 1.3.6, including the equations solved within the simulations, but further justifications of the mechanics of SCM are not detailed.

1.3.6 Finite Element Method Simulations

Previous sections have mentioned the use of FEM simulations to complement, understand and quantify experimental data. This section gives an explanation of what FEM modelling consists of and an overview of an example template for SICM FEM simulations used as a basic framework within this thesis. The results chapters expand on this basic system and the deviations and additions are detailed there.

FEM is a numerical technique that is used to perform finite element analysis on a given physical phenomenon. It allows processes that are governed by partial differential equations to be solved to a defined level of confidence. For a computer to be able to solve these equations, or attempt to converge on an answer, approximations are made. The transport of species in solution and electric field distribution are two such phenomena that are governed by partial differential equations and both of these systems are integral to understanding the behaviour of ion currents in SICM, making FEM modelling a suitable tool to analyse these experiments.

To best estimate these equations, a domain space is defined, in most cases a 2D area is modelled and divided into a finite number of regions and the equations solved at intersections of each of these regions known as meshing points. This is done using software capable of 'meshing' such as COMSOL Multiphysics, used throughout this thesis. The equations are solved to a desired degree of error via an iterative solving method that converges on a solution, when the error between each iteration is below a nominal value (in our models this value is 1×10^{-3}) the equations are considered solved at that point in the mesh.

To make the models as accurate as possible the geometry of the nanopipette is measured using STEM images from multiple angles. As well as the geometry, the constituents of the electrolyte, the biases applied to the electrode and the approached surface are also modelled. Figure 1.11 shows a diagram of the model. Only one wall of the nanopipette is accurately measured, as it is symmetric about its central axis it is then revolved about this axis during the calculations, simplifying the model. 3D simulations are possible and one is detailed in chapter 5, but they are computationally expensive with much longer calculation times. The area representing the bulk solution extends 100 microns away from the nanopipette surfaces, well past the point static

interactions would occur. For all simulations the bulk concentrations were set to be 50 mM KCl, mirroring the experimental conditions.

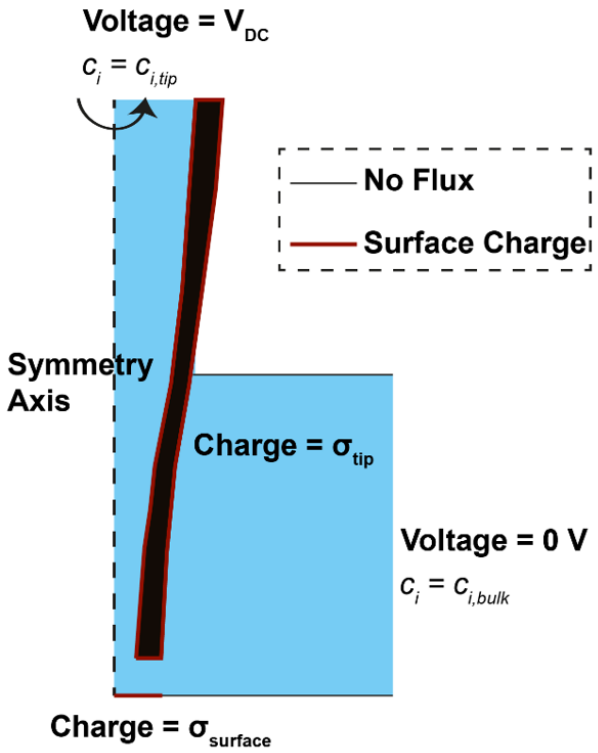

Figure 1.11 Typical Nanopipette Geometry in COMSOL

A representation of the nanopipette in COMSOL. The model is created by rotating along the axis of symmetry. The surface charge of the glass can be modelled, and the boundaries defined by the areas of no flux. Initial values for the voltages are applied to the boundaries at the top of the nanopipette and on the RHS of the bulk solution. The area in red at the bottom defines the surface charge of the sample.

Once the geometry has been built and the differential equations to be solved included, initial parameters are set. Typically, this is where starting electrolyte concentrations, permanent fluxes and initial biases applied to the relevant boundaries are defined. The initial parameters are usually applied to a set boundary, for example the surface charge on the nanopipette wall or a flux of ions being released from a reactive surface can be defined. Permeability of a boundary is also defined, no flux would be allowed to pass through a glass nanopipette wall but a cell membrane will have a defined rate that ions

may travel through. The resulting model is the best approximation of the area in 2D space that has all of the equations underpinning the physics and chemistry involved are applied.

For all the systems investigated in this thesis the electrostatics, transport of diluted species and laminar flow modules are used to model the experimental system. In all simulations the Nernst-Planck equation for ion transport (eq. 4) was solved:

$$J_i = -D_i \nabla c_i - z_i \frac{F}{RT} D_i c_i \nabla \phi + c_i u$$

4)

where D_i z_i and c_i are the diffusion coefficient, charge number and concentrations of species I and u is the solution velocity described below (eq. 5). Ion diffusion coefficients were taken from the CRC handbook[63] and the simulations accounted for the effect of locally varying ionic strength on these parameters. F, R and T are the Faraday constant, gas constant and absolute temperature. ϕ is the electric potential described by the Poisson equation (eq. 5):

$$\nabla^2 f = - \frac{F}{\varepsilon \varepsilon_0} \sum_i z_i c_i$$

5)

where ε is the dielectric constant of the solution and ε_0 is the vacuum permittivity. The solution velocity was described by the incompressible Navier-Stokes equation with electroosmotic flow (EOF) incorporated (eq. 6):

$$u \nabla u = \frac{1}{\rho} \left(-\nabla p + \mu \nabla^2 u - F \left(\sum_i z_i c_i \right) \nabla \phi \right)$$

6)

where ρ is the solution density, μ is the solution viscosity and p is the pressure. At each mesh point these partial differentials are resolved.

In chapter 4 FEM modelling is used to calculate the surface charge on dental substrates by following a sequence of steps. Firstly calculating a steady state CV to compare with

an experimentally obtained CV. Secondly, to determine the probe-substrate separation an approach curve is simulated. Thirdly FEM simulations are used to extract quantitative values of the surface charge by simulating multiple surface charges at the interface and correlating them with the experimentally observed normalized currents. A similar system is used in chapter 5 but a 3D model is required to properly analyse the bacterial cell wall. In chapter 3 FEM modelling of a dissolving enamel surface is used to calculate rate constants for induced proton attack at that surface. This differs from the other models in its requirement of speciation to properly calculate the hydroxyapatite (HAP) dissolution mechanism.

1.4 Surface Charge

1.4.1 The Electric Double Layer

Surface charge can be described as the accumulation of charged species, such as solvated ions or electrons on a surface that gives rise to a potential difference in comparison to the surrounding solution. The overall outcome is that a net negative or net positive charge builds up on a surface. Consider the case of the wall of a nanopipette, submerged in electrolyte solution. There are terminating groups that are exposed to the solution, some of these are silanol groups which contain an alcohol (OH) group. This alcohol can be deprotonated which, when it occurs, leaves behind a negatively charged terminating oxygen species.[61] With enough of the silanols deprotonated the overall surface will be negatively charged. The surrounding electrolyte compensates for the charge discrepancy by forming a solvated layer of counter ions, ions with the same charge as the surface are repelled. A simplistic view of two layers of oppositely charged ions gives rise to the term electric double layer (EDL.) There have been multiple revisions and modifications expanding on this simplistic view, the most important of which are detailed in Figure 1.12 which is taken from the model for the electrode/electrolyte interface and applies directly as the conductivity of the surface material plays no overall role.

With the EDL being important in understanding the reaction kinetics at the electrode-electrolyte interface many scientists have worked on increasing our understanding of the interface. In 1853 Helmholtz was the first to attempt to describe the solid-solution interface.[64] He deduced that charged electrodes immersed in electrolyte would attract

counter ions and repel ions of like charge. He modelled the EDL as a molecular dielectric, capable of storing charge linearly with voltage applied allowing the system to be described by a fixed capacitance that depends only on the dielectric constant of the electrolyte and the thickness of the EDL (Figure 1.12**A**). Whilst a solid foundation for further theory, the model does not consider the mixing of ions in solution, the possibility of ion adsorption onto the electrode surface or solvent interactions.[65]

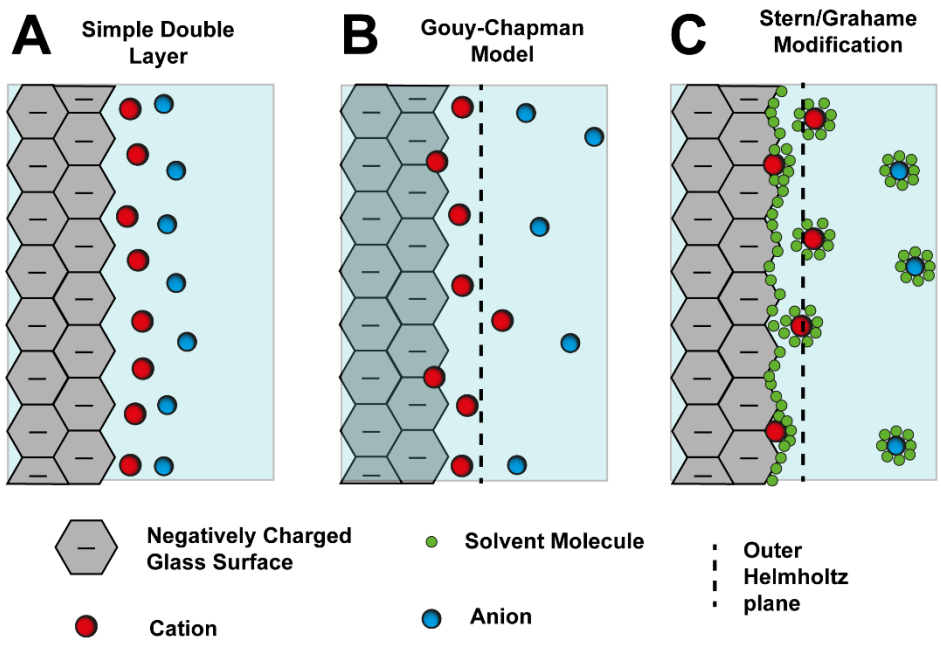

Figure 1.12 Electric Double Layer Models

Representations of the double layer formed on a glass surface submerged in electrolyte. A layer of cations with corresponding anions in a simple Helmholtz capacitive model (**A**). Gouy-Chapman model showing adsorbed cations at the surface and a diffuse layer of anions (**B**). Stern Grahame modifications of the Gouy-Chapman model accounting for solvated ions (**C**).

In 1910 Gouy and Chapman made independent modifications to incorporate some of these factors. In their model the capacitance is not fixed, instead scaling with voltage and ionic concentration of the electrolyte. They proposed the existence of a diffuse layer with an electric potential that decays exponentially away from the charged surface (Figure 1.12**B**).[66]

In the Gouy-Chapman model the relationship between surface charge σ_p and surface (or Stern) potential φ_0 is given by:[67]

$$\sigma_p = (8RT\varepsilon\varepsilon_0 C \times 10^3)^{\frac{1}{2}} \sinh\left(\frac{Z\varphi_0 F}{2RT}\right) \quad \textbf{7)}$$

where R is the gas constant, T the absolute temperature, ε the relative dielectric constant of water, ε_0 the permittivity of free space, C the molar concentration, Z the ionic charge of the electrolyte and F the faraday constant. It is important to note that this relationship breaks down for higher surface charges and potentials, but for the case of low potentials the Debye length is given by:[67]

$$K = \left(\frac{2F^2 I \times 10^3}{RT\varepsilon\varepsilon_0}\right)^{\frac{1}{2}} \quad \textbf{8)}$$

where I is the ionic strength of the electrolyte, leading to the inverse relationship between ionic strength and EDL thickness, I.E the double layer decreasing in thickness as the electrolyte concentration increases which is a known phenomenon when working in low electrolyte concentrations (<100 mM.) At high electrolyte concentrations the theory runs into some problems. As there is no parameter factoring the finite size of ions, unrealistic surface potentials can be reached at higher concentrations. However, if this is accounted for in the experimental build, Gouy-Chapman theory can still be used to give a good approximation of the surface kinetics and allows the Debye parameter, and therefore the double layer thickness to be calculated.

The next significant adaptions to the model where made by Grahame and Stern. Stern proposed a combined model. Implementing an inner Helmholtz layer of tightly bound surface ions with a surrounding Gouy-Chapman diffuse layer. Grahame expanded on this by suggesting the Helmholtz layer was composed of two individual layers, a layer of ions fully adsorbed onto the electrode and a compact layer of fully solvated ions beyond that. He also accounted for solvent caging around ions (Figure 1.12**C**.)

These modifications lead to a good mathematical representation of the double layer. Figure 1.13 shows how the electric potential decreases exponentially with distance

away from the charged surface. Also high-lighted are the Stern and slipping planes, arbitrary points in the system where different equations dominate, initially the potential drops off rapidly due to the screening of the ions in the tightly bound Stern layers and then more gradually as the ion density decreases in the diffuse layer. The point where zeta potential is calculated, at the edge of the slipping plane is also shown.[68] Whilst not routinely defined with regards to planar surfaces, zeta potential is a useful parameter in colloid science, giving some quantification of the stability of a suspended particulate. Measured through electrophoretic mobility, it gives a rough bulk approximation of surface charge. Zeta potential is covered in more detail in section 1.4.2.

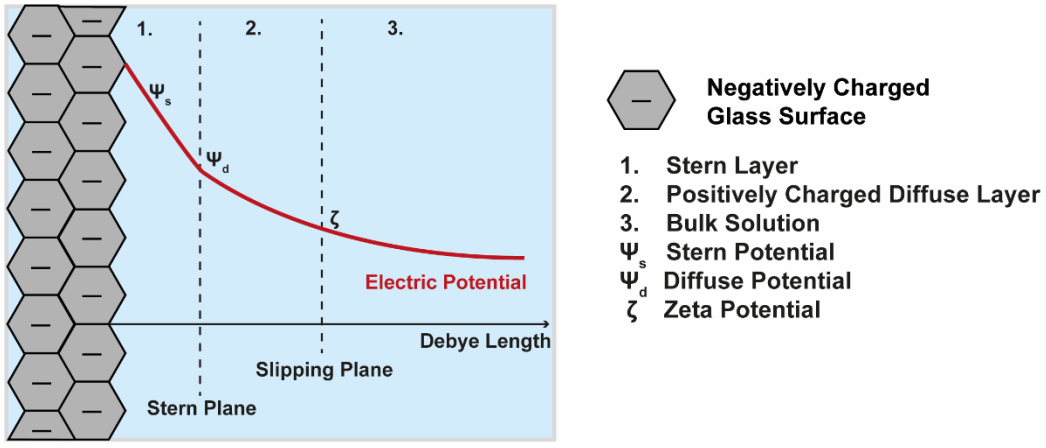

Figure 1.13 Electric Potential and Debye Length Plot

A plot showing the relative positions of the Stern plane, slipping plane and the point at which zeta potential is measured. The electric potential decreases linearly through the Stern layer and then exponentially through the diffuse layer into bulk solution.

For the FEM simulations in this thesis, as we are working in low electrolyte conditions, Gouy-Chapman theory is used to model the double layer. Although an approximation, it keeps calculation times more reasonable, and as the electrolyte concentrations are low, the point at which the theory breaks down (at high electrolyte concentrations) is not reached and the complex ion adsorption kinetics and their implications can be ignored. This makes Gouy-Chapman a good fit for these simulations when all factors are considered.

1.4.2 Measuring Surface Charge

Surface charge is a broad term that is relevant in many fields. From underpinning the complex interactions of proteins[68] and biological membranes[69] to defining the stability of colloidal suspensions like toothpaste,[70] understanding charge interactions is key to understanding fundamental biology as well as industrial processes. It should be of no surprise that there is no single technique capable of analysing all of these wide ranging and multifaceted systems. What existing techniques have in common is the need to asses and quantify a surface characteristic that is condition dependant, sensitive to external factors in the bulk solution such as pH or concentration. The nature of the measurement on some interfaces also means that direct stimulation of the area with a physical probe can interfere with the measurement itself. This is especially problematic when attempting to analyse surface charge in aqueous solution as the interface is easily perturbed by the flow profile around an oscillating probe, which is why distance modulated feedback is unsuitable for SCM.

1.4.2.1 Zeta Potential

The method of measuring surface charge most commonly used are electrophoretic zeta potential measurements. Limited, in most cases, to analysing particulates it is nevertheless helpful for establishing whether particles in a colloid will resist aggregation or not. If the particle is small enough, a high zeta potential (in either the positive or negative) is an indicator of good stability in its suspended state. The measurement is calculated at the slipping plane (Figure 1.13) and is not wholly representative of the charge of the system and is not equal to the Stern potential or the electric surface potential in the Helmholtz layer. This is because they are defined at different locations with the zeta potential specifically referring to the potential at the outer edge of the slipping plane. For most cases in colloid and polymer sciences this is enough, with the zeta potential being used as a rough indicator of stability.

It is measured using a zetasizer, which conducts an electrophoretic measurement. A sample of the particulate in question is suspended in a salt solution of known concentration. It is exposed to an electric field and the average movement of the particles is calculated. At the same time, dynamic light scattering is used to approximately size the particles. From their electrophoretic mobility and size an

estimate of the zeta potential can be calculated using the following equation from Smoluchowski theory:[71]

$$\mu_e = \frac{\varepsilon_r \varepsilon_0 \zeta}{\eta}$$

9)

where ε_r is the dielectric constant of the dispersion medium, ε_0 is the permittivity of free space, η is dynamic viscosity of the dispersion medium (Pa s), and ζ is zeta potential (i.e., the electro-kinetic potential of the slipping plane in the double layer, units mV.) This is connected to the electric field strength μ_e via:[72]

$$\mu_e = \frac{\upsilon}{E}$$

10)

where υ is the drift velocity of a dispersed particle and E is the electric field applied. The model makes some assumptions, the largest of which is that the double layer is thin in comparison to the radius of the particle. It is possible to account for a thicker double layer but this calls for further modification, not discussed here, proposed by Huckel.[73]

The limitations of zeta potential measurements for a wide array of applications are clear. The measurement itself is at best an approximation and limited to particulates. The method also assumes Brownian behaviour of particles and does not account for natural motion of a species that would occur when analysing say, a bacterial suspension. Though modifications for analysing zeta potential on planar surfaces have been attempted, the measurements are indirect and require a specialised flow cell.[74] SICM-SCM overcomes many of these issues and avoids disturbing the sample by being strictly non-contact.

1.4.2.2 AFM Based Techniques

Modifications to AFM cantilevers, to make them sensitive to the local chemical environment and complement the high-resolution topographical imaging, is a new method of analysing surface charge. Functionalising an AFM tip is an idea that has been around nearly as long as the technique itself. AFM tips that are also capable of SECM imaging are an example of this, obtaining chemically relevant information as well as topography has been made possible through recent advances in materials

science.[75,76] These specialised tips are capable of measuring electroactive species in conjunction with topography. For spatial charge mapping, AFM cantilevers functionalised with polar molecules (such as carbon monoxide) designed to produce force curves that are sensitive to the presence of charged species on the substrate surface, have been developed.[11]

By modifying the AFM probe with self-assembled monolayers (SAMs) with different terminating groups it is possible to create probes that respond to charged surfaces. The SAMs are made by first coating a commercial AFM tip in polycrystalline gold before exposing it to a solution containing functionalised thiols.[77] By performing multiple force distance curves on a surface it is possible to obtain information pertaining to the charged molecules on the surface. Modified cantilevers are capable of a multitude of different measurements, such as adhesion forces, friction and functional group mapping, all branching out of force sensitive AFM.[78] The methods for calculating surface charge with AFM are complex, in some cases needing a model to mathematically subtract the topographical interference.[79] More recent studies have managed to directly probe the dielectric constant of some biological substrates,[80] but detailed surface maps of charge heterogeneities of organic materials remain challenging.

Another AFM based technique that has had some success at resolving surface charge heterogeneities is electrostatic force microscopy (EFM). In this technique a conducting AFM like probe is oscillated in close proximity (sub 100 nm) to a conducting substrate under vacuum. The work functions of both the sample and cantilever have to be known. A bias is applied between the two and the electrostatic force can be measured by manipulating the applied voltage.[81] As the probe is scanned over the surface, electrostatic forces can reduce both the frequency and amplitude of the cantilever oscillation, and it is these variables that are the measurable quantities in an EFM.[82] EFM has found particular use in probing graphene surfaces,[83] with biological substrates proving a challenge due to the requirements of working in vacuum with conducting samples. Some recent studies have got around these limitations by using dehydrated proteins mounted on mica supports but are still a way off of live cell imaging.[84]

Another technique to discuss under the branch of force microscopies capable of imaging surface charge is kelvin probe force microscopy (KPFM.)[85–87] Utilising a conducting AFM like probe with an AC bias applied, the capacitance between the probe and the sample is quantified, in a very similar manner to EFM. When a DC current flow occurs between the tip and the surface, the cantilever vibrates, and the magnitude of that oscillation is then translated into the local potential difference between the tip and the surface, and thus the surface potential. Whilst preferentially used for analysing conducting and semi-conducting substrates,[85,87] mainly due to the need for high levels of information on the physical properties of the substrate, some studies have attempted to analyse biological substrates.[88,89]

Whilst some of these techniques are capable of high-resolution imaging, many have downsides that make them impractical for biological samples or operating under electrolyte. SICM provides a compromise with good resolution achievable on a diverse array of samples. In the next introductory section more detail is provided on the substrates investigated with SICM in this thesis.

1.5 Bacterial Surface Charge Mapping Background

Chapter 5 of this work is concerned with the SCM of bacterial substrates with SICM. Alternative techniques used in the literature are discussed in the chapter introduction. In this section motivations for undertaking these studies and some relevant background biology of the substrate is provided.

1.5.1 Bacteria: Biology and Structure

Bacteria are essential for life. They are one of the oldest lifeforms and exist in symbiotic and parasitic relationships with almost all flora and fauna on earth. They also inhabit every conceivable environment from deep sea hydrothermal vents to radioactive waste.[90] They are adaptable and survive in the most extreme conditions. What makes them ubiquitous with multicellular life is the ability to synthesize vitamin B_{12}, a trait shared with only a few species of archaea (simple single celled organisms).[91,92] B_{12} is involved in metabolism and is required by every cell of the human body.

Bacteria are prokaryotic microorganisms and can be grouped in several different ways. Commonly, their need for oxygen is considered. Aerobic bacteria require oxygen to

live, whilst anaerobic bacteria cannot tolerate gaseous oxygen and die when exposed to it. Facultative anaerobes prefer oxygenated environments but can survive without it.[93] The second factor often considered is how the bacteria obtain their energy. Autotrophs create their own energy through chemical reactions involving inorganic materials and usually, sunlight. Most bacteria are heterotrophs, meaning they consume organic molecules, or in simple terms, they require food. The structure of a typical bacteria is given in Figure 1.14.

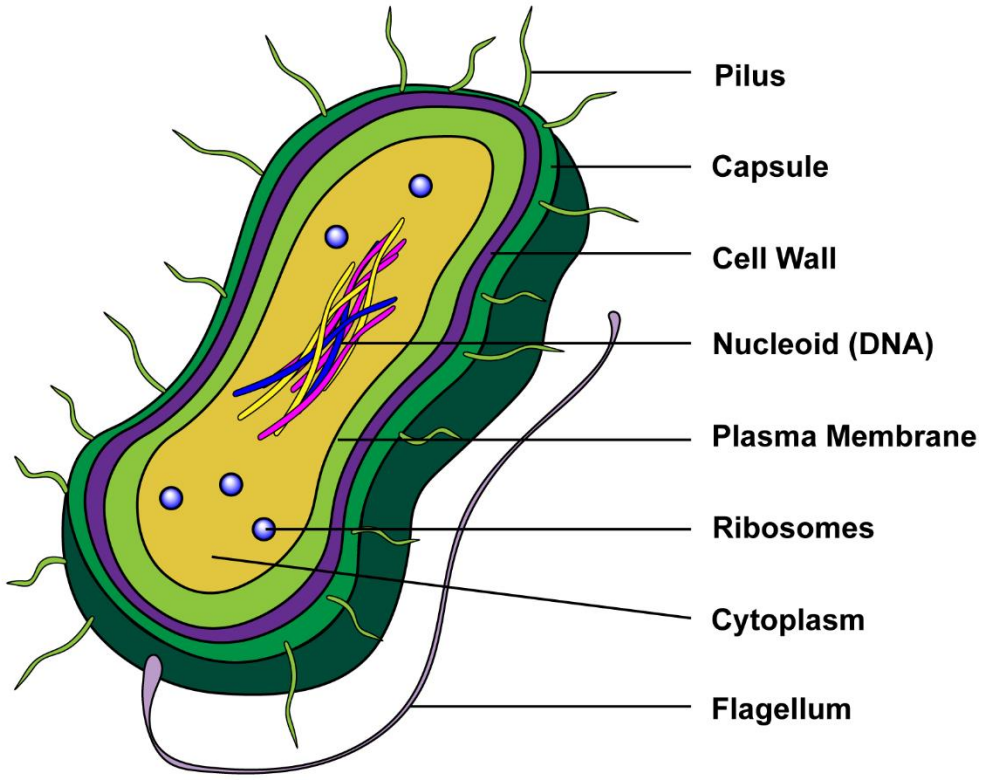

Figure 1.14 Typical Bacteria Cross-Section

A view of the internal structure of a bacterium. The membranes composing the cell envelope can be seen, along with the nucleoid and ribosomes suspended in the cytoplasm.

The outer layers of the bacteria (in dark green and purple) are collectively known as the cell envelope. The capsule is not present in all bacteria, but those that have one are more resistant to phagocytosis (being engulfed by white blood cells). This makes the capsule a major virulence factor, having one greatly increases bacterial resistance to

being denatured by external factors and many of the more dangerous disease-causing bacteria have a capsule. It also protects the bacteria from drying out and allows it to deal with a host of other threats.[94] The cell wall, as well as providing anchorage for pili and flagella, acts as a support structure, defining the cells shape and resists bursting when an extreme osmotic gradient exists between the bacterial cytoplasm and the external environment. The final component of the cell envelope, the plasma membrane, controls passage of ions in and out of the cell. It consists of a highly organised layer of phospholipids which allow interaction with the surroundings.[93,95]

The pili (singular pilus) are hair-like structures that allow bacteria to adhere to their environment, for example allowing them to cling to teeth, or the intestinal tract or other bacteria. The flagellum (plural flagella) is the transport mechanism for bacteria. They allow them to 'swim' by being swung in a propeller like fashion. They are often at one, or both ends of a bacterium but may be present all over the surface.[96] The internal components of a bacteria are often varied depending on its function but almost all contain ribosomes which produce proteins, and a nucleoid, which is a region of the cytoplasm that contains non membrane-bound DNA. Most bacteria have a single chromosome responsible for reproduction. The cytoplasm itself is a gel-like matrix that consists of proteins, enzymes, water, nutrients waste products and dissolved gases.[93,97]

1.5.2 Importance of Studying Bacterial Surface Charge

The study of bacteria is of increasing importance to society. With the rise of antibiotic resistant 'superbugs' the need to understand bacterial behaviours such as biofilm formation, bacterial signalling and bacterial nutrition may be key in developing the next generation of technologies to help combat bacterial infections. [98,99] It is not just for healthcare reasons we may want to increase our knowledge of bacteria. Specifically engineered bacteria may provide answers to some of mankind's greatest environmental challenges such as clean energy production[100,101] and plastic removal from the oceans.[102]

Heterogeneities in charge distribution are known to play a role in biofilm formation with changes in charge allowing bacteria to align and organise,[103] cellular uptake,[104] differentiation (e.g. persister cells and biofilm forming cells),[105] and the antimicrobial resistance of bacteria.[106–109] Often these charge density differences are subtle, difficult

to quantify and difficult to visualise, with only a handful of techniques being able to probe them.[110–112] Typically, bacteria outer cell membranes are net negatively charged, however the magnitude of the charge varies between bacterial species.[113,114] This has been found to be influenced by growth medium, bacterial age, and the bacteria surface structure features.[115] The surface charge is difficult to quantify directly, the study of live samples poses a unique set of challenges. SICM charge mapping circumvents many of them and the adaptions made to make it possible are documented in chapter 5.

1.5.3 Cell Wall Structure and the Gram Stain.

Another way of differentiating and grouping bacteria is the composition of their cell wall. Through use of a Gram stain it is possible to infer information about the make-up of a bacterial cell wall. The bacteria are stained with a purple hued stain, often safranin or fuchsine. In a gram-positive species the gram stain is absorbed by the thicker peptidoglycan layer and will not be washed away with alcohol or other solvents. In a gram-negative species minimal absorption occurs and the bacteria does not change hue. Example structures of gram-negative and gram-positive bacterial cell walls are given in Figure 1.15.

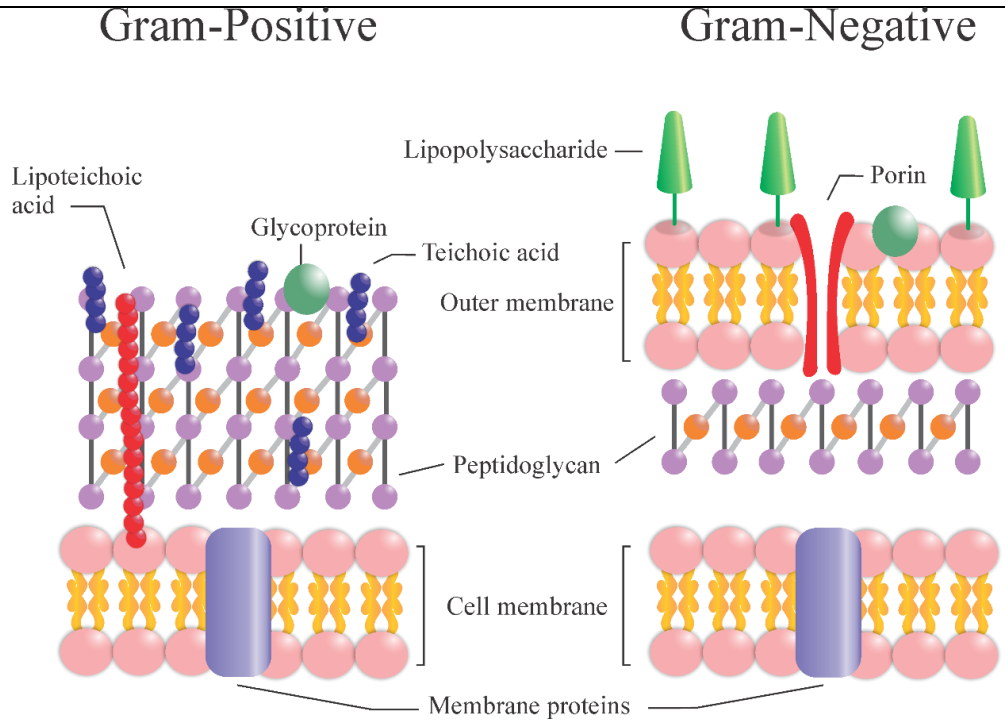

Figure 1.15 Gram-Negative and Gram-Positive Cell Wall Structures

The thicker peptidoglycan layer is the prominent feature of the gram-positive bacterial cell wall. It is dotted with teichoic and lipoteichoic acids. These are thought to help modulate the surface charge and are partly responsible for the increased net negative surface charge on gram-positive bacteria.[116,117]. The outer membrane and lipopolysaccharides that make up the outer structure of gram-negative bacteria are clearly shown on the RHS. (Image adapted from Jones et al., in preparation.)

The cell membrane is the plasma membrane referred to in Figure 1.14. It is similar in both Gram types. Gram-positive bacteria have a thick (~250 Å) peptidoglycan layer which consists of sugars and amino acids and bound surface acids. It does not have the outer membrane which is present in gram-negative bacteria. It is thought that the lack of this extra barrier coupled with the gram stains affinity for the surface bound acid group increase the amount bound in the peptidoglycan layer. In gram-negative bacteria the peptidoglycan layer is only 30 Å thick. It is also thought that the outer layer of lipopolysaccharides in gram-negative bacteria help repel the dye.[118]

Typically, both configurations present a net negative charge, however the magnitude of the charge varies between the two groups and between bacterial species.[113,114,119] Previously, it has been found that the surface charge is influenced by physical

conditions such as growth medium,[120] age,[121] and surface structural features relating to differences across strains.[121–123] Understanding the structure of the cell envelope is critical to understanding these interactions, and the localised bacterial charge relates to cellular uptake and metabolism,[112] growth and division,[124] cell signalling,[112] cell adherence to substances,[96] and antibiotic resistance.[115,109] In this work the surface charge of individual gram-negative and gram-positive bacteria are directly compared.

1.6 Enamel and Dentine

Chapters 3 and 4 are concerned with using SICM to analyse enamel and dentine substrates. It is therefore necessary to give background information on the formation and structure of these complex materials and outline the dental problems this work explores.

1.6.1 Tooth Structure and Mineral Formation

A tooth is formed of three clear sections. The entire visible section of a typical molar is the crown which makes up about a third of the tooth length, with the rest of the structure, the root and neck being below the gum line (Figure 1.16). The neck is the region joining the root and crown, where the tooth erupts from the gum line and the root secures the tooth in the mouth and contains the pulp which houses nerves and blood vessels (this does protrude above gum line, encased in the crown). Enamel makes up the hard outer surface of the tooth. Its incredible tensile properties offer a surface that is resistant to wear and tear and endures substantial mechanical forces when chewing food.[125] It is a protective covering for the softer dentine underneath which has more ‘give’ largely due to its increased collagen content, complementing the rigidness of the enamel, and helps to dissipate the tensile forces associated with mastication.

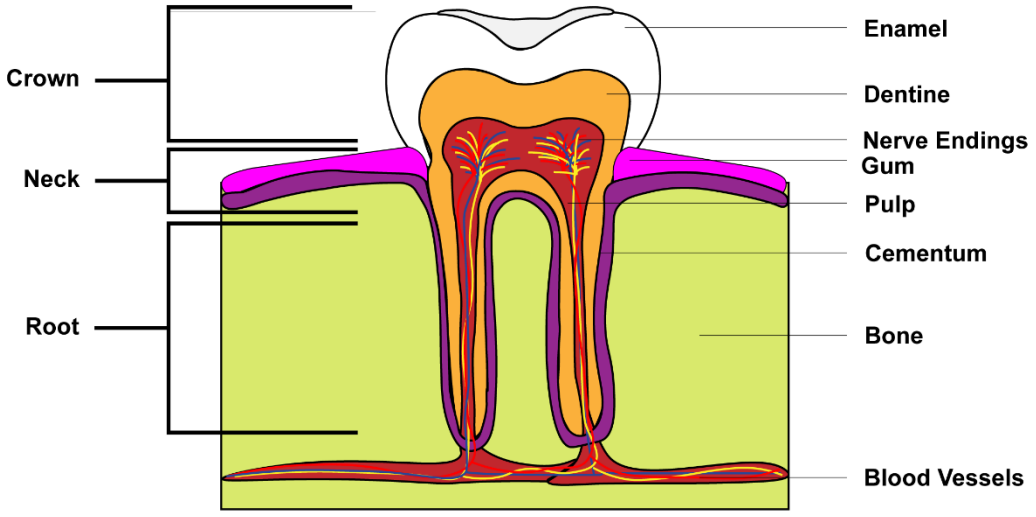

Figure 1.16 Structure of a Tooth

Diagram of a cross section of a typical human molar. Enamel is only present in the crown, the exposed part of the tooth that is tasked with chewing. The inner structure is made of dentine which supports the enamel layer and allows it to absorb pressure. The pulp which houses the nerves can be seen in red. The gum (pink) can be seen transitioning into the gingiva lining (purple) which surrounds the tooth root between the bone and cementum, a harder mineral phase of dentine, similar to enamel.

Both enamel and dentine are primarily comprised of HAP. The calcium and phosphate containing mineral has molecular formula $Ca_5(PO_4)_3(OH)$ and forms a twinned crystal unit cell, usually expressed as $Ca_{10}(PO_4)_6(OH)_2$. HAP is the main constituent of both enamel and dentine but is present in different ratios to complement their function. Enamel is around 90% HAP while dentine is around 70% HAP by weight.[126]

Both enamel and dentine have a complex multi-level structure. In enamel, the base building block is ~70 nm HAP crystals with a ~2 nm coating of enamelin surrounding each. They are packed into enamel rods, keyhole shaped structures around 6 µm across.[127] The rods themselves vary in length, depending on which section of the enamel is being observed, usually on the 10s of microns scale. Each rod is surrounded by a matrix of more disorganised HAP crystals, termed inter-rod enamel, it has a higher protein and water content than central rod enamel, with the crystals near perpendicular to the crystals in the rods.[128] This unique lattice like structure seen in Figure 1.17 arises due to the unusual formation of enamel in the gum. It begins with

ameloblast blast cells which are organised into a close packed structure by the dental proteins amelogenin and enamelin.[129] Once arranged in a grid the cells gradually calcify, forming the highly organised HAP packed structure.[128] HAP crystals also form in the area between the cells but they are not as tightly packed and contain more residual protein and trace elements such as magnesium as previously this area formed the cell wall of the ameloblast.[130] As the central regions of the enamel rods have a higher HAP % they are more prone to erosion. The inter-rod regions have a slower dissolution rate due to their increased biological component, the pure mineral being more vulnerable to dissolution.[131]

Structurally dentine is much more porous than enamel and is a living tissue, sensitive to pressure and pain. It is composed of thousands of fluid filled tubules which radiate outwards from near the pulp to the dentine enamel junction and cementum. The tubules represent the tracks taken by odontoblastic cells from the dentin-enamel junction to the pulp chamber. The density of tubules is highest closest to the pulp chamber where the odontoblastic cells lie in a closed packed array.[132] Lower tubule density is found in the root. As well as providing support for the inflexible enamel it allows transport of material through the tubules.

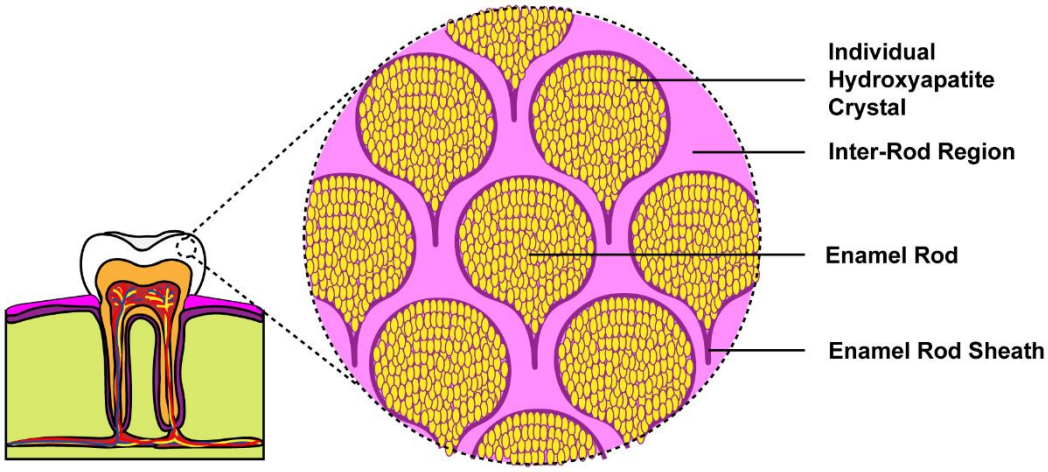

Figure 1.17 Enamel Rod Structure

An enhanced representation of enamel rod packing. Each rod is approximately 6 µm across. The close packed HAP crystals can be seen carefully aligned within the rod structure. The inter-rod enamel (pink) is also composed of HAP but is less ordered and contains more protein and trace elements. The rods alignment are key to the strength of the enamel, each one facing outward in an organised fashion, providing strength in a similar way to steel bars in concrete. The HAP crystals displayed are approximately 70 nm across.

Dentin is a complex hydrated biological composite structure for which only limited structure-property relationships are available. Furthermore, dentin is modified by physiological, aging and disease processes to create different forms of dentin. These forms are very poorly defined from the standpoint of structure and properties.[133] Some of the recognized variations include primary, secondary, reparative or tertiary, sclerotic, transparent, carious, demineralized, remineralised, and hyper-mineralised. The terms reflect alterations in the fundamental components of the structure, meaning statements on the overall structure and behaviour of dentine, in general, are often misleading. However, the lower mineral content, smaller HAP crystal size and less organised structure make dentine softer and less brittle than the overlaying enamel.

For comparative purposes, some SEM images of enamel, dentine and the enamel-dentine junction are provided for reference in Figure 1.18. The dentine tubules can be clearly seen and the contrast of the surface roughness between dentine and enamel is clear in the dentine-enamel junction image.

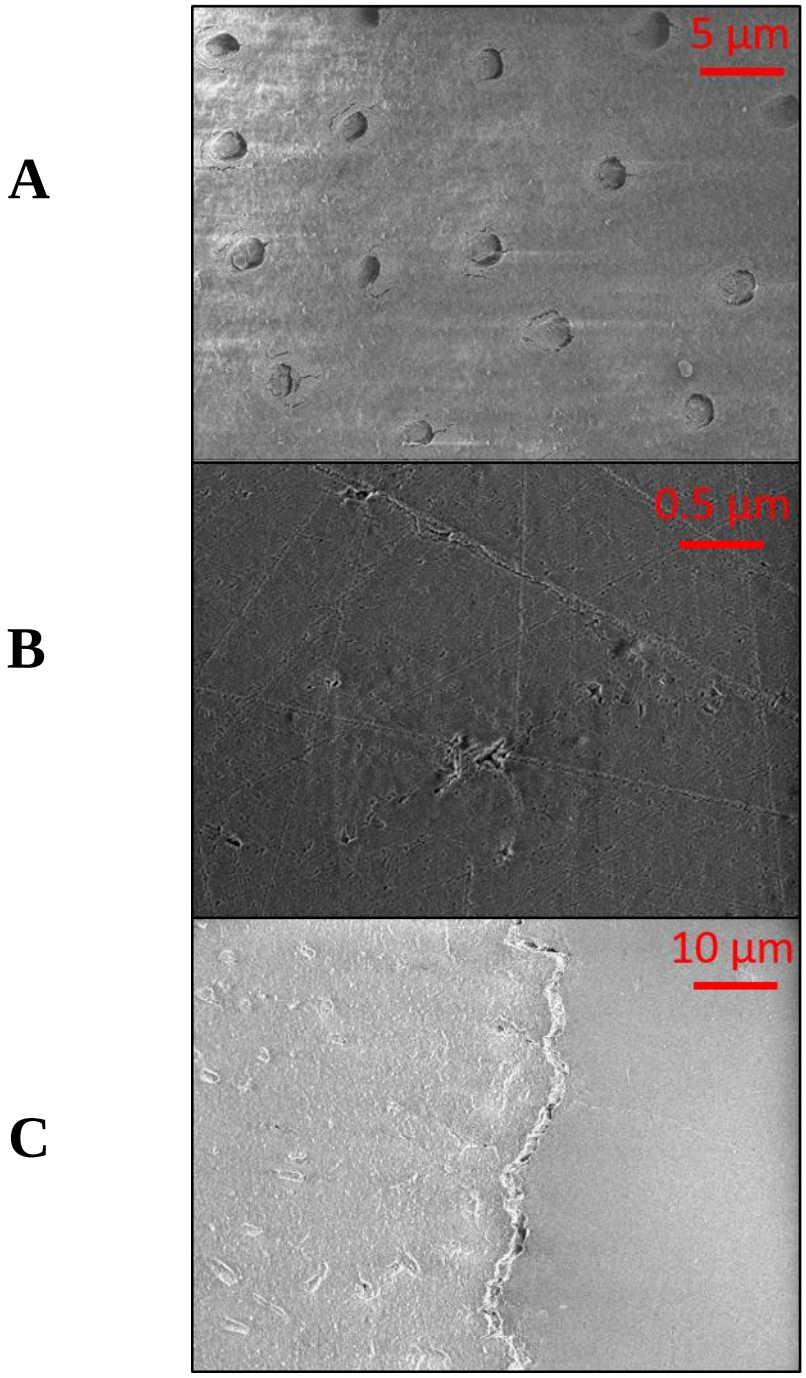

Figure 1.18 Dentine, Enamel and Enamel-Dentine Junction SEM Images

SEM images of dental surfaces. (A) Dentine with clear tubule structures. (B) Enamel surface with polishing lines. (C) Dentin-enamel junction with the dentine surface (LHS) appearing rougher than the enamel surface (RHS).

1.6.2 Dental Erosion

Dental erosion is widely prevalent throughout the globe, affecting all age groups and demographics and is on the increase.[134–136] Dental erosion can be defined as the irreversible loss of dental hard tissue without the action of microorganisms.[137] This is specifically not referring to dental caries, the clinical name for tooth decay, which requires the action of oral bacteria. *Streptococcus mutans* (as well as other bacteria) consume food debris, particularly sugars and excrete lactic acid as a by-product.[138] This cycle leads to cavity formation and is accelerated if the enamel layer is penetrated.[139] Good brushing habits can drastically reduce the effect of dental caries by removing the bacterial food supply, but the same is not true for acid erosion as the damage is done immediately upon exposure, not through the action of a by-product.

In this thesis the chemical action of dietary acids causing erosion through exposure is the area studied. Another under reported intrinsic cause of dental acid erosion that is considered within is repeated stomach acid exposure, particularly in cases of *bulimia nervosa* where sufferers experience repeated regurgitation, and therefore exposure to hydrochloric acid, with the back of the teeth being particularly susceptible.[140]

The problem of acid erosion is exaggerated by the modern diet, with increased consumption of carbonated acidic drinks and fruit juices being some of the worst contributors. The presence of dietary acids such as citric acid and phosphoric acid expose the enamel to a repeated corrosive challenge.[141,142] Studies investigating the contribution from dietary acid often focus on macro scale damage assessed by surface micro-hardness testing[143] and profilometry[141] with limited nanoscale damage assessments being undertaken using SEM [144], nano-scratch testing[145] and atomic force microscopy (AFM).[146] In this thesis SICM is employed to investigate dental erosion, with a particular focus on visualising early stage erosion.

The dissolution of HAP, the prime mineral component of enamel and dentine can be estimated by:[147]

$$Ca_{10}(PO_4)_6(OH)_{2(S)} + 8H^+_{(aq)} \rightleftharpoons 10Ca^{2+}_{(aq)} + 6HPO^{2-}_{4(aq)} + 2H_2O \quad \textbf{11)}$$

where protons provided by a dietary acid (or other source) react with the HAP and calcium ions, phosphates and water are produced. This equation provides the

foundation for dissolution investigated through FEM in this thesis. Due to the varied nature of enamel and dentine structure, and the different ratios of organic material and water to mineral within each, the dissolution processes modelled are only ever an estimate based on average densities and mineral contents. Attempts are made to account for these structural differences by altering the ratios of HAP to reflect the mineral being investigated, where applicable.

One of the underlying concerns of the damage caused by dental erosion is the prevalence of sub-surface lesions. If the enamel is eroded and the underlying dentine exposed, rates of chemical erosion increase drastically, facilitated partly by dentine being more susceptible to erosion and partly by the ease of transfer of acid through the dentine tubule system once exposed. Compound this with the cavities housing and sheltering bacteria which leads to carious decay and it is clear how the problem propagates to eventual tooth loss.[131,137,148]

For direct dissolution of HAP to occur the pH of the local environment needs to drop below pH 5. After eating, the pH of the oral cavity can remain between 5 and 7 for around 45 minutes but this varies from person to person and is dependent on what is eaten.[149] This risks HAP deprotonation but the buffering capacity of saliva (3–30 mg/100 ml) should minimize this in most individuals.[150] What causes distinct risk are transient periods of very low pH exposure. The pH of coca cola for example is around pH 2 and orange juice around pH 3. Consuming these shifts the pH into the erosive region for sustained periods and the mouths natural buffering capacity does not cope well with such large shifts, increasing the risk of damage.[141]

Figure 1.19 shows the relative solubilities of enamel, dentine and fluorapatite (FAP) and highlights the pH region where these dental minerals are most at risk of dissolution. The addition of fluoride to the HAP crystal has long been known to inhibit acid dissolution.[152] A detailed explanation of this is given in section 1.6.3.

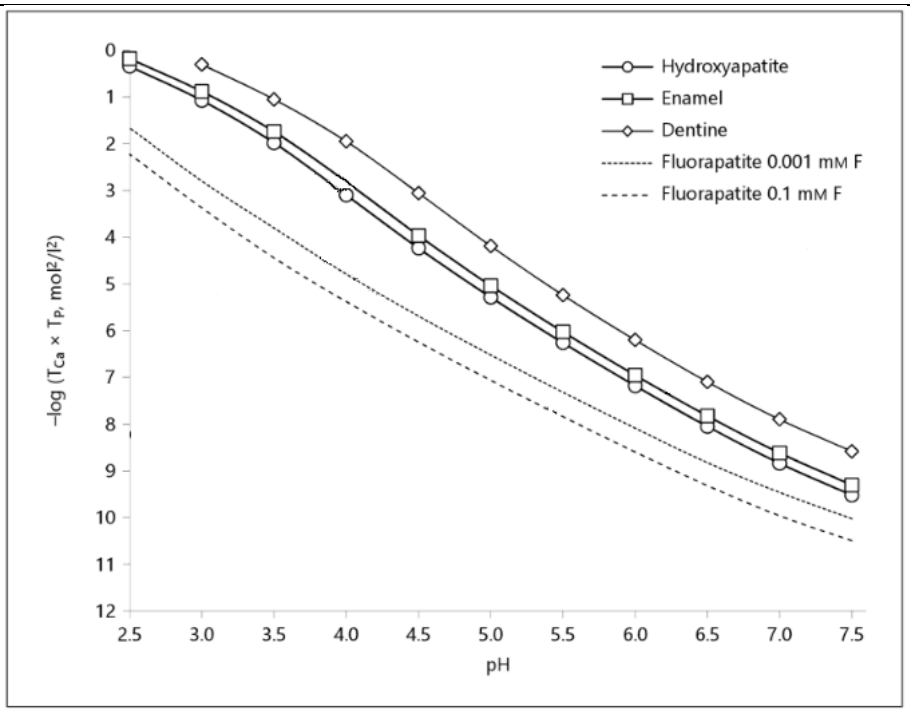

Figure 1.19 Relative Solubilities of Dental Hard Tissues

Adapted from Lussi et al.,[151] this figure shows the concentration at which the solutions saturate with respect to the respective solid. Each solid is dissolving in HCl with a Ca/P ratio of 5/3 at 37°C. The *y* axis is an inverted logarithmic scale referring to the total amount of solvated solid. A value of 0 represents a fully dissolved solid. Dentine is the most soluble, followed by enamel (which is close to the solubility of HAP) and fluoridated HAP has a drastically reduced solubility. As the scale is logarithmic a 1 unit change is a profound difference.

1.6.3 Fluoride

Fluoridation of drinking water is the single biggest contributor to improved dental health in the last century.[153,154] Since the 1950s rates of dental caries have dropped by some 40% in children in countries that have implemented fluoridation.[152] There is some debate that this benefit is not purely from the addition of fluoride to drinking water and that overall dental hygiene improvements and regular use of fluoride toothpastes have a larger impact. However, this passive improvement cannot be ignored. Due to the slow nature of the remineralisation process in the mouth a low-level continual supply of fluoride helps its inclusion in the outside protective layer of enamel.

Fluoride improves resistance to acid dissolution by substituting into the HAP lattice. OH groups present in HAP, which leave as water when substituted, are replaced with F^- ions that are more strongly bound. Once substituted the F^- ions stabilise neighbouring Ca^{2+} and a more difficult to remove than the OH groups they replace. If enough surface level HAP is substituted with F^- the surface behaves like FAP. As the dissolution kinetics of a crystal are governed by the dissolution properties of the surface, FAP only needs to form a surface layer to effectively alter the dissolution properties of the entire crystal, at least for a short time frame. This is indeed how fluoride is incorporated in the tooth structure with a thin layer of FAP forming at the interface due to the presence of low-level fluoride in saliva. Calcium and phosphates are present in low levels in human saliva as part of the mouths natural remineralisation process, which, when fluoride is present, produces a layer of FAP, or a fluoridated HAP depending on concentration.[151]

The inclusion of fluoride into the enamel surface is usually a gradual process, with fluoride incorporation happening over a period of months through passive accumulation.[155] In this work short treatments of moderate (single toothpaste usage level) concentration of fluoride are used on bovine enamel, primarily to test the sensitivity of the techniques used. Low level fluoride incorporation into the HAP lattice is difficult to detect and often transient, with the longer, repeated exposures leading to higher levels of fluoridation. In the cases of the dietary acid exposure studied, the moderate pH and short exposure times (30 s) lead to a low level of erosion, enough to be considered transient, because in the oral environment the tooth would be capable of repair through remineralisation. The purpose of the milder treatments is to test the limits of detection of the SICM based techniques and confirm the quantification of these initial, more subtle surface changes. Investigating this ‘early stage acid erosion’ is one of the key aims of this work.

1.6.4 Dietary Acids

An erosive challenge is a deliberate exposure of a substrate to an acidic substance in order to assess the damage caused and/or quantify the dissolution. As this thesis investigates dissolution processes in the oral cavity an explanation for the focus on dietary acids is warranted. From a dental perspective, dietary acids are good candidates for erosive challenges as they commonly come into contact with enamel in day to day

life. Citric acid and phosphoric acid are two of the most common and relevant, both being used heavily in the food and drinks industry as a flavour enhancer, acidity regulator and preservative.[155] Carbonated drinks often have a low pH due to addition of these chemicals. Orange juice is also naturally high in citric acid, giving it a naturally lower pH and sharp taste. Lactic acid (bacterial by-product) and hydrochloric acid (stomach acid) are the other two most relevant acids to dental erosion. This work focuses on citric acid and phosphoric acid due to their prevalence in food products.

Both citric and phosphoric acid are classed as weak acids, meaning they do not fully dissociate in aqueous solution. Both are tribasic acids, losing protons at 3 separate pK_a's (citric acid: 2.92, 4.28 and 5.21; phosphoric acid: 2.14, 7.2 and 12.4), fully dissociating around pH 2. Citric acid is also capable of metal chelation.[141,146,156] This is an important factor when considering its interaction with calcium containing HAP, the full details of which are discussed in chapters 4 where metal chelation caused by citric acid is inferred through SICM charge mapping experiments.

1.6.5 Salivary Pellicle

At several points in this work the effect of incorporating a salivary pellicle layer into the system is studied. The salivary pellicle is a protective film that is present in the oral cavity. It is a thin membrane like structure that coats all surfaces in the mouth. Varying in size from 10s to 100s of nanometres, it is composed of proteins secreted by the salivary glands and attaches to the enamel surface by selective binding of glycoproteins. It forms within minutes of a tooth being cleaned or within seconds after removal by chewing.[150,157–159] Its primary function is to protect the tooth from pH changes due to microbial activity or diet. Within minutes of the protein layer forming on a tooth, bacterial colonizers adhere. Many of these are harmless or beneficial to the mouth, but some, such as *Streptococcus mutans* play a role in carious decay. Others contribute to the build-up of plaque and have a role in the cycle that leads to anaerobic bacteria producing lactic acid and pushing the pH of the mouth towards the demineralisation zone.[160]

Historically, *in vitro* measurements on dental substrates often do not include a pellicle layer. It adds another layer of complexity and for many techniques, such as surface micro-hardness testing or SEM imaging, a dry sample is preferred. SICM only operates in a system with a liquid interface. This gives opportunity to study the effect

of the pellicle. There is a need to push to make *in vitro* studies more relevant to their *in vivo* counterparts. Closer simulation of a real oral environment will enhance the relevance of *in vitro* studies. Being able to introduce a pellicle, even though it is irradiated and sterile, is a step that is possible with SICM so should be capitalised upon. In this work we show the viability of incorporating a salivary pellicle into future *in vitro* experiments going forwards.

1.7 Aims of this Thesis

This introduction has detailed what SPMs are and discussed the pros and cons of the most widely used examples, particularly STM, AFM and SECM. SICM is introduced and its niche benefits high-lighted and a detailed explanation of its operating mechanics given. Background information on surface charge and the ion current response is provided and detailed information on the target substrates, particularly enamel, dentine and bacteria, are given. This sets the scene for a discussion of the main aims and motivations for undertaking this thesis and outlines what the work sets out to achieve.

SPM is a complex and ever-growing field and as the instrumentation becomes available to increasing numbers of research scientists the desire to expand its capability is a continuous endeavour. This work aims to contribute to this expansion of knowledge in two ways. Firstly, by using SICM to provide *in-situ* dissolution measurements of dental hard tissues. This is achieved by manipulating the bias applied to the nanopipette to deliver acid to a target substrate in a controlled manner. The conception, implementation and evaluation of this method for making quantifiable etch pits on a target surface is documented and its viability as a screening tool to measure dental erosion discussed. Secondly, SCM with SICM has recently emerged as a promising secondary mode of the technique, and this work concerns itself with expanding its use with more challenging biological substrates. SCM offers functional imaging of the ion concentration at the liquid solid interface and has so far been used to assess carefully chosen, stable substrates such as polymer films and fixed cells, this work expands this by attempting to use the surface charge as an indicator of acid damage to dental hard tissues and for the quantification of the charge of live bacterial substrates.

Utilising secondary modes of SICM requires careful experimental design, the details of which can be found in chapter 2. Chapter 3, the first results chapter covers, the conception of SICM potential controlled acid delivery (PCAD) as a secondary mode of SICM. The development is documented from single etch pit measurements to gathering statistically relevant data from multiple arrays of measurements across different samples.

Chapter 4 details the use of SCM on dental substrates. Charged domains on the substrate surface are assessed and quantified through FEM modelling. The charge response to demineralising and remineralising solutions are investigated. The viability of this method for assessing repair and surface damage is discussed.

Chapter 5 expands SCM to live bacterial samples. Adhesion methods for live sample imaging are tested. Gram-positive and gram-negative bacteria are compared and a suitable FEM model is used to assess the surface charge in each case. Conclusions are drawn on the suitability and limitations of the current models.

Overall, this thesis seeks to further the uses of SICM in the analysis of challenging substrates and explores advanced methods of extracting useful data on the physical and chemical properties of the samples studied. The niche advantages of SICM over other imaging techniques are utilised to provide robust data on previously under studied substrates and exciting secondary modes of SICM provide intriguing new insights.

1.8 References

1 P. K. Hansma, B. Drake, O. Marti, S. A. C. Gould and C. B. Prater, *Science (80-.).*, 1989, **243**, 641–643.

2 A. Cricenti, S. Colonna, M. Girasole, P. Gori, F. Ronci, G. Longo, S. Dinarelli, M. Luce, M. Rinaldi and M. Ortenzi, *J. Phys. D. Appl. Phys.*, , DOI:10.1088/0022-3727/44/46/464008.

3 G. Binnig, H. Rohrer, C. Gerber and E. Weibel, *Appl. Phys. Lett.*, 1982, **40**, 178–180.

4 E. DM and S. EK, *Nature*, 1990, **344**, 524.

5 M. F. Crommie, C. P. Lutz and D. M. Eigler, *Science (80-.).*, 1993, **262**, 218 LP – 220.

6 G. Binnig, C. F. Quate and C. Gerber, *Phys. Rev. Lett.*, , DOI:10.1103/PhysRevLett.56.930.

7 G. M. King, A. R. Carter, A. B. Churnside, L. S. Eberle and T. T. Perkins, *Nano Lett.*, 2009, **9**, 1451–1456.

8 F. J. Giessibl, *Rev. Mod. Phys.*, 2003, **75**, 949–983.

9 S. Akamine, R. C. Barrett and C. F. Quate, *Appl. Phys. Lett.*, 1990, **57**, 316–318.

10 H. J. Butt, B. Cappella and M. Kappl, *Surf. Sci. Rep.*, 2005, **59**, 1–152.

11 Y. F. Dufrene, *Microsc. Anal.*, 2003, **97**, 9–11.

12 C. Marlière and S. Dhahri, *Nanoscale*, 2015, **7**, 8843–8857.

13 Q. Thong and D. Inniss, .

14 N. A. Geisse, *Mater. Today*, 2009, **12**, 40–45.

15 C. Chen, Y. Zhou and L. A. Baker, , DOI:10.1146/annurev-anchem-062011-143203.

16 C. Li, N. Johnson, V. Ostanin, A. Shevchuk, L. Ying, Y. Korchev and D. Klenerman, *Prog. Nat. Sci.*, 2008, **18**, 671–677.

17 A. J. Bard, F. R. F. Fan, J. Kwak and O. Lev, *Anal. Chem.*, 1989, **61**, 132–138.

18 S. Amemiya, A. J. Bard, F.-R. F. Fan, M. V. Mirkin and P. R. Unwin, *Annu. Rev. Anal. Chem.*, 2008, **1**, 95–131.

19 A. L. Barker, M. Gonsalves, J. V. MacPherson, C. J. Slevin and P. R. Unwin, *Anal. Chim. Acta*, 1999, **385**, 223–240.

20 P. R. Unwin and A. J. Bard, *J. Phys. Chem.*, 1991, **95**, 7814–7824.

21 A. J. Bard, F. F. Fan, D. T. Pierce, P. R. Unwin, D. O. Wipf, D. Wipf and F. Zhou, *Science*, 2012, **254**, 68–74.

22 A. J. Bard, M. V. Mirkin, P. R. Unwin and D. O. Wipf, *J. Phys. Chem.*, 1992, **96**, 1861–1868.

23 N. Ebejer, A. G. Güell, S. C. S. Lai, K. McKelvey, M. E. Snowden and P. R. Unwin, *Annu. Rev. Anal. Chem.*, 2013, **6**, 329–351.

24 B. D. B. Aaronson, J. C. Byers, A. W. Colburn, K. McKelvey and P. R. Unwin, *Anal. Chem.*, 2015, **87**, 4129–4133.

25 C. L. Bentley, M. Kang and P. R. Unwin, *Curr. Opin. Electrochem.*, 2017, **6**, 23–30.

26 L. C. Yule, C. L. Bentley, G. West, B. A. Shollock and P. R. Unwin, *Electrochim. Acta*, 2019, **298**, 80–88.

27 C. L. Bentley, M. Kang, F. M. Maddar, F. Li, M. Walker, J. Zhang and P. R. Unwin, *Chem. Sci.*, 2017, **8**, 6583–6593.

28 B. Tao, L. C. Yule, E. Daviddi, C. L. Bentley and P. R. Unwin, *Angew. Chemie - Int. Ed.*, 2019, **58**, 4606–4611.

29 A. S. Parker, R. Al Botros, S. L. Kinnear, M. E. Snowden, K. McKelvey, A. T. Ashcroft, M. Carvell, A. Joiner, M. Peruffo, C. Philpotts and P. R. Unwin, *J. Colloid Interface Sci.*, 2016, **476**, 94–102.

30 C. L. Bentley, M. Kang and P. R. Unwin, *Curr. Opin. Electrochem.*, 2017, **6**, 23–30.

31 E. E. Oseland, Z. J. Ayres, A. Basile, D. M. Haddleton, P. Wilson and P. R.

Unwin, *Chem. Commun.*, 2016, **52**, 9929–9932.

32 C. L. Bentley, M. Kang and P. R. Unwin, *J. Am. Chem. Soc.*, 2017, **139**, 16813–16821.

33 C. Felipe, S. Albert and S. Wolfgang, *Proc. R. Soc. A Math. Phys. Eng. Sci.*, 2018, **474**, 20180409.

34 T. E. Lin, S. Rapino, H. H. Girault and A. Lesch, *Chem. Sci.*, 2018, **9**, 4546–4554.

35 M. A. O'Connell and A. J. Wain, *Anal. Methods*, 2015, **7**, 6983–6999.

36 N. Nioradze, R. Chen, J. Kim, M. Shen, P. Santhosh and S. Amemiya, *Anal. Chem.*, 2013, **85**, 6198–6202.

37 P. Sun and M. V. Mirkin, *Anal. Chem.*, 2006, **78**, 6526–6534.

38 J. Kim, C. Renault, N. Nioradze, N. Arroyo-Currás, K. C. Leonard and A. J. Bard, *J. Am. Chem. Soc.*, 2016, **138**, 8560–8568.

39 C. Felipe, S. Albert and S. Wolfgang, *Proc. R. Soc. A Math. Phys. Eng. Sci.*, 2018, **474**, 20180409.

40 P. Novak, C. Li, A. I. Shevchuk, R. Stepanyan, M. Caldwell, S. Hughes, T. G. Smart, J. Gorelik, V. P. Ostanin, M. J. Lab, G. W. J. Moss, G. I. Frolenkov, D. Klenerman and Y. E. Korchev, *Nat. Methods*, 2009, **6**, 279–281.

41 C.-C. Chen, Y. Zhou and L. A. Baker, *Annu. Rev. Anal. Chem.*, 2012, **5**, 207–228.

42 A. Page, D. Perry and P. R. Unwin, *Proc. R. Soc. A*, 2017, **473**, 1–34.

43 A. Page, D. Perry, P. Young, D. Mitchell, B. G. Frenguelli and P. R. Unwin, *Anal. Chem.*, 2016, **88**, 10854–10859.

44 B. Babakinejad, P. Jönsson, A. López Córdoba, P. Actis, P. Novak, Y. Takahashi, A. Shevchuk, U. Anand, P. Anand, A. Drews, A. Ferrer-Montiel, D. Klenerman and Y. E. Korchev, *Anal. Chem.*, 2013, **85**, 9333–9342.

45 R. Lazenby and R. White, *Chemosensors*, 2018, **6**, 24.

46 A. E. Weber and L. A. Baker, *J. Electrochem. Soc.*, 2014, **161**, H924–H929.

47 Y. Takahashi, H. Ida, Y. Matsumae, H. Komaki, Y. Zhou, A. Kumatani, M. Kanzaki, H. Shiku and T. Matsue, *Phys. Chem. Chem. Phys.*, 2017, **19**, 26728–26733.

48 A. I. Shevchuk, G. I. Frolenkov, D. Sánchez, P. S. James, N. Freedman, M. J. Lab, R. Jones, D. Klenerman and Y. E. Korchev, *Angew. Chemie - Int. Ed.*, 2006, **45**, 2212–2216.

49 C. C. Chen and L. A. Baker, *Analyst*, 2011, **136**, 90–97.

50 D. Perry, B. Paulose Nadappuram, D. Momotenko, P. D. Voyias, A. Page, G. Tripathi, B. G. Frenguelli and P. R. Unwin, *J. Am. Chem. Soc.*, 2016, **138**, 3152–3160.

51 K. McKelvey, D. Perry, J. C. Byers, A. W. Colburn and P. R. Unwin, *Anal. Chem.*, 2014, **86**, 3639–3646.

52 D. Perry, R. Al Botros, D. Momotenko, S. L. Kinnear and P. R. Unwin, , DOI:10.1021/acsnano.5b02095.

53 D. Perry, R. Al Botros, D. Momotenko, S. L. Kinnear and P. R. Unwin, *ACS Nano*, 2015, **9**, 7266–7276.

54 K. Mckelvey, S. L. Kinnear, D. Perry, D. Momotenko and P. R. Unwin, .

55 D. Perry, A. Page, B. Chen, B. G. Frenguelli and P. R. Unwin, *Anal. Chem.*, 2017, **89**, 12458–12465.

56 D. Perry, D. Momotenko, R. A. Lazenby, M. Kang and P. R. Unwin, *Anal. Chem.*, 2016, **88**, 5523–5530.

57 C. Wei, A. J. Bard and S. W. Feldberg, *Anal. Chem.*, 2002, **69**, 4627–4633.

58 H. S. White and A. Bund, *Langmuir*, 2008, **24**, 2212–2218.

59 D. Momotenko, F. Cortés-Salazar, J. Josserand, S. Liu, Y. Shao and H. H. Girault, *Phys. Chem. Chem. Phys.*, 2011, **13**, 5430–5440.

60 Z. Siwy, E. Heins, C. C. Harrell, P. Kohli and C. R. Martin, *J. Am. Chem. Soc.*, 2004, **126**, 10850–10851.

61 S. H. Behrens and D. G. Grier, *J. Chem. Phys.*, 2001, **115**, 6716–6721.

62 A. Page, D. Perry and P. R. Unwin, *Proc. R. Soc. A*, 2017, **473**, 1–34.

63 W. M. Haynes, *CRC handbook of chemistry and physics*, CRC press, 2014.

64 Helmholtz, *Ann Phys. Chemie*, 1853, **89**, 211–233.

65 D. C. Grahame, *Chem. Rev.*, 1947, **41**, 441–501.

66 B. J. Kirby and E. F. Hasselbrink, *Electrophoresis*, 2004, **25**, 187–202.

67 A. Bard and L. Faulkner, *Fundamentals and applications*, 2001.

68 X. Shi, Y. Bi, W. Yang, X. Guo, Y. Jiang, C. Wan, L. Li, Y. Bai, J. Guo, Y. Wang, X. Chen, B. Wu, H. Sun, W. Liu, J. Wang and C. Xu, *Nature*, 2013, **493**, 111–115.

69 A. Terada, K. Okuyama, M. Nishikawa, S. Tsuneda and M. Hosomi, *Biotechnol. Bioeng.*, 2012, **109**, 1745–1754.

70 R. W. O. and L. R. White and S. C. Particle, *J. Chem. Soc. Faraday Trans. 2 Mol. Chem. Phys.*, 1978, **74**, 1607–1626.

71 M. Marie, .

72 D. Hanaor, C. Sorrell, M. Michelazzi, P. Veronesi, C. Leonelli and M. Romagnoli, *J. Eur. Ceram. Soc.*, 2011, **31**, 1041–1047.

73 Y. W. Liu, S. Pennathur and C. D. Meinhart, *Phys. Fluids*, , DOI:10.1063/1.4901330.

74 J. C. W. Corbett, F. McNeil-Watson, R. O. Jack and M. Howarth, *Colloids Surfaces A Physicochem. Eng. Asp.*, 2012, **396**, 169–176.

75 J. V. Macpherson and P. R. Unwin, *Anal. Chem.*, 2000, **72**, 276–285.

76 C. Kranz, G. Friedbacher, B. Mizaikofft, A. Lugstein, J. Smoliner and E. Bertagnolli, *Anal. Chem.*, 2001, **73**, 2491–2500.

77 C. Vericat, M. E. Vela, G. Benitez, P. Carro and R. C. Salvarezza, *Chem. Soc. Rev.*, 2010, **39**, 1805–1834.

78 A. Noy, C. D. Frisbie, L. F. Rozsnyai, M. S. Wrighton and C. M. Lieber, *J. Am. Chem. Soc.*, 2005, **117**, 7943–7951.

79 W. F. Heinz and J. H. Hoh, *Biophys. J.*, 1999, **76**, 528–538.

80 D. Esteban-Ferrer, M. A. Edwards, L. Fumagalli, A. Juárez and G. Gomila, *ACS Nano*, 2014, **8**, 9843–9849.

81 *J. Phys. Condens. Matter*, 2000, **12**, 795–814.

82 S. Xu and M. F. Arnsdorf, *Proc. Natl. Acad. Sci.*, 2006, **92**, 10384–10388.

83 D. D. Kulkarni, S. Kim, M. Chyasnavichyus, K. Hu, A. G. Fedorov and V. V. Tsukruk, *J. Am. Chem. Soc.*, 2014, **136**, 6546–6549.

84 N. S. Malvankar, S. E. Yalcin, M. T. Tuominen and D. R. Lovley, *Nat. Nanotechnol.*, 2014, **9**, 1012–1017.

85 *J. Appl. Phys.*, 1998, **84**, 1168–1173.

86 Y. J. Li, H. Wen, Z. M. Ma, L. Kou, Y. Naitoh and Y. Sugawara, 2018, **2921**, 437–463.

87 W. Melitz, J. Shen, A. C. Kummel and S. Lee, *Surf. Sci. Rep.*, 2011, **66**, 1–27.

88 N. G. Clack, K. Salaita and J. T. Groves, *Nat. Biotechnol.*, 2008, **26**, 825–830.

89 E. Finote, Y. Leonenko, B. Moores, L. Eng, M. Amrein and Z. Leonenko, *Langmuir*, 2010, **26**, 1929–1935.

90 M. J. Daly, F. J. Brockman, H. M. Kostandarithes, M. F. Romine, D. Kennedy, J. M. Zachara, S. -m. W. Li, D. L. Balkwill and J. K. Fredrickson, *Appl. Environ. Microbiol.*, 2004, **70**, 4230–4241.

91 S. J. Moore and M. J. Warren, *Biochem. Soc. Trans.*, 2012, **40**, 581–586.

92 H. Fang, J. Kang and D. Zhang, *Microb. Cell Fact.*, 2017, **16**, 1–14.

93 M. Roberts, M. J. Reiss and G. Monger, *Advanced biology*, Nelson, 2004.

94 I. S. Roberts, *Annu. Rev. Microbiol.*, 2002, **50**, 285–315.

95 L. J. Alderwick, J. Harrison, G. S. Lloyd and H. L. Birch, 2015, 1–15.

96 H. J. Busscher and H. C. van der Mei, *PLoS Pathog.*, 2012, **8**, e1002440.

97 H. N. Schulz and B. B. Jørgensen, *Molecules*.

98 A. J. Alanis, *Arch. Med. Res.*, 2005, **36**, 697–705.

99 D. H. Williams and B. Bardsley, *ChemInform*, 2010, **30**, no-no.

100 L. D. R. Bond D.R, *Appl. Environ. Microbiol.*, 2003, **69**, 1548–1555.

101 A. T. W. M. Hendriks and G. Zeeman, *Bioresour. Technol.*, 2009, **100**, 10–18.

102 R. J. Müller, I. Kleeberg and W. D. Deckwer, *J. Biotechnol.*, 2001, **86**, 87–95.

103 H. Liu and H. H. P. Fang, *Biotechnol. Bioeng.*, 2002, **80**, 806–811.

104 R. Tedja, M. Lim, R. Amal and C. Marquis, *ACS Nano*, 2012, **6**, 4083–4093.

105 A. Adem Bahar, Z. Liu, M. Garafalo, N. Kallenbach and D. Ren, *Pharmaceuticals*, 2015, **8**, 696–710.

106 N. Malanovic, *Biochim. Biophys. Acta - Biomembr.*, 2016, **1858**, 936–946.

107 A. J. Park, J. P. Okhovat and J. Kim, *Clin. Basic Immunodermatology Second Ed.*, 2017, 81–95.

108 T. Koprivnjak, A. Peschel, M. H. Gelb, N. S. Liang and J. P. Weiss, *J. Biol. Chem.*, 2002, **277**, 47636–47644.

109 T. J. Silhavy, D. Kahne and S. Walker, *Cold Spring Harb. Perspect. Biol.*, 2010, **2**, 1–16.

110 D. J. Müller, D. Fotiadis, S. Scheuring, S. A. Müller and A. Engel, *Biophys. J.*, 1999, **76**, 1101–1111.

111 H. J. Wintle, *Meas. Sci. Technol.*, 1997, **8**, 508–513.

112 F. Wu, B. Zhou, J. Wang, M. Zhong, A. Das, M. Watkinson, K. A. Hing, D.-W. Zhang and S. Krause, *Anal. Chem.*, , DOI:10.1021/acs.analchem.9b00304.

113 W. A. Corpe, in *Adhesion in biological systems*, ed. R. S. Manly, Academic Press, Inc., New York, 1970.

114 J. S. Dickson, M. Koohmaraie and R. L. Hruska, *Cell Surface Charge Characteristics and Their Relationship to Bacterial Attachment to Meat Surfaces*, 1989, vol. 55.

115 J. Dankert, A. H. Hogt and J. Feijen, *Crit. Reu Biocompat*.

116 J. WECKE, M. PEREGO and W. FISCHER, *Microb. Drug Resist.*, 1996, **2**, 123–129.

117 J. Wecke, K. Madela' and W. Fixher, *The absence of D-alanine from lipoteichoic acid and wall teichoic acid alters surface charge, enhances autolysis and increases susceptibility to rnethicillin in Bacillus subtilis*, 2018, vol. 143.

118 R. Coico, in *Current Protocols in Microbiology*, John Wiley & Sons, Inc., Hoboken, NJ, USA, 2005, vol. Appendix 3, p. Appendix 3C.

119 A. Van Der Wal, W. Norde, A. J. B. Zehnder and J. Lyklema, *Determination of the total charge in the cell walls of Gram-positive bacteria*, 1997, vol. 9.

120 X. X. Sheng, Y. P. Ting and S. O. Pehkonen, *J. Colloid Interface Sci.*, , DOI:10.1016/j.jcis.2008.02.038.

121 Y. H. An and R. J. Friedman, *J. Biomed. Mater. Res.*, 1998, **43**, 338–348.

122 T. J. Beveridge, *Int. Rev. Cytol.*, 1981, **72**, 229–317.

123 J. Dankert, A. H. Hogt and J. Feijen, *Crit. Reu Biocompat*.

124 J. Y. Wong, R. Langer and D. E. Ingber, *Proc. Natl. Acad. Sci. U. S. A.*, 1994, **91**, 3201–4.

125 J. L. Cuy, A. B. Mann, K. J. Livi, M. F. Teaford and T. P. Weihs, *Arch. Oral Biol.*, 2002, **47**, 281–291.

126 R. Shellis, J. Featherstone and A. Lussi, in *Monogr Oral Sci*, 2012, vol. 25, pp. 163–179.

127 C. Robinson, S. Connell, J. Kirkham, R. Shore and A. Smith, *J. Mater. Chem.*, 2004, **14**, 2242–2248.

128 H. Warshawsky, *Anat. Rec.*, 1989, **224**, 242–262.

129 A. G. Fincham, J. Moradian-Oldak and J. P. Simmer, *J. Struct. Biol.*, 1999, **126**, 270–299.

130 R. E. Ferences, 2012, **192**, 565–568.

131 N. X. West and A. Joiner, *J. Dent.*, 2014, **42**, S2–S11.

132 J. R. Marshall, S. J. Marshall, J. H. Kinney and M. Balooch, *J. Dent.*, 1997, **25**, 441–458.

133 G. W. Marshall Jr., *Quintessence Int. (Berl).*, 1993, **24**, 606–617.

134 Y. H. Al-Dlaigan, L. Shaw and a J. Smith, *Br. Dent. J.*, 2002, **192**, 526–530.

135 N. J. Kassebaum, E. Bernabé, M. Dahiya, B. Bhandari, C. J. L. Murray and W. Marcenes, *J. Dent. Res.*, 2015, **94**, 650–658.

136 J. E. Frencken, P. Sharma, L. Stenhouse, D. Green, D. Laverty and T. Dietrich, *J. Clin. Periodontol.*, 2017, **44**, S94–S105.

137 T. Imfeld, *Eur J Oral Sci*, 1996, **104**, 151–155.

138 W. J. Loesche, *Microbiol. Rev.*, 1986, **50**, 353–380.

139 O. Fejerskov, *Community Dent. Oral Epidemiol.*, 1997, **25**, 5–12.

140 I. Rytömaa, V. Järvinen, R. Kanerva and O. P. Heinonen, *Acta Odontol. Scand.*, 1998, **56**, 36–40.

141 N. X. West, J. a Hughes and M. Addy, *J. Oral Rehabil.*, 2001, **28**, 860–864.

142 N. X. West, A. Maxwell, J. A. Hughes, D. M. Parker, R. G. Newcombe and M. Addy, *J. Dent.*, 1998, **26**, 329–335.

143 T. Attin, U. Koidl, W. Buchalla, H. G. Schaller, A. M. Kielbassa and E. Hellwig, *Arch. Oral Biol.*, 1997, **42**, 243–250.

144 M. Eisenburger, M. Addy, J. A. Hughes and R. P. Shellis, *Caries Res.*, 2001, **35**, 211–215.

145 S. X. R. Kwek, M. Mian, C. Hall, Z. Xie, R. Yong, J. Kaidonis, G. C. Townsend and S. Ranjitkar, *Aust. Dent. J.*, 2015, **60**, 12–17.

146 Z. J. Cheng, X. M. Wang, F. Z. Cui, J. Ge and J. X. Yan, *Biomed. Mater.*, , DOI:10.1088/1748-6041/4/1/015020.

147 J. A. Gray, *J. Dent. Res.*, 1962, **41**, 633–645.

148 B. Baird, 2007, **20**, 18–19.

149 P. Lingström, T. Imfeld and D. Birkhed, *J. Dent. Res.*, 2010, **72**, 865–870.

150 M. Hannig and C. Hannig, in *Monographs in Oral Science*, 2014, vol. 25, pp. 206–214.

151 R. Shellis, J. Featherstone and A. Lussi, in *Monogr Oral Sci*, 2012, vol. 25, pp. 163–179.

152 J. D. B. Featherstone, *Community Dent. Oral Epidemiol.*, 1999, **27**, 31–40.

153 C. Parnell, H. Whelton and D. O'Mullane, *Eur. Arch. Paediatr. Dent.*, 2009, **10**, 141–148.

154 Z. Iheozor-Ejiofor, H. V Worthington, T. Walsh, L. O'Malley, J. E. Clarkson, R. Macey, R. Alam, P. Tugwell, V. Welch and A. M. Glenny, *Cochrane Database Syst. Rev.*, , DOI:10.1002/14651858.CD010856.pub2.

155 P. Moynihan and P. E. Petersen, *Public Health Nutr.*, 2004, **7**, 201–226.

156 Y. Yoshida, B. Van Meerbeek, Y. Nakayama, M. Yoshioka, J. Snauwaert, Y. Abe, P. Lambrechts, G. Vanherle and M. Okazaki, *J. Dent. Res.*, 2001, **80**, 1565–1569.

157 A. T. Hara and D. T. Zero, in *Monographs in Oral Science*, 2014, vol. 25, pp. 197–205.

158 J. M. Tanzer, J. Livingston and A. M. Thompson, *J. Dent. Educ.*, 2001, **65**, 1028–37.

159 Y. F. Zhang, D. Y. Li, J. X. Yu and H. T. He, *J. Dent.*, 2016, **55**, 99–104.

160 A. Wiegand, A. Rosemann, M. Hoch, S. Barke, M. Dakna and P. Kanzow, *Caries Res.*, , DOI:10.1159/000500046.

2 Experimental Methods

This section details the chemicals and equipment used throughout the proceeding chapters. Bovine enamel sample preparation is detailed. The specifications for the SICM rigs and all supporting techniques are detailed.

2.1 Chemicals

Table 1 lists the materials and chemicals that were used including their purity and supplier. The exact concentrations of solutions used are detailed in the relevant chapters. Chemicals were weighed on an AE Adam AAA 100LE analytical balance to an accuracy of ± 0.1 mg. All solutions were made to volume in Milli-Q water (resistivity > 18.2 MΩ.m at 25 ºC) and all pH measurements were performed using a Mettler Toledo InLab expert pro pH meter.

Table 1 Chemical List

Chemical	Purity	Supplier	Concentration
Potassium Chloride	99.95%	Sigma-Aldrich	50 mM
Hydrochloric Acid	37%	Sigma-Aldrich	20 mM
Sodium Fluoride	99%	Fischer Scientific	35 mM
Zinc Chloride	98%	Sigma-Aldrich	10 mM
Citric Acid	99.5%	Fischer Scientific	1 % w/w
TRIS	99.9%	Sigma-Aldrich	Saturated
Phosphoric Acid	85%	Sigma-Aldrich	0.05 M
Magnesium Chloride Hexahydrate	99%	Sigma-Aldrich	0.2 mM
Calcium Chloride Dihydrate	99%	Sigma-Aldrich	1 mM
Potassium Dihydrogen Orthophosphate	99%	Sigma-Aldrich	4 mM
HEPES	99.5%	Sigma-Aldrich	20 mM

Ammonium Chloride	99.5%	Sigma-Aldrich	4.5 mM
Sodium Hydroxide	97%	Sigma-Aldrich	2 M
Agarose	99.95%	Cleaver Scientific	varied
Poly-L-Lysine	99.5%	Sigma-Aldrich	varied
Cel-Tak	N/A	Corning	varied
Clarified Human Saliva	N/A	Unilever	N/A
Bacteria growth media detailed in Appendix 7.4.			

Milli-Q reagent grade water (resistivity ca. 18.2MΩ cm at 25 °C) was used in the preparation of all solutions. (DI water), 50 mM potassium chloride (Sigma-Aldrich) was used as supporting electrolyte for the SICM charge mapping experiments, buffered to pH 7.2 with a saturated TRIS (tris(hydroxymethyl)aminomethane, Sigma-Aldrich) solution and adjusted dropwise with hydrochloric acid (1 M, Sigma Aldrich). Citric acid solution (1 % w/w, Fischer scientific, pH 3.6) was pH adjusted with saturated potassium hydroxide solution (Sigma-Aldrich.) Phosphoric acid (0.05 M, Sigma-Aldrich, pH 3.6) made by diluting 85% stock and was pH adjusted in the same manner as the citric acid. Hydrochloric acid (0.05 M, Sigma-Aldrich, pH 1.3) was used for the HCl stomach acid exposure experiment.

In chapter 4 for the remineralization experiments 1 L of remineralization solution was prepared using magnesium chloride hexahydrate (0.2 mM, Sigma Aldrich), calcium chloride dihydrate (1 mM, Sigma Aldrich), potassium dihydrogen orthophosphate (4 mM, Sigma Aldrich), HEPES (20 mM, Sigma Aldrich), potassium chloride (16 mM, Sigma Aldrich), and ammonium chloride (4.5 mM, Sigma Aldrich.) This was adjusted to pH 7 dropwise with sodium hydroxide (2 M, Sigma Aldrich.)

2.2 Bovine Enamel Preparation

There are structural differences between bovine and human enamel. The odontoblast cells that form the enamel are larger in cows, leading to an increased enamel rod and inter-rod region size compared with humans. It is difficult to know how much fluoride

exposure each sample has experienced without employing time consuming or destructive techniques such as XPS. The scale of the experiments and sheer number of samples required across the course of gathering the data for this thesis made working with human samples impractical from a cost and logistics perspective as human tissue has much stricter regulation. The trade-off was considered worthwhile as bovine enamel is considered a close representation by most dental scientists, though small differences in biology must rightly be acknowledged.

2.2.1 Polished Bovine Enamel

Bovine enamel blocks 4×4 mm area and 1.5 mm thickness were acquired from Intertek (Wirral, UK). Cut from buccal sections of bovine molars. A clear division can be seen when the sample is viewed side on, the top half of the sample being enamel and the bottom half dentine. The rough cutting is done with a diamond saw and the samples polished to a 3 µm finish with aluminium oxide suspension and a polishing disc before leaving the supplier. Before use, each sample is hand polished with diamond polish sprays (Kemet ltd) and polishing pads (Buehler), working down through the following grain sizes: 3 µm, 1 µm, 0.5 µm, 0.25 µm and 0.1 µm. A 50 nm diamond lapping compound (Buelher) for use with silk polishing pads (Struers) was used for the final polish. Samples were thoroughly rinsed between grain sizes and sonicated for 2 minutes (Decon F5200b) after the final polish. Samples were typically mounted onto glass petri dishes (4 cm diameter, WilcoWells) using a small amount of nail polish which is allowed to set for 1 hour. The petri dishes have an attachable plastic rim (WilcoWells) which forms the SICM cell which allows the sample to be submerged in electrolyte when mounted into the rig. AFM measurements reveal the sample surface roughness to be sub 20 nm after this procedure.

2.2.2 Aligned Bovine Samples

The aligned bovine enamel samples used in section 3.2.5 were prepared by first carefully aligning and then mounting the samples on a steel anvil with dental wax by their undersides. 2 thin (150 µm) sections are then cut from each sample down the transverse axis. Samples are then polished to remove any ridges remaining from the sectioning a process ensuring their thickness remains constant at 80 µm. Samples are mounted on a removable acetate sample frame for transporting. This process was

performed in house at Unilever (Wirral, UK) by Dr Gareth Owens and the samples posted to Warwick.

2.2.3 Bovine Dentine Blocks

The dentine samples are simply the underside of the enamel samples detailed in section 2.2.1. They undergo the exact same polishing regime as the polished bovine enamel, with the dentine side polished. The surface roughness is more difficult to discern due to the dentine tubule pitted surface but is estimated by AFM to be sub 50 nm after this procedure.

2.3 Bacterial Sample Culturing and Preparation

Bacterial samples were cultured at Warwick by Kelsey Cremin, a MAS student with training in the microbiology. Samples were prepared by her and brought to the SICM lab to study. Kelsey completed her masters and continued working on bacterial imaging projects as part of her PhD. Her contributions were invaluable to this section of the project and work load for chapter 5 was split equally between her and I.

B. subtilis (NCIB 3610 - *Δhag* depleted, obtained from the Kearns lab, *via* the Asally lab, University of Warwick), *B. subtilis* (NCIB 3610 - Δ*eps*, obtained from the Kearns lab, Asally lab), and *E.coli K12* (wild type, obtained from DSMZ) were cultured in a modified M9 media containing 0.4% w/v glucose (full media composition can be found in the Appendix section 7.3.2). Bacteria were taken from freezer stocks (50% glycerol, -80^{o}C) and grown in 40 mL volumes of media, occupying 100 mL sterile Erlenmeyer flasks. The cultures were grown overnight prior to SICM measurements on a shaking incubator at 37^{o}C and 150 rpm.

For SICM scanning, adhesive layers of poly-L-lysine (PLL), Cell-Tak, or thin (< 0.5 mm) agarose gels were deposited on the glass surface of a 50 mm glass bottomed dish (WillCo Wells, USA, HBST-5040). All adhesion methods were able to anchor and restrict inherent bacterial movement, whilst not inhibiting culture survival, and further details of the adhesion procedures and viability tests can be found in chapter 5.

For all adhesion methods and bacterium species, a 100 μL aliquot of an overnight culture (optical density at 600 nm ~0.45) was drop cast to the substrate. The sample is then left for 30 minutes at room temperature for the bacteria to adhere to the adhesive.

2.3.1 Bacterial Adhesives

During the optimisation stages of these experiments several adhesives were investigated for their ability to retain bacteria to the cover glass bottomed sample dishes across the SICM experiments. Those used in this chapter are described below.

2.3.1.4 Thin Agarose Layers

As the agarose layer is transparent and thin, visualisation of the bacteria using the inverted microscope was possible, facilitating positioning of the tip over areas of interest. Based on the agarose pads method by Young *et al*,[22] agarose solutions were made using 0.8% (w/v) Cleaver Scientific low melt agarose (CSL-LMA100) in artificial seawater media (ASWm) basal salts and 50 mM sodium acetate (as described in Zerfaβ *et al.* (2018)).[23] The solution was autoclaved for 30 minutes to melt the agarose whilst maintaining sterility. At 80°C the agarose solution flask was transferred to a water bath at 50°C to keep the agarose liquefied.

For sterility, the agarose layers were prepared inside a laminar flow hood. 450 μL of agarose solution was pipetted in an outwards expanding spiral from the centre of a 50 mm cover glass bottomed dishes (WillCo Wells, USA, HBST-5040, glass thickness approximately 170 μm), the dish was swiftly rotated to evenly spread the agarose then placed in the laminar flow hood until set, creating a uniform layer. From the volume of agarose added to the dish, the agarose layer thickness is calculated to be approximately 0.25 mm. Solidified agarose plates were sealed and refrigerated until use for up to one week.

Prior to scanning, 100 μL of an overnight culture (optical density at 600 nm ~0.3) is pipetted dropwise across the agarose layer, and rotated to evenly spread. The sample is then left for 30 minutes at room temperature. Following this, the dish is placed into an incubator at 37°C for 30 minutes to dehydrate the agarose and evaporate any residual liquid. Whilst it is possible to adapt this method to in cooperate other media instead of the ASWm, due to the transparency and minimal crystallisation and clouding, the ASWm pads had the best optical properties.

2.3.1.5 Poly-L-Lysine

Poly-L-lysine (PLL) has minimal effect on bacterial viability if the substance is adhered to a substrate, and not free in solution where it is known for its antimicrobial

properties.[24] In order to adhere bacteria using PLL, 50 mm cover glass bottomed dishes (glass thickness approximately 170 μm) were coated in 500 μL of 0.01% poly-L-lysine (Sigma Aldrich, sterile-filtered) for 15 seconds. The PLL solution was then extracted via pipette and the dish washed with 5 applications of 1 mL DI water, this leaves behind a nm thin surface layer of PLL. An overnight bacteria culture (100 μL, OD600 approximately 0.3) was added to the dish, which was rotated to evenly coat the surface. The sample was then allowed to incubate for 30 minutes at room temperature. The dish was then washed with 3 applications of 1 mL DI water to remove un-adhered bacteria.

2.3.1.6 Corning Cell-Tak

Cell-Tak was used in accordance with the adsorption method provided in the instructions for use provided by Corning (Catalog 354240, 354241). Cell-Tak was purchased at 2.36 mg/mL concentration, in acetic acid, where 200 μL of formalised Cell-Tak adhesive was prepared per each 50 mm glass bottomed dish used.

For coating each sample dish 7 μL of Cell-Tak was added to 193 μL of sterile 100 mM sodium bicarbonate solution; adjusted to pH 8 with 5% acetic acid, and vortexed for 10 seconds. The solution was then immediately added to the centre of the dish and spread to cover approximately two thirds of the dish base. The dish was then placed in a 30°C incubator for 20 minutes. Following this the dish was washed with MilliQ water to remove of residual sodium bicarbonate, and 20 μL of an overnight bacterial culture (OD_{600} approximately 0.8) was added to the middle of the dish and swirled to cover the Cell-Tak layer. The sample was then left for 30 minutes allowing adherence prior to SICM. Adhesion appeared to reduce over time, however was sufficient for up to 8 hours.

2.4 Nanopipette preparation

Nanopipettes used throughout are either 30 nm pipettes made from quartz capillaries (o.d. 1 mm, i.d. 0.5 mm, Sutter Instruments, QF100-50-10) used for acid delivery experiments (chapter 3) or 150 nm borosilicate pipettes (o.d. 1.2 mm, i.d. 0.69 mm, Harvard Apparatus) used for charge mapping (chapters 4 & 5).

Both were pulled using a laser puller (P-2000, Sutter Instruments). The pulling parameters are as follows:

30 nm pipettes: Line 1: Heat 750, Fil 4, Vel 30, Del 150, Pul 80; Line 2: Heat 650, Fil 4, Vel 40, Del 135, Pul150.

150 nm pipettes: Line 1: Heat 330, Fil 3, Vel 30, Del 220, Pul -; Line 2: Heat 330, Fil 3, Vel 40, Del 180, Pul120.

The inner radius of the probes was measured using a Zeiss Gemini 500 SEM (operating in scanning transmission electron microscopy mode) and for these pulling parameters the radius was found to be consistently 15 nm +/- 10% and 75 nm +/- 10% respectively for these pulling programs. (Estimated from methods previously used within the Unwin group and catalogued here.[1])

2.5 SICM Set-Up

The newly fabricated nanopipettes are filled with electrolyte using a 1 ml luer lock syringe (Medicina) passing through a 0.2 μm filter (Sartorious Minisart) and a MicroFil (World Precision Instruments, 34 gauge). The electrolyte generally consisted of 50 mM KCl for all charge mapping experiments and bulk solution in SICM-Potential Controlled Acid Deliver (PCAD) experiments (unless stated) and a 20 mM HCl with 50 mM KCl back ground for the nanopipette solution in SICM-PCAD. Any solution used as bulk electrolyte or placed in the nanopipette was filtered. Two Ag/AgCl QRCEs were used, one in the nanopipette and a second in bulk solution and were fabricated by electrolysis of silver wire in saturated KCl solution. The working electrode placed in the top of the nanopipette was made from a 0.125 mm silver wire (99.99% purity Goodfellow, Cambridge) and the bulk electrode made from a 0.25 mm silver wire. (99.99% purity Goodfellow, Cambridge)

The SICM instrumentation is described in detail previously here.[2–4] The nanopipette probes were mounted on a mechanical micro-positioner (Newport, M-461-XYZ-M) for coarse probe positioning over a sample. The fine horizontal movement of the probe was controlled using a two-axis piezoelectric positioning system with a range of 30 μm (Physik Instrumente, model P-733.2 XY nanopositioner), while vertical movement was controlled using a single Z axis piezoelectric positioning stage of range 15 μm (Physik Instrumente, model P-753.1 LISA.) Both the XY nanopositioner and the Z piezo are regularly calibrated by experienced group members and assumed to be valid. The piezoelectric positioners were mounted inside a faraday cage, built on an air

pressurised optical table (Newport, RS 2000) to avoid mechanical vibrations, which incorporated acoustic insulation. Vacuum insulating panels (Kevothermal) and aluminium heat sinks (aimed to reduce thermal fluctuations and drift of the piezoelectric positioners) were also utilised. The stage housing the piezo is mounted on a vibration isolation platform (Minus K) also incorporated within the faraday cage. The electrometer and current−voltage converter used were bespoke, both made in-house, while user control of probe position, voltage output, and data collection was *via* custom-made programs in LabVIEW (2017, National Instruments) through a field programmable graphics array card (7852R, National Instruments).

For the bacterial imaging in chapter 5 the instrumentation is similar but incorporates a microscope for sample locating and coarse positioning. The lateral movement of the probe was controlled using a two-axis piezoelectric positioning system with a range of 300 μm (Nano- BioS300, Mad City Laboratories, Inc.), while movement normal to the substrate was controlled using a single axis piezoelectric positioning stage with a range of 38 μm (P-753-3CD, Physik Intrumente). All electrochemical measurements were performed using in-house built instrumentation controlled via a custom-made LabVIEW interface (2016, National Instruments) through an FPGA card (7852R, National Instruments). The instrumental setup is vibration and thermal insulated, and all measurements are performed inside a faraday cage to mitigate interference. An integrated Zeiss Axiovert inverted microscope was used for course positioning of the nanopipettes over the bacterial substrate and collection of optical images.

2.6 Enamel Surface Treatments

2.6.1.1 Fluoride and Zinc Treatments

In section 3.2.2 protective treatments of fluoride and zinc are administered. The sample had its baseline measured with SICM-PCAD and was then removed from the SICM rig and placed in a bath of the protective treatment, in an incubator at 37ºC for 30 mins. Enough solution was used to completely cover the enamel surface, around 10 ml. The protective solutions were prewarmed to 37ºC. After this the enamel was rinsed thoroughly with DI water and returned to the SICM rig.

2.6.1.2 Pellicle Layer Deposition

To establish a pellicle layer the sample was incubated in 5 ml of whole clarified saliva for 30 minutes at 37°C. Studies have shown this is long enough for salivary proteins to adhere to an enamel surface and create a film that acts as a natural protective barrier[5]. After incubation, the sample was thoroughly rinsed and reanalysed with SICM-PCAD. The saliva was collected by having volunteers chew flavourless gum and expectorate into 100 ml centrifuge tubes at Unilever Port Sunlight research facility and sterilised on site.

2.6.1.3 Citric Acid Treatment

Section 3.2.3 investigates the effect of citric acid exposure on the enamel. The aim here was to simulate a typical dietary acid exposure. 1% citric acid at pH 3.6 was chosen as it is a good representation of orange juice. The acid was administered at room temperature as drinking lowers the temperature in the mouth and for only a 30 s time frame as the exposure is often short. This treatment can be administered on the rig after a baseline measurement has been taken by retracting the nanopipette to a safe distance, extracting the electrolyte with a syringe and injecting the acid into the sample dish. After 30 s the acid is in turn syringed away and the sample rinsed with DI water multiple times. Fresh electrolyte can then be returned to the sample dish. As the probe can be moved vertically to be placed at a safe distance, its X Y position is retained, making the placement of the next etch pit array easier.

2.6.1.4 Multi-Step Treatment Regime

Figure 2.1 gives the full details of the multistep process used for the study in 3.2.4. In summary, a section of the enamel block is masked off with tape to protect half of it from a fluoride treatment and then each measured. The fluoride is administered as above (2.6.1.1). A citric acid treatment is then administered as in 2.6.1.3. The sample sections are then reanalysed in a different area to that previously measured, giving an insight into the protection benefit offered by fluoride against a citric acid exposure as well as gathering data for sound enamel treated with citric acid.

This method allows for one side of the enamel to be exposed to fluoride for 30-mins whilst the other half remains sound. The response to citric acid for both halves can then be measured without removing the sample from the rig.

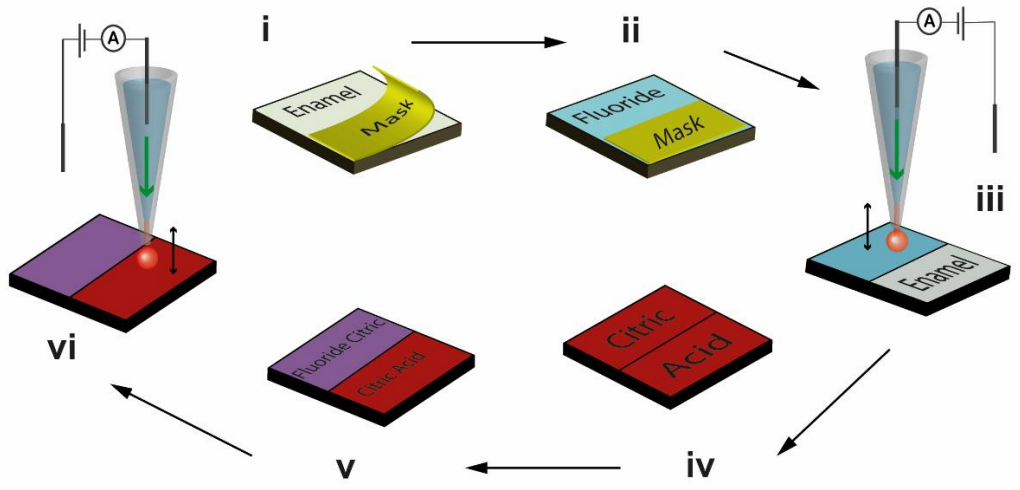

Figure 2.1 Multi-step Treatment Regime

Experimental treatment process. **i.** Polished enamel block is half masked with Kapton tape. **ii.** The Unmasked enamel is then treated with sodium fluoride solution for 30 minutes at 37°C. **iii.** Mask is removed, sample thoroughly rinsed and SICM etch pit analysis undertaken on both sides of sample. **iv.** The electrolyte is then removed, and the entire sample is exposed to a 1% citric acid solution for 30 s. **v.** The sample is then thoroughly rinsed, and the electrolyte replaced. **vi.** SICM etch pit analysis is then repeated for the fluoride treated citric acid exposed enamel and citric acid exposed enamel, taking care that this second SICM analysis is performed far away from the initial region studied.

N = 5 enamel blocks were polished down to a 50 nm finish with diamond lapping suspension (2.2). 6x6 arrays were made to give 36 measurements for each treatment type. This gives results from each sample reflecting the sound, fluoride treated, citric acid treated, and fluoride followed by citric acid treated enamel.

A control study was run alongside this study to ensure the Kapton tape was not adversely affecting the results by leaving any residue. The sample was prepared identically to those used in **i-iii** of the multistep process in Figure 2.1, except 37°C deionized water was used in place of the 30-minute sodium fluoride exposure. The taped and un-taped sides of the sample were then compared with SICM-PCAD.

2.6.1.5 SICM–PCAD Method

Once treated the sample is mounted in the SICM and the nanopipette filled with the H^+ containing electrolyte solution described above and brought into close proximity of the surface with manual micrometre and the aid of a camera. The bulk electrolyte solution was then added and the final approach undertaken utilising LabVIEW software and DC feedback. Once at the surface an oscillation of 10 nm is applied to the *z*-position of the tip at a frequency of 210 Hz using an external lock-in amplifier and the resulting AC current used to provide a stable feedback signal for final positioning and maintaining the probe-substrate separation distance during etch pit generation. LabVIEW software for controlled surface delivery in patterned arrays was used to carry out 36 dissolution measurements in a confined area. The probe position, AC and DC currents are recorded and monitored simultaneously throughout.

2.7 Surface Charge Mapping Procedure

In most cases, after a sample is mounted a baseline SICM-SCM is taken. The SICM probe is filled with electrolyte solution and brought into the proximity of the surface with the aid of a camera (Pixel link with Edmund Optics lens, 6.0x magnification, 65 mm focal length.) The electrolyte solution is then added to the petri dish and the final approach undertaken utilising LabVIEW software and ion current feedback. The SICM image was collected using a bespoke LabView software that approaches and pulses at the surface and in bulk as detailed in Figure 4.1**B**.

The conditions used were as follows: 50 mM KCl electrolyte solution buffered with TRIS to pH 7. 150 nm borosilicate glass nanopipettes. 6×6 µm scan area with 150 nm hops giving a 40×40 pixel grid with 1600 individual points (or approaches). An approach speed of 3 μms^{-1} was used throughout with a retract distance from the surface of 2 µm (though this was increased for acid exposed samples). A DC feedback threshold of 2% was used unless otherwise stated. The applied approach bias was -50 mV, generating a corresponding current of around -400 pA (though this varied by up to 20% from probe to probe). This means the feedback threshold of 2% corresponded to a current of around 8 pA, which was much greater than the baseline peak-to-peak noise in the current of around 2 pA. The pulse potential was 500 mV throughout unless stated.

The full details of SICM charge mapping have been described in detail elsewhere.[11,25–27] Briefly, the nanopipette is approached towards the surface with a small applied bias between the internal and bulk QRCEs (Figure 2.2**A**), typically 50 mV, where the ionic current response is insensitive to surface charge (Figure 2.2**B** a).

When a set current threshold (usually 2% change in current magnitude) is reached, the tip bias is either pulsed to -500 mV or scanned from -500 mV to 500 mV, depending if a pulsed-potential or scanned-potential program is employed (Figure 2.2**B** b). The corresponding ionic current response is measured for the duration of the potential pulse or scan and the nanopipette is then retracted 2 µm into the bulk solution, held at 50 mV, and the same potential pulse or scan program is repeated at the bulk (Figure 2.2**B** c to d). This allows for each surface current measurement to be normalized against a bulk measurement. The probe is then laterally translated by a set distance and re-approached, starting the process over again. This procedure is repeated at every pixel of the electrochemical map. As the z height at each approach is also recorded, a topographical map is synchronously acquired. The nanopipette current response during the potential programs (pulse or potential sweep) gives a direct measurement of the local ion concentration in the footprint of the nanopipette, be that at the surface or in bulk[26]. At the surface previous work has shown, through a combination of experiments and FEM simulations, that the nanopipette is sensitive to the composition of the double layer without directly probing it.[11]

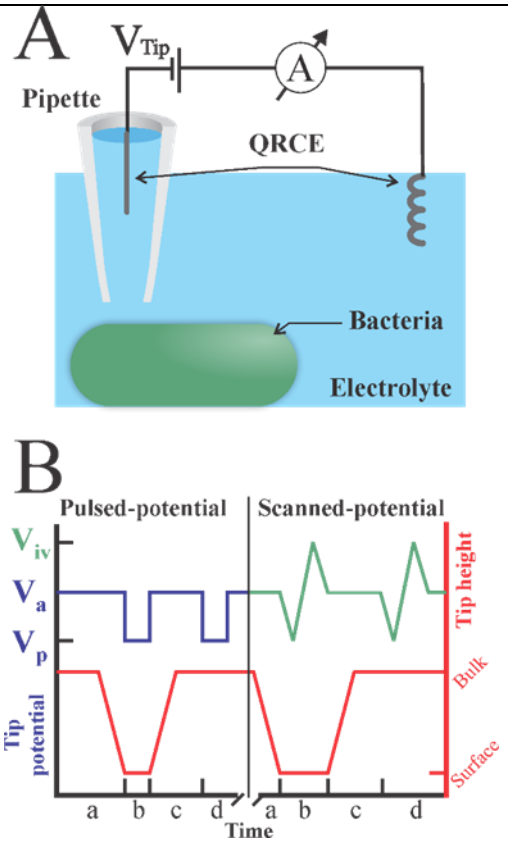

Figure 2.2 SICM Schematic with Varying Potential Protocol Infographic

(A) SICM schematic depicting a nanopipette probe submerged in electrolyte and connected by two QRCE's. (**B**) An infographic to show probe vertical motion alongside change in potential for both pulsed and scanned potential programs.

Post baseline imaging, the tip is retracted to the maximum distance from the surface (roughly 1 cm) whilst maintaining x and y position and the electrolyte extracted with a syringe. The sample is then carefully rinsed with DI water before the surface treatment applied. In the experiments investigating an erosive challenge the sample was exposed to the chosen acid for 30 s, followed by 5 rinsing cycles. The probe was then re-approached, and the electrolyte replaced. A second 'post acid' SICM scan was then collected. This method allowed for a 'before and after' analysis of the same sample area and the integrity of the tip was validated by insuring it was passing the same current by running a cyclic voltammogram before and after each scan.

For the remineralisation, a further step was undertaken in which the tip was retracted, the electrolyte again removed, and the sample exposed to the remineralisation solution, which had been previously heated to 37 ˚C, for 15 minutes. The solution was then removed again and replaced with fresh preheated solution for a further 15

minutes. The sample was then rinsed, the SICM imaging electrolyte replaced, and the final SICM completed.

In the case of the pellicle adhered sample, the enamel was immersed in 5 ml of whole clarified saliva for 30 minutes at 37°C. The saliva was collected from volunteers at Unilever Port Sunlight research facility and sterilised on site. Studies have shown this is long enough for salivary proteins to adhere to an enamel surface and create a film that acts as a natural protective barrier[28]. After incubation the sample was thoroughly rinsed, the electrolyte replaced, and the sample reanalysed with SICM-SCM.

2.8 AFM

AFM images where taken using an Innova ex situ AFM (Bruker) using NanoDrive v8.05 software. Tips were antimony doped silicon (Bruker, 225 µm by 35 µm by 3 µm.) Images were taken in contact mode and processed in Scanning Probe Image Processor version 6.0.14.

2.9 SEM

Field emission-SEM images were recorded using the In-lens and STEM detector on a Zeiss Gemini operating at low voltages to avoid charging on enamel surface. Transmission mode was used to image nanopipettes for obtaining the geometry of the inner wall and cone angle for modelling purposes.

2.10 Cryo-TEM

Transition electron microscopy carried out with a Jeol 2100 with an FEG electron gun. The samples were frozen in liquid ethane for cryo purposes. Images taken at 200 kV.

2.11 FEM Simulations

2.11.1 SICM-PCAD Model

To simulate the acid dissolution of enamel and dentine a 2D axisymmetric model of the nanopipette near a substrate was constructed in COMSOL Multiphysics (v. 5.4) with the Transport of Diluted Species, Laminar Flow and Electrostatics modules. The dimensions of the nanopipettes were extracted from SEM images of example nanopipettes, taken in scanning transmission electron microscopy mode. Full details of the simulation are given in section 3.2.6 but briefly, the reaction between HAP and H^+ is simulated in real time for the duration of a delivery pulse. Simulations were run to assess the validity of using a steady state, constant separation distance model, despite the applied oscillation of the nanopipette, this was found to be a reasonable approximation. Etching rates were calculated from the depth of HAP removed in the region underneath the nanopipette, using the molar volume of HAP in the target substrate. This allows for experimentally obtained etching depths to be converted into rate constants and fluxes of calcium and various phosphates from the substrate surface.

2.11.2 Enamel and Dentine Charge Mapping Model

A 2D axisymmetric model of the nanopipette in bulk solution and near a substrate was constructed in COMSOL Multiphysics (v. 5.4) with the Transport of Diluted Species, Laminar Flow and Electrostatics modules. The dimensions of the nanopipettes were extracted from SEM images of example nanopipettes, taken in scanning transmission electron microscopy mode. To obtain working distances for experimental SICM measurements, simulations were performed at varying probe−substrate separation with an applied probe bias of -50 mV (the experimental approach bias). Once the working distance, corresponding to the experimental feedback threshold was known, time-dependent simulations were performed at this separation distance with varying surface charge applied to the domain boundary below the nanopipette. Simulations were performed with the nanopipette positioned in bulk solution and the near-surface values of the ionic current, with different applied surface charge, were normalized to those in bulk to elucidate surface charge from experimental normalized current maps. For all of these simulations, the initial conditions used were obtained from steady-state simulations performed with the same conditions except the tip bias was -50 mV (the

approach bias). Further information regarding this FEM simulation can be found in section 4.3.

2.11.3 Bacteria Surface Charge Mapping Model

For the FEM simulations of gram-negative and gram-positive bacteria in this chapter different models were required. For gram-negative bacteria the standard model from chapter 4 was used. Simulating the area under the nanopipette as a flat insulating surface was deemed acceptable for reasons detailed within. The full details of this model can be reviewed in chapter 4 section 4.3. For gram-positive bacteria a new model was required.

A 2D axisymmetric model of the nanopipette in bulk solution and near the substrate was constructed in COMSOL Multiphysics (v. 5.4) with the Transport of Diluted Species, Laminar Flow and Electrostatics modules. A schematic of the simulation domain and boundary conditions is presented in Figure 5.11. The dimensions of the nanopipettes were extracted from STEM images of the nanopipettes.

E. coli were simulated as a non-porous insulating charged surface to describe the interface with the outer membrane. *B. subtilis* were simulated with a charge density applied to a volume which describes the permeable and charged cell wall. The SICM scanning procedure was simulated in full, with the approach simulated by steady-state simulation of different tip-substrate separations with the approach bias applied (50 mV), followed by time-dependent simulations of the potential pulse or potential scanning regime at the calculated approach height and bulk retract height. Full details are available in section 5.3.

2.12 References

1 J. W. Young, J. C. W. Locke, A. Altinok, N. Rosenfeld, T. Bacarian, P. S. Swain, E. Mjolsness and M. B. Elowitz, , DOI:10.1038/nprot.2011.432.

2 C. Zerfaß, J. A. Christie-oleza and O. S. Soyer, *bioRxiv*, 2018, **https://do**, 1–31.

3 M. Hyldgaard, T. Mygind, B. S. Vad, M. Stenvang, D. E. Otzen and R. L.

Meyer, *Appl. Environ. Microbiol.*, 2014, **80**, 7758–7770.

4 D. Perry, D. Momotenko, R. A. Lazenby, M. Kang and P. R. Unwin, *Anal. Chem.*, 2016, **88**, 5523–5530.

5 A. Page, D. Perry, P. Young, D. Mitchell, B. G. Frenguelli and P. R. Unwin, *Anal. Chem.*, 2016, **88**, 10854–10859.

6 M. Kang, D. Perry, C. L. Bentley, G. West, A. Page and P. R. Unwin, *ACS Nano*, 2017, **11**, 9525–9535.

7 D. Perry, B. Paulose Nadappuram, D. Momotenko, P. D. Voyias, A. Page, G. Tripathi, B. G. Frenguelli and P. R. Unwin, *J. Am. Chem. Soc.*, 2016, **138**, 3152–3160.

8 Y. F. Zhang, J. Zheng, L. Zheng and Z. R. Zhou, *J. Mech. Behav. Biomed. Mater.*, 2015, **42**, 257–266.

9 A. Page, D. Perry, P. Young, D. Mitchell, B. G. Frenguelli and P. R. Unwin, *Anal. Chem.*, 2016, **88**, 10854–10859.

10 D. Perry, R. Al Botros, D. Momotenko, S. L. Kinnear and P. R. Unwin, *ACS Nano*, 2015, **9**, 7266–7276.

11 K. McKelvey, S. L. Kinnear, D. Perry, D. Momotenko and P. R. Unwin, *J. Am. Chem. Soc.*, 2014, **136**, 13735–13744.

3 Scanning Ion Conductance Microscopy – Potential Controlled Acid Delivery

3.1 Introduction

This chapter details the conception and application of SICM-PCAD. By utilising the ion current to selectively deliver protons to an enamel surface, controlled dissolution occurs forming etch pits. By tracking the development of multiple etch pit by monitoring the nanopipettes *z* height change over time it is possible to build a data set that reflects the surfaces susceptibility to dissolution. The investigated surface can then undergo treatments or acid challenges before being re-measured to study the effect on the enamel. This provides a robust way of measuring acid erosion on the nanoscale and opens the door to quantify the effect of short, subtle treatments that proved challenging with existing methods.

3.1.1 Methods of Measuring Dissolution

Understanding dissolution processes is important to advances in many fields. The medical field will benefit from preventative treatments for diseases caused by the accumulation of by-product material such as kidney stones caused by cystinuria.[1] Pharmaceutical manufacturers investigate crystal dissolution to improve their products with targeted drug release and improved understanding of required dosages.[2,3] How crystals respond to moisture is vital to improving building materials such as gypsum in plasterboard and mixes for industrial cements, industries where improving products could save billions on a global scale.[4,5] Dental erosion is a small subset of this research with potential benefits for the quality of life of large demographics of people.[6,7]

Previous work to measure the dissolution of dental materials focus on rotating disc electrodes (RDEs).[8–10]. Whilst these studies do have some merit as mass-transport is well defined, the large size of the electrodes in comparison to the substrate only make macroscale measurements possible. Localised nanoscale measurements, capable of investigating heterogeneities within the enamel structure are not possible with this

method. Nanoscale measurements are possible through multiple SEM (or some other form of high resolution microscopy) images of a sample area, however the mass transport is often ill defined when calculated from still images and the limitations of the equipment often require the enamel to be exposed to solutions away from the microscope with limited options for direct monitoring of topographic changes.[11,12]

In dental research is often desirable to quantitatively assess the corrosive damage imparted to a surface by a particular acidic challenge. Conversely it is also common to use these methods to assess the protection benefit offered to the surface by a preventative pre-treatment such as a toothpaste with a novel active ingredient. With a large enough sample size, a measure of whether a particular treatment is effective compared to controls can be obtained. A popular method of achieving this is surface micro-hardness (SMH) testing.[13–15] Specially cut, flat, polished enamel sections are prepared. Their baseline surface hardness is tested, giving an average Knoop[16] or Vickers[17] hardness value after multiple measurements. The samples can then be treated and the SMH re-measured. An acid wash can be introduced and the samples SMH measured at any point during the treatment regime.

The measurement is made by physically indenting the sample surface with a sharpened diamond head. The load applied to make each indent is consistent and can be altered depending on the sample. The resulting indent is measured by the researcher with an attached microscope. The size of the indent varies but for sound (untreated or unadulterated) enamel around 50 μm width is normal. Whilst the technique is adaptable and provides insight into the changing properties of a sample surface at any point during a multi-step process there are drawbacks. The experiments are slow with each indent needing to be measured individually. Indents are large in comparison to the enamel microstructure, nanoscale precision being impossible with this system. The measurements must be taken on dry samples therefore any transient effects to the enamels surface imparted by the treatment may be missed. Also, the hardness of the surface, whilst a good indicator, may not be a useful measure of any surface chemistry changes. No information about dissolution or rates of reaction can be extracted from these measurements.

Within the Unwin group, multiple researchers have investigated the dissolution of HAP and enamel using SPM and the scale and scope of what can be achieved has

advanced as scanning probe technologies evolve.[18,19] In 2010 experiments by McGeouch et al. utilised an UME (radius 12.5 µm) to locally dissolve enamel by splitting water with the electrode to generate protons in close proximity to the surface.[18] White light interferometry was used to measure the resulting etch pits and dissolution rates were calculated by modelling the pit formation with FEM. An enamel dissolution rate constant of 0.08 ± 0.04 cm s^{-1} was calculated for the area under the UME during proton delivery. This technique is accurate to a certain degree but limited due to the comparatively large size of the disc shaped UME working area and a reliance on a follow up technique for the etch pit topography. Issues approaching the UME to the same point on a surface and a requirement for a redox mediator may cause inconsistencies in this kind of measurement. The system is also limited by the mass transport as defined by the rate of proton delivery from the UME.

A follow up enamel dissolution study in 2016 by Parker et al utilised SECCM to make arrays of etch pits with incrementally increasing exposure time to acid.[19] The gradually deepening pits were topographically measured with AFM. From the AFM maps etch pit depths were measured and an FEM model was built to calculate the enamel dissolution rate constant, quoting a value of 0.099 ± 0.008 cm s^{-1}. Improvements over the 2010 work are a reduction in scale, each etch pits measuring around 1 µm diameter, multiple measurements on a faster time scale due to the automated nature of SECCM and a well-defined working distance with the SECCM providing a clear indication that the meniscus is in contact with the surface. Disadvantages are that the dissolution reaction may continue once the SECCM probe has retracted, due to residual acid being left behind. This potentially causes a consistent over-estimate of the etch pit size. Again, this method requires a secondary technique to analyse the etch pit depth. In this chapter we discuss SICM as an alternative to these methods and demonstrate how these measurements can be made with a single technique.

3.1.2 SICM – Potential Controlled Acid Delivery

Iontophoresis, the method of introducing ionic medicinal compounds into the body through the skin, has long been utilised in the fields of neurobiology and cellular signalling. [20,21] SICM, with its needle like probes, can be used to deliver a target species locally, to a cell or biological sample, even piercing membranes.[22–25] Recently, it was shown that charged molecules can be delivered in pulses to a carbon fibre UME

and the UME current response correlated to the delivery.[26] Such experiments are possible due to the manipulation of charged ions *via* the potential applied to the nanopipette electrodes. The electric field can be employed to hold the species within the nanopipette by applying an oppositely charged field, attracting the ions and overcoming any outward flow forces. Alternatively, a like charge can be employed to deliver the ions by repelling them away from the electrode and out of the nanopipette pore. If the approached surface is susceptible to acid dissolution, an etch pit rapidly forms in the area underneath the probe when the protons are delivered.

Herein we position SICM as a tool for quantifying nanoscale corrosive damage through using the SICM bias to deliver protons from a reservoir in the probe to the enamel surface, whilst employing distance (*z* position) modulated feedback to track the induced surface dissolution, providing *in-situ* etch pit depth measurements. Figure 3.1 depicts an SICM probe retaining protons and delivering them to a surface upon reversal of the applied bias.

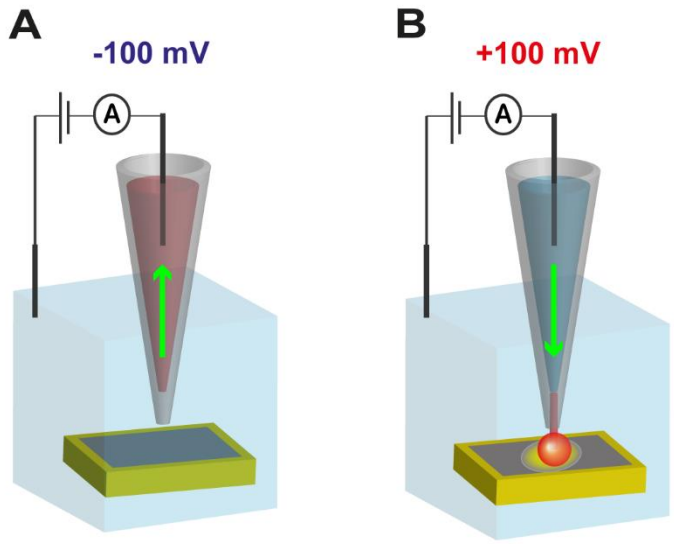

Figure 3.1 Proton Holding and Delivery with SICM

The protons, in red, are being held in the nanopipette by a negative 100 mV bias applied to the electrode in the top of the nanopipette (**A**). When the bias is reversed the protons are repelled and delivered to the enamel surface (**B**). The green arrow shows the pull of the electric field retaining or expelling the protons.

Careful control of the bias, ensuring the protons are retained when away from the surface and delivered when in close proximity allows for production of multiple similar etch pits.

3.1.3 Surface Tracking Through AC Feedback

To quantify the extent of the erosive damage caused by the proton attack, the depth of the etch pits is measured *in-situ*. By applying a physical oscillation to the probe in the *z* direction, an AC component is introduced into the ion current. This modulated AC signal originates from any change in the ion current over the course of an oscillation, which is usually only significant when the probe is brought into close proximity of a surface. In essence, when in bulk solution there is negligible change in the current from peak to trough (*i.e.*, AC signal is zero), as the system resistance remains constant. However, when the oscillating probe is within a tip diameter of the surface, there is an appreciable AC component as the tip-surface distance is modulated (Figure 3.2). This

is due to the restricted ion flow (resulting from the access resistance) close to the substrate surface.

Unlike the DC component of the ion current, which is sensitive to both the access resistance (tip-substrate distance) and local ionic environment (*i.e.*, induced by surface charge or chemical reactions), the AC component is far less susceptible to changes in the local ionic environment at the surface. As discussed in depth by Korchev et al. in 2008,[47] a distance modulated feedback method is less affected by sample slope, changes in ionic strength and partial blockages of the nanopipette.

To best understand this, it easiest to consider what happens during a partial blockage in each case. For a non-modulated DC feedback, the current is at a maximum when the probe is far away from the surface and reduces rapidly at close separation distances. This means a large drop in bulk current caused by a blockage would be similar to the probe approaching the surface. The probes approach is halted in either case, but when the drop in current is due to a blockage this could be before the probe is anywhere near the surface. In the case of distance modulated DC feedback, the AC component is only generated at close separation distances and is proportional to the bulk current and stays within the optimal range of 0.2-3% of the bulk current. This means a large change in the bulk current due to a partial blockage will only introduce a proportional change in the AC (equivalent to going from say, 1% to 2% of the bulk current). This means a close separation distance can be maintained even with large changes in the bulk current when AC feedback is used.

This is especially important when attempting to measure the extent of a dissolution process, which generates a local flux of ions from the target surface and therefore may affect the DC component of the ion current. It follows that by imposing a constant AC feedback condition (achieved in practice by lowering or retracting the probe very rapidly over small increments), a constant probe-surface separation distance, *d*, can be achieved.

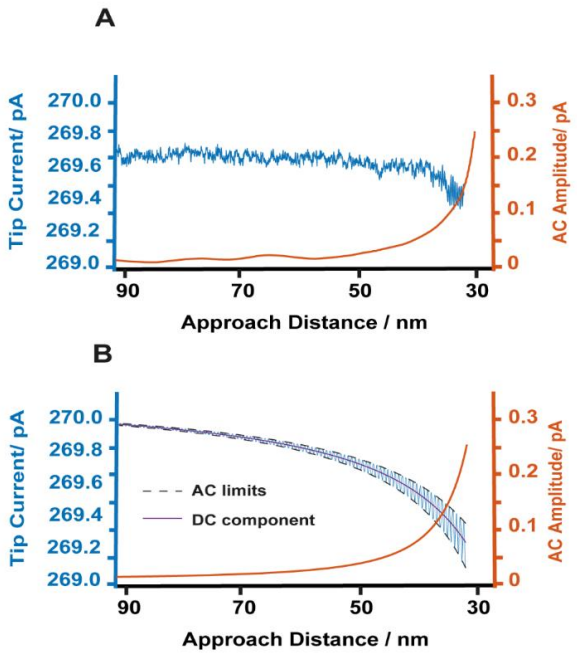

Figure 3.2 Experimental and Simulated Approach Curves

Experimental (**A**) and FEM simulated (**B**) approach curves showing the changing AC and DC currents as the nanopipette approaches an enamel surface. The DC signal drops as the tip approaches the substrate and the AC amplitude increases dramatically. The simulated data fits the real experimental data well. The approach distances in **A** are calculated based upon simulated approach curves.

This work exploits the robustness of the AC feedback and uses the fact that it only occurs at close separation distances from the surface and maintains that close separation through large changes in bulk current to create a system capable of actively measuring a developing etch pit in a dynamic local environment.

3.2 Results and Discussion

3.2.1 Preliminary Experiments

To validate the technique some initial experiments were undertaken. Due to its novelty it is beneficial to document the development of the technique as it progressed from generating and imaging single etch pits to establishing parameters to producing arrays of measurements in a single experiment which provide detailed statistics relevant to the acid resistance of the surface.

3.2.1.1 Topographical Map of a Single Etch Pit

Once an etch pit is made a topographical image can be taken of the eroded area using the same SICM probe used to deliver the acid, as long as the potential used to drive the ion current for topographical feedback also retains the protons. Experiments showed a potential of -100 mV to be sufficient for this purpose with a 30 nm pipette. Figure 3.3 shows the topography of a section of bovine enamel before and after a proton delivery pulse.

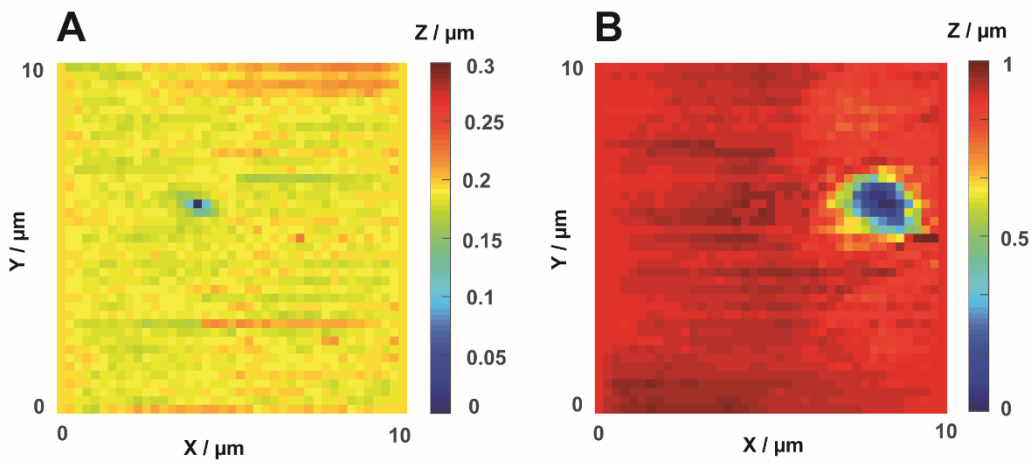

Figure 3.3 Singular Etch Pit Topography SICM Maps

The polished bovine enamel topography before a 10 second acid delivery (**A**). The same area post-delivery with a large etch pit (**B**). -100 mV was used as the holding potential to drive the DC current for topographical mapping.

Conditions: 30 nm pipette with 50 mM KCl background electrolyte present in the tip and bath. 20 mM HCl was delivered to the target area at 400 mV for 10 seconds. 1-hour topography scan duration with 3µm retract and 250 nm hopping distance.

A clear etch pit is visible with a depth of 1 µm and a diameter of roughly 3 µm. Further experiments were carried out to establish an effective holding potential and delivery duration to make arrays of etch pits to obtain statistically relevant averages within a 30-minute time frame.

3.2.1.2 Delivery Potential

It was hypothesised that altering the delivery potential may alter the etching rate or resulting etch pit depth. Logically, it was assumed that an increase in potential, and

therefore bigger driving force, would deliver more protons into the reaction space. Experiments have proven this to not be the case. Figure 3.4 shows the etch pit depth over 30 seconds for varying delivery potentials.

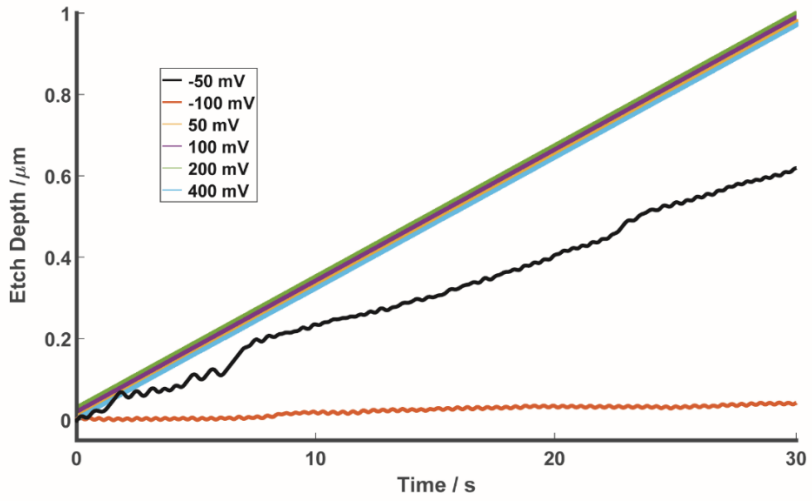

Figure 3.4 Etch Pit Depth with Varying Delivery Potential

30 second etch traces with varying delivery potential. The same threshold was used for each trace, and therefore the same distance from the surface can be assumed. All traces were carried out on the same enamel sample and a fresh area was approached for each trace.

Conditions: 30 nm pipette with 50 mM KCl background electrolyte present in the tip and bath. 20 mM HCl was delivered to the target area for 30 seconds. 10 nm oscillation at 200 Hz. 2.3×10^{-13} A AC amplitude threshold.

It is clear from the graph that minimal etching occurs at -100 mV (orange line) showing that at this potential the protons are not being delivered. All of the higher potentials (50 mV to 400 mV) result in a clear etching trace that are identical to one another. This implies that when the potential is positive, enough protons are being delivered to the reaction space that the limiting factor is diffusion of species away from the surface. In other words, the reaction is surface limited, increasing the rate of protons entering the reaction space is not directly increasing the etching rate. The black -50 mV trace supports this. At -50 mV the protons are not fully retained in the nanopipette. Some of the protons overcome the holding potential and enter the reaction space. This leads to a reduced etching rate compared to the positive potentials but

some, slower etching does occur, and a shallower pit is formed. Full retention of protons is only seen at larger negative potentials. -100 mV was selected as a holding potential for all subsequent experiments as, at this potential, few protons escape the probe and a sizeable ion current is generated for topographical mapping feedback.

3.2.1.3 Etch Pit Arrays

From Figure 3.4 the gradients of the delivery traces for higher potentials is constant after a short time frame. The decision was taken to use 10 second etch pits with a delivery potential of +100 mV. By retracting a few microns away from the surface after an etch pit is generated the probe can be automatically translated and then re-approached to the surface. Through repeating this process an array of similar etch pits can be made. Figure 3.5**A** shows one such array. With multiple approaches, multiple etch pits are made and their depths can be recorded. This gives relevant statistics on the susceptibility of the surface to acid attack which can then be subsequently compared to enamel surfaces that have undergone a treatment or erosive test.

Figure 3.5**B** shows a close-up image of the recorded Z trace. It shows the 3 µm retract after each etch pit and the region at the end of each approach (red box) is where the bias is flipped, and the proton delivery commences. Figure 3.5**C** shows the Z height change for each of the 36 etch pits, displaying the consistency. The raw etch pit depth data is displayed in table **D** (Figure 3.5). From this information an average etch pit depth of 477 ± 42 nm (± one standard deviation) is established for this particular sample.

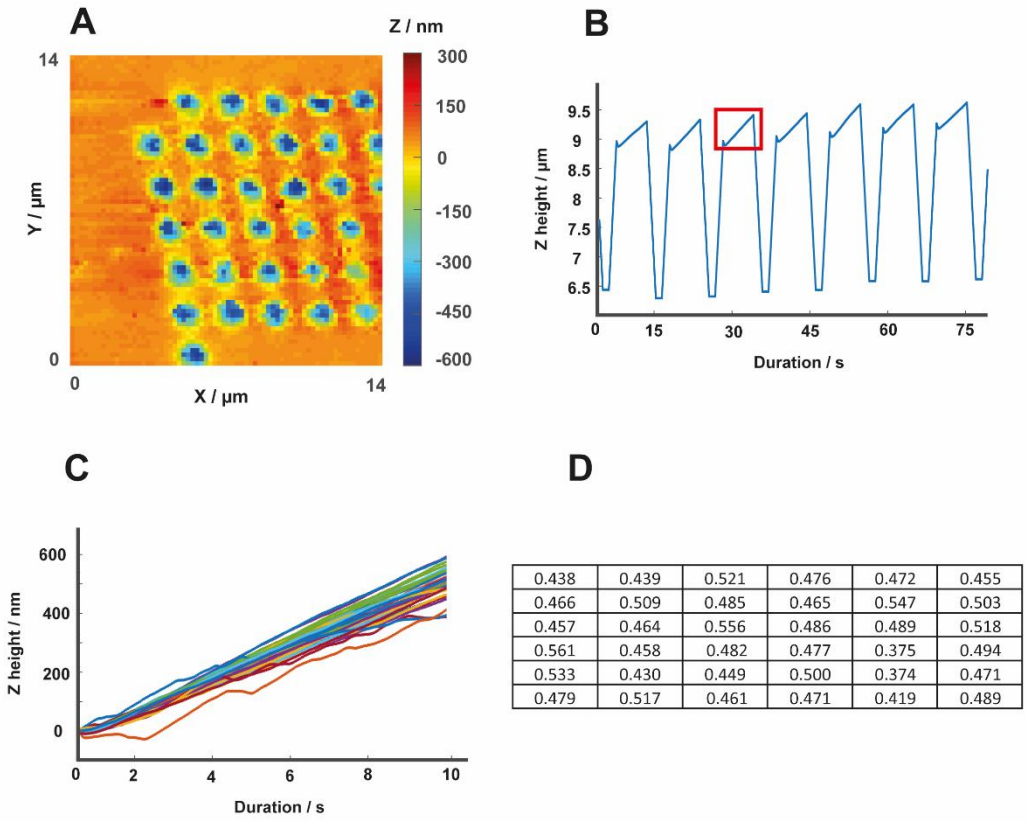

0.438	0.439	0.521	0.476	0.472	0.455
0.466	0.509	0.485	0.465	0.547	0.503
0.457	0.464	0.556	0.486	0.489	0.518
0.561	0.458	0.482	0.477	0.375	0.494
0.533	0.430	0.449	0.500	0.374	0.471
0.479	0.517	0.461	0.471	0.419	0.489

Figure 3.5 Array of Etch Pits on Bovine Enamel with Accompanying Data

A. SICM topography image of SICM-PCAD array of 36 etch pits on polished bovine enamel. Conditions: 30 nm pipette with 50 mM KCl background electrolyte present in the tip and bath. 20 mM HCl was delivered after each approach at +100 mV for 10 seconds. 10 nm oscillation at 200 Hz. 2.5×10^{-13} A AC amplitude threshold. **B.** Zoomed in Z trace showing the approach and then etching during delivery potential (red box). **C.** All of the Z etch traces from image A. **D.** Table of etch pit depths in µm taken from graph C, N=36, mean = 477 ± 42 nm. (1 S.D.)

The majority of delivery pulses result in a steady etching of the surface and a *Z* etch trace with a consistent gradient with no pauses or rapid changes in slope. However, after many experiments it is estimated that around 10 % of attempts do not result in a consistent etch trace (though this did increase on samples with rougher surfaces). This is likely due to the variable roughness of the surface or a poorly chosen AC feedback threshold or blockages occurring due to material rapidly evacuating the reaction space. Thankfully, when reviewing the data, it is clear and obvious when etching has not

commenced in a particular *Z* trace. Denoted as 'false engagements' the probe fails to track the surface and no forward progression is seen at the apex of the z trace, where the delivery bias is applied. This is illustrated in Figure 3.6 where a false engagement is compared to a standard etching trace and all sections of the approach and delivery are explained. Some raw z traces are given as examples in appendix section 7.1.

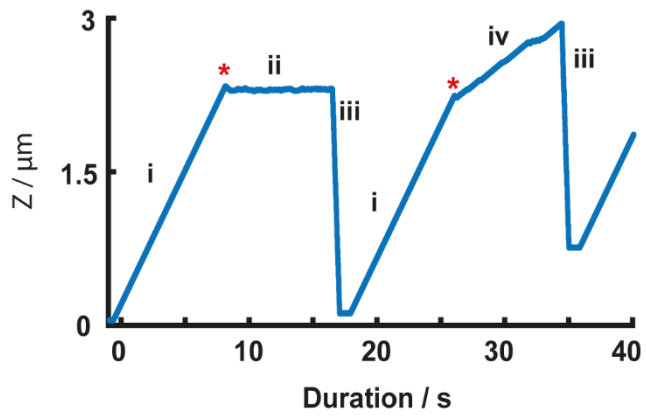

Figure 3.6 Z Trace for False Engagement and Typical Etch Pit

Two *Z* profiles from which the etch pit depths are calculated, LHS trace being a false engagement and RHS a valid etch trace **i.** Approach to the surface at holding potential. **ii**. Delivery during a false engagement, note no further progress is made into the surface and the etch trace is flat and featureless. In this case it is likely the threshold chosen led to the probe retracting too far from the surface and not re-engaging. **iii**. Retracting away from the surface at holding potential. **iv**. Delivery to the surface during a valid etch pit formation. Note the steady progress into the surface. * Notates the point the probe engages the surface in each trace. In the first trace it is clear no etching occurs as the z value does not change during delivery.

As false engagements directly impact the usefulness of the statistics gathered, they are removed from the data sets. A visual inspection of the *Z* traces is used, and any clear false engagements, where no etching occurs or the gradient varies erratically, are removed as outliers. To establish the robustness of the technique inter-probe variability and reproducibility on the same sample was investigated.

3.2.1.4 Statistical Significance Testing

All datasets were tested for normality using the Shapiro-Wilk test, yielding significant values ($p < 0.05$) for several datasets, therefore non-parametric statistical tests are used throughout analysis. The Bonferroni correction is also used wherever multiple comparisons are employed as this accounts for spurious false positives which increase as the number of comparisons increase. To ensure consistency between etch arrays, a 30 nm nanopipette was used to make 3 identical arrays of 36 pits on the same enamel sample. (See Table 2 for raw data.) A Kruskal-Wallis test showed no statistically significant difference between the arrays ($\chi^2 = 3.261$, $p = 0.196$) with means of 600 ± 77 nm, 565 ± 123 nm and 611 ± 82 nm.

To test inter-probe variation 3 probes, all 30 nm but pulled from different capillaries, were used on discrete areas of the same sample. Kruskal-Wallis testing shows no statistically significant difference between tips ($\chi^2 = 0.506$, $p = 0.777$), with means of 624 ± 93 nm, 613 ± 101 nm and 625 ± 120 nm. This indicates that there is experimental consistency between experiments using different tips and between repeated tests of the same sample, with variation due to spatial heterogeneity. It is notable that the mean etch pit depths of the two enamel blocks in this experiment are different. This was seen throughout the experiments and reflects the heterogeneous nature of organic dental samples, the irregularities arising from a number of possible sources. Namely, the cut angle of the initial slice through the tooth, the degree of polishing the sample underwent before delivery (enamel hardness varies with depth) and even the fluoride exposure and natural mineral density of the donor animal would have an impact.

The conclusions from these tests is that nanopipettes pulled with the same program, on the same puller return statistically similar etch pit depth averages when used on the same sample. This indicates that probes pulled with the same program and capillary type can be used to compare different samples and will return results that can be used to compare the samples directly. It also indicates that consistency across individual enamel blocks is good, and as long as obvious heterogeneities are avoided variability across a sample should be low. This bodes well for making comparisons between samples as the average measurement is indicative of the entire surfaces' susceptibility to dissolution. Probe variability does not seem to affect the measurement made with different nanopipettes returning statistically similar averages for the same sample.

Table 2 Repeatability and Inter-Probe Variability Test

	Same tip etch pit depths in microns		
	Array 1	**Array 2**	**Array 3**
	0.767	0.767	0.781
	0.764	0.749	0.776
	0.732	0.727	0.743
	0.697	0.726	0.716
	0.678	0.717	0.706
	0.667	0.701	0.635
	0.654	0.669	0.569
	0.653	0.665	0.559
	0.651	0.658	0.537
	0.646	0.636	0.531
	0.617	0.635	0.528
	0.609	0.618	0.524
	0.602	0.611	0.485
	0.601	0.609	0.460
	0.600	0.609	0.451
	0.588	0.598	0.438
	0.580	0.592	0.436
	0.567	0.580	0.434
	0.563	0.579	0.428
	0.558	0.551	0.559
	0.556	0.534	
	0.542	0.533	
	0.531	0.523	
	0.530	0.517	
	0.525	0.502	
	0.518	0.496	
	0.513	0.495	
	0.502	0.501	
	0.499		
	0.487		
	N=30	N=28	N= 20
Mean:	**0.600**	**0.611**	**0.565**
S.D:	0.077	0.082	0.123

	Different tips etch pit depths in microns		
	Tip 1	**Tip 2**	**Tip 3**
	0.812	0.793	0.801
	0.787	0.773	0.798
	0.767	0.769	0.797
	0.749	0.761	0.787
	0.727	0.749	0.775
	0.726	0.721	0.768
	0.717	0.709	0.764
	0.701	0.700	0.735
	0.669	0.669	0.714
	0.665	0.631	0.703
	0.658	0.630	0.678
	0.636	0.624	0.668
	0.635	0.616	0.663
	0.618	0.601	0.656
	0.611	0.595	0.650
	0.609	0.583	0.640
	0.609	0.567	0.633
	0.598	0.566	0.631
	0.592	0.558	0.624
	0.580	0.558	0.616
	0.579	0.522	0.608
	0.551	0.522	0.567
	0.534	0.521	0.556
	0.533	0.502	0.542
	0.523	0.487	0.540
	0.517	0.482	0.513
	0.502	0.473	0.511
	0.496	0.468	0.498
	0.495		0.487
	0.501		0.436
			0.414
			0.410
			0.424
	N=30	N=28	N=33
Mean:	**0.623**	**0.612**	**0.624**
S.D:	0.093	0.101	0.120

3.2.2 Protective Treatments

Now that the mechanics of the technique have been established and repeatability of measurements proven to be robust SICM-PCAD was used to assess some well-known protective actives in dental care.

3.2.2.1 Fluoride

A sample was prepared, and the baseline measured with SICM-PCAD. The sample was then exposed to sodium fluoride solution as described in 2.6.1.1. The raw etch pit depths are given in Table 3.

Table 3 Pre and Post Fluoride SICM-PCAD Etch Pit Depths

Individual etch pit depth pre fluoride / µm					
0.226	0.323	0.295	0.324	0.317	0.309
0.347	0.278	0.280	0.308	0.179	0.270
0.331	0.328	0.287	0.299	0.300	0.279
0.353	0.290	0.283	0.287	0.264	0.303
0.318	0.306	0.211	0.275	0.296	0.242
0.300	0.265	0.303	0.206	0.245	0.250

Mean: 286 ± 39 nm

Individual etch pit depth post fluoride / µm					
0.264	0.253	0.235	0.177	0.216	0.218
0.179	0.268	0.222	0.230	0.166	0.227
0.260	0.230	0.206	0.246	0.235	0.218
0.253	0.270	0.205	0.235	0.226	0.227
0.223	0.253	0.195	0.249	0.217	0.222
0.352	0.247	0.219	0.224	0.226	0.206

Mean: 231 ± 32 nm

Although the standard deviations overlap slightly simple t-testing shows the data sets are significantly different. A paired students T-test gives a one tailed P value of 7.97×10^{-9}, significantly lower than the standard confidence threshold of 0.05. The average etch pit depth decreased by 20% after the sample was exposed to fluoride solution. This can be attributed to the fluoride incorporating into the HAP lattice. The short exposure to toothpaste levels of sodium fluoride resulted in a change detectable by SICM-PCAD. Figure 3.7 shows SICM topography maps taken before and after fluoride treatment.

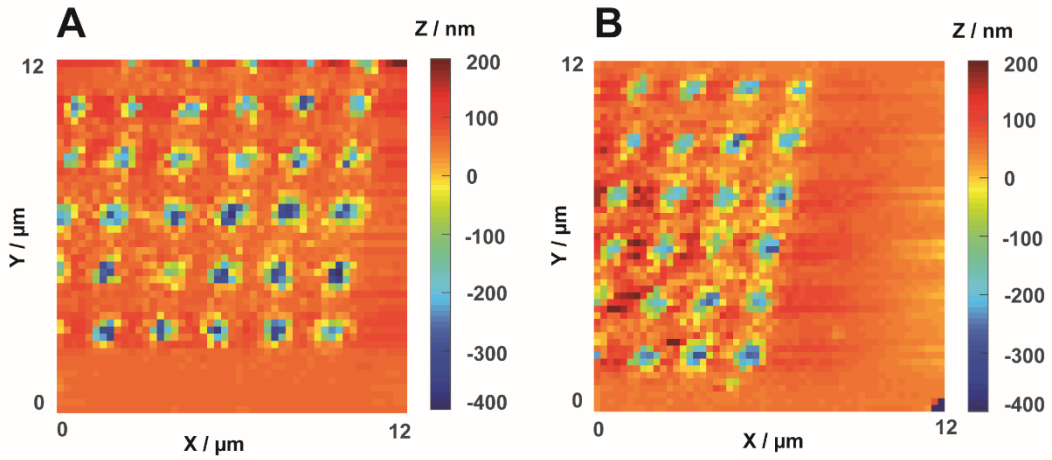

Figure 3.7 SICM Etch Pit Topography Pre and Post Fluoride Treatment

A. Shows the topography of the pre fluoride treatment etch pit array. **B.** Shows the topography of the post fluoride treatment etch pit array. Note that the etch pits in **A** are deeper. The image for **B** misses some of the array however the overall trend and the comparative shallowness of the etch pits can still be inferred. Conditions: 30 nm pipette with 50 mM KCl background electrolyte present in the tip and bath. 20 mM HCl was delivered after each approach at +100 mV for 10 seconds. 10 nm oscillation at 200 Hz. 2.5×10^{-13} A AC amplitude threshold. Topography taken with 2% DC threshold with -100 mV bias applied. 200 nm hopping distance with 3 µm retract.

The effect of the fluoride can clearly be measured by SICM-PCAD and the protection benefit quantified. Following this success, the effect of a zinc solution was investigated.

3.2.2.2 Zinc

Multiple studies have cited the beneficial properties of zinc with regards to protecting against dental erosion. It is thought that substituting small amounts of zinc into the HAP lattice stabilises the anions and makes the surface more impervious to acid attack.[27–29] The procedure in 2.6.1.1 was carried out, replacing the sodium fluoride solution with a zinc chloride solution. The raw data is given in Table 4.

Table 4 Pre and Post Zinc Etch Pit Depths

Individual etch pit depth pre zinc / µm					
0.451	0.436	0.475	0.440	0.434	0.389
0.432	0.459	0.385	0.458	0.315	0.396
0.453	0.418	0.422	0.401	0.448	0.397
0.360	0.526	0.424	0.489	0.374	0.396
0.417	0.521	0.437	0.428	0.402	0.398
0.445	0.393	0.435	0.515	0.431	0.314

Mean: 463 ± 116 nm

Individual etch pit depth post zinc / µm					
0.366	0.335	0.356	0.314	0.326	0.301
0.349	0.360	0.357	0.302	0.325	0.302
0.314	0.322	0.341	0.301	0.313	0.306
0.344	0.336	0.288	0.316	0.309	0.298
0.368	0.347	0.374	0.291	0.327	0.309
0.336	0.331	0.294	0.296	0.295	0.295

Mean: 324 ± 25 nm

Again, the standard deviations overlap slightly t-testing shows the data sets are significantly different. A paired students T-test gives a one tailed P value of 1.13×10^{-14}, significantly lower than the standard confidence threshold of 0.05. The average etch pit depth decreased by 24%. This can be attributed to the zinc treatment which has provided an enhanced protective benefit over the fluoride treatment. This may be due to the zinc being incorporated more easily into the enamel lattice than the fluoride, the zinc ions more easily substituting into calcium vacancies. Figure 3.8 shows SICM topography maps taken before and after zinc treatment.

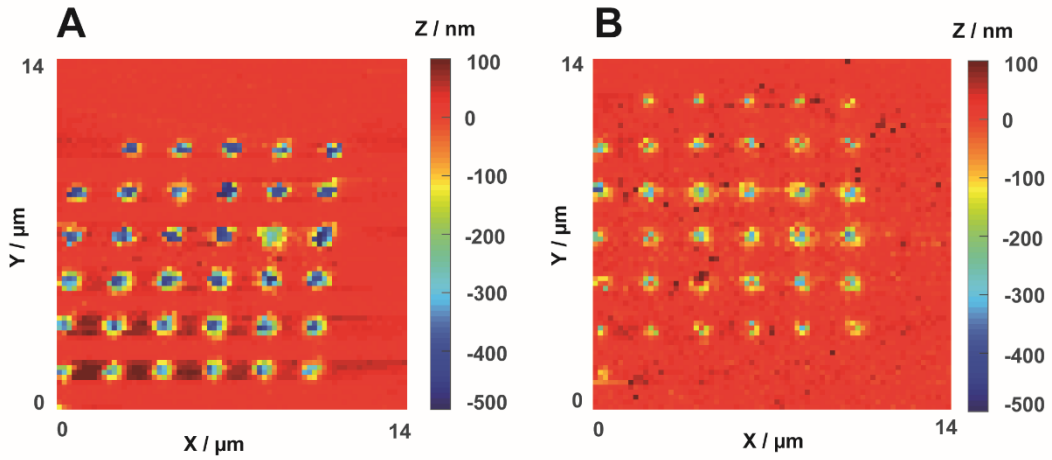

Figure 3.8 SICM Etch Pit Topography Pre and Post Zinc Treatment

A. Shows the topography of the pre zinc treatment etch pit array. **B.** Shows the topography of the post zinc treatment etch pit array. Note that the etch pits in **A** are visibly deeper, good evidence the zinc has protected the surface in image **B.** Conditions: 30 nm pipette with 50 mM KCl background electrolyte present in the tip and bath. 20 mM HCl was delivered after each approach at +100 mV for 10 seconds. 10 nm oscillation at 200 Hz. 2.5×10^{-13} A AC amplitude threshold. Topography taken with 2% DC threshold with -100 mV bias applied. 200 nm hopping distance with 3 µm retract.

The modification to the surface is again evident in the average etch pit depths. Multiple measurements allow for an overall assessment of the protection benefit offered by the zinc. With multiple repeats conclusions could be drawn on the relative effectiveness of each treatment. This work focuses on assessing numerous treatments and gives a measure of what the capabilities of the technique are. It is only in the combinatory study in 3.2.4 that enough repeats are conducted to attempt to account for sample variance. Investigating multiple surface actives and an erosive challenge was prioritised over multiple repeats in any given study, partly due to the time constraints of multiple sample preparations. In the next section the protective benefit of an applied salivary pellicle is investigated.

3.2.2.3 Pellicle Layer

To produce the pellicle layer the bovine block is immersed in irradiated human saliva for 30 minutes at room temperature. The block is thoroughly rinsed after exposure. This is enough time for a rudimentary pellicle to form. As before, a pre and post SICM-PCAD analysis is undertaken. Table 5 shows the raw etch pit depth data.

Table 5 Pre and Post Pellicle Layer Etch Pit Depths

Individual etch pit depth pre pellicle / µm					
0.390	0.417	0.348	0.342	0.364	0.277
0.346	0.378	0.291	0.419	0.362	0.228
0.425	0.342	0.402	0.412	0.255	0.311
0.449	0.370	0.411	0.388	0.334	0.224
0.403	0.404	0.369	0.368	0.312	0.271
0.512	0.382	0.351	0.354	0.395	0.343

Mean: 360 ± 61 nm

Individual etch pit depth post pellicle / µm					
0.245	0.263	0.301	0.242	0.407	0.201
0.262	0.278	0.344	0.196	0.294	0.197
0.313	0.338	0.107	0.316	0.343	0.189
0.303	0.270	0.299	0.309	0.184	0.224
0.299	0.360	0.276	0.205	0.225	0.296
0.375	0.173	0.163	0.355	0.269	0.203

Mean: 267 ± 68 nm

Figure 3.9 compares the size of etch pit arrays on a bovine enamel sample, with and without a salivary pellicle present. The protection benefit to the surface is evident in the reduction of the depth and width of the etch pits. The average depth of the pits without pellicle layer is 360 ± 61 nm and with pellicle present, 267 ± 68 nm. The *p*-value between the groups was 1.13E-14 (n=36), clearly showing a significant difference. The 93 nm difference in etching depth is greater than the approximated pellicle layer thickness of 40 nm.[30] This shows that the protective benefit of the pellicle against acid erosion is not solely sacrificial, *i.e.* the proteins and make-up of the layer inhibit the dissolution, potentially through a buffering effect that keeps the local pH higher.[31] The images help to visualise the significant reduction in erosion offered by the pellicle layer. An exact measurement in the etch pit width is hindered by the resolution employed which is limited by the 200 nm hopping distance used, but an at-a-glance comparison shows a drastic reduction when compared to the bare enamel.

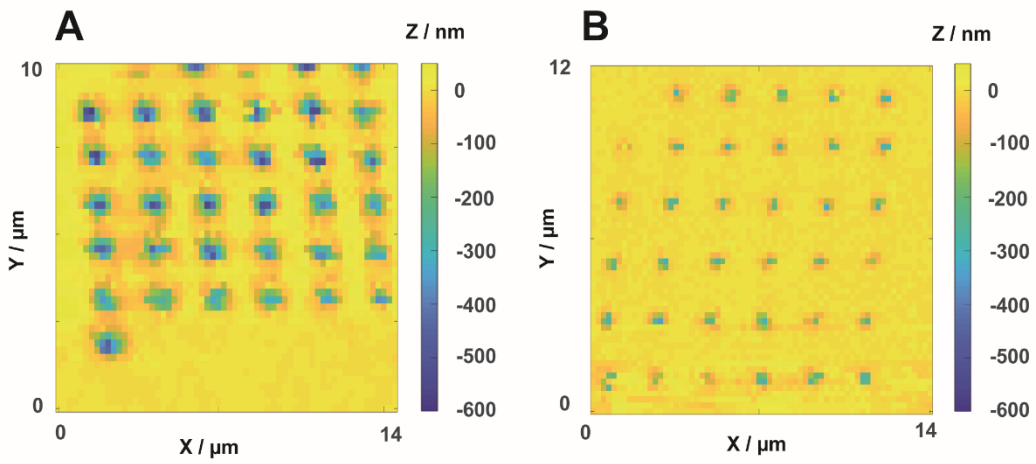

Figure 3.9 SICM Etch Pit Topography Pre and Post Pellicle Layer Adhesion

A. Shows the topography of the pre pellicle adhesion etch pit array. **B.** Shows the topography of the post pellicle adhesion etch pit array. Note that the etch pits in **A** are visibly deeper, clear evidence the pellicle has protected the surface in image **B.** Conditions: 30 nm pipette with 50 mM KCl background electrolyte present in the tip and bath. 20 mM HCl was delivered after each approach at +100 mV for 10 seconds. 10 nm oscillation at 200 Hz. 3.5×10^{-13} A AC amplitude threshold. Topography taken with 2% DC threshold with -100 mV bias applied. 200 nm hopping distance with 3 µm retract.

These data show that the technique is adaptable and for future studies on dental substrates the system can be made more representative of real-world conditions by adding an *in vitro* pellicle layer. Going forward SICM can be utilised to further enhance the effectiveness of *in-vitro* studies and help bridge the knowledge gap with *in-vivo* counterparts by simulating conditions within the body as accurately as possible. The next section details the quantification of early stage acid damage from a weak citric acid challenge.

3.2.3 Acidic Challenge

Citric acid is a prevalent dietary acid and one of the key contributors to dental erosion. Here we are able to detect very subtle acid damage. The citric acid exposure used was a 30 second submersion in 1%, pH 3.6 citric acid. This is equivalent exposure to

consuming a glass of orange juice. Table 6 gives the summary of etch pit depths before and after the citric acid challenge.

Table 6 Pre and Post Citric Acid Etch Pit Depths

Individual etch pit depth pre citric acid / µm					
0.439	0.440	0.521	0.477	0.472	0.456
0.467	0.509	0.486	0.466	0.548	0.503
0.458	0.464	0.556	0.486	0.489	0.519
0.561	0.458	0.482	0.478	0.375	0.494
0.534	0.431	0.449	0.500	0.374	0.472
0.480	0.518	0.461	0.472	0.419	0.489

Mean: 477 ± 17 nm

Individual etch pit depth post citric acid / µm					
0.649	0.535	0.569	0.506	0.541	0.501
0.601	0.653	0.510	0.457	0.651	0.496
0.517	0.679	0.566	0.524	0.710	0.497
0.689	0.627	0.505	0.606	0.723	0.647
0.564	0.492	0.525	0.554	0.417	0.548
0.658	0.510	0.576	0.618	0.484	0.675

Mean: 572 ± 6 nm

Figure 3.10 compares the topography of etch pit arrays on a bovine enamel sample, before and after a mild citric acid challenge. The increased damage to the surface is evident in the increase in depth of the etch pits. Interestingly, the pits appear wider in the before image. This may be because the pit gets deeper quicker on the acid exposed surface as the enamel is removed at a faster rate, this in turn funnels the acid downward. The average depth of the pits before the erosive challenge is 477 ± 17 nm and 572 ± 6 nm afterwards. The consistency of these results is very good with low standard deviations compared to earlier data. This may be due to increased skill on part of the experimentalist or the cut on this specific sample giving a surface with reduced heterogeneity. The *p*-value between the groups was 2.2E-8 (n=36), clearly showing a significant difference. The average increase in etch pit depth is 19%.

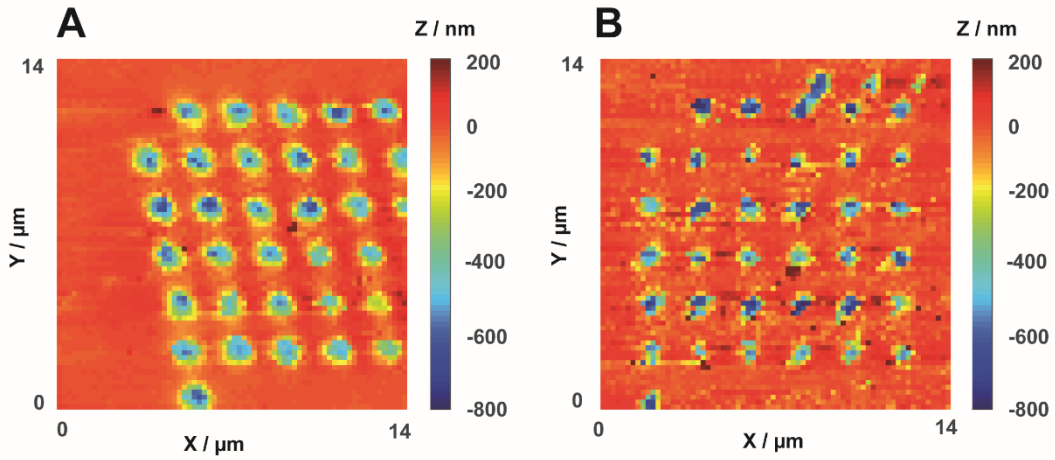

Figure 3.10 SICM Etch Pit Topography Pre and Post Citric Acid Challenge

A. Shows the topography of the pre citric acid array. **B.** Shows the topography of the post citric acid challenge etch pit array. Note that the etch pits in **B** are visibly deeper, clear evidence the citric acid has weakened the surface in image **B** resulting in deeper etch pits. Conditions: 30 nm pipette with 50 mM KCl background electrolyte present in the tip and bath. 20 mM HCl was delivered after each approach at +100 mV for 10 seconds. 10 nm oscillation at 200 Hz. 3.5×10^{-13} A AC amplitude threshold. Topography taken with 2% DC threshold with -100 mV bias applied. 200 nm hopping distance with 3 µm retract.

The etch pits in Figure 3.10**B** are narrower and deeper, perhaps due to the weakened enamel dissolving more quickly than the sound, leading to a steeper, deeper etch pit. It should also be noted that in the top right of this image there is an overlap with 3 points from an array that was started and then stopped. After this incident the spacing of arrays was increased. The 3 points affected where originally removed from the statistical analysis but the result did not vary by much, so the points were included.

This result shows that even a mild erosive treatment can be detected though this method demonstrating that the technique can be used to assess very early stage erosion and by extension, assess potential treatments and actives for their protection benefits. The next section details a larger study, in which samples under-go a multistep treatment regime to assess the viability of using SICM-PCAD for screening of actives.

3.2.4 Combinatory Study

To investigate whether the technique has the potential to be used as a screening test for enamel repair and protection assays a multiple treatment study was undertaken following the method in section 2.6.1.4. These experiments allow for the investigation of inter-sample variability, fluoride protection benefits for sound enamel, quantification of the weakness caused by citric acid exposure and an assessment of the protective benefit offered by fluoride against citric acid erosion. Table 7 provides a summary of the mean etch pit depths, these are also displayed in Figure 3.11 alongside the full treatment distributions.

For this set of experiment topography was not carried out between each step as further validation of this procedure was deemed unnecessary and the relevant etch pit depth data can be obtained without the topographical images. This also speeds up the experiments and increases the potential output. The Table 7 also contains a value for the calcium flux calculated from the FEM model. The model and how this calculation were performed are explained in full in section 3.2.6.

Table 7 Summary of Mean Etch Pit depth and FEM Calculated Dissolution Rates

	Sound Enamel Mean Etch Pit Depth / µm	**Fluoride Mean Etch Pit Depth / µm**	**Fluoride Citric Acid Mean Etch Pit Depth / µm**	**Citric Acid Mean Etch Pit Depth / µm**
Sample 1	0.292	0.23	0.318	0.528
Sample 2	0.342	0.282	0.385	0.446
Sample 3	0.362	0.355	0.651	0.742
Sample 4	0.361	0.244	0.492	0.528
Sample 5	0.483	0.462	0.65	0.729
Mean	0.368	0.315	0.499	0.594
Standard Deviation	*0.07*	*0.096*	*0.151*	*0.133*
Etching rate k_{eff} / cm s^{-1}	***0.151 ± 0.011***	***0.129 ±0.015***	***0.206 ± 0.026***	***0.246 ± 0.022***
Calcium rate $j_{Ca2+} \times 10^{-5}$ / mol m^{-2} s^{-1}	***1.8 ± 0.2***	***1.5 ± 0.2***	***2.4 ± 0.1***	***2.9 ± 0.3***

Comparing the means reported in Table 7 it is evident that fluoridation of the enamel leads to a decrease in the etch pit depth and citric acid exposure causes an increase, Figure 3.11 also demonstrates the spatial heterogeneity observed over the samples with regards to the sample response, giving a detailed display of the spread of results in the form of a bar chart of the mean etch depths per sample and a histogram. Due to the complex nature of this experiment additional statistical analysis was carried out, expanding on the basic T-testing.

Differences between treatments were significant when analysed by Kruskal-Wallis test (χ^2 = 247.91, p < 2.2E-16) and analysis by pairwise Wilcoxon rank sum test also indicates that each group is significantly different from each of the others (p <0.05, Table 7).

Table 8 Calculated p-values from Pairwise Analysis of Aggregate Data by the Wilcoxon Rank-Sum Test with Bonferroni Adjustment

	Citric acid	**Fluoride**	**Fluoride/Citric acid**
Fluoride	$< 2 \times 10^{-16}$	-	-
Fluoride/Citric acid	2.8×10^{-7}	$< 2 \times 10^{-16}$	-
Untreated	$< 2 \times 10^{-16}$	3.1×10^{-7}	6.1×10^{-13}

Table 7 shows that the treatments cause a significantly different mean etch depth when compared to baseline (untreated) enamel and shows that each group is significantly different from one another.

Ratios of mean (hence no error provided on the values) etch pit depths demonstrate protective effect of fluoride vs. sound enamel (0.856), weakening effect of citric acid vs. sound enamel (1.614), and weakening effect of citric acid treatment to fluoride exposed enamel (0.84). Being able to classify and rank erosive and restorative treatments will improve understanding of low-level dental erosion.

The relatively brief citric acid treatment has a strong weakening effect upon enamel, increasing etching rates under subsequent SICM-PCAD by 1.61 times. This is caused by a sustained increase in etching rate over the 10 seconds of the experiment, suggesting that citric acid is able to structurally destabilise the lattice more than 500 nm into the enamel surface where it is at sufficiently high concentration to cause significant weakening of the enamel. This weakening occurs through two mechanisms; simple acid attack which dissolves the enamel and increases the porosity of the surface, and chelation of Ca^{2+} which leaves less stable HAP.[11,32,33]

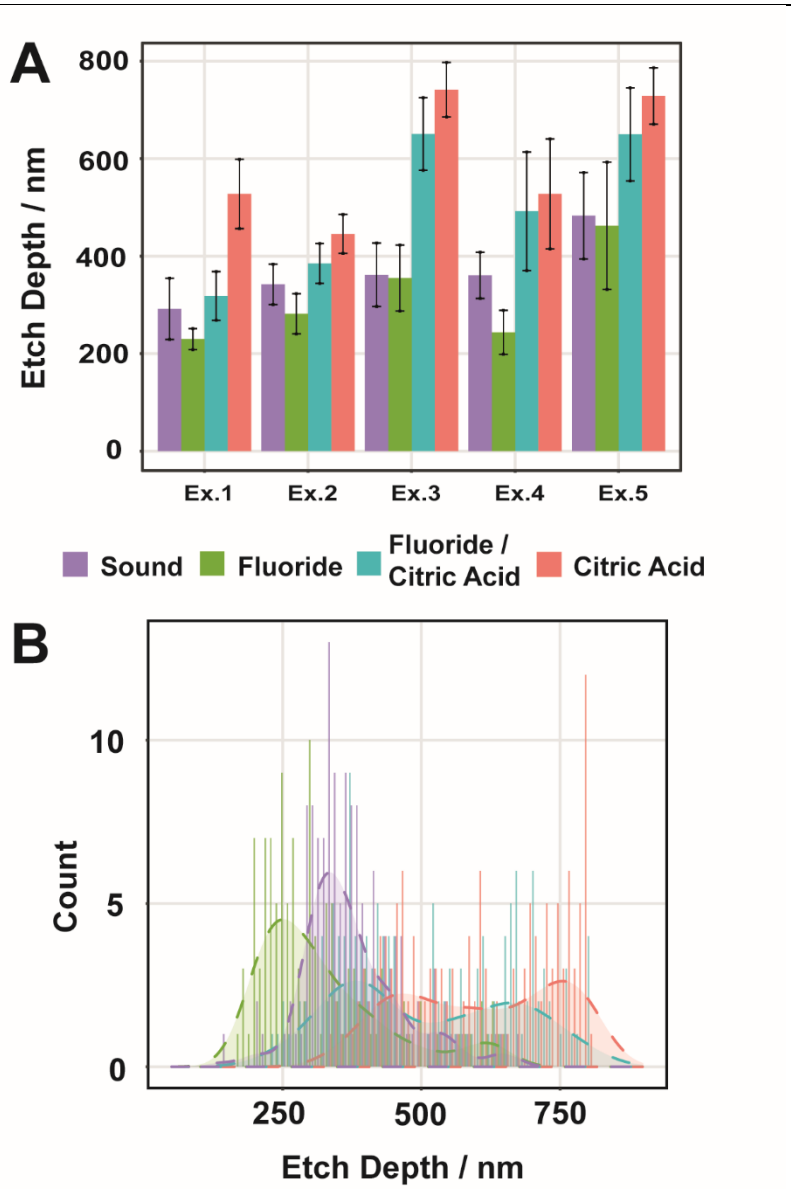

Figure 3.11 Multi-step Study Results Graphs

A. Bar chart showing mean etch pit depth for sound, fluoride treated, fluoride then citric acid and citric acid treated enamel across the 5 experiments. Error bars are one standard deviation. **B.** A histogram showing the spread of all results for sound, fluoride treated, fluoride then citric acid treated, and citric acid treated enamel. General trends can be distinguished, primarily fluoride decreasing etch pit depth compared to sound enamel and citric acid exposure greatly increasing etch pit depth.

Fluoride etch depths are 0.85 those of sound enamel, indicating a protective effect of fluoride from acid attack, suggesting that fluoride is also able to permeate into the enamel. While it is known that fluorapatite is more resistant to acid dissolution than

HAP, the penetration depth of fluoride ions into the enamel layer is debated, with some reports suggesting only 10s of nanometres being substituted.[34] This debate could be addressed through employing SICM and longer delivery times in future work. If there exists a surface layer of HAP that has been substituted for fluorapatite rather than a bulk change in the material, there should be a point at which the gradient of the etching curve begins to change with the rate of dissolution increasing when moving from the fluorapatite to HAP region. However, many estimates consider enamel as a perfect crystalline HAP surface, while in reality enamel is a heterogeneous biomaterial made up of small HAP crystals in a biopolymer matrix and could therefore allow deeper permeation, especially as the samples have been cut to expose the lattice and may experience surface dislocations and cracking.

Interestingly, where the citric acid treatment is preceded by fluoride there is a similar reduction in etch rates (0.84 that of citric acid only) when compared with the effects when citric acid is not applied (0.85). This suggests that fluoride does not provide any extra protection against citric acid compared to general protection against acid attack and fluorapatite may be as susceptible to calcium chelation as HAP.[35]

For each sample, differences in the magnitude of response to citric acid and fluoride treatments were apparent (Figure 3.12), therefore a more detailed analysis was performed on each sample individually.

The differences between treatments are once again significant for all samples as shown by the Kruskal-Wallis (Table 8) however not all treatments are significantly different for each sample individually (Table 9). Figure 3.13 demonstrates the effect of each treatment when compared with the sound enamel along with the p-value for each comparison.

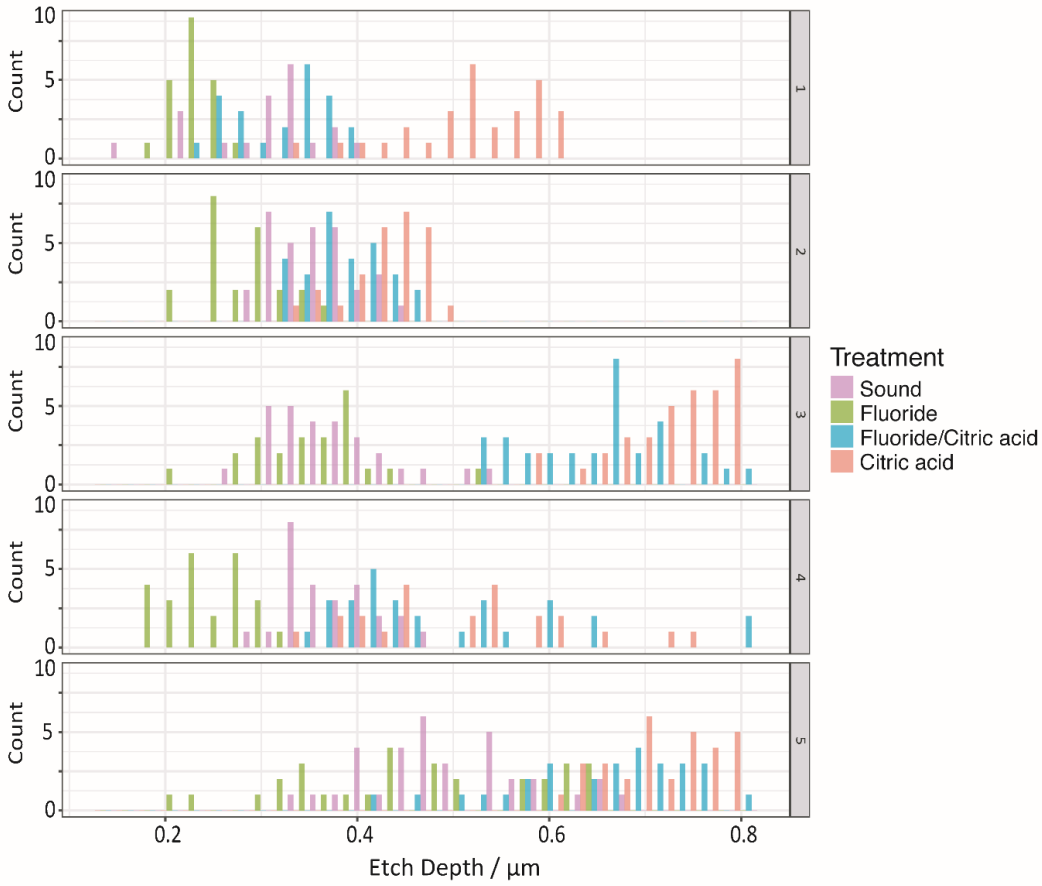

Figure 3.12 Distribution of Etch Pit Depth per Sample in Combinatory Study

Distribution of etch pit depths generated through SICM-PCAD for 5 separate enamel samples with various surface treatments; (pink) sound enamel, (green) 30 minute exposure to fluoride (1450 ppm), (red) 30 s exposure to citric acid (1%), and (blue) exposure to fluoride followed by citric acid.

Table 9 Calculated p-values from Pairwise Analysis of 5 Individual Samples by the Wilcoxon Rank-Sum Test with Bonferroni Adjustment.

Sample 1	**Citric acid**	**Fluoride**	**Fluoride/Citric acid**
Fluoride	1.40×10^{-8}	-	-
Fluoride/Citric acid	2.20×10^{-12}	2.30×10^{-6}	-
Untreated	3.40×10^{-8}	0.004	1
Sample 2	**Citric acid**	**Fluoride**	**Fluoride/Citric acid**
Fluoride	1.20×10^{-8}	-	-
Fluoride/Citric acid	3.30×10^{-5}	9.60×10^{-8}	-
Untreated	1.30×10^{-8}	0.00014	0.00315
Sample 3	**Citric acid**	**Fluoride**	**Fluoride/Citric acid**
Fluoride	7.80×10^{-10}	-	-
Fluoride/Citric acid	8.50×10^{-6}	6.40×10^{-15}	-
Untreated	5.70×10^{-11}	1	2.00×10^{-10}
Sample 4	**Citric acid**	**Fluoride**	**Fluoride/Citric acid**
Fluoride	1.90×10^{-8}	-	-
Fluoride/Citric acid	0.72	2.00×10^{-9}	-
Untreated	1.70×10^{-6}	5.20×10^{-8}	8.90×10^{-6}
Sample 5	**Citric acid**	**Fluoride**	**Fluoride/Citric acid**
Fluoride	3.80×10^{-10}	-	-
Fluoride/Citric acid	0.0042	3.80×10^{-6}	-
Untreated	9.20×10^{-11}	1	5.90×10^{-7}

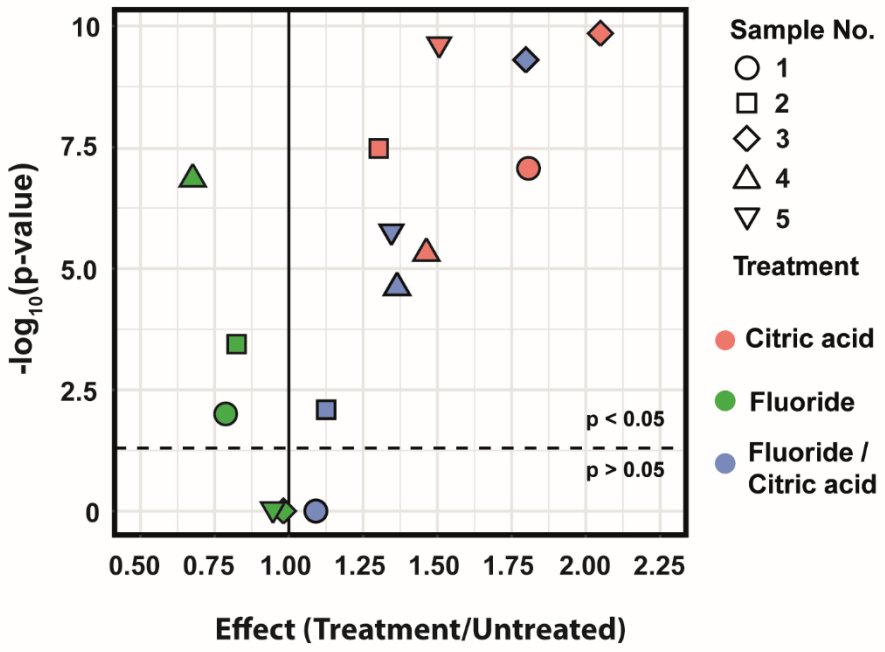

Figure 3.13 Volcano Plot Comparing each Treatment Against Sound Enamel

For each sample (represented by different shapes) the ratio between etch depth of sound enamel and each treatment (shape colour) is shown against the p-value comparing the treated array with the sound enamel, as determined by Wilcoxon ranked-sum tests with Bonferroni correction. The dashed line indicates the significance threshold of $p = 0.05$ and the solid line shows the sound enamel.

The citric acid treatment shows a consistently significant weakening effect on the enamel, however both fluoride treatments show varied sample dependent protection efficacies. Fluoride treatment alone always reduces mean pit depth, however in two cases (Figure 3.13 3 and 5) these effects are small and the arrays not significantly different compared to the sound enamel. The effect of fluoride pre-treatment upon citric acid weakening is also complex, sample 1 demonstrates the strongest fluoride protection response in both cases, while 3 and 5 reflect poor response to fluoride overall. On the other hand, 2 and 4 are protected well against induced acid dissolution alone but poorly against the citric acid treatment.

Overall, these data suggest that there are properties of the different samples and different sites which make the response from fluoride treatment variable. A likely

explanation for this is natural differences in the porosity and the frequency of dislocations which affect permeation into the sample, where some sites are only protected by fluoride at the surface. However, the same samples would therefore be expected to be least affected by citric acid exposure and this is not the case, suggesting that there are uncounted for factors influencing the sample response. These factors are difficult to standardise due to differences in the samples cut direction and depth (with no way of accounting for this), along with variability between each sample which may well be from different donor animals.

There is also often large standard deviations within measurements on the same sample, and it appears that there are often 2 distributions within each sample, suggesting 2 distinct surface environments with overlapping distributions, evident to some extent in Figure 3.11**B** were two distinct regions are outlined in the histogram, particularly that of citric acid in red. The presence of 2 distributions may be due to the length scale on which SICM-PCAD operates; the nanopipette pore diameter is much smaller (35 nm) than the 200-400 nm estimates of the size of inter-rod regions within the enamel lattice, with the etch pits generated being on a similar scale (Figure 3.14).[36] It is possible that these 2 distributions correspond with inter-rod and central region enamel, a short experiment was performed to check for this. The data for 6×36 arrays performed on the same sound enamel sample was analysed to look for distinct distributions in the data set. A histogram was plotted (Figure 3.15).

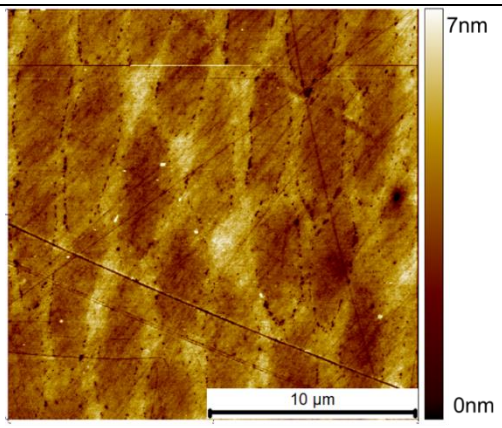

Figure 3.14 Bovine Enamel AFM Showing Inter-Rod Regions

AFM image of polished bovine enamel sample. Stereotypical honeycomb pattern of the enamel rods can be seen. On average the inter-rod regions are 400 nm across. This is wide enough that some SICM-PCAD etch pits are made solely on either inter-rod or central enamel.

The histogram does show the outline of a bimodal distribution but is not clearly defined enough to say conclusively either way. This is probably due to the inconsistent alignment of the rods and is investigated further in section 3.2.5. A higher number of points may also make the distinction clearer. In the case of the citric acid damaged samples in Figure 3.11**B** the bi-modal distribution is quite clear. This may be due to the acid exposure weakening the central rod enamel more than the inter-rod enamel thus making the distribution more pronounced, a known phenomenon in dental erosion studies.[18]

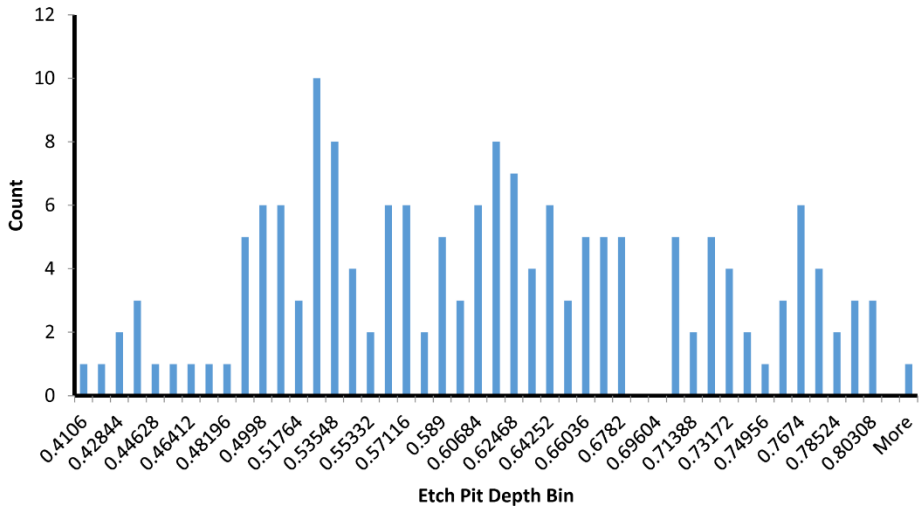

Figure 3.15 Histogram of Sound Enamel Etch Pit Depths

Histogram with 45 bins between the deepest and shallowest etch pit depths in µm. The data shows a wide spread of etch pit depths. This led to an adjustment in the experimental design to attempt to elucidate the differences between the inter-rod and central enamel regions that are present in the structure. As the angle of the cut through the sample was not controlled for in this data set high variance was expected.

Although we cannot conclusively report on the nanoscale heterogeneities from this data set it is encouraging that the information may be obtainable through this method with finer tuned experiments.

3.2.5 Dentine and Orientated Enamel

The final set of experiments in this chapter focused on assessing the comparative susceptibility to acid erosion by SICM-PCAD of polished bovine enamel, dentine and a specifically cut section of enamel that has the rods aligned perpendicular to the dentine enamel junction. The ends of the rods face upwards so the cross section appears as depicted in Figure 1.18 with the rods orientated perpendicular to the surface, so the smaller front face of the rod is aligned with the probe. This alignment exposes the largest area of the central enamel regions and ensures the inter-rod region

are not approached from an angle, making it more likely etching occurs on either the central region or the inter-rod region, not a mixture of the two.

This study was carried out by Marlene Hill a master's student who used this work in her master's thesis. This was a smaller study across 3 enamel and dentine samples. A higher number of false engagements occurred per array. Notably this issue was most apparent on dentine. The increased surface roughness and presence of dentine tubules made false engagements a more common occurrence, with only a third of the etch traces being usable. Although the robustness of this study is inferior to previous studies the concluding data is worth discussing.

The mean etch pit depth for enamel was 336.5 ± 61.74 nm (*n = 82* from three different enamel blocks. The mean etch pit depth for dentine was 652.3 ± 103.94 nm (*n = 41* from three different enamel blocks). The mean etch pit depth for the aligned samples was 1249 ± 311.9 nm (n = 57 from three different aligned enamel samples). Even accounting for sample variability there is a clear difference in the results for enamel, dentine and aligned enamel. Dentine on the whole was more susceptible to erosion, as predicted by the literature.

Interestingly, the alignment of the rods had a huge effect. Although false engagements were again more common, when the etch traces did successfully occur the pits were deeper than any seen previously. It is thought that when etching occurred on the central enamel regions the more resistant rod sheathes channelled the acid leading to very deep etch pits. This leads to a very clear bimodal distribution in the histogram when all of the obtained data for the aligned samples is plotted (Figure 3.16).

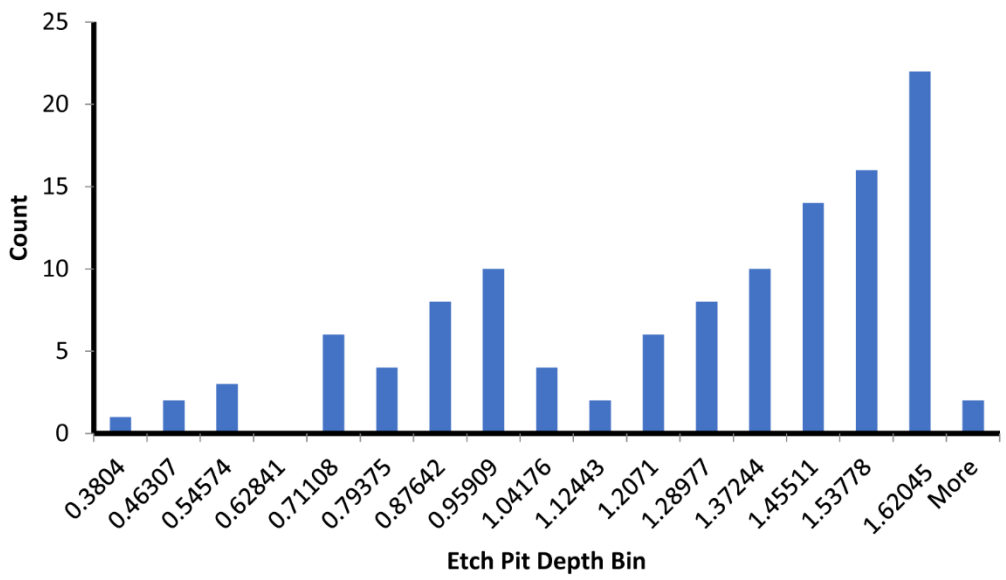

Figure 3.16 Histogram of Aligned Enamel Etch Pit Depths

Histogram showing the distribution of etch pit depths in µm for the aligned enamel sample. The consistent alignment of the rods leads to a bimodal distribution with the central enamel regions likely etching much deeper than the inter-rod regions due to their reported increased susceptibility to acid erosion in the literature.

This data shows the ability of SICM-PCAD to elucidate differences in surface heterogeneities. The mean etch pit depths acquired for the different samples in this section and those collected previously were used to calculate etching rates using the FEM model in the following section. Through this combinatory technique it is possible to estimate etching rates for a variety of samples and study how surface treatments and erosive challenges alter the dissolution processes.

3.2.6 FEM Modelling

FEM simulations were constructed in COMSOL Multiphysics (v5.4) to extract the effective rate of reaction for acid induced enamel erosion. The nanopipette and substrate were modelled as a 2D axisymmetric geometry (Figure 3.18), with the nanopipette dimensions extracted from representative transmission electron micrographs of experimental nanopipettes (Figure 3.17).[37] The radius of the pipette opening was measured as 15 nm and the height of the simulation domain of the

nanopipette was chosen sufficiently large enough to not affect the results of the simulation (650 µm), likewise the outer boundaries (Figure 3.18, Boundary B2) were sufficiently far away to be considered bulk (100 µm).

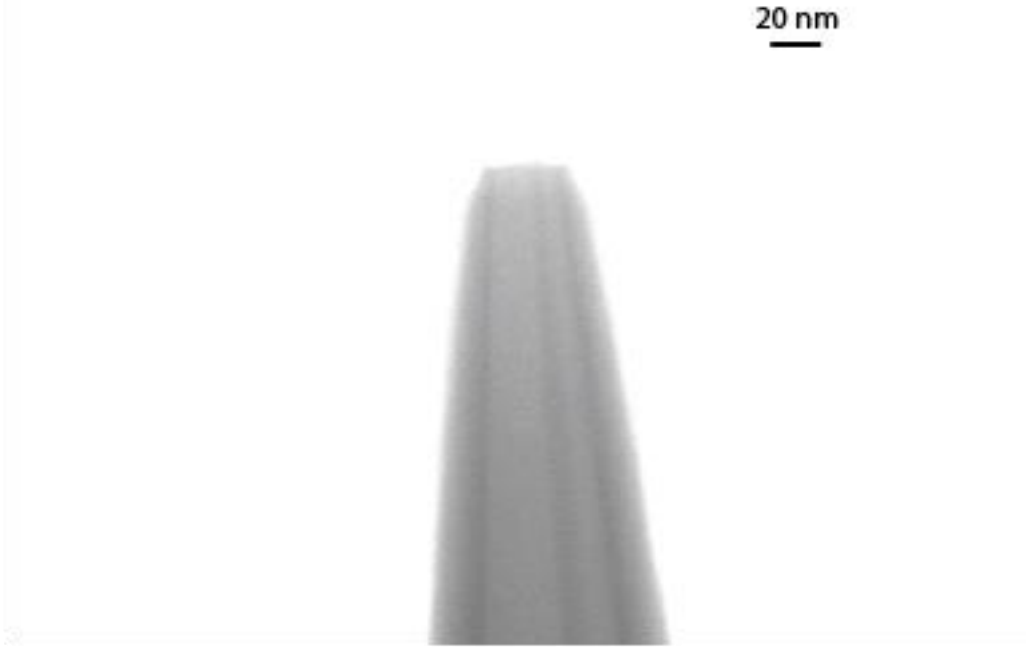

Figure 3.17 STEM Image of 30 nm Pipette

Scanning transmission electron microscopy (STEM) image of a representative nanopipette with a pore diameter of approximately 30 nm.

Table 10 Table of Diffusion Coefficients and Charges of Species used in FEM Simulations, Obtained from the CRC Handbook.[38]

Species	Diffusion Coefficient (D) / $cm^2\ s^{-1}$	Charge (z)
H^+	9.311×10^{-5}	1
OH^-	5.273×10^{-5}	-1
HPO_4^{2-}	0.759×10^{-5}	-2
$H_2PO_4^-$	0.959×10^{-5}	-1
H_3PO_4	0.882×10^{-5}	0
Ca^{2+}	0.792×10^{-5}	+2

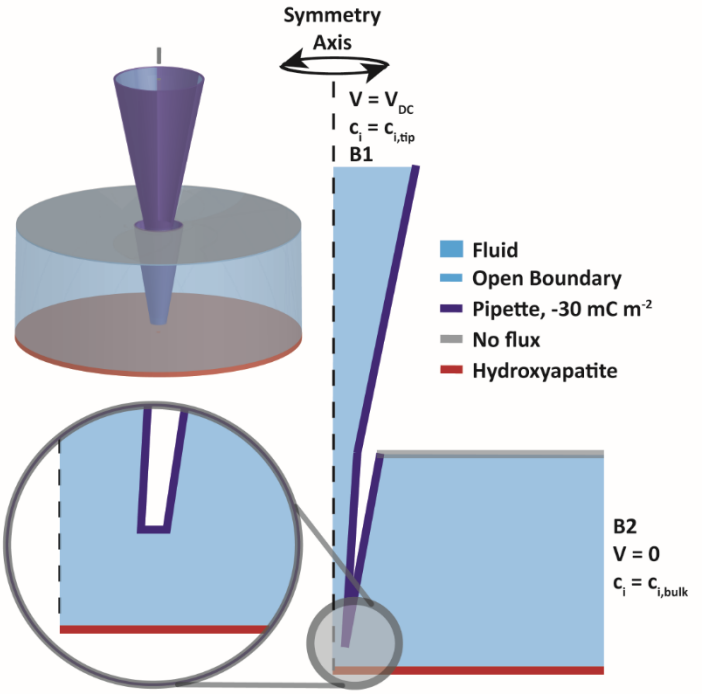

Figure 3.18 FEM Model Geometry

Schematic of the FEM simulation domain for SICM-PCAD of enamel substrates (red). Nernst-Planck, Poisson and Navier-Stokes equations (Eqs. 2-4) are solved throughout the simulation domain as described in the main text. Boundaries were prescribed as labelled, with B1 and B2 as open boundaries for fluid with set concentrations and voltages. Dashed line shows the 2D axisymmetric axis. All other boundaries are no-slip fluid boundaries, with charge of -30 mC m^{-2} in the case of the pipette (purple) and 0 mC m^{-2} for all other boundaries.

The proton induced dissolution of HAP is approximated by equation 1[39] for the purposes of the FEM simulations.

$$Ca_{10}(PO_4)_6(OH)_{2(s)} + 8H^+_{(aq)} \rightleftharpoons 10Ca^{2+}_{(aq)} + 6HPO^{2-}_{4(aq)} + 2H_2O \quad (1)$$

Transport of dissolved species were described by the Nernst-Planck equation (Eq. 2):

$$J_i = -D_i \nabla c_i - z_i \frac{F}{RT} D_i c_i \nabla \phi + c_i u \tag{2}$$

Where F, R and T are the Faraday constant, gas constant and absolute temperature (298 K), and D_i z_i and c_i are the diffusion coefficients, charge number and concentrations of species i (Table 10). This is coupled to the Poisson equation (Eq. 3) to describe the electric potential (ϕ), and the Navier-Stokes equation to describe solution velocity (u) accounting for movement due to EOF:

$$\nabla^2 \phi = -\frac{F}{\varepsilon \varepsilon_0} \sum_i z_i c_i \tag{3}$$

$$u \nabla u = \frac{1}{\rho}(-\nabla p + \mu \nabla^2 u - F(\textstyle\sum_i z_i c_i) \nabla \phi) \tag{4}$$

At the enamel/solution interface (Red boundary) the dissolution of HAP is modelled through the reaction described in Eq. 2, where the inward flux of dissolution products is defined by the reaction rate (k_0), local proton activity $\{H^+\}$, and unit vector normal to the boundary (n):

$$-n \cdot N_{Ca^{2+}} = k_0 \cdot \{H^+\} \cdot \left(\frac{10}{8}\right) \tag{5a}$$

$$-n \cdot N_{H_2PO_4^{2-}} = k_0 \cdot \{H^+\} \cdot \left(\frac{6}{8}\right) \tag{5b}$$

$$-n \cdot N_{H^+} = -k_0 \cdot \{H^+\} \tag{5c}$$

Throughout the simulation domain, species equilibrium was controlled by a set of reactions which were defined as follows:

$$H_3PO_4 \rightleftharpoons H^+ + H_2PO_4^- \qquad K_{a1}^+ = \frac{\{H_2PO_4^-\}\{H^+\}}{\{H_3PO_4\}}$$

(6a)

$$H_2PO_4^- \rightleftharpoons H^+ + HPO_4^{2-} \qquad K_{a2}^+ = \frac{\{HPO_4^-\}\{H^+\}}{\{H_2PO_4^-\}}$$

(6b)

$$H_2O \rightleftharpoons H^+ + OH^- \qquad K_w = \frac{\{OH^-\}\{H^+\}}{55.5\ M}$$

(6c)

Where K_{a1}^+, K_{a2}^+ and K_w are the dissociation constants and the local activity (a_i) of each ion (Eq 7) is calculated through the Truesdell-Jones equation (Eq 8) from Debye-Hückel theory.

$$a_i = \gamma_i \frac{c_i}{c_0}$$

(7)

$$log_{10}\,\gamma_i = -Az_i^2\left(\frac{\sqrt{I}}{1+\sqrt{I}} + 0.2I\right)$$

(8)

$$I = \frac{1}{2}\sum_{i-1}^{n} c_i z_i^2$$

(9)

Where local γ_i is the activity coefficient of each ion, A and B are empirical parameters with values of 0.5 and 0.2 respectively and I is the local ionic strength (Eq 9). All electric potentials were applied to the upper nanopipette boundary (B1) at which concentrations were maintained corresponding to those of the acid filled pipette; ($[K^+]$ = 50 mM, $[Cl^-]$ = 70 mM, $[H^+]$ = 20 mM) with the concentration of phosphate species set to 0 mM and $[OH^-]$ set by the resulting pH of 1.70. At the bulk boundary (B2}, electric ground (V = 0) was applied alongside bulk concentrations ($[K^+]$ = 50 mM, $[Cl^-]$ = 50 mM, $[H_3PO_4] = [HPO_4^{2-}] = 0$ mM), where $[H^+]$ and $[OH^-]$ were defined by the

solution pH of 6.8. Each of these boundaries (B1 and B2) was also defined as an open fluid boundary, while a no-slip condition was enforced at all remaining boundaries. Surface charge was only applied to the walls of the pipette (-30 mC m^{-2}), resulting in electro-osmotically driven flow. The approach was first simulated with the holding bias of -100 mV as a steady state simulation, corresponding to the DC component from which the AC amplitude was calculated from the DC amplitude of a 5 nm peak to peak oscillation of the tip. For visualisation of the approach characteristics, the DC approach was fitted with an accepted semi-empirical formula[40] and the distance modulated current calculated as a sum of the DC component and AC perturbation (Figure 3.2**B**). The AC amplitude approach set point of 0.25 pA was calculated as a tip-substrate separation of 36.5 nm, at this point the proton flux is low, with a surface pH of 5, marginally more acidic than the accepted critical pH of 5.5,[8] indicating that the holding potential is effective and the substrate is stable throughout the approach.

Acid delivery was simulated as a steady state simulation with +100 mV bias applied at the top of the pipette, the AC amplitude set point of 0.25 pA is maintained and the calculated tip-substrate separation is 39 nm as the centre of the ± 5 nm oscillation. Simulations at 39 ± 5 nm indicate that the AC amplitude is insensitive to changes in surficial fluxes across the range of k_0, thereby maintaining a constant tip-substrate separation independent of local surface dissolution (Figure 3.19).

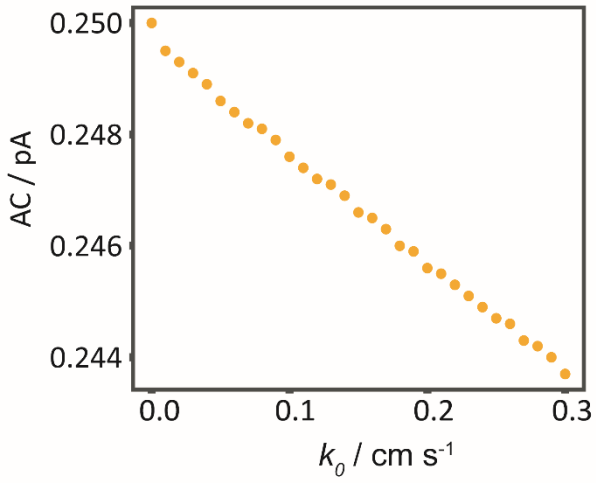

Figure 3.19 FEM Simulation of AC during SICM-PCAD

Simulation of AC during SICM-PCAD at across the range of k_0 corresponding to the experimental K_{Etch} at 39 nm tip-substrate separation ± 5 nm sinusoidal oscillation.

These simulations also show that over a full period of oscillation, the resulting tip-substrate separation causes very small differences in estimates of k_0, with only 2% deviation between the peak (44 nm) and trough (34 nm) of the perturbation (Figure 3.20). Steady state simulations are therefore considered reasonable because the surface tracking is able to maintain a constant tip-substrate separation and the etching rate is independent of the sinusoidal perturbation in tip-substrate separation. Additionally, the etching rates (up to 70 nm s^{-1}) are slow in comparison to the time required to reach steady state (10's of ms), particularly considering that there will be additional mixing induced by pipette oscillation.

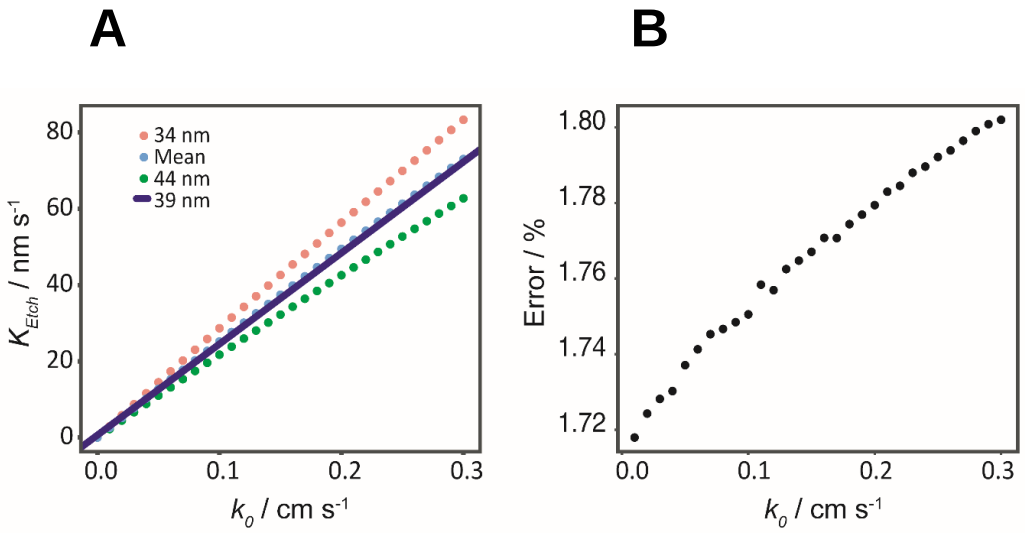

Figure 3.20 FEM Simulations of the Relationship between Etching Rate and k_0

FEM simulations of the relationship between the etching rate and k_0 (A) for the peak (44 nm, red) and trough (34 nm, grey) of the oscillation during distance modulated surface tracking for the delivery pulse. The etching rate calculated from the mean of the peak and trough within one period of oscillation (orange) shows the maximum deviation from the etching rate calculated by steady state simulations at the centre of the oscillating tip-substrate separation (39 nm black). B shows the percentage difference between the two estimations is 1.7-1.8% within the relevant range of k_0.

Etching rates were calculated from the depth of HAP removed in the region underneath the pipette, using the molar volume of HAP (V_m = 3147.4 mol m^{-3}) (Eq. 10):

$$K_{etch} = \frac{-k_0 \cdot \{H^+\}}{\frac{1}{8} V_m} \qquad (10)$$

While enamel is not pure HAP estimates suggest it is around 90%,[41] the scale of the tip diameter (30 nm) and associated SICM resolution being smaller than that of individual HAP crystals which are 75 nm in diameter (*vida infra*).[42] By applying different k_0 values in the simulations, a calibration between etching rate and effective rate constant can be attained (Figure 3.21), the high degree of linearity in this plot indicates that the mass transfer of protons to the surface is sufficiently high to ensure

that the reaction is kinetically limited even at high reaction rates. As such, the fully surface limited regime generated by SICM delivery techniques ensures experimental values are a direct measurement of surface kinetics, demonstrating ability to specifically probe even very fast interfacial processes.

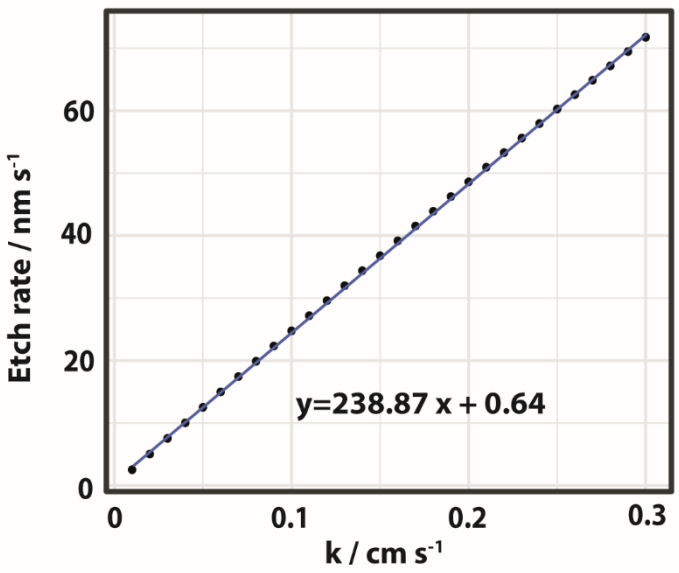

Figure 3.21 Etching Rate vs Reaction Rate Calibration Curve

Output from the FEM model for varying k, rate of HAP removal corresponding to change in etching rate (etch depth over time). From this calibration plot approximate rates of HAP removal for enamel, dentine, aligned enamel and surface treated enamel can be calculated.

The etch pit depths, in conjunction with FEM modelling, allow for the dissolution rate and calcium release rate from the surface to be calculated. Using the calibration plot in Figure 3.21 the experimental etch depths can be converted to etching and calcium dissolution rates. The calculated rates are shown in Table 11, along with the mean depth value for each etch pit array on each sample.

Table 11 Mean Etch Pit Depths, Etching Rate and Calcium Release Rate

	Mean etch pit depth (S.D) / nm	Rate / nms^{-1}	k_{eff} / cm s^{-1}	j_{Ca2+} x 10^{-5} / *mol* m^{-2} s^{-1}
Sound Enamel	368 (70)	37 ± 7	0.1522 ± 0.02	1.81 ± 0.2
Fluoride	315 (96)	32 ± 10	0.131 ± 0.04	1.5 ± 0.4
Fluoride then Citric Acid	499 (151)	50 ± 15	0.206 ± 0.06	2.4 ± 0.6
Citric Acid	0.594 (133)	59 ± 13	0.244 ± 0.05	2.9 ± 0.5
Sound Enamel Study 2	337 (62)	34 ± 6	0.139 ± 0.02	1.65 ± 0.2
Dentine	652 (104)	65 ± 10	0.269 ± 0.04	3.2 ± 0.4
Aligned Enamel	1249 (312)	125 ± 31	0.520 ± 0.12	6.1 ± 1.2

The k values are converted directly from the experimental etching rates. The calcium release rate is calculated from the proton rate, incorporating the stoichiometry

FEM simulations of the acid delivery conditions show that the concentration of protons at the surface results in a pH of 2.8 at areas proximal to the probe Figure 3.22, this corresponds to a moderate to strong acid attack treatment, comparable to exposure to stomach acid.[6,43]

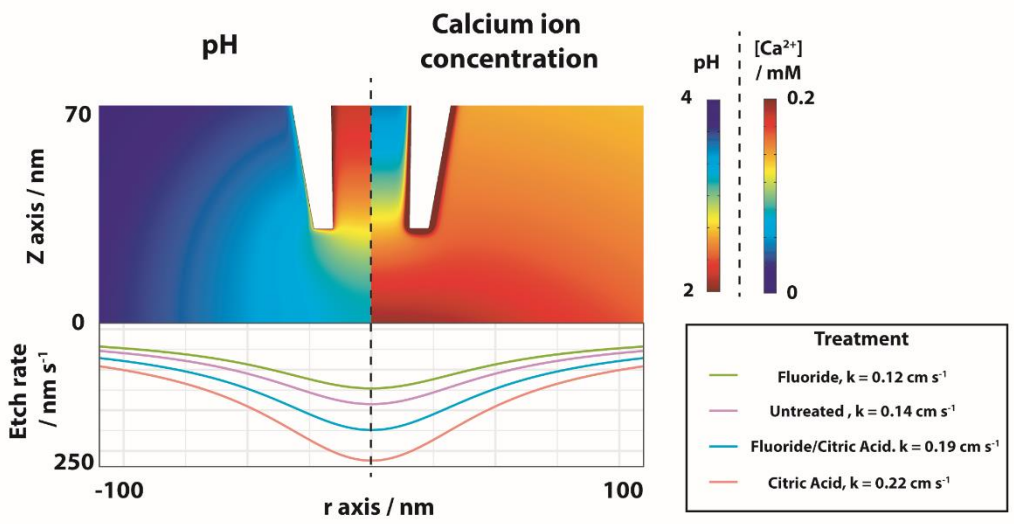

Figure 3.22 FEM Simulation of the SICM-PCAD Process on Enamel with Various Surface Treatments.

pH distribution created by controlled proton flux from the pipette in proximity to the surface are shown for k = 0.15 cm s^{-1} (left), with the corresponding concentrations of Ca^{2+} due to dissolution flux (right). Surface etching rates are shown across the surface (bottom) for rates of interest from table 7.

The average effective rate constants for each treatment are shown, with sound enamel calculated to be 0.15 cm^{-1}, comparable with literature values[34,44] and previous research from the Unwin group.[18,45] As the reaction has been shown to be surface limited, there is a linear relationship between etching rate and effective kinetic rate constant. The shape of etch pits is also shown for each treatment mean as the etching rate, as the pH decreases to bulk (pH 6.8) across the surface, the etching rate decreases accordingly.

The rate constant for fluoride treated enamel is less well represented in the literature due to the increased number of factors involved which define the ratio of fluoride substitution. The effective rate constant for fluoride treated enamel from this work is 0.1 cm^{-2}, this is far slower than that of FAP, which is estimated to be an order of magnitude lower than HAP,[46] and suggests that at least some FAP is incorporated into the surface enamel. The flux of calcium from the surface is also shown, capped at 0.2 mM as it is concentrated within the double layer of the glass. It is excluded from the nanopipette due to the applied bias. The phosphate products form more complex

spatial distributions. H_3PO_4 is localised only within the last 2.5-3.5 µm of the nanopipette (Figure 3.23) due to flux of phosphate products from the surface and the local pH gradient within the tip, generating spatially confined speciation which may be of interest to crystallisation studies.

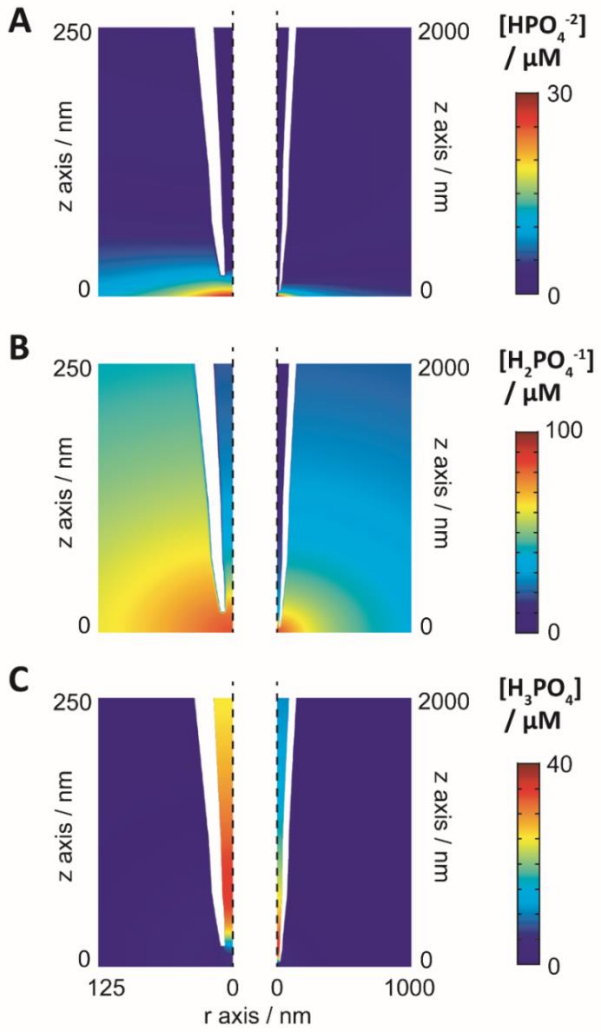

Figure 3.23 Distribution of Phosphate Species in Steady-State FEM Simulations of SICM-PCAD

(**A**) HPO_4^{2-} is produced by acid induced dissolution of HAP at the substrate surface, this is quickly protonated to (**B**) $H_2PO_4^-$ which mainly diffuses into bulk but also migrates into the tip where it is again protonated to (C) H_3PO_4which is only present in the first few microns of the pipette due to the relatively small amounts generated at the surface and the protonation due to the presence of the HCl.

3.3 Conclusions and Future Work

The work presented in this chapter covers the development of a new secondary mode for SICM. The system that allows SICM to be an effective topography mapping instrument in solution is exploited to provide dissolution measurements of a target surface in a way that is unique to SICM. The solution filled nanopipette and the fine control of acid release achieved by bias manipulation combine to provide a method of making local dissolution measurements on the nanoscale. Careful experimental design and the constant distance surface tracking resulting from the AC feedback mode causes the dissolution to occur in a controlled and measurable way. The rate of dissolution is clearly relatable to the change in Z height measured by the piezo as the etch pits form. This data can be used in conjunction with FEM modelling to estimate dissolution rates and rates for release of ions of interest such as calcium.

When all other factors are kept the same, the average measurement on a sample is consistent. The average pit depth on a sample changes in a logical and predictable way when the sample is exposed to an outside stimulus, i.e. the etch pits made are deeper when the enamel is softened with citric acid and shallower when the enamels resistance to acid is increased by fluoride or zinc exposure. The ability to perform multiple measurements and obtain immediate feedback on the surface's susceptibility to acid attack *in situ* is a powerful tool for gathering statistically relevant data about a difficult to study phenomenon. As the treatments used are fairly mild (1% citric acid for 30 seconds is not a particularly caustic treatment) the technique shows promise for being able to measure and quantify subtle changes imparted by low level exposures to test solutions.

Whilst the experiments can be deemed a success as usable data was obtained via a previously unreported method putting the data acquired into context is more difficult. The measurements on different samples can be assessed relative to one another but further work involving other materials and systems with varying hardness, density and susceptibility to dissolution need to be studied to fully interpret the data. The technique will be able to fulfil niche applications such as measuring the benefits or drawbacks of novel toothpaste ingredients designed to strengthen enamel and increase acid

resistance but its usefulness in a wider field could rightly be debated due to the intricate nature of the experimental setup and the fragility of the probes.

The experiments themselves are complex to set up and require a high degree of understanding of a bespoke set of instrumentation and careful sample preparation, the results being inconsistent if the sample is not polished extremely flat. This means this method of testing is only available to universities with scanning probe technology already implemented or would require a large investment (both monetary and in time and training) from a curious industrial party to replicate. Whilst herein, this platform is focussed on dental ceramics and their relative susceptibility to acid attack, we envision this technique is widely applicable and could provide a wealth of information about additives, protective coatings and oxide layers on surfaces required to be corrosion resistant.

Whilst not a complete exploration of the area, this work does show the potential of the technique for acquiring statistically relevant data. The work uses a robust FEM model to better understand a dynamic system and provides a blueprint for extracting reaction rates of individual components of a multifaceted dissolution process. The final set of experiments in this chapter attempt to elucidate the difference in etching rates of enamel from the inter-rod and central rod regions. Whilst not conclusive from the data gathered it does indicate that the method may be capable of distinguishing this with further experiments.

In future work, to enhance the capability of the technique higher resolution topography images need to be acquired with SICM post etching and then repeated with AFM for confirmation. Most of the topography images gathered were too low resolution for accurate measurements and only showed that it is possible to obtain undistorted topographic measurements with an acid filled probe. This is the most obvious next step and the aim is to undertake it before this work is published post thesis. As the works stands a secondary technique such as AFM would provide a more robust topographical measurement to support the Z height data obtained *in situ*.

3.4 References

1 M. Adobes-Vidal, A. G. Shtukenberg, M. D. Ward and P. R. Unwin, *Cryst. Growth Des.*, 2017, **17**, 1766–1774.

2 N. Blagden, M. de Matas, P. T. Gavan and P. York, *Adv. Drug Deliv. Rev.*, 2007, **59**, 617–630.

3 F. M. Maddar, M. Adobes-Vidal, L. P. Hughes, S. A. C. Wren and P. R. Unwin, *Cryst. Growth Des.*, 2017, **17**, 5108–5116.

4 M. M. Mbogoro, M. Peruffo, M. Adobes-Vidal, E. L. Field, M. A. O'Connell and P. R. Unwin, *J. Phys. Chem. C*, 2017, **121**, 12726–12734.

5 E. Gartner, *Cem. Concr. Res.*, 2004, **34**, 1489–1498.

6 L. Shaw and a J. Smith, *Br. Dent. J.*, 1999, **186**, 115–8.

7 J. E. Frencken, P. Sharma, L. Stenhouse, D. Green, D. Laverty and T. Dietrich, *J. Clin. Periodontol.*, 2017, **44**, S94–S105.

8 H. G. Linge and G. H. Nancollas, *Calcif. Tissue Res.*, 1973, **12**, 193–208.

9 M. S. wu, W. I. Higuchi, J. L. Fox and M. Friedman, *J. Dent. Res.*, 1976, **55**, 496–505.

10 W. White and G. H. Nancollas, *J. Dent. Res.*, 1977, **56**, 524–530.

11 N. X. West, A. Maxwell, J. A. Hughes, D. M. Parker, R. G. Newcombe and M. Addy, *J. Dent.*, 1998, **26**, 329–335.

12 Z. J. Cheng, X. M. Wang, F. Z. Cui, J. Ge and J. X. Yan, *Biomed. Mater.*, , DOI:10.1088/1748-6041/4/1/015020.

13 Y. T. Cheng and C. M. Cheng, *Mater. Sci. Eng. R Reports*, 2004, **44**, 91–149.

14 D. Elkassas and A. Arafa, *J. Dent.*, 2014, **42**, 466–474.

15 A. Joiner, G. Thakker and Y. Cooper, *J. Dent.*, 2004, **32**, 27–34.

16 D. B. Marshall, T. Noma and A. G. Evans, *J. Am. Ceram. Soc.*, 1982, **65**, c175–c176.

17 A. E. Giannakopoulos, P. L. Larsson and R. Vestergaard, *Int. J. Solids Struct.*, 1994, **31**, 2679–2708.

18 C. A. McGeouch, M. A. Edwards, M. M. Mbogoro, C. Parkinson and P. R. Unwin, *Anal. Chem.*, 2010, **82**, 9322–9328.

19 A. S. Parker, R. Al Botros, S. L. Kinnear, M. E. Snowden, K. McKelvey, A. T. Ashcroft, M. Carvell, A. Joiner, M. Peruffo, C. Philpotts and P. R. Unwin, *J. Colloid Interface Sci.*, 2016, **476**, 94–102.

20 D. R. Curtis, *Electrophysiol. Methods*, 1964, 144–190.

21 T. P. Hicks, *Prog. Neurobiol.*, 1984, **22**, 185–240.

22 A. Bruckbauer, P. James, D. Zhou, J. W. Yoon, D. Excell, Y. Korchev, R. Jones and D. Klenerman, *Biophys. J.*, 2007, **93**, 3120–31.

23 J. D. Piper, C. Li, C.-J. Lo, R. Berry, Y. Korchev, L. Ying and D. Klenerman, *J. Am. Chem. Soc.*, 2008, **130**, 10386–10393.

24 B. Babakinejad, P. Jönsson, A. López Córdoba, P. Actis, P. Novak, Y. Takahashi, A. Shevchuk, U. Anand, P. Anand, A. Drews, A. Ferrer-Montiel, D. Klenerman and Y. E. Korchev, *Anal. Chem.*, 2013, **85**, 9333–9342.

25 S. Schobesberger, P. Jönsson, A. Buzuk, Y. Korchev, J. Siggers, J. Gorelik, A. Buzuk¤, Y. Korchev¤, J. Gorelik¤, P. Jö, A. Buzuk, Y. Korchev, J. Siggers and J. Gorelik, *Nanoscale, Voltage-Driven Application of Bioactive Substances onto Cells with Organized Topography*, 2016, vol. 110.

26 B. Chen, D. Perry, A. Page, M. Kang and P. R. Unwin, *Anal. Chem.*, 2019, **91**, 2516–2524.

27 Y. Honda, T. Anada, S. Morimoto, Y. Shiwaku and O. Suzuki, *Cryst. Growth Des.*, 2011, **11**, 1462–1468.

28 Y. Xu, F. W. Schwartz and S. J. Traina, *Environ. Sci. Technol.*, 1994, **28**, 1472–1480.

29 E. Boanini, M. Gazzano and A. Bigi, *Acta Biomater.*, 2010, **6**, 1882–1894.

30 M. Hannig and C. Hannig, in *Monographs in Oral Science*, 2014, vol. 25, pp. 206–214.

31 A. T. Hara and D. T. Zero, in *Monographs in Oral Science*, 2014, vol. 25, pp. 197–205.

32 Y. Yoshida, B. Van Meerbeek, Y. Nakayama, M. Yoshioka, J. Snauwaert, Y. Abe, P. Lambrechts, G. Vanherle and M. Okazaki, *J. Dent. Res.*, 2001, **80**,

1565–1569.

33 B. Me, P. Dm, A. Gc, J. Kd, M. E. Barbour, M. David, G. C. Allen and D. Klaus, *Eur. J. Oral Sci.*, 2003, **111**, 258–262.

34 N. H. de Leeuw, *J. Phys. Chem. B*, 2004, **108**, 1809–1811.

35 R. Shellis, J. Featherstone and A. Lussi, in *Monogr Oral Sci*, 2012, vol. 25, pp. 163–179.

36 S. Habeliz, S. J. Marshall, G. W. M. Jr, M. Balooch, S. Habelitz, S. J. Marshall, G. W. M. Jr and M. Balooch, *Arch. Oral Biol.*, 2001, **46**, 173–183.

37 D. Perry, D. Momotenko, R. A. Lazenby, M. Kang and P. R. Unwin, *Anal. Chem.*, 2016, **88**, 5523–5530.

38 J. R. Rumble, D. R. Lide and T. J. Bruno, *CRC handbook of chemistry and physics 98th edition*, CRC Press, Cleveland, 2017.

39 J. A. Gray, *J. Dent. Res.*, 1962, **41**, 633–645.

40 J. Rheinlaender and T. E. Schäffer, *Anal. Chem.*, 2017, **89**, 11875–11880.

41 R. Shellis, J. Featherstone and A. Lussi, in *Monogr Oral Sci*, 2012, vol. 25, pp. 163–179.

42 A. G. Fincham, J. Moradian-Oldak and J. P. Simmer, *J. Struct. Biol.*, 1999, **126**, 270–299.

43 D. A. Lazarchik and K. B. Frazier, *Gen. Dent.*, 2009, **57**, 151–156.

44 O. Ilie, M. C. M. van Loosdrecht and C. Picioreanu, *J. Theor. Biol.*, 2012, **309**, 159–175.

45 A. S. Parker, R. Al Botros, S. L. Kinnear, M. E. Snowden, K. McKelvey, A. T. Ashcroft, M. Carvell, A. Joiner, M. Peruffo, C. Philpotts and P. R. Unwin, *J. Colloid Interface Sci.*, 2016, **476**, 94–102.

46 K. O. Aileen Chin and G. H. Nancollas, *Langmuir*, 1991, **7**, 2175–2179.

4 SICM Surface Charge Mapping of Dental Substrates

4.1 Introduction

This chapter details use of SICM-SCM for visualising the charged domains within polished dental enamel and dentine structures. The repeating honeycomb structure that is revealed when a section of dental enamel is cut and polished makes a good test subject for SICM-SCM. Subtle changes in the crystal orientation and compositional changes in the enamel give rise to a surface charge differential across the surface. The subtle nature of the heterogeneities, arising from little more than a change in crystal orientation and protein content of the interlocking enamel offers a unique test on the limit of detection for SICM-SCM. For the first time these features are mapped with SICM-SCM and the surface charge discrepancy quantified. The tubule studded surface of dentine is also imaged, revealing its own surface charge heterogeneities which give insight into tubule function

Subsequently, SICM-SCM is used to assess and quantify early stage acid erosion on enamel imparted by two dietary acids, phosphoric acid and citric acid. SICM-SCM is used to probe differences in the mode of action of the two acids and contrasted with a mineral acid. Following on from this SICM-SCM is utilised to measure remineralisation of an acid damaged surface. Methods of quantifying subtle surface repair are niche and limited and SICM is explored as a platform to provide such analysis. Finally, the surface charge changes associated with applying salivary pellicle to dental enamel are explored.

The aim is to present SICM as an exemplary choice for investigating subtle changes in the surface chemistry of dental substrates and use its unique strengths to decisively quantify previously unobserved phenomena.

4.1.1 Charged Domains in Dental Enamel

Charged domains have been documented in enamel structures before.[1–3] Focusing on the formation of enamel, the surface charge of the crystals in the developmental stage

is thought to be important in the interaction of the mineral with enamelin and other proteins responsible for orchestrating HAP formation in the body.[4] This work focuses on mature enamel and aims to position SICM as a premier technique for resolving surface charge heterogeneities on dental substrates.

There are well documented differences in the structure and mineral content of enamel.[5–7] The variation is small, an estimated 5% increase in the organic component and an increase in metal substitutions at the calcium sites, most notably, magnesium.[8–11] The work presented herein is, to our knowledge, the first full visualisation and quantification of the surface charge heterogeneities imparted by these structural differences.

4.1.2 Remineralisation in the Oral Cavity

The oral cavity has its own remineralisation cycle. Enamel can naturally repair under the right conditions. This is a gradual remineralisation process that occurs more readily at neutral pH as solvated calcium and phosphate ions repopulate the surface enamel. Human saliva can provide the calcium and phosphate rich environment and this process is well documented, as is the ability to replicate it *in vitro* with calcium and phosphate containing solutions.[12–14] Many toothpaste and dental care products aim to accelerate this process by flooding the mouth with excess calcium and phosphate ions and stabilising the pH in the remineralisation region. As repair is a subtle surface effect it is difficult to directly assess and quantify the extent of with current methods. Approximations with AFM based on the roughness of the enamel and surface micro-hardness testing are the only available options and neither can easily quantify low level (early stage) acid erosion. In this chapter the potential for using SICM-SCM to quantify remineralisation is explored.

4.1.3 SICM Surface Charge Mapping

The sensitivity of SICM to surface charge has been discussed in depth in the introduction (1.3.3-6) of this thesis and published elswhere.[15–18] In previous work by the Unwin group at Warwick it has been documented that as an SICM probe approaches a substrate surface, the physiochemical properties of that surface can convolute, or modify, the measured ion current.[16,19] Through careful experimental design using different feedback types[20,21] and scan hopping regimes,[22,23] SICM can be

extended beyond topographical mapping to probe the physical and chemical properties of a surface.[17,18,24] This has allowed SICM to be used to monitor interfacial electrochemical reactions[25] and for the quantification of the surface charge of cellular membranes and polymeric microstructures.[15]

Several different approaches to charge mapping have been utilised with SICM and these have been documented in detail in previous publications from the Unwin group.[15,24] The most recent protocol, which is used herein, utilises the DC to both sense the surface and elucidate surface charge information. A DC signal is used to sense the surface as this allows faster probe approach rates to be employed by removing the inherent time constraints imposed by the lock-in amplifier, which limited previous SCM regimes.[20] In this work the approach bias was kept small (-50 mV) as it has been established in previous studies (as described in section 1.3.5) that the sensitivity to surface charge scales with the magnitude of the applied SICM bias between the two QRCEs.[19] Thus, this allows faithful topographical mapping to be achieved. In order to elucidate the surface charge of a sample, a short (100 ms) pulse to 500 mV is performed (and the corresponding *i-t* curve measured) both with the probe near the surface and in bulk solution.[17] The *i-t* curves are normalized by dividing the surface value for the current at the extreme of the curve by the corresponding bulk value to give a single value displayed as a pixel on the normalized current map (Figure 4.1).

Typically under moderate – high electrolyte conditions (> 10 mM) the diffuse double layer at a charged interface is compressed to the order of a few nanometres or less.[26] At low approach biases, the surface topography can usually be faithfully reproduced independent of surface charge, as the probe does not approach to within the double layer dimensions. Under these conditions the SICM response is thus insensitive to surface charge.[24,27]

During the potential pulse, the SICM response becomes sensitive to the surface charge of the probed substrate. This becomes possible even at large probe-substrate separation distances as the double layer in the region directly under the nanopipette becomes perturbed by the electric field at the end of the nanopipette, causing it to extend beyond the usual Debye length. The surface charge of the substrate and of the nanopipette walls also induce an EOF, which must be properly considered, as this contributes to the sensitivity of SICM to surface charge, influencing the ionic current response.[24]As

such, EOF is incorporated into the FEM simulations (section 4.3) in order to quantify the enamel surface charge shown in numerous figures in the results section (4.2).

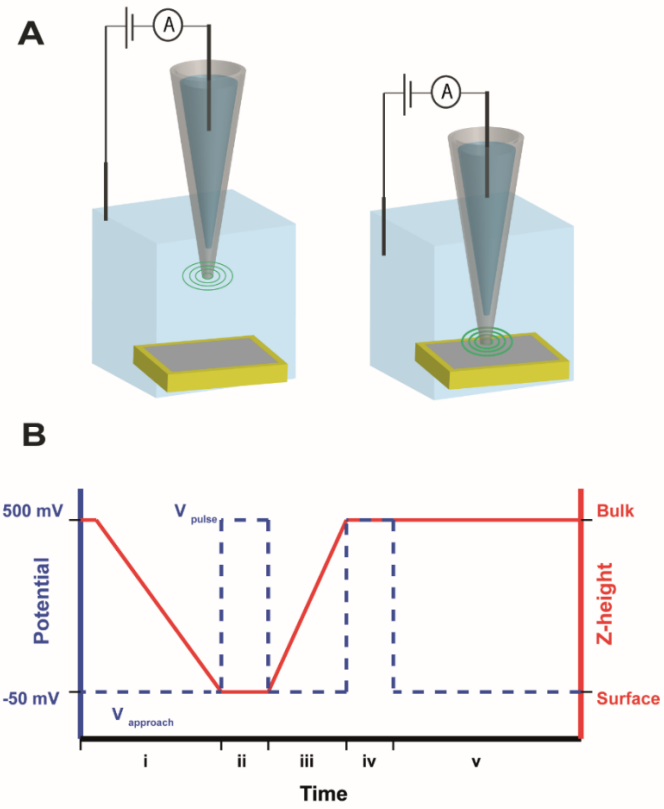

Figure 4.1 SICM Schematic and Approach-Potential Chart

A SICM schematic depicting pulses in bulk (LHS) and at the enamel surface (RHS).

B Potential change during a hop.

Figure 4.1**B** details the changing potential of the nanopipette relative to its approach height. Each section of the *y* axis is explained: **(i)** The nanopipette probe is moved toward the surface at 2 μm/s with the QRCE in the probe biased at -50 mV *vs.* the QRCE in bulk solution ($V_{approach}$). When the ionic current between the two electrodes has reduced by a chosen threshold value, nominally 2%, the approach is halted before **(ii)** a 100 ms pulse of the probe potential to 500 mV, (V_{pulse}). After this pulse **(iii)**, the probe potential is returned to -50 mV and the probe retracted into the bulk solution. The retract distance is large enough that the following pulse is characteristic of the bulk solution (5 times the dimensions of the nanopipette opening away from the surface). **(iv)** A second 100 ms pulse in the bulk solution; **(v)** the probe is then

translated laterally to the next pixel. The $i-t$ curve at the surface and the $i-t$ curve in bulk are analyzed to extract the normalized current at each pixel.

4.2 Results and Discussion

Presented here are the results of SICM-SCM experiments conducted over an 18-month period of PhD research. Much of the initial experimental time was spent establishing the parameters to perform SCM experiments successfully. Many combinations of conditions were tried before settling on a standard of 50 mM KCl electrolyte at pH 7 with a 150 nm borosilicate nanopipette. Lower electrolyte concentration typically results in lower bulk currents meaning a lower peak to noise ratio that made false approaches and tip crashing more likely. A higher electrolyte concentration thins the double layer and makes the resulting surface charge images harder to interpret as the normalised currents observed were much lower.

Due to the unforgiving nature of the extremely hard enamel surface, any minor contact between the probe and surface resulted in nanopipette breakage, this is less of an issue with softer biological samples such as cells, but was initially a stumbling block for the ceramic dental substrates. As SICM is supposed to be a non-contact technique this was attributed to the probe speed being too high and causing an overshooting during an approach which led to breakages or vibration issues. A marked improvement was seen in the images when vibration isolation was upgraded with a pressurised air-cushioned anti-vibration table, this points to vibration being a key contributor to tip breakages.

These are points to note for anyone looking to repeat this work or apply SICM mapping to any other ceramic or metallic substrate. An approach speed of 3 μms^{-1} was used for the majority of the images collected as this offered a compromise between the length of an individual scan and the risk of tip crash by overshooting. With the anti-vibration table speeds of 10 μms^{-1} are achievable but on an unforgiving surface slower approach rates are advised.

4.2.1 Inter Rod Enamel Charge Mapping

All the SICM images shown in this section utilised the same scanning conditions. Given in detail in section 2.5, a 150 nm probe with 50 mM KCl was used. The

approach speed was of 3 μms^{-1} was throughout with a retract distance from the surface of 2 µm. Each SICM image on average took approximately 1 hour to complete.

Figure 4.2 shows an AFM image (**A**) and a SICM-SCM scan (**B & C**) of a section of polished bovine enamel. Image **D** is an FEM calculated approximation of the actual surface charge based on the measured normalized current.

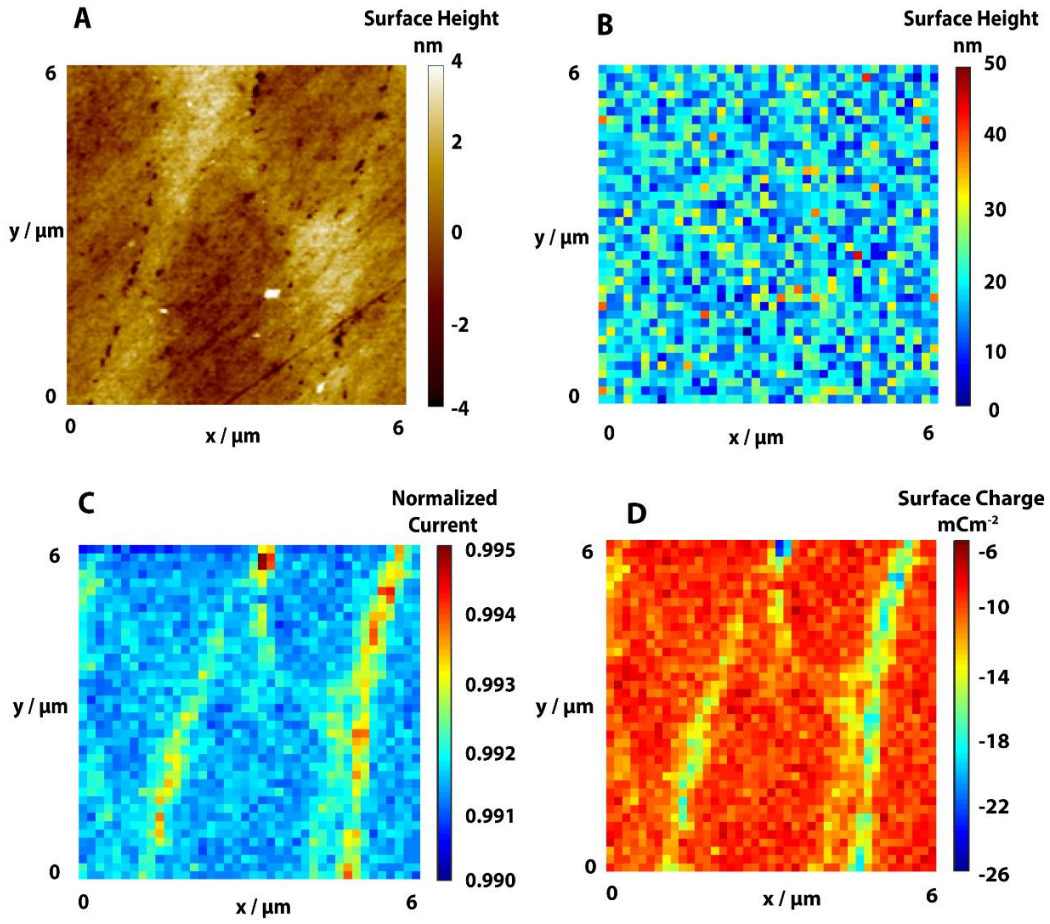

Figure 4.2 Inter-Rod Enamel Surface Charge Map 1

A. AFM image of inter-rod enamel (note image is a well-matched representation and not the exact area subsequently analysed with SICM). **B.** SICM topography collected concurrently with normalized current. Note the flat topography as relief seen with AFM is not visualised with SICM as the ~5 nm features are too small to be detected. **C.** Normalized current map revealing charge differential over inter-rod regions. **D.** FEM surface charge calculated from normalized current. SICM conditions: 220 nm borosilicate pipette. 50 mM KCl pH 7. 50 mV approach bias, 424 pA current. 150 nm hop. 6 μm^2 area.

It is clear from the images that the normalized current map (**C**) is revealing features in the surface charge that are not prominent in the SICM topography (**B**). They match the size and pattern of the microstructure revealed by AFM. The FEM calculations reveal a change in charge over the inter-rod regions of around 15 mCm^{-2}. The

background charge of the central enamel regions appears to be slightly negative which corresponds to reports in literature.[1,28] A repeat experiment was carried out on another polished enamel sample and the charged features are also visible (Figure 4.3). Again, a clear surface charge heterogeneity can be seen which corresponds to the lattice of inter-rod enamel seen in the AFM.[1] As the topography in this case is subtle, to the degree were it is not clearly visible in the SICM topography map, the local ion environment and not topographic convolution is responsible for the enhanced surface charge measurements across the inter-rod regions. This has been reported in the literature before and is due to the increase in residual proteins and a different crystal structure of the HAP in the inter-rod enamel. These subtle stages give a stark contrast in the normalised current images indicating that these features have a different local ion environment compared to the central rod enamel.

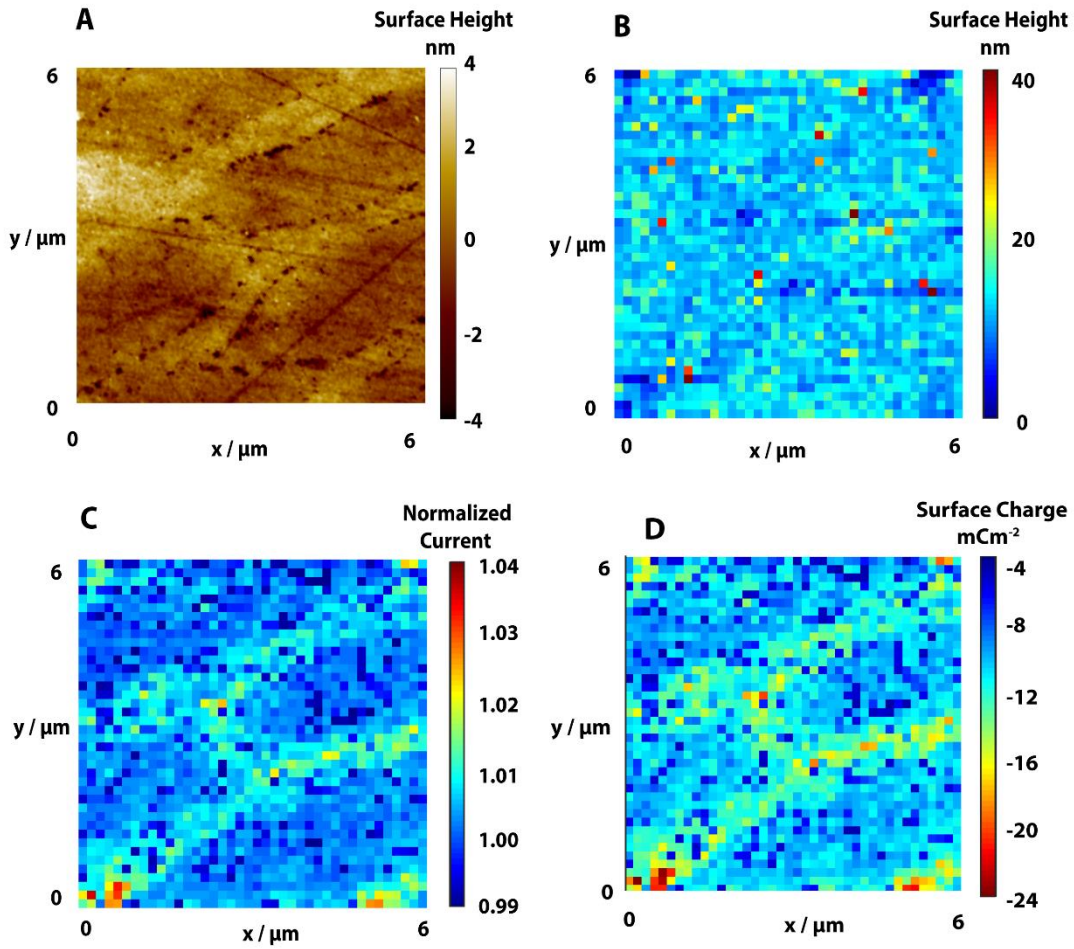

Figure 4.3 Inter-Rod Enamel Surface Charge Map 2

A. AFM image of inter-rod enamel (note image is a well-matched representation and not the exact area subsequently analysed with SICM). **B.** SICM topography collected concurrently with normalized current. In this topography image a faint outline of the relief can be seen but as before the topography is largely featureless**.** **C.** Normalized current map revealing charge differential over inter-rod regions. **D.** FEM surface charge calculated from normalized current. 160 nm borosilicate pipette. 50 mM KCl pH 7. 50 mV approach bias, 403 pA current. 150 nm hop. 6 μm^2 area.

Given the success of these initial measurements the experiment was repeated on dentine.

4.2.2 Dentine charge mapping

Figure 4.4 shows the AFM and SICM-SCM images for dentine. Unlike enamel, it was not predicted that charge heterogeneities would be seen. However, in Figure 4.4 **C** it can be seen that there is a change in normalized current around the opening of the tubules.

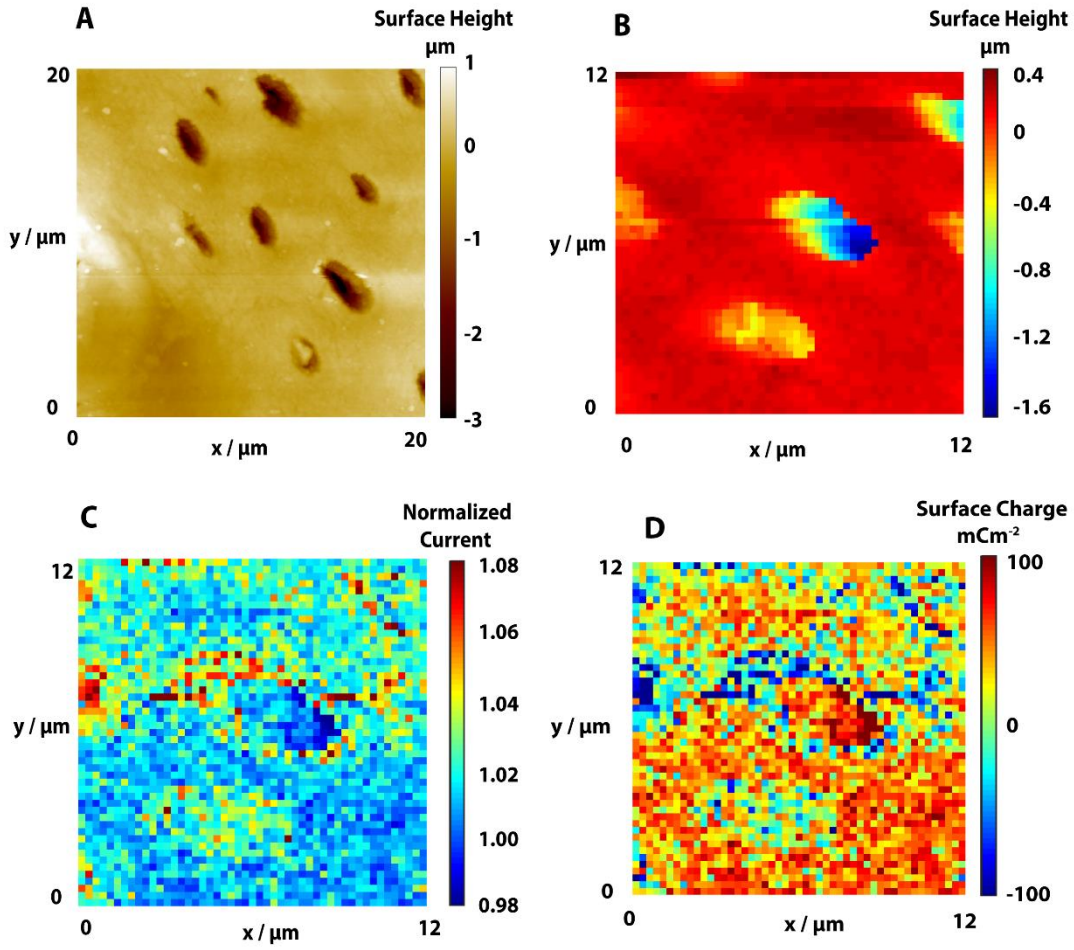

Figure 4.4 Dentine AFM and Surface Charge Mapping

A. AFM image of dentine. **B.** SICM topography collected concurrently with normalized current. In this topography image the dentine tubules can be clearly seen**. C.** Normalized current map revealing charged regions around the opening of tubules. **D.** FEM surface charge calculated from normalized current. 150 nm borosilicate pipette. 50 mM KCl pH 7. 50 mV approach bias, 380 pA current. 300 nm hop. 12 μm^2 area.

This was unexpected but may reflect on the function of dentine tubules. Tubules are fluid filled and act as a transport system within the tooth structure. This means there may be a biological incentive for the tubules to draw ions towards themselves and the charged differential would play a role in that. Biologically, attracting positive ions into and out of tubules is beneficial for the tooth and aides in mineral flow throughout the tooth structure. The FEM modelled image (**D**) is calculated, in this case, from an example nanopipette, meaning the geometry is an approximation as the original was unavailable in this case. This has led to inflation in the reported values of the surface charge with the model giving a very large range of values. Despite this the information it does provide is useful and comparisons of regions of charge within the image are insightful. Although the magnitude is likely inflated the general polarity of the charge and the assertion that the area around the tubules is more negative is a valid observation.

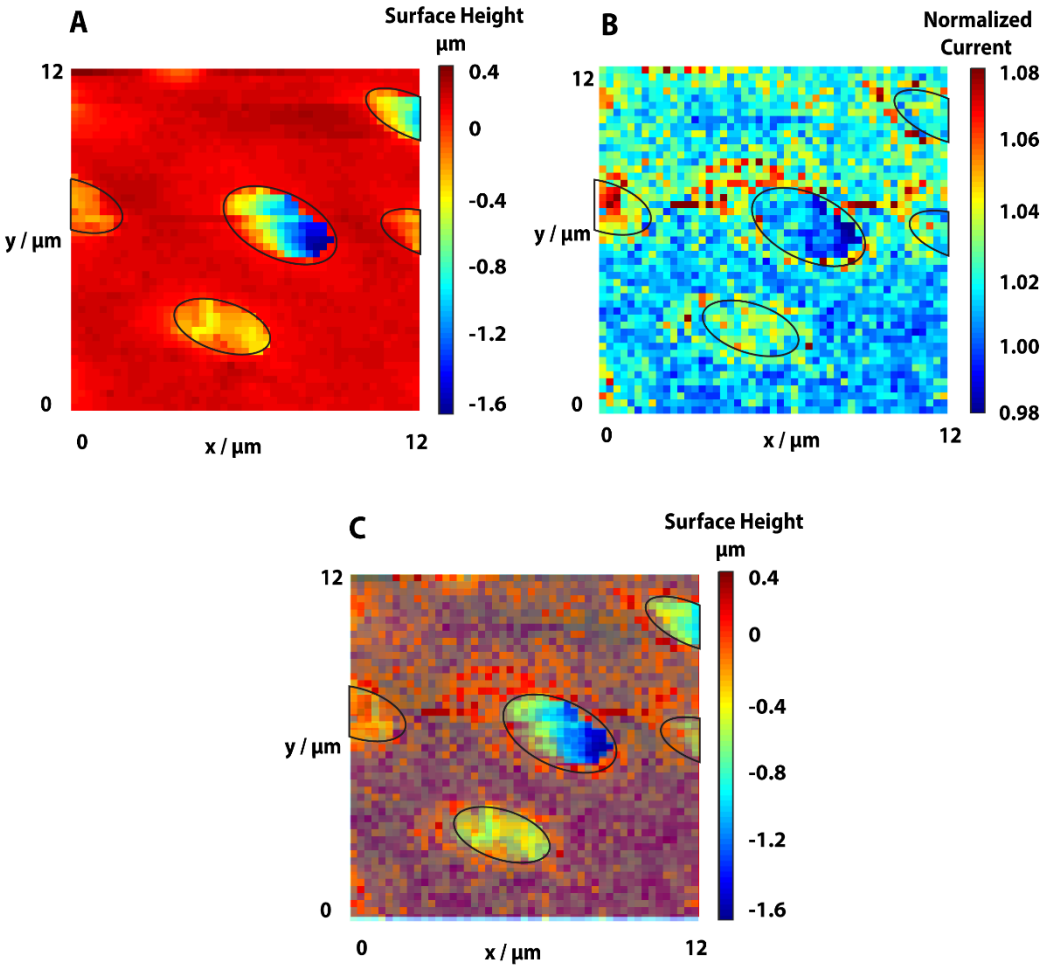

Figure 4.5 SICM Normalized Current Overlaid on Topography

The ellipses aid the eye in seeing the halo effect of the measured charge. **A.** Shows the topography with black ellipses highlighting the edges of tubules. **B.** The same ellipses are overlaid on the normalized current map. **C.** The entire normalized current map is over-laid (at 50% opacity) on the topography map, complete with ellipses.

Figure 4.5 is a schematic that shows conclusively that the normalized current discrepancy forms a halo around the edge of the tubule and is not related to the change in topography caused by the tubule itself. This is good evidence that the observed effect is not an imaging artefact and the change in the normalized current is reflective of an underlying property or structural irregularity in the dentine surrounding the tubule openings, likely due to its function in transporting fluid within the tooth.

4.2.3 Dietary Acid Erosion

SICM-SCM was successfully used to visualise surface charge of enamel and dentine microstructure. Following on from this an attempt was made to use the calculated surface charge to monitor low level erosive damage. It was hoped that any subtle dissolution would correlate with a change in the measured charge at the enamel surface and the magnitude and polarity of the charge may reveal some information about the surface chemistry or dissolution mechanism. Citric acid was studied due to its role as a prominent dietary acid.

4.2.3.1 Citric Acid

To investigate the effect of surface treatments, an experimental protocol of pre and post treatment SCM was implemented. The flexibility of the SICM setup allows for the nanopipette to be retracted to a safe distance (~1 cm) allowing the electrolyte to be removed and treatment solutions to be applied to the surface. The solution can then be removed, and the sample washed and dried. If no lateral movements are made with the piezo the nanopipette can then be re-approached to the same area (approximately, some drift will occur) of the surface. To simulate a low-level erosive challenge, a 1% citric acid solution is used. This weak solution will cause minimal erosion, but it is hypothesized that it may have an effect on the enamel surface charge by depleting the surface of calcium and hydroxyl groups.

Figure 4.6 shows the results from this procedure. **A** and **B** show the pre citric acid topography and FEM calculated surface charge and **C** and **D** show the post citric acid. In this case the topography map does faintly detect the inter-rod regions and again these are clearly visible in the surface charge. The magnitude of the surface charge pre-treatment is higher than in previous experiment, the scale bar has been set to show the clear contrast between the before and after scans (comparing **B** to **D**). The over-all background charge detected is lower (-20 mCm^2) but this is reflective of enamel being negative and inter sample variability would account for changes in the magnitude of the background charge. Comparatively, the inter-rod regions are roughly 20 mCm^2 more negative, showing a similar trend to the previous samples.

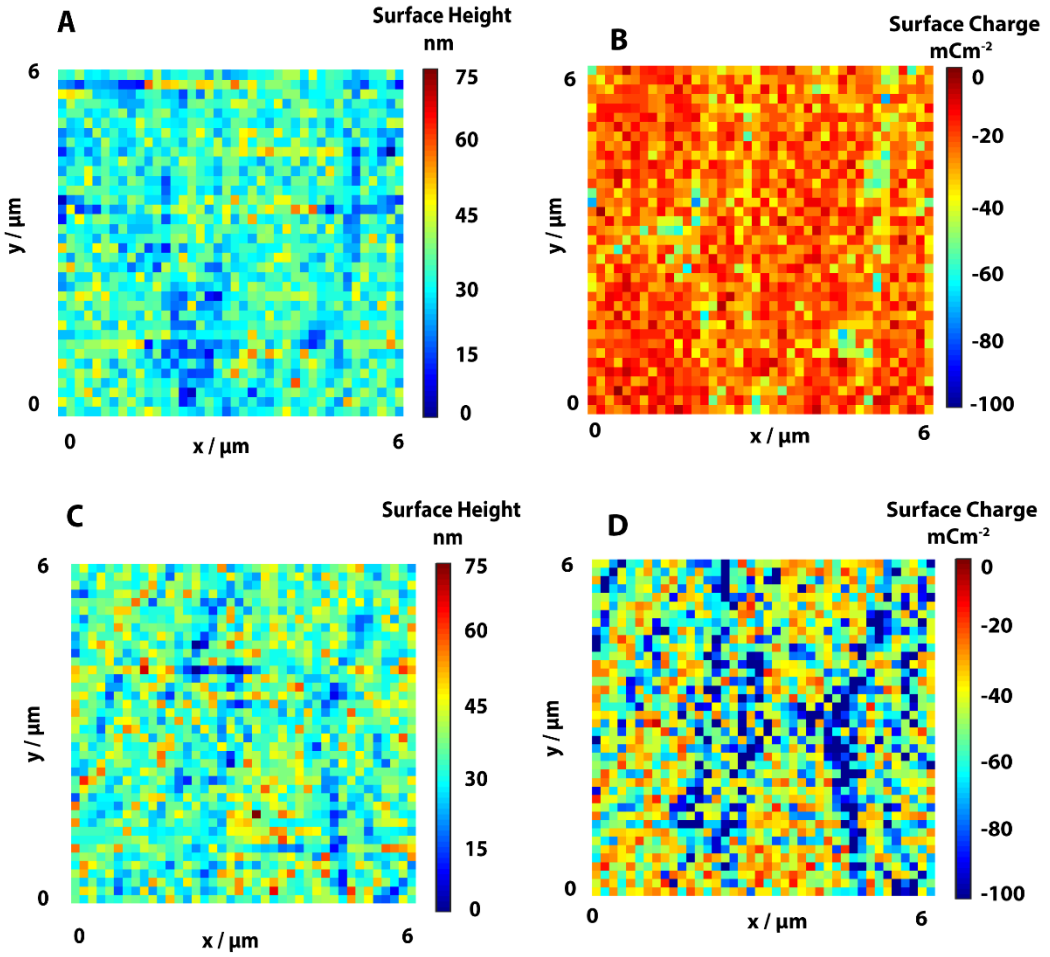

Figure 4.6 Pre and Post Citric Acid Erosion SICM-SCMs

SICM topography (**A**) and FEM simulated surface charge (**B**) before citric acid treatment. SICM topography (**C**) and FEM simulated surface charge (**D**) after citric acid treatment. Topography and FEM calculated surface charge before and after a 30 second citric acid treatment at a pH and concentration similar to orange juice. 160 nm borosilicate pipette. 50 mM KCl pH 7. 50 mV approach bias, 290 pA current. 150 nm hop. 6 µm^2 area.

After citric acid exposure there is a large change in the calculated surface charge, particularly along the inter-rod regions. The background charge has decreased by ~20 mCm^2 and the inter-rod regions changed by a drastic 60 mCm^2 to the negative (**D**). The topography in image **C**, it should be noted, is largely unchanged in terms of surface roughness, the acid treatment is too mild to induce large changes in topographic relief through dissolution. The shift to the negative has been attributed to

the removal of calcium, preferentially at the inter-rod regions as these experienced the largest change and this seemed a logical way that the surface could become more negative. Combined with the chelation effect that citric acid is known for this seemed a reasonable conclusion. To test this a second dietary acid was tested, one which does not chelate calcium, to compare with these findings.

4.2.3.2 Phosphoric Acid

A 30 second treatment with 0.05 M phosphoric acid at pH 3.6 was investigated in the same manner as the citric acid. Before and after treatment SICM-SCM measurements were made and the resulting surface charges calculated by FEM. Figure 4.7 shows the results. As with the citric acid the FEM modelled charge is shown. This is calculated from the normalized current (Figure 4.17).

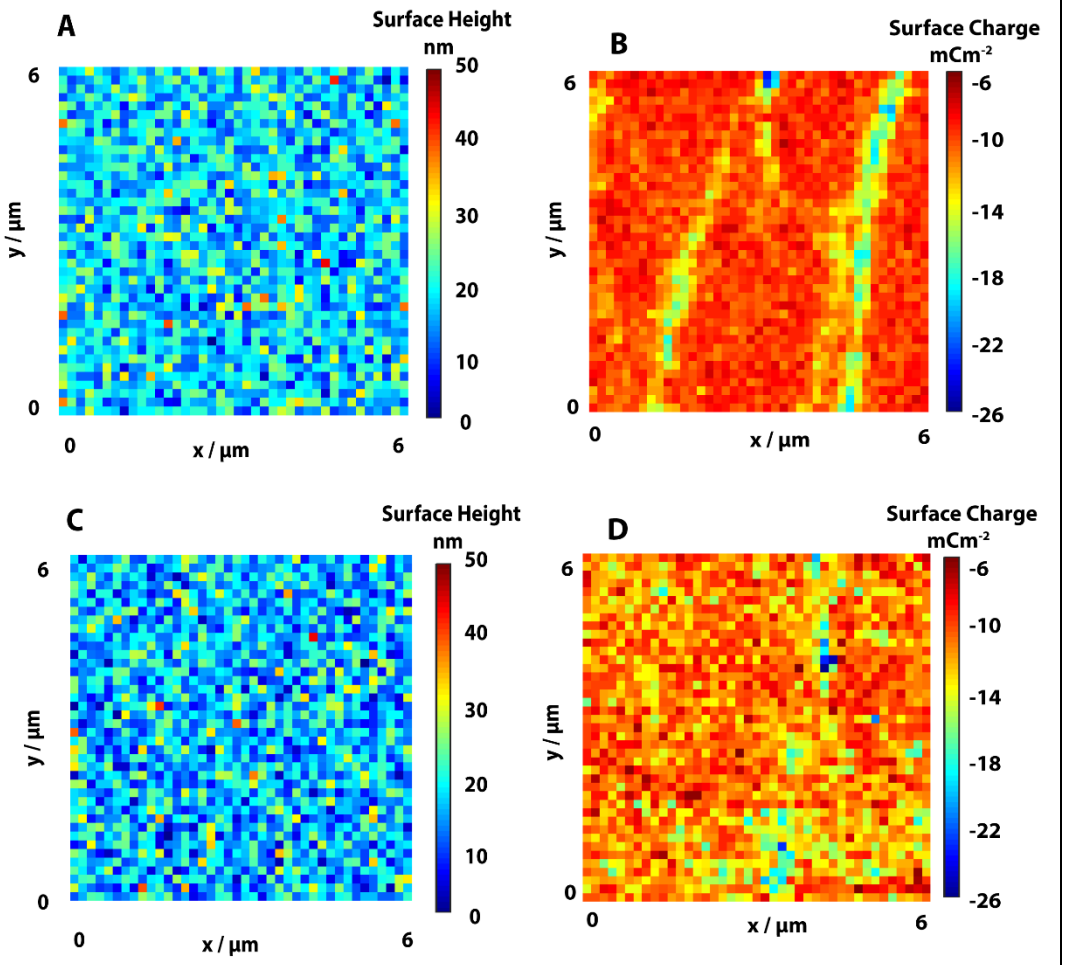

Figure 4.7 Pre and Post Phosphoric Acid Erosion SICM-SCMs

SICM topography (**A**) and FEM simulated surface charge (**B**) before phosphoric acid treatment. SICM topography (**C**) and FEM simulated surface charge (**D**) after phosphoric acid treatment. SICM conditions. A solution of equivalent molarity to the citric acid solution was employed. 220 nm borosilicate pipette. 50 mM KCl pH 7. 50 mV approach bias, 424 pA current. 150 nm hop. 6 μm^2 area.

In this instance there is no major change in the background surface charge and no drastic change in the magnitude of the surface charge over the inter-rod regions (comparing **B** to **D**). The inter-rod regions are not as pronounced in the surface charge after the phosphoric acid treatment but the overall charge on the surface is similar to the before image. The lack of a major change to the surface charge when phosphoric acid is used may point to an inherent difference to the mechanism of acid erosion between the two acids studied. Citric acid is a well-known metal chelator. [29,30] It is

proposed that the enhancement seen in the surface charge in Figure 4.6 is due to increased removal of calcium by this erosion pathway, not possible in phosphoric acid erosion.

To investigate the data further and attempt to quantify the charge discrepancies a selection of points from the FEM modelled data were considered. Pixels along the boundary regions and pixels from the central rod regions were compared. 30 pixels from each region were compared to obtain an average charge value for the inter-rod region and central region for both phosphoric acid and citric acid treated enamel. The findings are displayed in Table 12.

Table 12 Mean Charge Values for Regions of Enamel Surface by Treatment

	Pre Phosphoric Acid	**Post Phosphoric Acid**	**Pre Citric Acid**	**Post Citric Acid**
Mean Surface Charge Central Regions (S.D) (mCm^{-2}) *	-9.60 (0.90)	-10.03 (1.30)	-20.20 (5.42)	-39.88 (15.44)
Mean Surface Charge Boundary Regions (S.D) (mCm^{-2}) *	**-15.23** (1.68)	**-16.03** (3.12)	**-37.63** (13.65)	**-89.79** (16.28)

These averages confirm the scale of the heterogeneities within the images. Namely, that the phosphoric acid has had little to no effect on the surface charge and that the citric acid has had a profound one, particularly over the inter-rod regions and show an increase in the variability of the surface charge post treatment in both cases. (This is seen in the increased standard deviations.) To demonstrate the mechanistic differences that may lead to the discrepancy between the two dietary acids, Figure 4.8 shows their chemical structures and details the metal complexing pathway available to the citrate ligand.

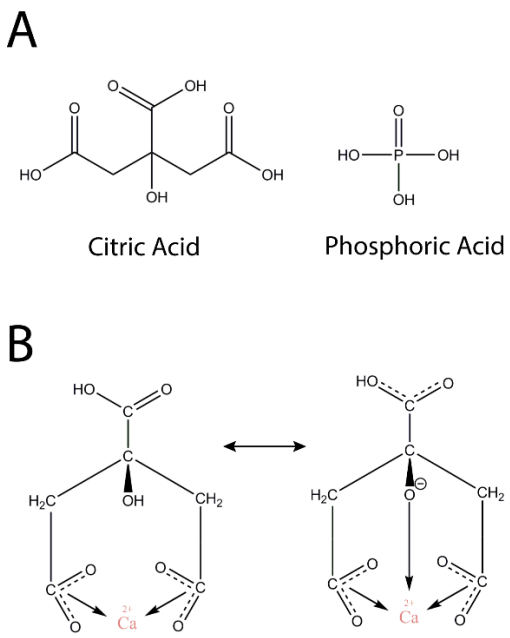

Figure 4.8 Dietary Acid Structures and Citric Acid Chelation Mechanism

The chemical structures for Citric Acid and Phosphoric Acid (**A**) and a schematic depicting a citrate ion chelating a calcium ion (**B**). Initially the citrate is depicted with two of the COOH groups having lost the hydrogen and are negatively charged and thus forming coordinate bonds to the calcium ion. In more basic conditions (RHS) the complex is further stabilized by the formation of another coordinate bond with the polar alcohol group on the C2 carbon.

Citric acid inducing a negative shift in the observed surface charge was seen in every experiment and is documented twice more in section 4.2.5 as part of a remineralisation experiment. To further understand the phenomenon an experiment to compare these results with a mineral acid was undertaken. HCl is the acidic component of stomach acid so does have relevance to dental erosion. A stronger concentration was used (0.05 M, pH 1.3) to reflect biological conditions and monitor the charge change a more drastic dissolution may impart.

4.2.4 HCl Erosion

This experiment follows the same pattern as the previous, with a ‘before’ and ‘after’ treatment SICM-SCM to attempt to analyse and quantify the disruption of the surface charge caused by mineral acid exposure. Due to the increased erosion potential of this

experiment a clear topographical change is also observed. Figure 4.9 details the results, showing the topography before and after and the normalized currents. Figure 4.10 gives a comparison of the calculated FEM surface charges, set to the same scales which clearly demonstrates the large change in the surface charge.

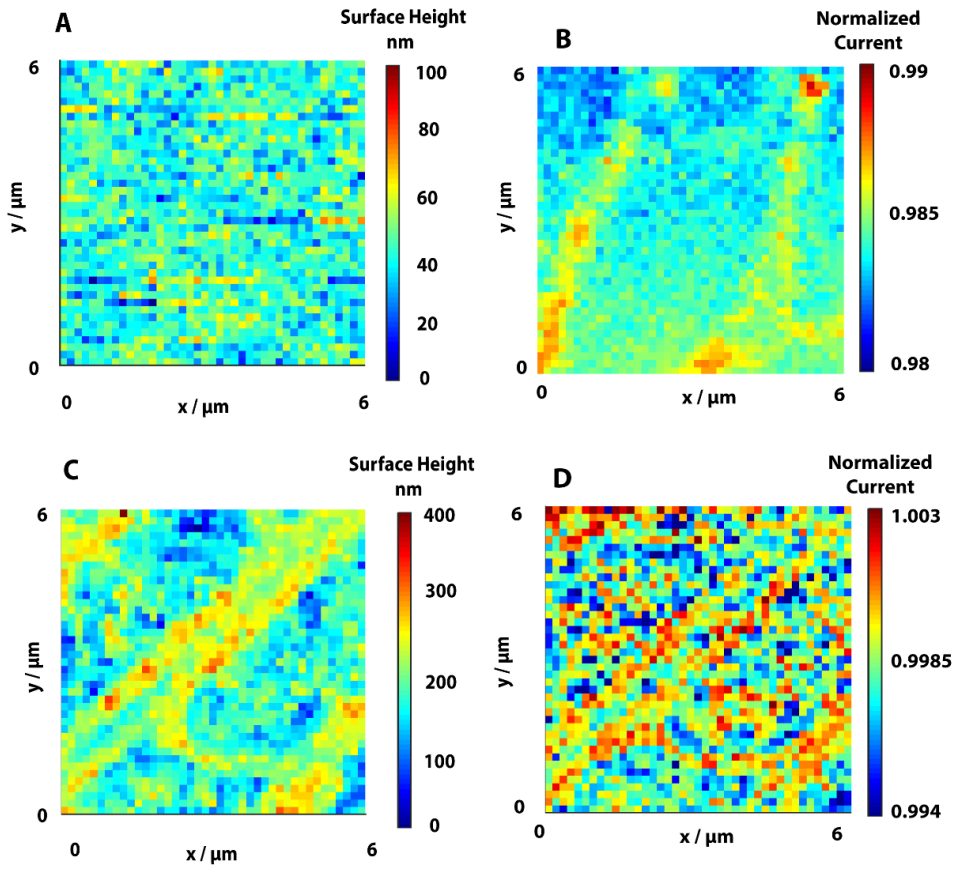

Figure 4.9 Pre and Post HCl Erosion SICM-SCMs

SICM topography (**A**) and normalized current (**B**) before HCl erosion. SICM topography (**C**) and normalized current (**D**) after HCl erosion. Note the large topography change. Again, the inter-rod regions are pronounced and appear to be a focal point for change in the observed charge.

The visible etching of the surface demonstrates the increased resistance to acid erosion of the inter-rod regions as they stand out from the central regions which are more prone to erosion. This also shows how comparatively mild the previous acid treatments have been, not altering the topography to any detectable degree. HCl is a much more

aggressive acid, causing more damage due to its lower pH. Figure 4.10 shows that the surface charge has shifted largely to the negative after HCl exposure.

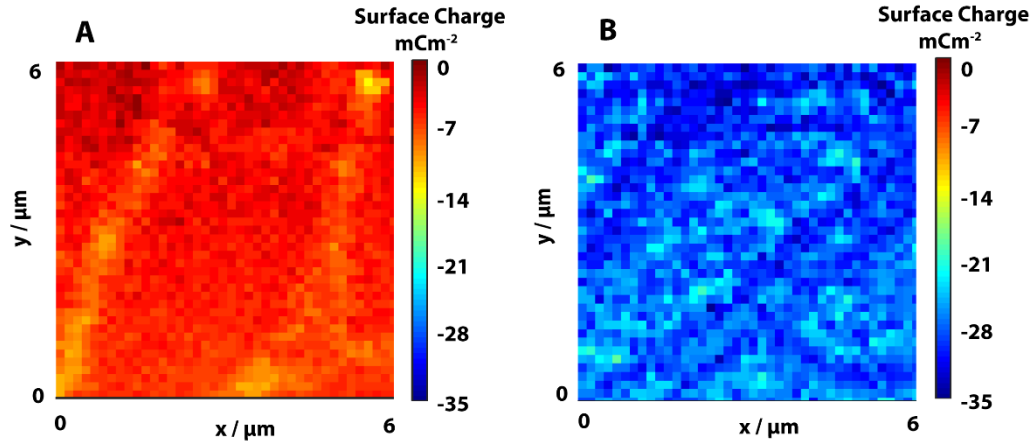

Figure 4.10 FEM Calculated Surface Charge Pre and Post HCl Exposure

The FEM modelled surface charge pre (**A**) and post (**B**) a 30 second hydrochloric acid exposure (0.05 M, pH 1.3). The change in surface charge is evident between the two images

The shift to the negative with HCl exposure is interesting. It again points to positive ions being removed from the surface. Again, there is an increased negative charge at the inter-rod regions. As this is a stronger mineral acid more obvious erosion has occurred and from the topography it can be seen that the central regions have been eroded further than the inter-rod enamel, leaving a raised lattice of inter-rod enamel that is visibly more charged. Whilst the overall surface charge is shifted to the negative, the exposed inter-rod regions remain the most negative due to their protein content and more disorganise crystal structure.

At pH 3.6 (for the dietary acids) the dissolution occurs preferentially at exposed sites (the inter-rod regions) and minimal erosion is seen without the chelation mechanism present. It is likely

The next study focuses on assessing remineralisation by following a similar method to the previous experiments with an added final step of exposing the enamel to a remineralisation solution containing calcium and phosphate. Citric acid was chosen as

the erosive challenge as at the concentrations measured a consistent surface charge change was observed without deforming the surface topography.

4.2.5 Remineralisation Assessment

The experiment follows the same procedure as that in 4.2.3.1 with the addition of a 30 minute exposure to a calcium and phosphate remineralisation solution (formulation given in 2.1) after the citric acid challenge. The topography was not included with the surface charge images as no major structural changes of note were observed. Figure 4.11 details the results. As with the previous data, the citric acid makes the surface more negative. The remineralisation solution then goes someway to returning the surface to its baseline surface charge. The exposure to the remineralisation solution may be repairing the surface, filling some of the calcium vacancies caused by the citric acid exposure. It should be noted that only a partial repair is seen. Remineralisation studies in an industrial setting often take place over days, with multiple over-night exposures to simulated saliva and other remineralisation solutions. To see improvement after one half an hour treatment shows the potential of the technique to visualise small chemical changes on the enamel surface.

The central enamel rod regions show more of a change towards baseline than the inter-rod regions. It may be that these regions can more preferentially absorb calcium from the remineralisation solution due to their increased HAP content compared to inter-rod enamel and less inhibition from the organic matrix present in the inter-rod region which has been shown to slow remineralisation.[31] Another factor could be the crystal orientation favouring remineralisation in the central rod regions, this would be dependent on the crystal faces exposed but the more uniform alignment may facilitate calcium reabsorption.

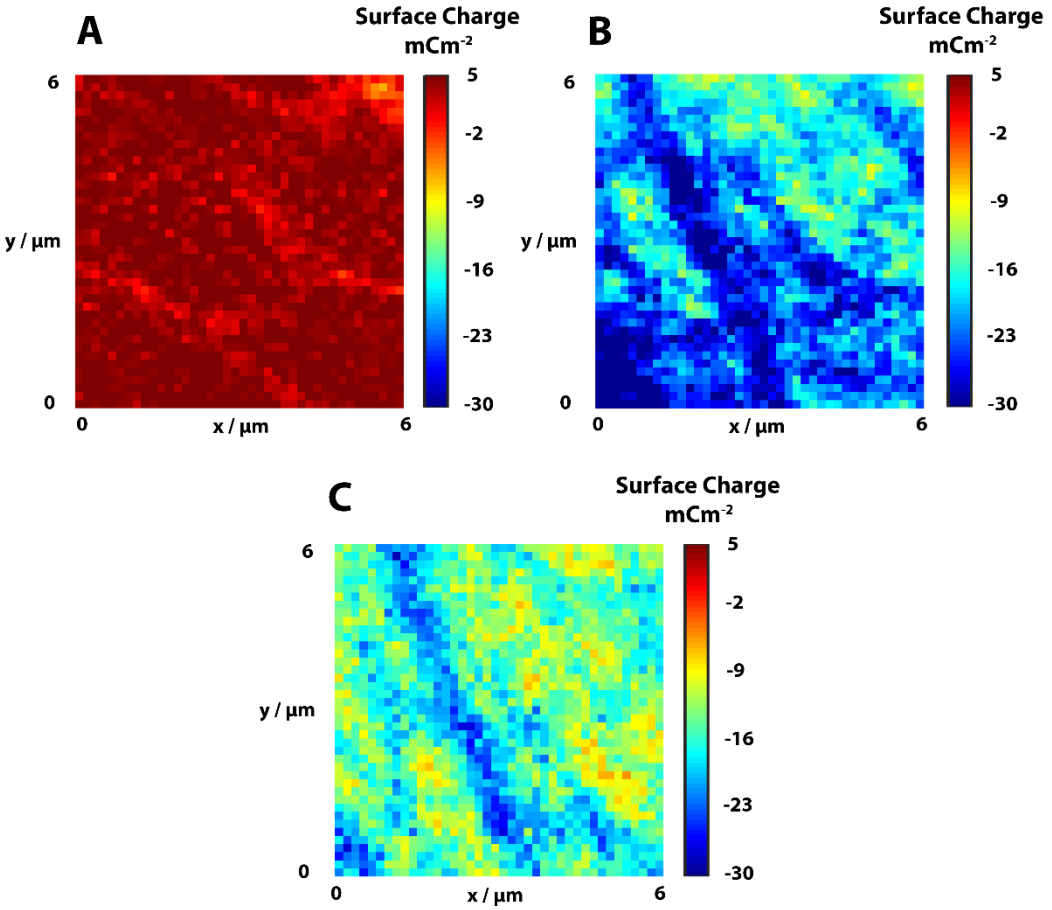

Figure 4.11 Baseline, Eroded and Remineralised Enamel SICM-SCMs

FEM calculated surface charge for bovine enamel before treatment (**A**), after a 30 second citric acid exposure (**B**) and after 30-minute remineralisation at 37ºC (**C**). The surface is made more negative after citric acid exposure (as before) and begins to return to baseline after remineralisation. A complete recovery of the surface is not achieved.

The experiment was repeated in Figure 4.12 to confirm the result. The inter-rod regions were not visible in this particular set of images (bar the first) however, the same trend presents itself and the background charge values follow a similar pattern to that observed in Figure 4.11.

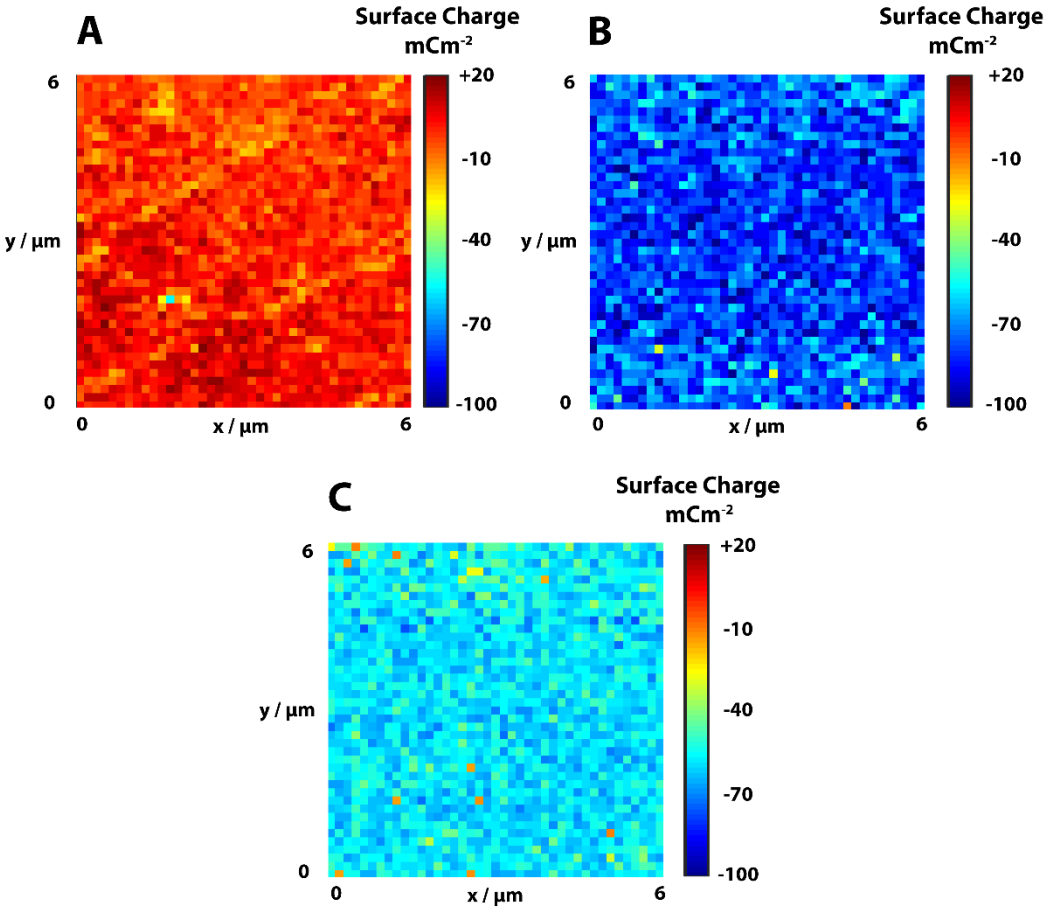

Figure 4.12 Baseline, Eroded and Remineralised Enamel SICM-SCMs Repeat

FEM calculated surface charge for bovine enamel before treatment (**A**), after a 30 second citric acid exposure (**B**) and after 30-minute remineralisation at 37ºC (**C**). The surface is made more negative after citric acid exposure (as before) and begins to return to baseline after remineralisation. A complete recovery of the surface is not achieved.

The change in surface charge values follows the same pattern as before and the calculated charges are larger. This shows that the remineralisation can be assessed but sample variability may make quantification difficult. Assessments on a sample by sample basis are valid but inter-sample variability is difficult to account for without a much larger study to incorporate this factor.

4.2.6 Pellicle Layer

A before and after experiment was undertaken with salivary pellicle. To form a pellicle, the enamel block was immersed in clarified whole saliva for 30 minutes at 37ºC. This is enough time for pellicle proteins to adhere. The sample was washed thoroughly before SICM-SCM analysis.

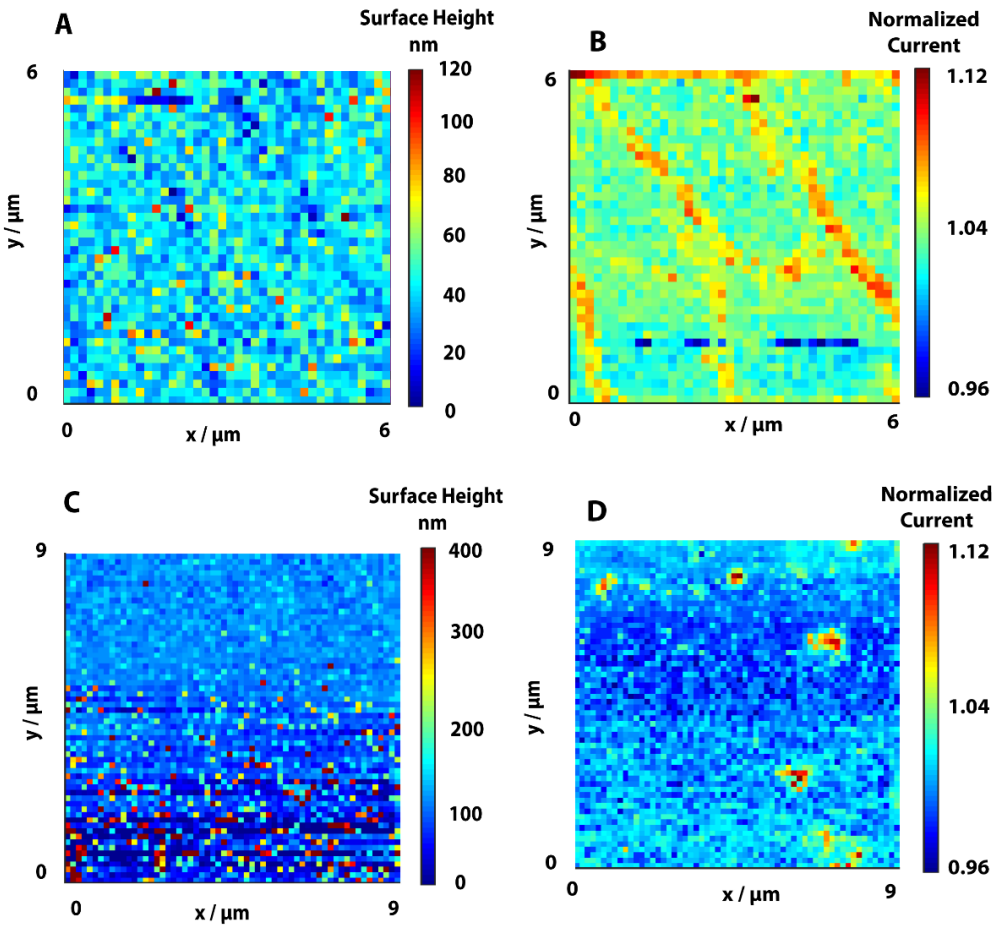

Figure 4.13 Topography and Normalized Current Pre and Post Salivary Pellicle

SICM topography (**A**) and normalized current (**B**) before salivary pellicle application. SICM topography (**C**) and normalized current (**D**) after salivary pellicle. The pellicle layer seems to make false approaches to the surface more common as is seen in **C** (more individual red pixels). This is likely due to the probe acquiring protein residue over the duration of the scan. The inter-rod enamel regions are not visible after being coated by the pellicle with small circular points of charge being the prominent feature (**D**).

In Figure 4.13 the topography and normalized current before and after pellicle adherence can be seen. Due to the presence of the layer multiple false approaches are seen. The inter-rod regions are no longer visible and blanket charge covers the surface with points of high normalized current. A surface charge FEM model was not calculated for this scan. However, the large change in normalized current is indicative of a blanket positive charge from the pellicle layer with points of high negative charge.

From the size of the particulates (~1 µm) present in **D** it is proposed that these discrete areas of high normalized current are deceased bacteria present in the pellicle layer or bundles of protein residues. It is possible that they are small indents in the surface revealing the inter-rod regions below but there is no sign of a pit or depression in the surface in these areas in the topography map. It is likely that they are charged objects submerged in the pellicle layer and that the pellicle observed is thicker than the 100 nm or so predicted in the literature.[32,33]

This data was included to show the ability of SICM to monitor surface changes and leads into the next chapter were SICM is used to image live bacterial samples for the first time. No dental bacteria are imaged but this work sets out the groundwork for analysing bacteria that can thrive in a multitude of systems and could easily be expanded to oral bacteria in future work.

In the next section the details of the FEM model covered which were used to approximate the surface charge at multiple points during section 4.2 from the observed normalized current.

4.3 FEM Simulation Details

The FEM simulations used followed a set protocol. Here for complete understanding a step by step method detailing a conversion of an experimental normalized current SICM image to a surface charge map. All the other conversions in the preceding section follow a similar process but are not detailed in full. Relevant conversions and raw data are included in the appendix section 7.2.

First, the geometry was built from STEM images of the nanopipette used, when this was not possible a placeholder geometry for that pulling parameter, based on previous studies, was used. After the geometry was built the equations to be solved, concentration of ions, voltages applied, and electrostatic considerations such as the

charge on the nanopipette wall were inputted into the model. A current potential plot (CPP) is then simulated in bulk. If the values obtained are similar to the experimental CPP taken with that nanopipette the next step of the simulation was undertaken. If the CPP is different from the experimental, the applied charge to the glass and small changes to the geometry (within the considerations of the STEM images) are made until a reasonable CPP is produced. Figure 4.14 shows an example experimental CPP compared to a modelled CPP which was used to model the phosphoric acid experiment in section 4.2.3.2.

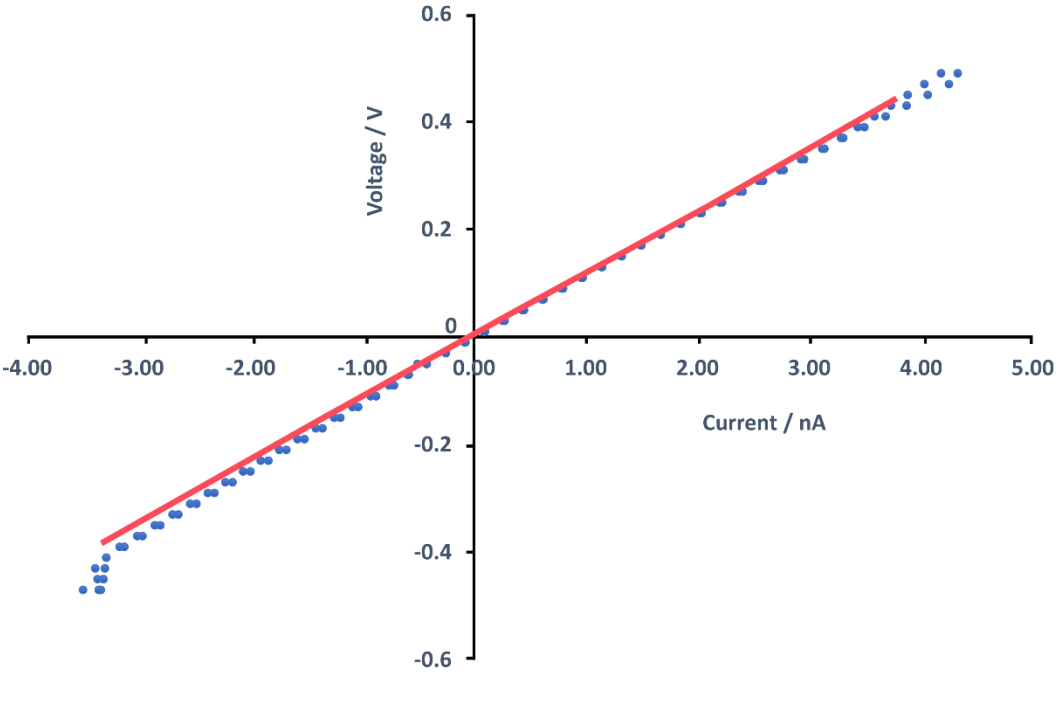

Figure 4.14 Experimental and FEM Simulated CPP

Experimental CPP (red) for the phosphoric acid experiment compared to its modelled counterpart (blue). A simulated CPP is used to confirm the modelled nanopipette is passing similar currents to the experimentally obtained CPP before the approach and surface charges are modelled. This is simulated in bulk solution, 2 µm from the surface. While not identical the fit is close enough for the purposes of the model.

Once a comparable CPP is simulated next is an approach curve. The currents the probe passes are simulated at different distances from the surface. The current measurements are taken at increment heights approaching surface. The current drops during an

approach. At the point the current drops by the experimental threshold, nominally 2% for the experiments herein, this point is known as the approach distance d. It is then assumed that at each pixel in the map the probe approached to distance d from the surface, usually between 25 and 60 nm.

Once the approach distance is calculated, different surface charges are simulated at the surface, in the area directly under the nanopipette pore. The current is measured at the pulse potential for each surface charge, with the nanopipette at distance d and in bulk. At the small distance d, the charge on the surface affects the magnitude of the current at the pulse potential. A range from -100 mCm^2 to +100 mCm^2 is routinely simulated and expanded upon if necessary. From these values a normalised current can be calculated (surface current divided by bulk current) corresponding to a surface charge increment. From this a calibration curve is made, giving an approximation of the surface charge at each normalized current pixel in the map. The equation of the line given by this curve is used to replot the data with the simulated surface charge shown at each point.

A schematic of the FEM simulation domain (**A**) is shown in Figure 4.15 and the approach curves for the phosphoric acid (**B**) and the normalized current to surface charge conversion curve (**C**). To generate the final surface charge map, a conversion based on the equation of the line from calibration curve is applied.

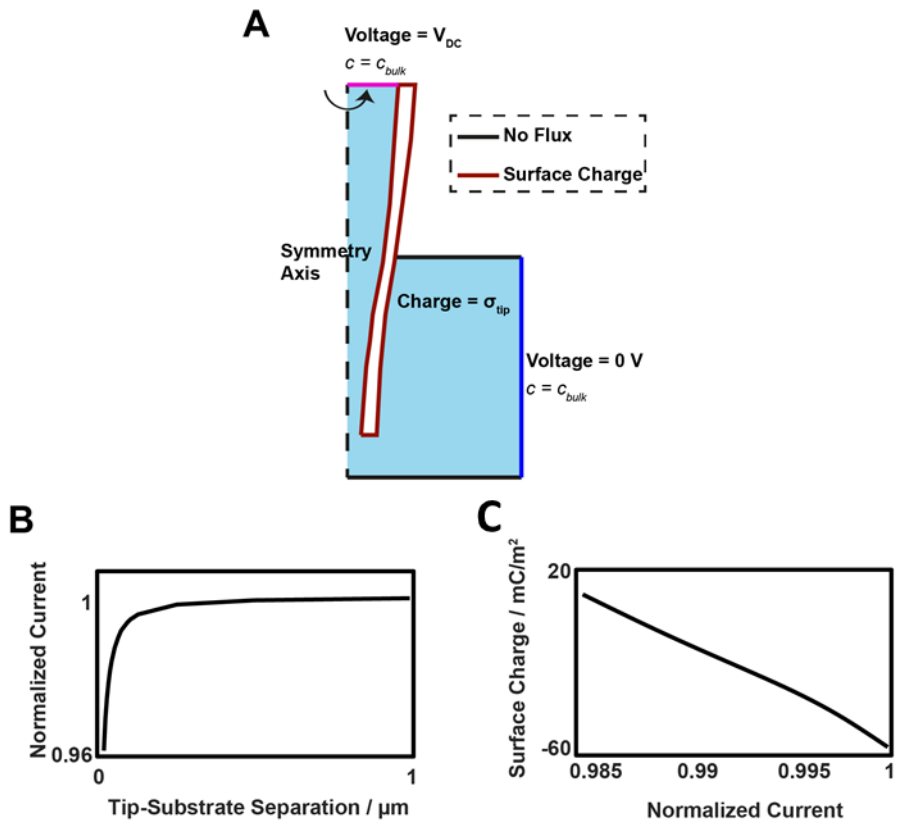

Figure 4.15 FEM Domain and Calculation Curves for Phosphoric Acid

Schematic of FEM simulation domain (**A)** together with simulated approach curve corresponding to the phosphoric acid (**B)**. Calibration curves used for converting normalized current data to surface charge values shown for phosphoric acid data (**C)** at a separation distance of 60 nm.

Typical dimensions of the nanopipettes used experimentally were extracted from scanning transmission electron microscopy (STEM) images shown in Figure 4.16 and used to construct the nanopipette simulation domain.

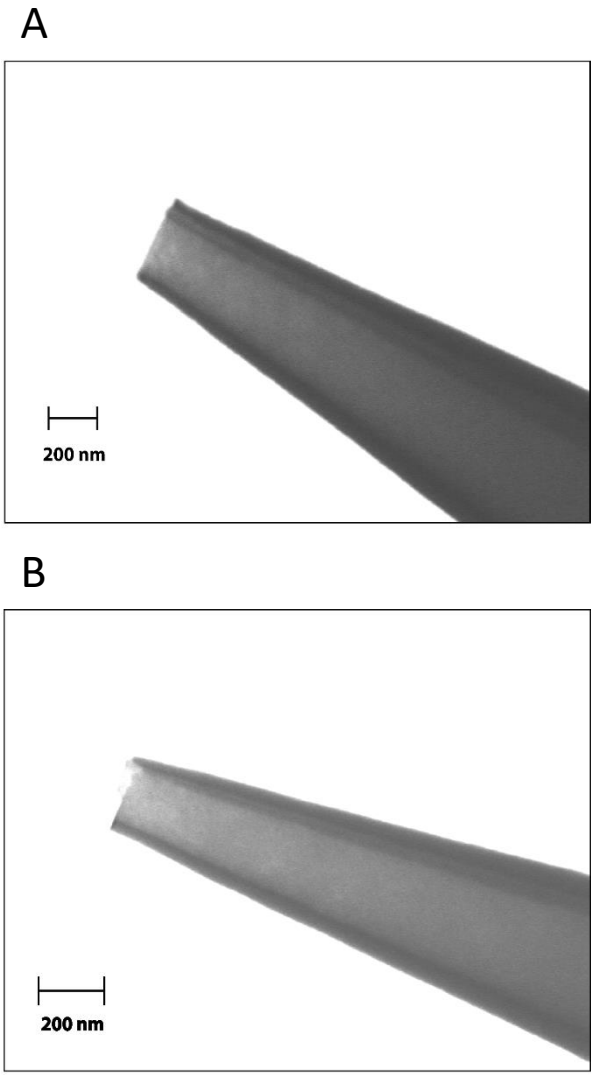

Figure 4.16 STEM Images of Nanopipettes used in Dietary Acid Experiments

Two examples of a series of Scanning Transmission Electron Microscopy (STEM) images of borosilicate glass nanopipettes pulled with an inner radius of 110 ± 20 nm (**A**) and 80 ± 15 nm (**B**). Images taken with a Zeiss Gemini 500 SEM operating in STEM mode and utilised to provide tip geometries for the FEM models.

For all simulations, the bulk concentrations were set to be 50 mM KCl. The electrostatics, transport of diluted species and laminar flow modules were used to model the experimental system. In all simulations the Nernst-Planck equation for ion transport (eq. 1) was solved:

$$J_i = -D_i \nabla c_i - z_i \frac{F}{RT} D_i c_i \nabla \phi + c_i u$$

(1)

where D_i z_i and c_i are the diffusion coefficients, charge number and concentrations of species I and u are the solution velocity described below (eq. 3). Ion diffusion coefficients were taken from the CRC handbook[34] and the simulations accounted for the effect of locally varying ionic strength on these parameters. F, R and T are the Faraday constant, gas constant and absolute temperature. ϕ is the electric potential described by the Poisson equation (eq. 2):

$$\nabla^2 f = - \frac{F}{\varepsilon \varepsilon_0} \sum_i z_i c_i$$

(2)

where ε is the dielectric constant of the solution and ε_0 is the vacuum permittivity. The solution velocity was described by the incompressible Navier-Stokes equation with EOF incorporated (eq. 3):

$$u \nabla u = \frac{1}{\rho}(-\nabla p + \mu \nabla^2 u - F(\textstyle\sum_i z_i c_i)\nabla \phi)$$

(3)

where ρ is the solution density, μ is the solution viscosity and p is the pressure.

Steady-state simulations were first performed for the nanopipette geometry corresponding to those used in the phosphoric acid study to estimate the experimental working distance at which SCM experiments were performed with the approach curves shown in Figure 4.15**B**. Once the working distance corresponding to the experimental set up was known, time dependent simulations were performed jumping the nanopipette bias from the hold potential used experimentally (50 mV) to the surface charge sensing potential (-500 mV). Repeating this process with different surface charge densities present on the surface beneath the nanopipette domain and performing the same procedure with the nanopipette in bulk solution allowed for calibration curves of surface charge against normalized ionic current to be generated which are shown in Figure 4.15**C**. This was used to convert the experimental normalized current maps shown below in Figure 4.17

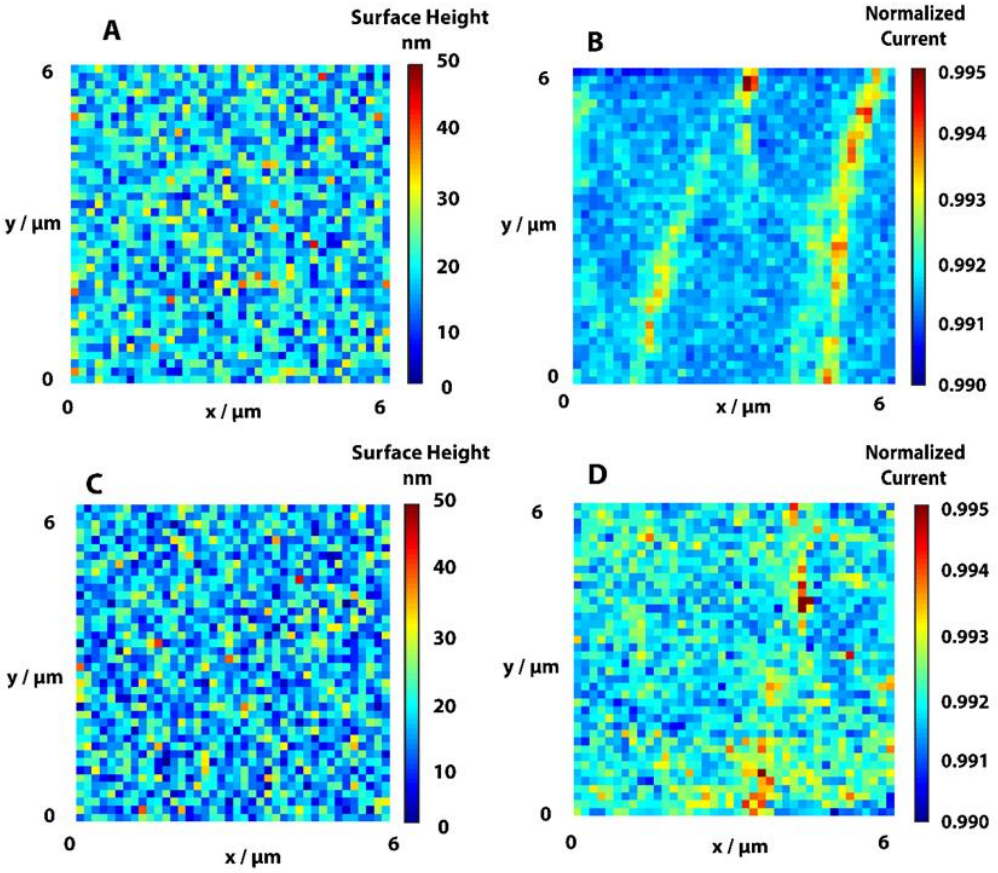

Figure 4.17 Experimental Normalized Current Maps for Phosphoric Acid Study

SICM topography (**A**) and normalized current (**B**) before phosphoric acid treatment. SICM topography (**C**) and normalized current (**D**) after phosphoric acid treatment. SICM conditions: 50 mM KCl, 220 nm borosilicate nanopipette, -50 mV approach bias, +500 mV pulse bias, displayed data calculated 100 ms after pulse applied.

This process results in an approximate measurement of the surface charge, shown in Figure 4.7. Whilst some variables such as the approach distance and the charge on the nanopipette glass can have a large impact on the resulting surface charge, overall this system gives a reasonable approximation of the charge and is useful for assessing the polarity and magnitude of the charged interface.

4.4 Conclusions and Future Work

This chapter has explored SICM charge mapping of dental hard tissues. The technique has been used to identify and quantify charged domains within the HAP lattice that correlate with the underlying microstructure. It shows the kind of insights the technique can give about biological interfaces. From these measurements some of the functionality of the surface can be inferred that is not obvious from the topography alone. Following this, experiments were designed to investigate how exposure to dietary acids affected the measured surface charge. Whilst a repeated and considerable change was seen when the sample was exposed to citric acid the difficulty of the measurements and the variation in the baseline charge measurements from sample to sample makes it hard to draw clear conclusions.

The surface charge modification seen with citric acid and not with phosphoric acid points to a mechanistic difference in the dissolution, most likely due to the calcium chelation by citrate ligands. The method shows some promise for assessing very subtle changes to the surface occurring in the first stages of dental erosion. Expanding the study to more acids and different concentrations and exposure times would further understanding in this area and is an obvious next step for these experiments. The difficulty in initially obtaining the data without breakages to the nanopipettes and making clear repeatable measurements hindered the study. Time constraints did not allow for the data gathered to be expanded upon with the studies involving remineralisation, pellicle layer and HCl exposure prioritised. If the study were to be repeated or expanded upon, data could be acquired more effectively with the lessons learned within this chapter, primarily the need for improved vibration isolation.

More AFM analysis of samples before and after acid exposure would also benefit the study as the topographic damage by the weak acids was often too subtle to detect via SICM. This could potentially support the promising data gathered during the remineralisation study in which the surface charge does indicate that some repair has taken place.

Overall utilising the surface charge in this way, as an indicator of subtle surface changes is promising but ultimately flawed due to the difficulty reproducing measurements and comparing different samples. The data was most reliable when a single sample was studied before and after a treatment with the same nanopipette. Due

to the high occurrence of breakages or damage to the nanopipette during or between scans this made the experiments particularly challenging. Scaling up the effort to multiple repeats would be time consuming and difficult and would need to involve and standardisation method to account for the different geometries of individual nanopipettes, an endeavour that was decidedly beyond the scope of this chapter. However, on a positive note, charged domains on the enamel and dentine surface where visualised for the first time with this technique and an FEM model was used to quantify the difference across the boundaries. SICM charge mapping also showed promise for investigating the mechanistic differences between dietary acids and further experiments may be able to expand upon which dental hard tissues are particularly at risk to which acids.

The analysis of the salivary pellicle on the enamel surface, although brief, led to a new avenue of study as the research expanded into looking at bacterial substrates which became chapter 5, the final results chapter of this thesis.

4.5 References

1 J. Kirkham, J. Zhang, S. J. Brookes, R. C. Shore, S. R. Wood, D. A. Smith, M. L. Wallwork, O. H. Ryu and C. Robinson, *J. Dent. Res.*, 2000, **79**, 1943–1947.

2 D. A. Smith, S. D. Connell, C. Robinson and J. Kirkham, *Anal. Chim. Acta*, 2003, **479**, 39–57.

3 C. Robinson, S. Connell, J. Kirkham, R. Shore and A. Smith, *J. Mater. Chem.*, 2004, **14**, 2242–2248.

4 A. G. Fincham, J. Moradian-Oldak and J. P. Simmer, *J. Struct. Biol.*, 1999, **126**, 270–299.

5 M. Shahmoradi, L. Bertassoni, H. M Elfallah and M. Swain, 2014, pp. 511–547.

6 S. Habeliz, S. J. Marshall, G. W. M. Jr, M. Balooch, S. Habelitz, S. J. Marshall, G. W. M. Jr and M. Balooch, *Arch. Oral Biol.*, 2001, **46**, 173–183.

7 C. Robinson, S. Connell, J. Kirkham, R. Shore and A. Smith, *J. Mater. Chem.*, 2004, **14**, 2242–2248.

8 M. C. Maas and E. R. Dumont, *Evol. Anthropol.*, 1999, **8**, 133–152.

9 S. F. Ang, M. Saadatmand, M. V. Swain, A. Klocke and G. A. Schneider, *J. Mater. Res.*, 2012, **27**, 448–456.

10 D. Deutsch and A. Alayoff, *Growth*, 1987, **51**, 342–354.

11 C. R. Hiller, C. Robinson and J. A. Weatherell, *Calcif. Tissue Res.*, 1975, **18**, 1–12.

12 M. Eisenburger, M. Addy, J. A. Hughes and R. P. Shellis, *Caries Res.*, 2001, **35**, 211–215.

13 X. Li, J. Wang, A. Joiner and J. Chang, *J. Dent.*, 2014, **42**, S12–S20.

14 Z. Dong, J. Chang, Y. Deng and A. Joiner, *Appl. Surf. Sci.*, 2010, **256**, 2388–2391.

15 A. Page, D. Perry, P. Young, D. Mitchell, B. G. Frenguelli and P. R. Unwin, *Anal. Chem.*, 2016, **88**, 10854–10859.

16 K. McKelvey, S. L. Kinnear, D. Perry, D. Momotenko and P. R. Unwin, *J. Am. Chem. Soc.*, 2014, **136**, 13735–13744.

17 D. Perry, R. Al Botros, D. Momotenko, S. L. Kinnear and P. R. Unwin, *ACS Nano*, 2015, **9**, 7266–7276.

18 D. Perry, B. Paulose Nadappuram, D. Momotenko, P. D. Voyias, A. Page, G. Tripathi, B. G. Frenguelli and P. R. Unwin, *J. Am. Chem. Soc.*, 2016, **138**, 3152–3160.

19 D. Perry, R. Al Botros, D. Momotenko, S. L. Kinnear and P. R. Unwin, , DOI:10.1021/acsnano.5b02095.

20 K. McKelvey, D. Perry, J. C. Byers, A. W. Colburn and P. R. Unwin, *Anal. Chem.*, 2014, **86**, 3639–3646.

21 Y. Zhou, C. C. Chen and L. A. Baker, *Anal. Chem.*, 2012, **84**, 3003–3009.

22 P. Novak, C. Li, A. I. Shevchuk, R. Stepanyan, M. Caldwell, S. Hughes, T. G. Smart, J. Gorelik, V. P. Ostanin, M. J. Lab, G. W. J. Moss, G. I. Frolenkov, D. Klenerman and Y. E. Korchev, *Nat. Methods*, 2009, **6**, 279–281.

23 C.-C. Chen, Y. Zhou and L. A. Baker, *Annu. Rev. Anal. Chem.*, 2012, **5**, 207–228.

24 D. Perry, A. Page, B. Chen, B. G. Frenguelli and P. R. Unwin, *Anal. Chem.*, 2017, **89**, 12458–12465.

25 D. Momotenko, K. McKelvey, M. Kang, G. N. Meloni and P. R. Unwin, *Anal. Chem.*, 2016, **88**, 2838–2846.

26 M. A. Brown, A. Goel and Z. Abbas, *Angew. Chemie - Int. Ed.*, 2016, **55**, 3790–3794.

27 A. Bard and L. Faulkner, *Fundamentals and applications*, 2001.

28 A. H. Weerkamp1, H. M. Uyen and H. J. Busscher2, *J Dent Res*, 1988, **67**, 1483–1487.

29 Y. Yoshida, B. Van Meerbeek, Y. Nakayama, M. Yoshioka, J. Snauwaert, Y. Abe, P. Lambrechts, G. Vanherle and M. Okazaki, *J. Dent. Res.*, 2001, **80**, 1565–1569.

30 Z. J. Cheng, X. M. Wang, F. Z. Cui, J. Ge and J. X. Yan, *Biomed. Mater.*, , DOI:10.1088/1748-6041/4/1/015020.

31 D. Elkassas and A. Arafa, *J. Dent.*, 2014, **42**, 466–474.

32 Y. F. Zhang, D. Y. Li, J. X. Yu and H. T. He, *J. Dent.*, 2016, **55**, 99–104.

33 A. T. Hara and D. T. Zero, in *Monographs in Oral Science*, 2014, vol. 25, pp. 197–205.

34 W. M. Haynes, *CRC handbook of chemistry and physics*, CRC press, 2014.

5 SICM Bacterial Surface Charge Mapping

5.1 Introduction

This chapter details the implementation of SICM-SCM for analysing live bacterial substrates. The surface charge of gram-negative and gram-positive bacteria is compared by modelling (with FEM) the normalized currents obtained through SCM. The work aims to account for the discrepancies observed by establishing a more advanced FEM model to account for the complex structure of the bacterial cell envelope. The findings are supported by SEM and cryo TEM images and the origins of the charge discrepancies between bacterial types and intra-sample charge heterogeneities are discussed.

SICM is well established in its ability to perform nanoscale functional mapping of biological substrates providing an abundance of information about the surface topography,[1,2] interfacial properties,[3] and dynamic processes of living systems such as mammalian and plant cells.[4–10] In this chapter SICM is utilised for the analysis of live bacterial substrates, to our knowledge, for the first time. Developments in SICM scanning procedures and FEM simulation have allowed SICM to be employed as a quantitative tool for SCM,[11,12] reaction mapping,[6] and controlled delivery of analytes to samples.[13–15] Combined with the robust topographical feedback, this places SICM as one of the most powerful and versatile tools for probing living systems.

A major challenge over-come by this work is the preparation of live bacterial samples for analysis with SICM. Different methods of bacterial mounting (without fixing) are investigated and the merits of each option discussed. A specific protocol for analysis with agarose gel is detailed which traps live bacteria for the 60-minute time period required to complete an SICM scan. Other options including Poly-L-lysine monolayers (PLL) and Corning cell-tak are also demonstrated.

5.1.1 Techniques to Measure Bacterial Surface Charge

The pros and cons of using AFM, KPFM and EFM for analysing live substrates and assessing surface charge is discussed in detail in the introduction. There are some newly developed techniques capable of assessing surface charge on bacteria and living cells in physiological conditions. Krause et al have adopted a photo-electrochemical imaging system (PEIS) capable of measuring the surface charge of the underside of cells (and bacteria) adhered to indium tin oxide (ITO) coated glass substrates in physiological conditions.[16] The images are made by scanning a focused, modulated laser beam across the back of the ITO coated glass under an applied bias. The photocurrent is sensitive to the negative surface charge of the substrate, in this case the basal side of the cell of interest. Whilst the findings are interesting, the spatial resolution of the technique is lower than that of SICM, the study focusing on large osteosarcoma cells (cells ~40 μm across). Other than those previously mentioned in the introduction to this thesis, techniques with this capability are otherwise limited.

The general consensus is that the bacterial cell wall is negative.[17,18] Studies to confirm and quantify this often resort to protein titrations attempting to assess the number of anionic and cationic groups present in the cell wall structures.[18,19] This approach obviously does not maintain the viability of the cells in question. In this chapter the measurement of bacterial surface charge at viable living bacteria is reported for the first time using SICM. The work aims to show the advantages of SICM and the relative simplicity of obtaining surface charge information through structured FEM analysis.

5.1.2 Bacterial Substrate Overview

The basic biology of bacteria is covered in the introduction section 1.5.1. All the bacteria analysed are heterotrophs, requiring a food source to sustain them in their environment. Bacteria placed in conditions of very high or low salt concentration, extreme pH or temperature may experience osmotic stress so maintaining a stable environment for analysis is important. Bacteria that are stressed may respond in non-typical ways such as producing excess signalling proteins or expelling or consuming a larger number of ions than normal. Stressed for too long the bacteria will denature.

For comparative purposes SEM images of the bacteria strains analysed are provided in Figure 5.1. *E. coli* and *Bacillus subtilis* are shown. Note the larger size of the *E. coli* (**A**) compared to the *Bacillus* (**B**).

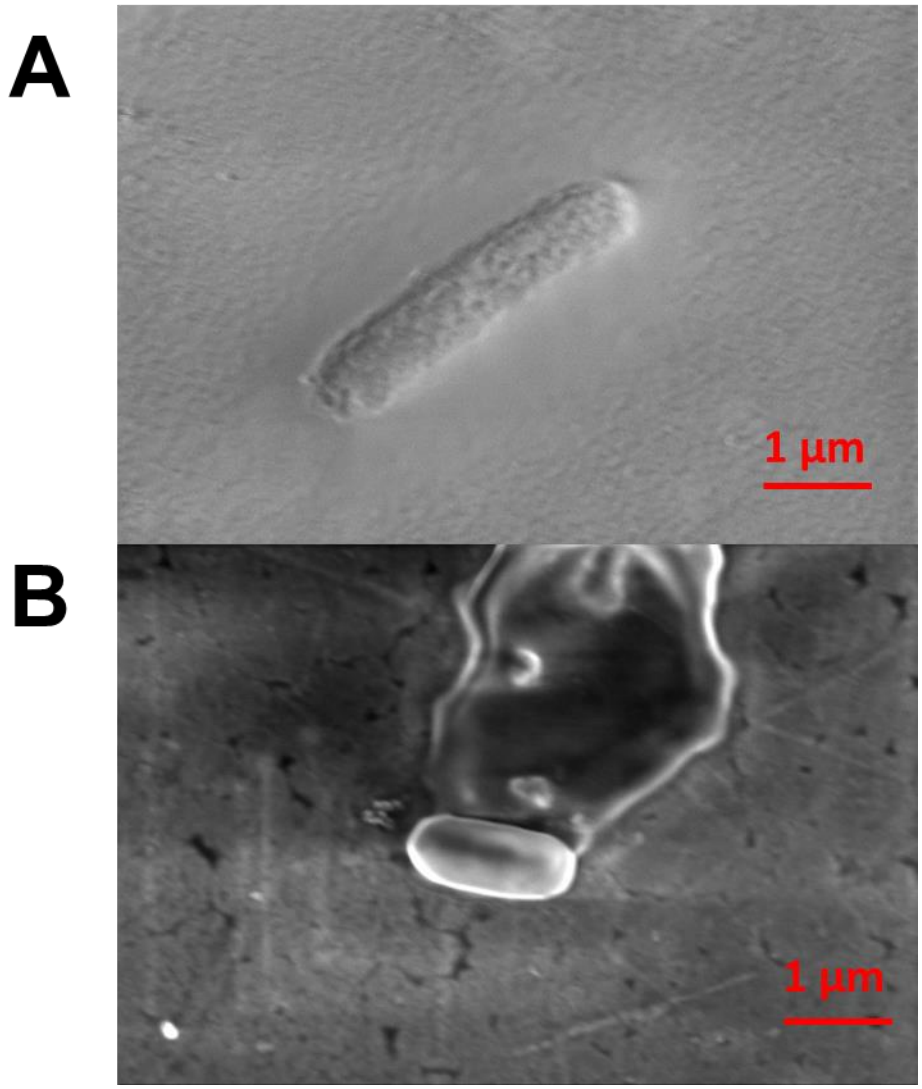

Figure 5.1 SEM Images of E-coli and Bacillus Subtilis

SEM image of *E. coli* cell (wild type) (**A**), EHT= 0.500 kV, Magnification x37950. SEM image of *Bacillus subtilis* (Δhag) cell (**B**), EHT= 2.00 kV, Magnification x37800. Both observed on carbon-laced copper TEM grids.

The structural differences of the gram-negative and gram-positive cell envelopes are shown in Figure 1.15. This is discussed in detail in the introduction section 1.5. In summary, the gram-positive cell wall is thicker due to the much larger peptidoglycan layer (250 Å compared to 30 Å). The lack of a lipopolysaccharide outer layer (and

other contributing factors) make the gram-positive cell wall permeable to the Gram stain and the increased peptidoglycan layer uptakes the dye leading to the famous colour change.

In the following experiment the surface charge contributions of both types of cell wall are considered and experiments to explain the contributions and build a more realistic model based on those observations.

5.2 Results and Discussion

5.2.1 Bacterial Adhesion

Before detailing the results of the study, it is worth while making some general comments regarding the efficacy of each adhesion method. Remembering that the goal is to restrict movement of the sample without denaturing it for a sufficient time to allow an SICM image to be taken. This requires a window of roughly 2 hours when the scan time, initial probe positioning, approach and any repeats are considered. This is nearly impossible with the bacteria active and mobile when suspended in KCl with no attempt to anchor them. They visibly move on the microscope screen, 10s of microns per second, meaning precise SICM imaging is impossible without securing them to the surface.

5.2.1.1 Agarose

The general method with agarose was successful, with adaptions being made throughout the preliminary work. A 0.8% agarose solution was settled on after initial experimentation, this percentage being pliable enough to pour when heated and coat the glass slide and providing enough resistance that the bacteria were often immobilized. The key to this was a dehydration step just before adding electrolyte and analysing the sample. The agarose (with bacteria added) was incubated at 37°C for 30 minutes immediately before analysis. This evaporated off any water layer on the surface and may have caused the agarose to dry slightly, often trapping specimens on the surface. Indentations in the mould can be seen in the SICM topography, this suggests the bacteria are slightly imbedded in the gel (the indents remaining when some bacteria free themselves.) With this modification it was possible to find live, immobile specimens with the microscope. The agarose appeared to be neutrally charged as a background substrate, as revealed by SICM-SCM. Repeated performance

with the agarose was tricky and relied on enough of the bacteria becoming imbedded and not freeing themselves.

5.2.1.2 Poly-L-Lysine

PLL utilises a different mechanism than the agarose for immobilizing the bacteria. PLL is positively charged and a layer on the glass sticks the negatively charged bacteria. PLL was semi-successful as an adhesive. Un-intuitively the more negatively charged bacteria *(Bacillus*) was less secure on PLL, it being more difficult to find immobilized specimens or specimens becoming unstuck during an experiment. Potentially due to its increased size, the *E. coli* adhered well. It remains a viable alternative to the agarose gel if submerging the substrate is a concern but is not be useful for investigating positively charged samples and the Cell-Tak performed better in our anecdotal experience.

5.2.1.3 Cell-Tak

Cell-Tak worked well for both species. The manufacturer does not specify the mechanism of adherence but from the SICM-SCM the surface was revealed to be more positively charged than the PLL. This points to a mechanism like that of the PLL, perhaps more effective due to an increased charge or a more physical adhesive. Again, its performance is likely to be reduced with positively charged samples.

5.2.2 E-coli Surface Charge Mapping

The images presented here summarize a year of imaging bacterial substrates. As with the dental charge mapping, perfecting the imaging and obtaining complete SICM images, with no tip breakages, of these substrates is non-trivial and involved adjusting parameters and conditions to optimize the images obtained. For the *E. coli* the two image sets show the sample topography, the normalized current and the FEM modelled surface charge. For these samples, the same model used in chapter 4 was employed. This approximates the area of the sample in the nanopipette footprint as a flat insulating surface. The values calculated are sensible and, as explained in the modelling section, are reasonable approximations for gram-negative bacteria as the insulating lipid membrane behaves similarly enough to samples in previous studies. How these deviates for gram-positive bacteria and the modifications made to the model are explained in depth in the subsequent sections.

The structure of the gram-negative cell envelope provides an interface which is primarily an insulating lipid membrane (Figure 1.15). Therefore SICM scans of *E. coli* were expected to behave in a similar way to previous reports of this technique when applied to mammalian cells and lipid bilayers.[28,29]

Figure 5.2 shows an SICM image of an *E. coli* cell on agarose. This is a particularly large individual. The rod like shape of the bacteria is not clear in the topography, potentially due to the partial submersion in agarose. The cylindrical shape is more evident in the normalized current, the body of the bacteria clearly being more charged than the agarose background. The FEM modelled surface charge reveals that the bacteria is extremely charged, approaching -100 mCm^{-2} in some areas. These values correspond to literature studies which shows *E. coli* have a strong negative zeta potential.[30]

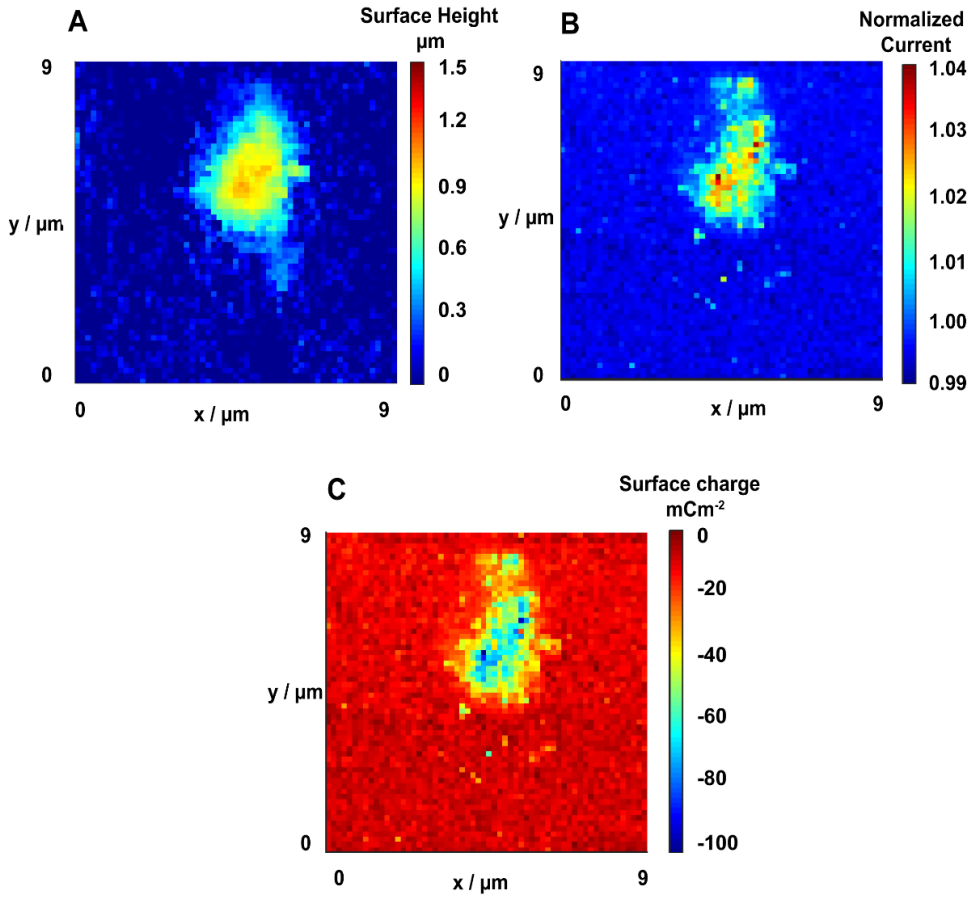

Figure 5.2 E. Coli on Agarose

E. coli on agarose. Topography (**A**), normalized current (**B**) and FEM modelled surface charge (**C**) are shown.

Conditions: 50 mM KCl pH 7. 150 nm borosilicate nanopipette with 150 nm hopping distance. 50 mV approach voltage producing 407 pA current using a 2% threshold. 0.5 V pulse voltage.

The surface charge values are high but fall within the range predicted by the FEM model. Due to the restraints placed on the model, such as the density of ions and the maximum charge on an ion it predicts charge density values below a magnitude of 150 mC m^{-2} with parameters having to be increased beyond normal physical limits to exceed this. There may be a functional aspect to the charge, with the bacteria needing to draw nutrients to itself. The agarose support appears to be fairly neutral, though it varied slightly through-out the experiments, mildly negative or mildly positive on

some occasions, potentially related to its components and production (layer thickness etc).

The normalized current measured matches the topographic relief well. Figure 5.3 shows a higher resolution *E. coli* on PLL. These images show the progress made in the scan quality and the removal of the need to immerse the sample in agarose due to the use of PLL makes the topography much sharper in the *E. coli* cases.

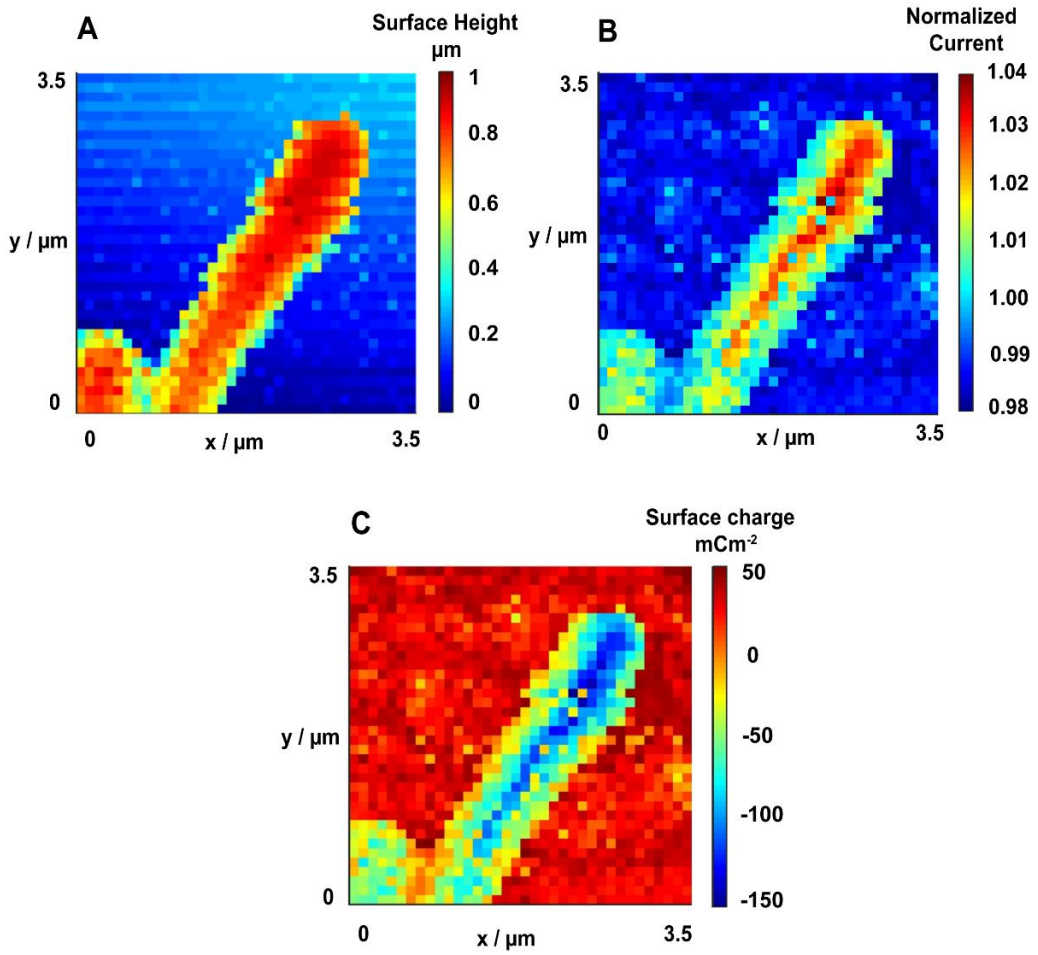

Figure 5.3 E. coli High Resolution on PLL

SICM topography (**A**), normalized current (**B**) and local charge (mC m^{-2}) FEM simulation following (**C**) of *E. coli* collected concurrently. SICM conditions: 50 mM tris buffered KCl at pH 7. 50 mV approach bias passing 440 pA current utilising a 2% feedback threshold. 150 nm nanopipette with 100 nm hopping distance.

The normalized currents obtained fall within the expected values from the model. The conversion curves for surface charge for both *E. coli* images are given in Figure 5.4. A dense region of surface charge is visible down the central axis of the bacteria. Modelling experiments detailed later in this section show that this charge discrepancy is not convoluted with topography and is a real phenomenon. Non-topographic heterogeneities could be derived from the structure of the *E. coli* bacterial cell envelope, the gross structure of which is comprised of an outer membrane, underneath which is the periplasmic space containing the peptidoglycan cell wall, followed by the inner membrane.[31]

E. coli outer membranes are primarily insulating phospholipid bilayers interspersed with lipopolysaccharides and proteins, forming a 3D structure with heterogeneous but generally negative charge density which could contribute to the observed experimental variation. Among these structures are the bacterial porins (Figure 1.15), these channels are up to 2 nm in diameter and allow non-specific transport across the membrane, between the external environment and the ion dense periplasmic space.[32,33] It is possible that ion transport through these channels could be induced by the biases applied within the experimental framework, however due to the small channel size, ion flow through these channels should be a relatively minor contribution to the currents observed. An exception to this would be if there is a large degree of spatial heterogeneity in the distribution of these channels causing highly porous areas which could significantly change the local ionic composition by ion transport from the periplasmic space.

E.coli have been reported to have heterogeneous expression of membrane proteins, resulting in recombinant proteins (such as ion channels) are often produced in aggregated form.[34,35] Depolarisation of this membrane is not considered to be likely due to the small voltages actually applied to the membrane; due to the high resistance at the pipette lumen (on the order of G Ω), the large majority of the voltage drop is in the first few microns within the pipette,[36] with ~30 mV applied between the end of the pipette and the surface (Figure 5.5) highlighting the advantages of the non-invasive nature of SICM methodologies.

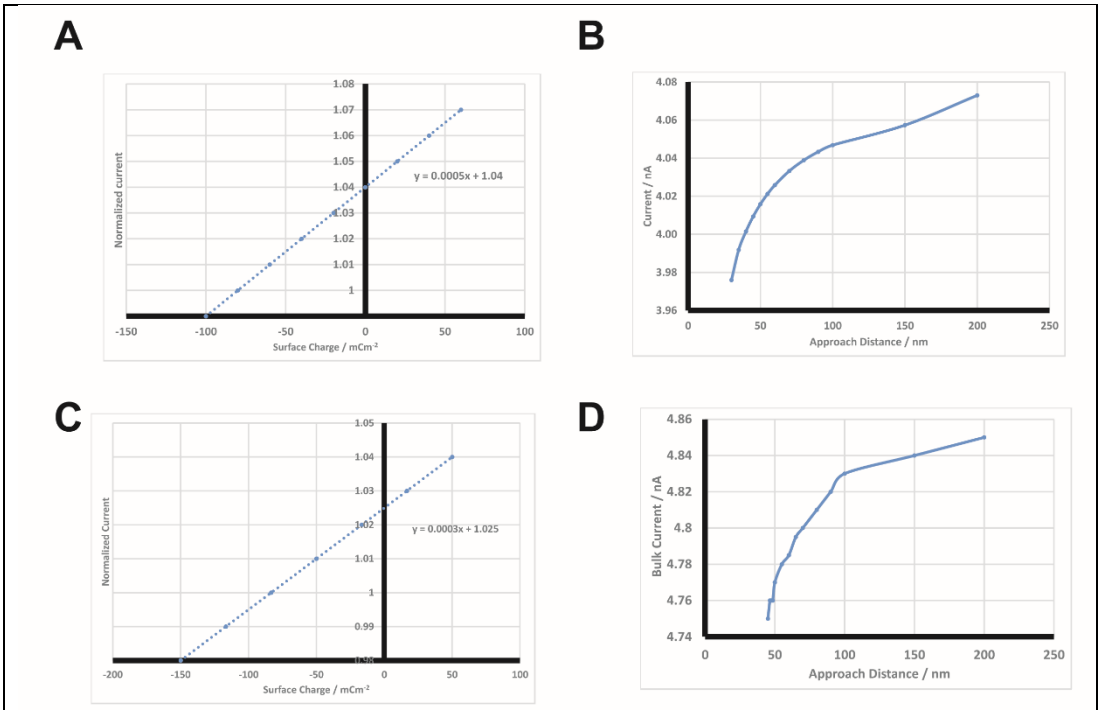

Figure 5.4 E. coli Calibration and Approach Curves.

Normalized current to surface charge calibration for *E. coli* on agarose (**A**) and corresponding approach curve (**B**). 2 % current drop at 35 nm. Normalized current to surface charge calibration for E. coli on PLL (**C**) and corresponding approach curve (**D**). 2 % current drop at 47 nm.

Metabolic activity is another possible contributor to the electrochemical response of the bacterial cell, with a large number of redox active complexes present in the cell envelope.[37] Bacterial metabolism is generally dependent upon generation of a proton gradient by pumping of protons into the periplasmic space (or surrounding area in the case of Gram-positive bacteria), furthermore, there will be a gradient of metabolic and homeostatic products in proximity to the bacterium. We expect the contribution of this to be minimal due to the absence of a carbon source and the sub-isotonic electrolyte concentration driving homeostasis towards ionic retention.[38] However, these factors could equally cause a certain degree of cellular stress which has been shown to cause changes in the composition and charge of the bacterial cell envelope. However, in the case of our experimental protocols' viability testing has shown the bacteria to remain viable (Appendix section 7.3.3). Some contribution to sub-cellular heterogeneities

from complex biological pathways and local ionic gradients cannot be ruled out but for the reasons mentioned we expect the response to be dominated by charge effects.

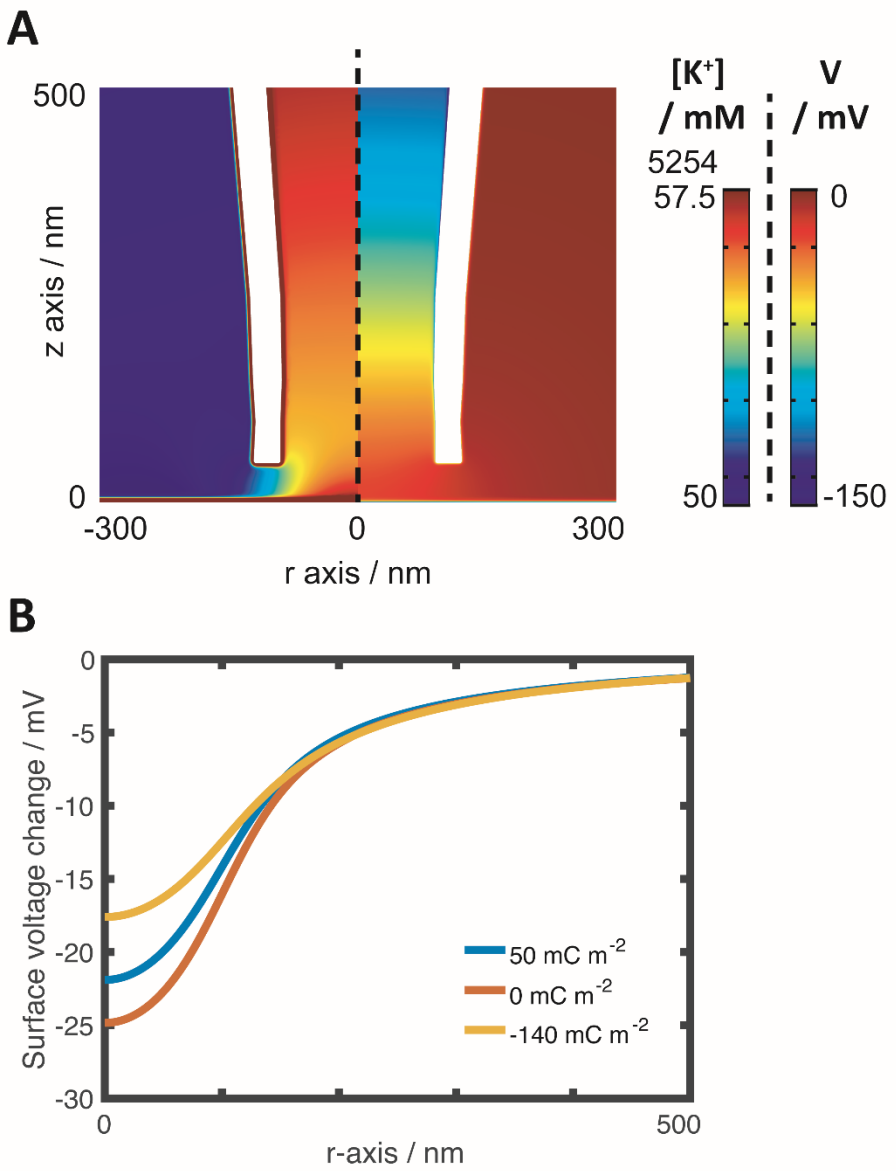

Figure 5.5 FEM Simulations Investigating Potential Applied to Bacterial Surface

FEM simulation of pulse-potential SICM measurements at a charged surface. (**A**) The $[K^+]$ (LHS) at the end of a -500 mV pulse for 20 ms at a -140 mC m^{-2} surface, with (RHS) the corresponding electrostatic potential. (**B**) The potential changes at differently charged surfaces relative to the equilibrium surface potential, demonstrating a small charge dependent potential drop at the surface.

All the normalized currents measured on *E. coli* samples resulted in FEM modelled surface charges that were within the realms predicted by the model (roughly between 150 and -150 mC m^{-2}). This is not true for the gram-positive *Bacillus* species as detailed below.

5.2.3 *Bacillus Subtilis* Surface Charge Mapping

We now consider experiments performed upon the gram-positive *Bacillus subtilis*; typical pulsed-potential SICM results are displayed in Figure 5.6 and the topography corresponds well with microscopic images in Figure 5.1. Normalized currents (Figure 5.6 **B**) are significantly higher than in the *E. coli* case, this implies a high density of stationary negative charge at the interface and can be attributed to differences in the structure of the cell envelope between the gram-negative *E. coli* and the gram-positive *B. subtilis* (Figure 1.15). In this case, the permeable and ion dense peptidoglycan layer is not shielded by an insulating membrane and can therefore be a major contributor to the electrochemical response in SICM experiments.

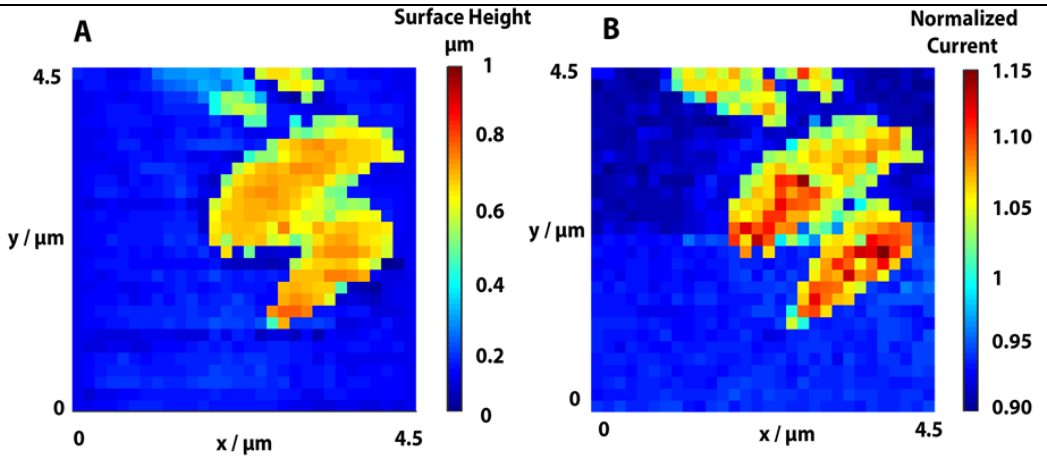

Figure 5.6 Bacillus 1 Agarose

SICM topography (**A**) and normalised current (**B**) of *Bacillus Subtilis* collected concurrently. SICM conditions: 50 mM tris buffered KCl at pH 7. 50 mV approach bias passing 440 pA current utilising a 2% feedback threshold. 150 nm nanopipette with 0.1 µm hopping distance. 4.5 μm^2 area.

Inter-cellular heterogeneity in both size and normalized current can easily be observed in Figure 5.6, this could have a number of causes, including microenvironment, cell physiology,[39] population variation, osmoregulation,[40] and differences in cell cycle

stage. The same mechanisms could also underpin the sub-cellular heterogeneities which can be observed across each cell.[41] Accessing information about these single entity heterogeneities demonstrate how powerful scanning probe techniques are in the fields of biology and materials science[6,8].

Figure 5.7 and Figure 5.8 detail further *Bacillus* scans on agarose. They show a higher resolution image and a larger view of the same area. The intensity of the normalized current is similar across all of the *Bacillus* cells imaged in Figure 5.8.

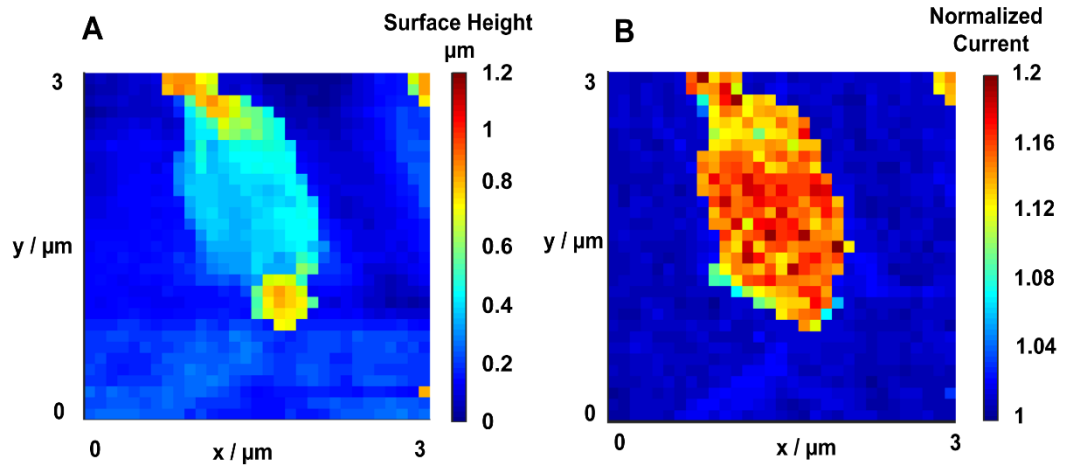

Figure 5.7 Bacillus 2 High Resolution Agarose

SICM topography (**A**) and normalised current (**B**) of *Bacillus Subtilis* collected concurrently. SICM conditions: 50 mM tris buffered KCl at pH 7. 50 mV approach bias passing 432 pA current utilising a 2% feedback threshold. 150 nm nanopipette with 0.1 µm hopping distance. 3 μm^2 area.

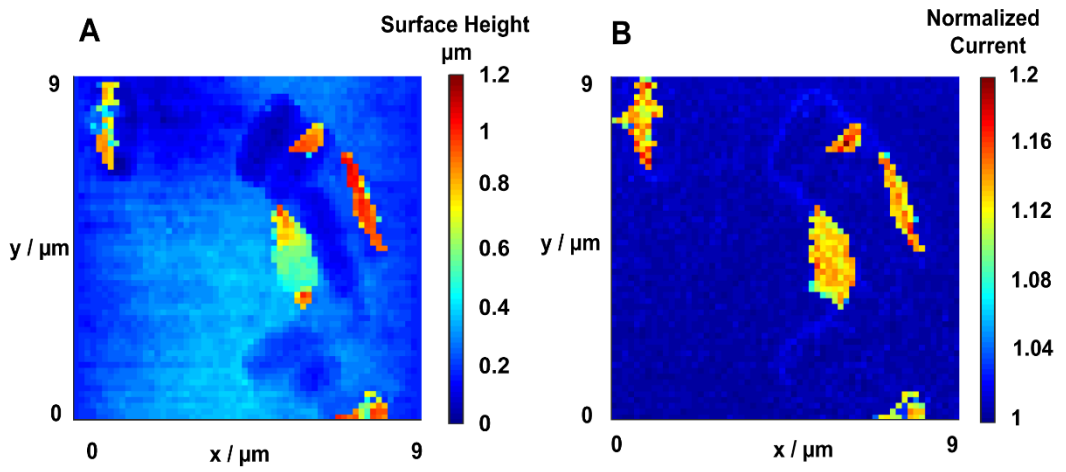

Figure 5.8 Bacillus 3 Expanded Area Agarose

SICM topography (**A**) and normalised current (**B**) of *Bacillus Subtilis* collected concurrently. SICM conditions: 50 mM tris buffered KCl at pH 7. 50 mV approach bias passing 443 pA current utilising a 2% feedback threshold. 150 nm nanopipette with 0.15 µm hopping distance. 9 μm^2 area.

Using the previous model, the normalized currents in these images results in large surface charge values. Far exceeding the +/- 150 mCm^{-2} deemed reasonable from the modelling sanity checks. The normalized currents observed are significantly higher than the *E. coli* cases. This implies a high density of stationary negative charge at the interface and can be attributed to differences in the structure of the cell envelope between the gram-negative *E. coli* and the gram-positive *B. subtilis* (Figure 1.15). The older model does not allow for such large normalized currents to be converted. To attempt to account for these values a new model was created. The aim was to simulate the bacteria as a 2D structure and to add reasonable constraints and contributions from its many cell envelope layers. Section 5.3 details this endeavour. Before going to such lengths to account for this an experiment to confirm these abnormal normalized current values was undertaken.

More information can be gained from SICM-SCM if instead of a potential pulse map of the target substrate a cyclic voltammogram is undertaken. The methodology is largely the same and the experimental conditions are kept constant. The main difference is that during the measurement the voltage is swept from -0.5 V through to

+0.5 V at 1 Vs^{-1}. This generates a considerable wealth of information and the CVs at each pixel in the resulting map can be analysed. The trade-off is that this measurement is time consuming. For these experiments, a lower resolution scan was undertaken. The experimental time was still over 3 hours. The results and their implications are discussed in the following section.

5.2.4 Potential Sweep Mapping

SICM charge mapping capabilities can be further extended by employing a scanned-potential protocol instead of a pulsed one (Figure 2.2**B**). Although resulting in increased scanning times, it provides a greater depth of information about the system and local ion concentration which can potentially help to elucidate more complex and dynamic processes. To further investigate the gram-positive cell envelope, a potential scanning protocol was implemented in which *i-V* curves are generated upon approach to the substrate. Firstly, the protocol was run on *E. coli* as a baseline measurement.

Figure 5.9 details the results. Two *E. coli* bacteria can be seen in close proximity. As stipulated the resolution is not as high but the image is clearly of two cells and the normalized currents align well. The normalized current seen in image **C** corresponds to that in the figures in section 5.2.2, the bias in question being applied to the bulk in all experiments. The normalized current over the bacteria obtained at this potential is in line with what was observed previously. There is minimal rectification in the CVs presented in image **D**.

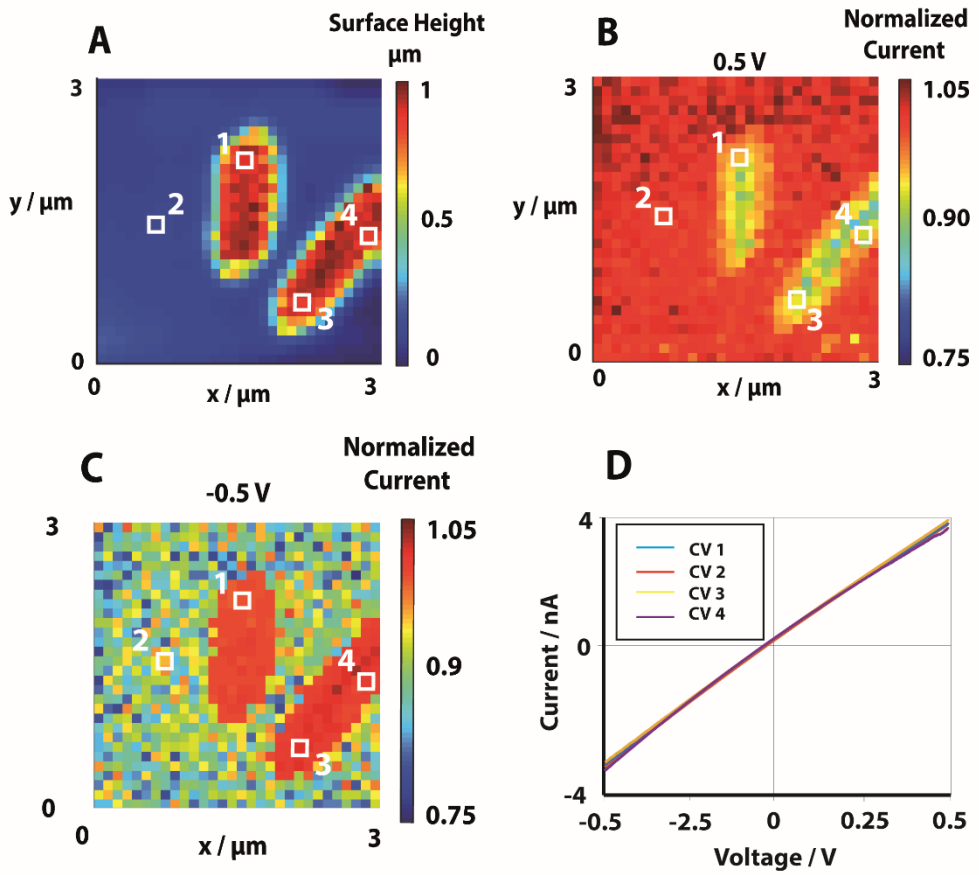

Figure 5.9 E. coli Potential Sweep on Cell-Tak

SICM topography (**A**) and normalized current at the highest potential in the sweep (**B**) and lowest potential (applied to tip) in the sweep (**C**) of *E. coli* collected concurrently. An over-lay of full *i-V* curves from 4 indicated pixels from the images (**D**).

SICM conditions: 50 mM tris buffered KCl at pH 7. 50 mV approach bias passing 443 pA current utilising a 2% feedback threshold. 150 nm nanopipette with 0.15 µm hopping distance. 9 μm^2 area.

The same experiment was conducted on *Bacillus* (Figure 5.10). Agarose was used as this option encountered less adherence issues with *Bacillus*. Again, the bacterium can be clearly seen in the topography in **A**. The normalized currents at both extremes (**B & C**) were much higher. Large rectification can be seen in the CVs in image **D**. There are areas of high normalized current that are not on the bacterial surface. We propose that these regions of charge may be residues from the extra polymeric substance (EPS) layer.

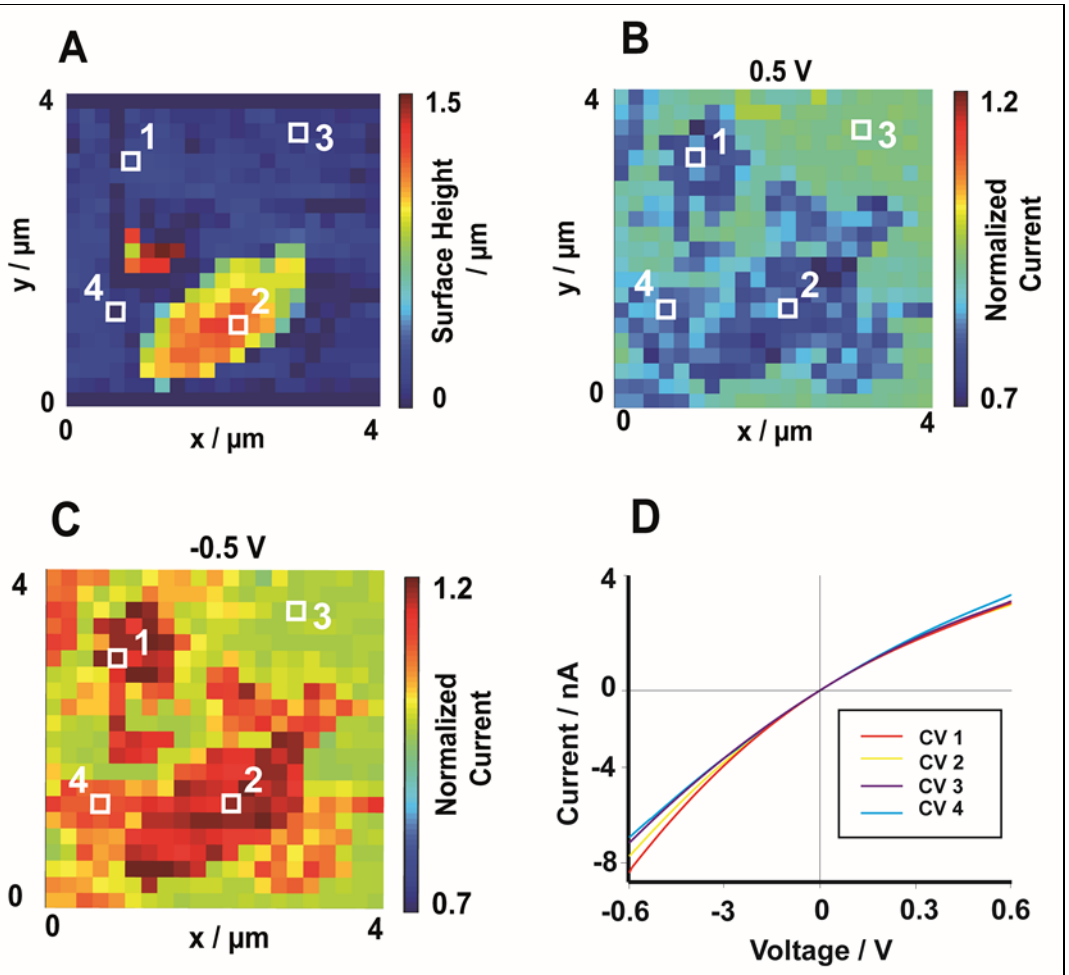

Figure 5.10 Bacillus Potential Sweep Map on Agarose

SICM topography (**A**) and normalized current derived from CVs at 0.5 V (**B**), -0.5 V (**C**) of *Bacillus Subtillus* collected concurrently. An over-lay of full *i-V* curves from 4 indicated pixels from the images (**D**).

SICM conditions: 50 mM tris buffered KCl at pH 7. CV from -0.5 V to 0.5 V, starting at 0.05 V with a scan rate of 1 V/s. At -50 mV approach bias passing 381 pA current, utilising a 2% feedback threshold. 0.2 um hopping distance with a 150 nm nanopipette

This protocol allows analysis of whether the high normalised currents in the pulsed-potential regime are due to the structure of the cell envelope rather than dynamic processes involving ionic fluxes from the cell. Image **D** shows the results of this analysis; *i-V* curves above the bacterium and above the adherence substrate demonstrate similar results to those generated due to surface induced rectification in the literature, indicating that the increased normalised current in pulsed-potential

SICM is not due to a general increase in ionic strength near the cell and is more likely from an increased charge on the substrate surface.[42] Although ruled out already due to the low electric field at the pipette tip (Figure 5.5), the smooth rectification profiles provide further evidence that voltage induced depolarisation of the membrane is not occurring, and no voltage-dependent ion transport mechanism is being gated by either the pulsed or scanned protocol employed herein.

The normalized current maps also exhibit features which do not correlate with the presence of bacteria in the topography map (Images **B & C**), these features are clustered around the bacteria and have a similar current response (however typically to a smaller magnitude/less charged). This is attributed to the EPS layer, or at least by some form of polymeric residue secreted by the bacteria. The substance is clearly more charged than the supporting agarose and does not correlate with a detectable change in the topography. The charge measured is significant and investigating this will be the focus of a future study. Its contribution may explain to some degree the shortcomings of the model in the following section.

5.3 Modelling the Gram-Positive Cell Wall

FEM simulations were made in COMSOL Multiphysics (v5.4) as 2D axisymmetric domains, constructed using dimensions from STEM images of the nanopipettes. Figure 5.11 gives the simulation domain and details where the fluxes and charge densities were applied. The electrostatics, transport of diluted species and laminar flow modules were used to model the experimental system. All boundaries not specifically labelled (grey) were set as no flux boundaries with no surface charges applied, and a no-slip flow condition was applied these boundaries and the pipette walls (blue). The pipette walls (blue) had a surface charge density of -30 mC/m^2 applied in all simulations, reasonable for borosilicate glass in aqueous solution under the conditions of our experiments. All potentials stated herein were applied to the upper boundary within the nanopipette (B1), positioned 1 mm above the base of the nanopipette, whilst B2 was held at ground. The concentrations at B1 and B2 were set to $[K^+]$ = 50 mM, $[Cl^-]$ = 50 mM, representing bulk solution in the nanopipette and bath. B2 was positioned 1 mm away from the nanopipette opening laterally, sufficient to be considered bulk.

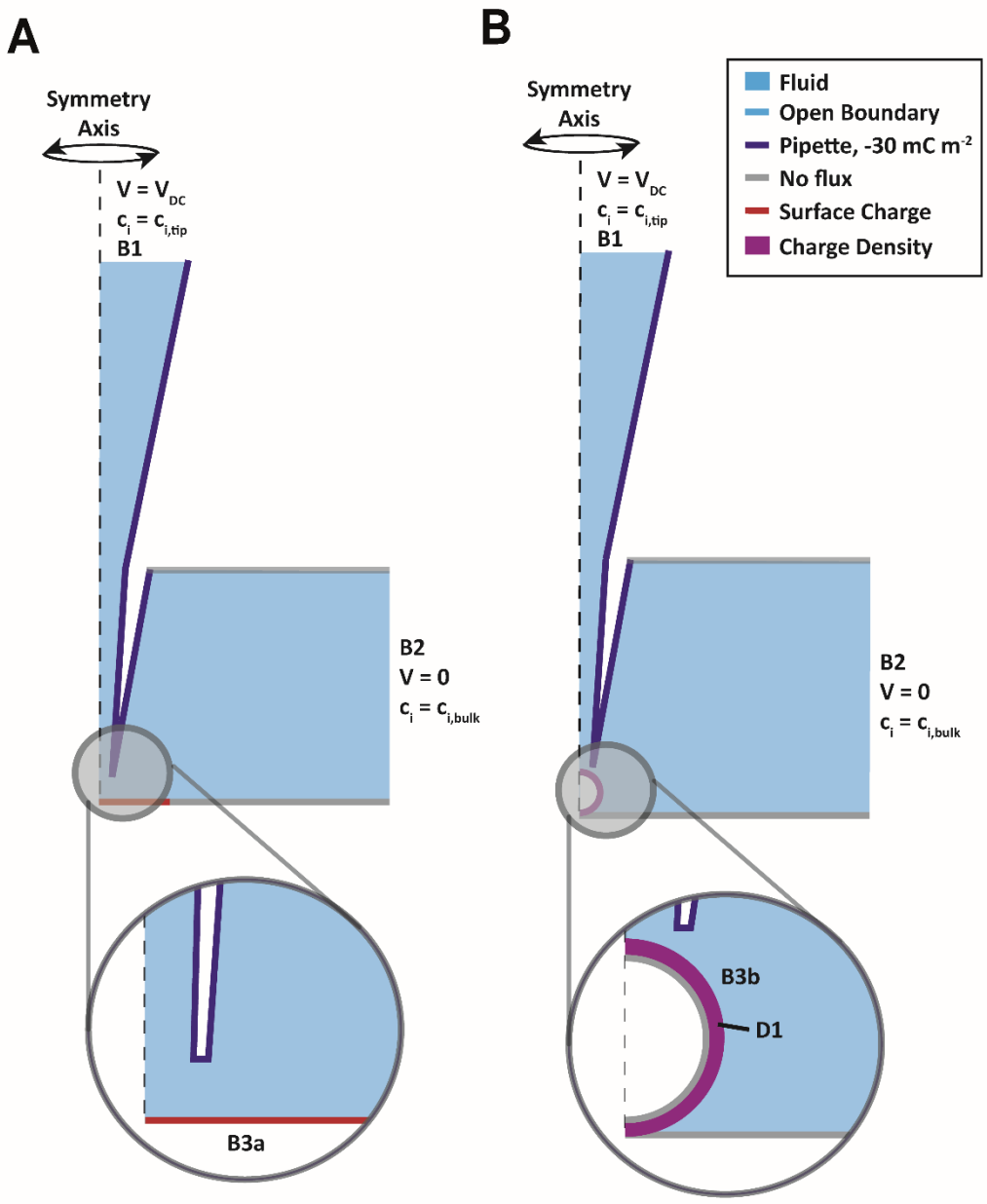

Figure 5.11 Schematic of FEM Simulations for Comparison

Schematic (not to scale) of FEM simulation domain for gram-negative bacteria (**A**) and gram-positive bacteria (**B**). The main boundaries are labelled. Bacteria is modelled as a 2D object with tuneable boundary properties in **B.**

Figure 5.11A depicts the simulations used to describe the *E. coli* case, where the substrate is treated as an impermeable charged insulator, therefore B3a (red) is set to a no-flux condition with varied surface charge. The system describing the gram-

negative simulations was defined the following differential equations. The flux J_i of each species i, was described by the Nernst-Planck equation:

$$J_i = -D_i \nabla c_i - z_i \frac{F}{RT} D_i c_i \nabla \phi + c_i u \quad (1)$$

and the Poisson equation defined the electric potential ϕ:

$$\nabla^2 \phi = -\frac{F}{\varepsilon \varepsilon_0} \sum_i z_i c_i \quad (2)$$

where D_i z_i and c_i are the diffusion coefficients, charge number and concentrations of species i and u is the solution velocity described below (eq. 3). F, R and T are the Faraday constant, gas constant and absolute temperature (298 K), ε is the dielectric constant of the solution (78) and ε_0 (8.85×10^{-12} F/m) is the vacuum permittivity. The diffusion coefficients at infinite dilution for K^+ (1.96×10^{-5} cm^2/s) and Cl^- (2.05×10^{-5} cm^2/s) were taken from the CRC handbook. These values are reasonable because of the sufficiently dilute concentrations used and the self-referencing nature of experiments.[43] The solution velocity was described by the incompressible Navier-Stokes equation with EOF incorporated (eq. 3):

$$u \nabla u = \frac{1}{\rho}\left(-\nabla p + \mu \nabla^2 u - F\left(\sum_i z_i c_i\right)\nabla \phi\right) \quad (3)$$

The simulations for the gram-positive cell envelope of *B. Subtilis* were defined in a similar way with some exceptions (Figure 5.11B). Instead of an insulating charged surface, the substrate is defined as a permeable domain (D1 - purple) with a concentration of fixed stationary negative charge (ρ_f). The thickness of the cell wall was estimated from cryo-TEM images (and literature values.[44] Therefore a thickness of 34 nm was used a but a range of values from 30-70 nm were explored to examine the effects of the thickness of the cell wall. This domain is bounded by an uncharged boundary below (grey) and a permeable interface above (B3b) at which the chloride permeability was varied in order to assess the effect of anion exclusion from the cell

wall. The inclusion of a domain representing a periplasmic space with the same physics as bulk was also examined, this was introduced beneath the cell wall domain (replacing the no-flux boundary) and had variable electrolyte concentration within. Two geometric configurations were used for initial parameter testing: a flat cell wall domain and a sphere with diameter 1 μm as shown in B. The response of each were found to be similar, the glass-wall approach distance and normalised currents were similar in each. However, the sphere model gave slightly higher responses which were closer to experimentally determined currents and was considered to be more representative of the experimental conditions.

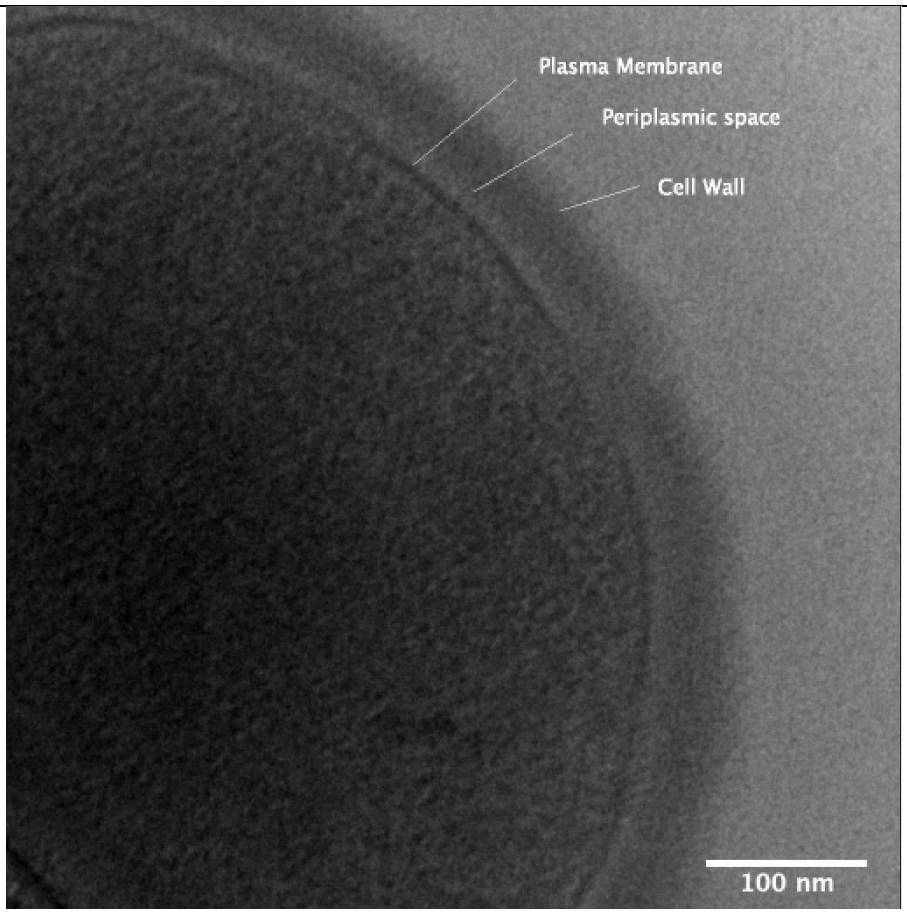

Figure 5.12 Cryo-TEM of Bacillus Subtilis

Example of cryo-TEM image used to estimate bacterial cell wall thickness. The sample was frozen in liquid ethane for cryo purposes. Images taken at 200 kV.

The Poisson equation (Eq 2) is still used to describe the potential, however the total charge incorporates the stationary fixed charge within the volume of the cell wall (ρ_f).

$$\nabla^2\phi = -\frac{1}{\varepsilon\varepsilon_0}(\rho_f + F\left(\sum_i z_i c_i\right)) \quad (4)$$

This model of the gram-positive cell wall as a soft polyelectrolyte layer is well established in literature and has previously been used to calculate the Donnan potential within the cell wall for various species. is similar to previous considerations of interfaces in electrophoretic measurements.[45,46] The charge density of the *B. subtilis* cell wall has been calculated previously using electrokinetic theory, providing charge concentration values (ρ_f/F) of approximately 15-25 mM.[47] However this is highly dependent upon strain, electrolyte composition, substrate, and pH so a wider range of charges were examined.[48] Varying the relative dielectric permittivity ε of the cell wall from 78 to 20 (taken from literature EFM measurements)[49] was found to have no effect upon approach or normalised currents.

The transport in all domains was described by the Nernst-Planck equation, however within the cell wall domain (D1) the effective diffusion coefficients were varied to be assess the effect of the tortuosity of the cell wall. The mobility of ions within the cell wall was again defined by the Nernst-Planck equation however mobility of each ion was considered within the cell wall by using an effective diffusion coefficient (D_{eff}). Alteration of the diffusion coefficient in polyelectrolyte layers is due to the tortuosity of the channels which form the free space of the layer or interaction with the cell walls. D_{eff} was calculated as a product of the diffusion coefficient in ideal solutions (D) and a factor representing mobility within the wall (μ_{wall}). This factor can be estimated by the Renkin equation[50] based upon the pore size of the *B. subtilis* cell wall (2.12 nm)[51] and the hydrodynamic radius of ions.[52] This gives probable values for μ_{wall} in the range of 0.5 to 0.75, however a wider range was explored.

The permeability of anions in the cell wall was found to be an important factor in simulations and the approach threshold of 2% was unobtainable with a fully permeable model of the cell wall for reasonable values of ρ_f and μ_{wall}, including full contact between the cell wall and nanopipette. While approach was possible with specific combinations of anion permeability and charge, applying the potential pulse at these heights did not replicate experimental currents. Therefore, it is assumed that an anion permeable cell wall model does not provide a realistic representation. This is

considered reasonable because anions would be more effectively excluded from the cell wall than by simply solving the Poisson equation as the reduction of accessible volume will create channels with high stationary negative charge and effective anion exclusion is predicted in the literature.[18] Therefore the exterior of the cell wall, boundary B3b, was set to be impermeable to chloride and μ_{wall} was only applied to potassium.

EOF is not incorporated into these simulations for a number of reasons. Previous work on charge mapping simulations in have shown that EOF has a negligible effect upon the simulated normalised current due to the self-referencing nature of the experiment.[53] Furthermore, the flow properties within the cell wall are usually described by the Brinkman equation:[45]

$$u\nabla u = \frac{1}{\rho}\left(-\nabla p + \frac{\mu}{K}\nabla^2 u - F\left(\sum_i z_i c_i\right)\nabla\phi\right) \quad (3)$$

where K is a permeability coefficient which represents the increase in stress due to confinement, tortuosity, and interactions with the channel walls and is on the scale of 10^{-17} for the bacterial cell wall.[48,54] This indicates that fluid flow is severely inhibited within the cell wall and therefore is not expected to significantly contribute to the ionic current response in SICM modalities.

First the experimental working approach distance between the nanopipette and the surface was estimated by steady-state simulations with the boundary at the top of the pipette (Boundary B1) held at V_{hold}, the distances were taken from the distance at which the ionic current normalized to the bulk current reached the experimental approach set point of a 2% decrease from bulk current. Approach curves for the *E. coli* are presented alongside the corresponding images, approach height was approximately 30 nm (Figure 5.13).

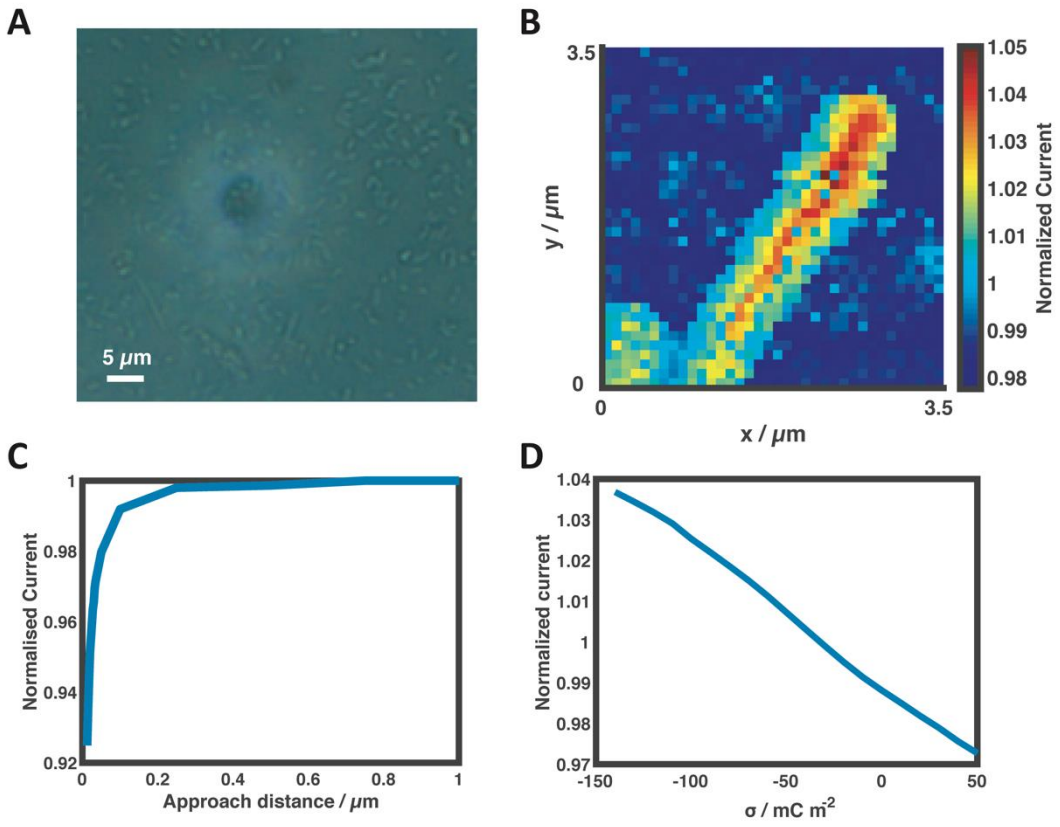

Figure 5.13 E. coli Normalized Current and Approach Curves

Optical microscopy image (**A**), normalized current SICM map (**B**), approach curve (**C**) and calibration curve (**D**) for E. coli presented together for ease of viewing.

Initially parameters of the *Bacillus* model were changed to see if the large normalized currents could be accounted for by the inclusion of charged membranes and layers within the cell wall. Figure 5.14**A** shows the change in the approach curve when the charge density concentration in the cell wall (Figure 5.11 boundary D1) is varied. There is minimal effect on the approach curve with charge as the nanopipette is insensitive to the surface charge at approach potentials.

Figure 5.14**B** shows the difference in the tip current when the potential is pulsed in surface and in bulk with a 100 mM charge applied to the cell wall. The change in current at the surface is the underpinning phenomenon that makes SICM-SCM possible.

Figure 5.14**C** shows the effect on the observed normalized current when the thickness of the cell wall (Figure 5.11 boundary D1) is changed (blue, red and yellow lines

representing the minima maxima and average values of cell wall thickness found in the literature) and the wall charge is varied. Even at the maximum reported values the predicted normalized current was well below the experimentally observed 1.2.

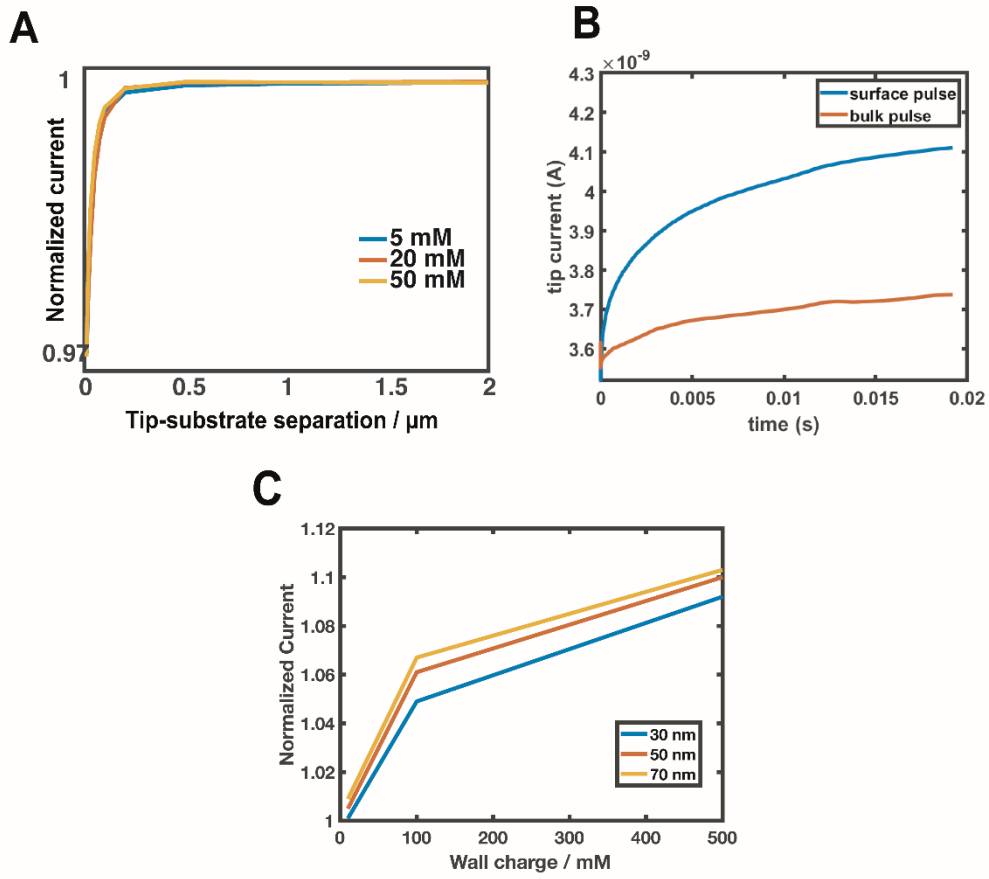

Figure 5.14 FEM Simulations for Functional Mapping of B. Subtilis

Simulated approaches to gram-positive cell walls of various charge density (**A**). Example simulated pulses of -500 mV at a wall with 100 mM charge density (**B**). The effect of cell wall thickness on simulated normalised currents (**C**).

Figure 5.15 details further findings from the gram-positive model. **A** shows the potential change with approach distance from the interface (bacterial cell wall) along the axis of rotational symmetry for the model (dashed line in **C** & **D**). The potential drops sharply in both cases at the interface due to the charge on the surface. The unperturbed line is a measure of the potential without the nanopipette present, at 50 mV the change in the potential is minor. In the case of the pulse bias the potential further away from the interface is lower due to the bias applied at the top boundary

(B1 Figure 5.11) and at the interface the magnitude of the potential drop is reduced as ions migrate out of the cell wall increasing the local ion conductivity.

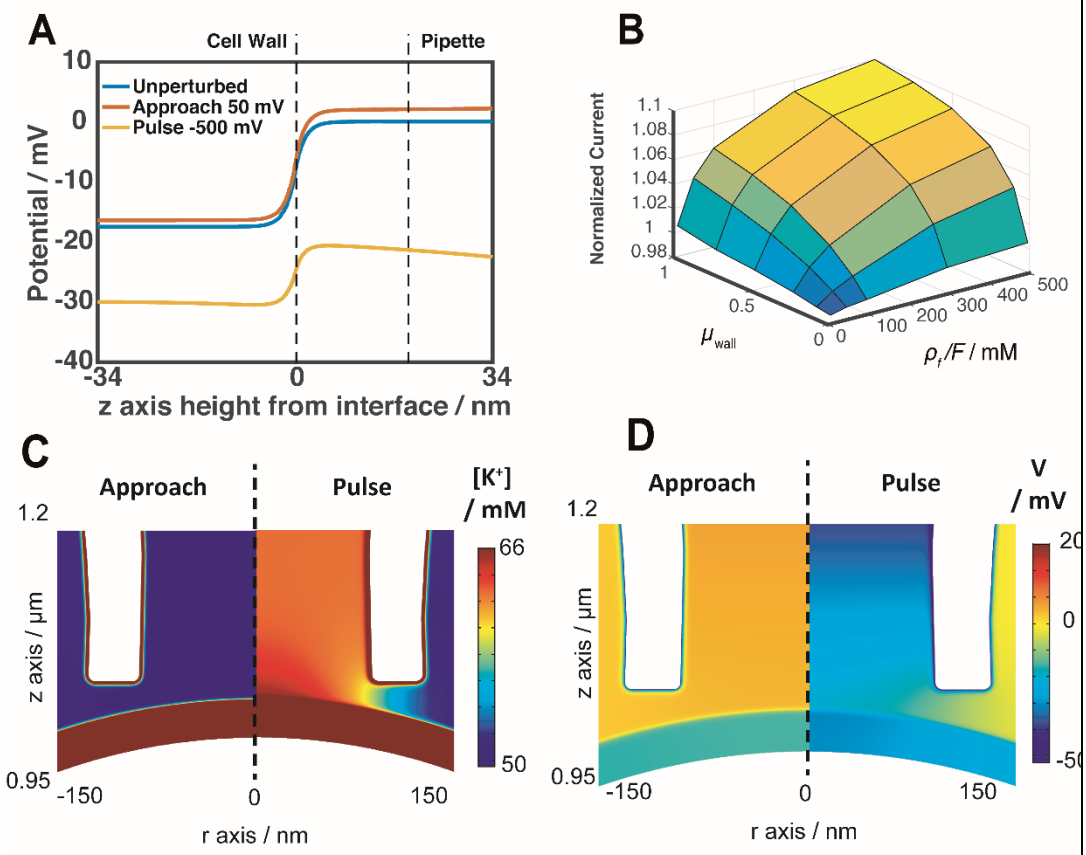

Figure 5.15 FEM Simulations of the Pulse-Potential SICM at the Gram-Positive Cell Wall.

The potential gradient across the cell wall with the externally applied potential subtracted. The potential distribution when the pipette at approach potential (50 mV) in bulk (blue) and approached to the surface (orange), alongside the potential at the end of the -500 mV pulse (yellow) (**A**). Normalised current plotted for combinations of mobility (μ_{wall}) and charge density in the cell wall (ρ_f) showing diminishing feedback outside of expected physiological values (**B**). Potential distribution (**C**) and [K^+] at the approach potential (left) and end of the pulse (right) for charge density of 100 mM (**D**).

B shows a 3-axis plot of the maximum normalized current (*z* axis) when parameters of the cell wall are varied. The *y* axis shows the ion mobility (μ_{wall}) within the cell

wall. This had a small effect and did not account for the large normalized currents. The *x* axis shows the charge density (ρ_f) (over faradays constant) in the cell wall.

This caused the largest change in normalized current. Literature values predict a charge density of around 20 mM. Increasing this to extremes did not reach the 1.2 normalized current values observed experimentally and past around 200 mM lead to diminishing returns (likely due to screening). This means the new model does not fully explain the high normalized currents observed.

C and **D** show the potential distribution and potassium concentration (respectively) in the foot of the nanopipette in close proximity to the surface. In **C** the change in potential as ions are liberated from the surface during the pulse is clear. In **D**, the concentration of potassium during the pulse gives rise to the detectable change in current. Interestingly, what can also be seen is a subtle discolouration of the blue semi-circular bacteria in the area squarely under the central axis of the nanopipette. This is a sign that some depletion of the surface ions is occurring, I.E the pulse is causing some perturbation of the surface though not a large enough potential is applied to stimulate ion channels.

The model demonstrates that the experimentally observed surface charge is not accounted for by the factors studied. Further conditions to be applied to fully understand the phenomenon are difficult to model and baseline values are disputed or unobtainable in the literature. Candidates for this include a fully 3D of the structure (which is incredibly computationally heavy) and simulating a charged gradient within the periplasmic space. The surface layer of the bacteria is particularly charged, the thickness of the interface having minimal effect on the simulated normalized current implying the surface groups have the largest effect. Although the normalized current is not explained fully, the discrepancy between the gram-negative and gram-positive is well documented and the improved model serves as a functional baseline for further improvements.

5.4 Conclusions

The ability to interrogate the surface of live bacterial cells by employing different SICM potential scanning protocols is demonstrated. Clear differences are observed between gram-negative and gram-positive bacteria and further investigation through potential scanning infers the observed discrepancy is repeatable and can be attributed to the structural differences in the composition of the bacterial cell walls relative to Gram type.

In achieving these data multiple adherence substrates are tested resulting in protocols capable of trapping live bacteria for long enough durations to undergo SICM analysis. These methods provide a platform for further, repeatable, live bacterial imaging which has been shied away from by the field due to its difficulty.

The data collected provide a wealth of information which can be used to assess and verify models of the bacterial cell envelope while also providing information on inter-cellular and sub-cellular heterogeneities. From our findings it is clear that the simplistic view of the cell envelope adopted enlarge is not sufficient to describe the charged nature of the gram-positive bacterial cell wall and further developments on more comprehensive models are required. A more thorough understanding of the bioelectrical response at the interface of bacterial cells and their environments will benefit a broad range of research areas including bacterial adhesion, antibiotic resistance, and biofilm formation, with a significant impact on life science research and development. The proven ability of SICM to probe charged interfaces with sub-cellular resolution now extends to live bacterial samples and is a key tool towards further development in these fields.

Future work stemming from this chapter has already begun. This work reports the foundations of a new area of study for the Warwick electrochemistry and interfaces group and multiple PhD students are now exploring it. The obvious next steps are to develop the model further and investigate other bacterial strains. Exciting work on visualising bacterial cell division and measuring surface charge discrepancies when antibiotic resistant bacteria are exposed to antibiotics is also underway. The findings from these studies may lead to advances in the development of antibiotics, an area of major interest for scientific and medical professionals.

5.5 References

1 P. K. Hansma, B. Drake, O. Marti, S. A. C. Gould and C. B. Prater, *Science (80-.).*, 1989, **243**, 641–643.

2 Y. E. Korchev, L. C. Bashford, M. Milovanovic, I. Vodyanoy and M. J. Lab, *Biophys. J.*, 1997, **73**, 653–658.

3 Y. E. Korchev, Y. A. Negulyaev, C. R. W. Edwards, I. Vodyanoy and M. J. Lab, *Nat. Cell Biol.*, 2000, **2**, 616–619.

4 M. Miragoli, A. Moshkov, P. Novak, A. Shevchuk, V. O. Nikolaev, I. El-Hamamsy, C. M. F. Potter, P. Wright, S. H. S. A. Kadir, A. R. Lyon, J. A. Mitchell, A. H. Chester, D. Klenerman, M. J. Lab, Y. E. Korchev, S. E. Harding and J. Gorelik, *J. R. Soc. Interface*, 2011, **8**, 913–925.

5 A. Page, D. Perry and P. R. Unwin, *Proc. R. Soc. A*, 2017, **473**, 1–34.

6 D. Momotenko, K. McKelvey, M. Kang, G. N. Meloni and P. R. Unwin, *Anal. Chem.*, 2016, **88**, 2838–2846.

7 M. Kang, D. Perry, C. L. Bentley, G. West, A. Page and P. R. Unwin, *ACS Nano*, 2017, **11**, 44.

8 M. Kang, D. Momotenko, A. Page, D. Perry and P. R. Unwin, *Langmuir*, 2016, **32**, 7993–8008.

9 C.-C. Chen, Y. Zhou and L. A. Baker, *Annu. Rev. Anal. Chem.*, 2012, **5**, 207–228.

10 J. Seifert, J. Rheinlaender, F. Lang, M. Gawaz and T. E. Schäffer, *Nat. Sci. Reports*.

11 D. Perry, R. Al Botros, D. Momotenko, S. L. Kinnear and P. R. Unwin, *ACS Nano*, 2015, **9**, 7266–7276.

12 K. McKelvey, S. L. Kinnear, D. Perry, D. Momotenko and P. R. Unwin, *J. Am. Chem. Soc.*, 2014, **136**, 13735–13744.

13 D. Momotenko, K. McKelvey, M. Kang, G. N. Meloni and P. R. Unwin, *Anal. Chem.*, 2016, **88**, 2838–2846.

14 B. Chen, D. Perry, A. Page, M. Kang and P. R. Unwin, *Anal. Chem.*, 2019, **91**, 2516–2524.

15 B. Babakinejad, P. Jönsson, A. López Córdoba, P. Actis, P. Novak, Y. Takahashi, A. Shevchuk, U. Anand, P. Anand, A. Drews, A. Ferrer-Montiel, D. Klenerman and Y. E. Korchev, *Anal. Chem.*, 2013, **85**, 9333–9342.

16 S. Schobesberger, P. Jönsson, A. Buzuk, Y. Korchev, J. Siggers, J. Gorelik, A. Buzuk¤, Y. Korchev¤, J. Gorelik¤, P. Jö, A. Buzuk, Y. Korchev, J. Siggers and J. Gorelik, *Biophys. J.*, 2016, **110**, 141–146.

17 F. Wu, B. Zhou, J. Wang, M. Zhong, A. Das, M. Watkinson, K. A. Hing, D.-W. Zhang and S. Krause, *Anal. Chem.*, , DOI:10.1021/acs.analchem.9b00304.

18 C. Marlière and S. Dhahri, *Nanoscale*, 2015, **7**, 8843–8857.

19 A. Van Der Wal, W. Norde, A. J. B. Zehnder and J. Lyklema, *Determination of the total charge in the cell walls of Gram-positive bacteria*, 1997, vol. 9.

20 A. Van der Wal, W. Norde, B. Bendinger, A. J. B. Zehnder and J. Lyklema, *J. Microbiol. Methods*, 1997, **28**, 147–157.

21 J. WECKE, M. PEREGO and W. FISCHER, *Microb. Drug Resist.*, 1996, **2**, 123–129.

22 J. Wecke, K. Madela' and W. Fixher, *The absence of D-alanine from lipoteichoic acid and wall teichoic acid alters surface charge, enhances autolysis and increases susceptibility to rnethicillin in Bacillus subtilis*, 2018, vol. 143.

23 A. Page, D. Perry, P. Young, D. Mitchell, B. G. Frenguelli and P. R. Unwin, *Anal. Chem.*, 2016, **88**, 10854–10859.

24 C. Zhu, L. Zhou, M. Choi and L. A. Baker, *ChemElectroChem*.

25 A. Terada, K. Okuyama, M. Nishikawa, S. Tsuneda and M. Hosomi, *Biotechnol. Bioeng.*, 2012, **109**, 1745–1754.

26 T. J. Silhavy, D. Kahne and S. Walker, *Cold Spring Harb. Perspect. Biol.*, 2010, **2**, a000414.

27 O. D. Novikova and T. F. Solovyeva, *Biochem. Suppl. Ser. A Membr. Cell Biol.*,

2009, **3**, 3–15.

28 H. Nikaidos, *Porins and Specific Diffusion Channels in Bacterial Outer Membranes**, 1994, vol. 269.

29 D. Drew, L. Fröderberg, L. Baars and J.-W. L. de Gier, *Biochim. Biophys. Acta - Biomembr.*, 2003, **1610**, 3–10.

30 B. Martinac, M. Buechner, A. H. Delcour, J. Adler and C. Kung, *Pressure-sensitive ion channel in Escherichia coli (bacteria/spheroplast/patch-clamp technique/osmoregulation)*, 1987, vol. 84.

31 M. Babu, C. Bundalovic-Torma, C. Calmettes, S. Phanse, Q. Zhang, Y. Jiang, Z. Minic, S. Kim, J. Mehla, A. Gagarinova, I. Rodionova, A. Kumar, H. Guo, O. Kagan, O. Pogoutse, H. Aoki, V. Deineko, J. H. Caufield, E. Holtzapple, Z. Zhang, A. Vastermark, Y. Pandya, C. C. Lai, M. El Bakkouri, Y. Hooda, M. Shah, D. Burnside, M. Hooshyar, J. Vlasblom, S. V Rajagopala, A. Golshani, S. Wuchty, J. F Greenblatt, M. Saier, P. Uetz, T. F Moraes, J. Parkinson and A. Emili, *Nat. Biotechnol.*, 2018, **36**, 103–112.

32 J. M. Wood, *J. Gen. Physiol.*, 2015, **145**, 381–388.

33 E. M. Sonnenfeld, T. J. Beveridge and R. J. Doyle, *Can. J. Microbiol.*, 1985, **31**, 875–7.

34 J. M. Wood, *J. Gen. Physiol.*

35 J. Y. Wong, R. Langer and D. E. Ingber, *Proc. Natl. Acad. Sci. U. S. A.*, 1994, **91**, 3201–4.

36 N. Sa and L. A. Baker, *J. Am. Chem. Soc*, 2011, **133**, 45.

37 A. Page, D. Perry and P. R. Unwin, *Proc. R. Soc. A*, 2017, **473**, 1–34.

38 V. R. F. Matias and T. J. Beveridge, *Mol. Microbiol.*, 2005, **56**, 240–251.

39 S. S. Dukhin, R. Zimmermann, J. F. L. Duval and C. Werner, *J. Colloid Interface Sci.*, 2010, **350**, 1–4.

40 J. F. L. Duval and F. Gaboriaud, , DOI:10.1016/j.cocis.2009.12.002.

41 S. Okuda, R. Igarashi, Y. Kusui, Y. Kasahara and H. Morisaki, *J. Bacteriol.*,

2003, **185**, 3711–3717.

42 J. F. L. Duval and F. Gaboriaud, *Curr. Opin. Colloid Interface Sci.*, 2009, **15**, 184–195.

43 D. Esteban-Ferrer, M. A. Edwards, L. Fumagalli, A. Juá rez and G. Gomila, 2019, **13**, 9.

44 *Biochim. Biophys. Acta - Biomembr.*, 1972, **255**, 273–303.

45 P. Demchick and A. L. Koch, *The Permeability of the Wall Fabric of Escherichia coli and Bacillus subtilis*, 1996, vol. 178.

46 J. Cervera, P. Ramírez, J. A. Manzanares and S. Mafé, , DOI:10.1007/s10404-009-0518-2.

47 D. Perry, R. Al Botros, D. Momotenko, S. L. Kinnear and P. R. Unwin, *ACS Nano*, 2015, **9**, 7266–7276.

48 F. Gaboriaud, M. L. Gee, R. Strugnell and J. F. L. Duval, , DOI:10.1021/la800258n.

6 Conclusions

This thesis continues to build the case for SICM as a viable technique for advanced interfacial surface analysis. Chapter 3 establishes SICM-PCAD as a new technique. Whilst still offering the high-resolution topography for which it is well established, powerful SICM dissolution measurements can be employed to assess a surfaces susceptibility to erosive damage at the nanoscale. SICM-PCAD is demonstrated, detailing its progress from conception to practical application in a large multifaceted study.

The potential of the technique is explored by analysing dental enamel, successfully extracting kinetics for dissolution in the nanopipette footprint by measuring the depth of etch pit forming as protons are delivered to the surface and simulating the process in a FEM model. The SICM platform allows for automated repeats of the etching process, providing data for relevant statistical analysis to draw conclusions about the susceptibility of the measured surface to acid attack. The technique is shown to be reproducible and the error between nanopipettes small. Being able to assign an etch pit depth to a sample as a benchmark value means pre and post treatment analysis can be used to measure and quantify any surface changes imparted by an experimental treatment. In this way low level acid erosion is measured at the nanoscale and the protective benefit to enamel through additive exposure (such as zinc and fluoride) is assessed.

SICM-PCAD is shown to work through an applied salivary pellicle and the option to visualise etching sites post analysis is utilised to conclusively display the protection benefit calculated from the etching depths. The technique is utilised to investigate the importance of enamel rod alignment and through careful statistical analysis the increased acid resistance of the inter-rod regions of enamel is demonstrated, showcasing the techniques ability to extract subtle information about surface composition and heterogeneities at the nanoscale.

The technique offers a unique platform to expand knowledge in materials science, directly investigating the dissolution kinetics of complex multifaceted surfaces. In future studies SICM-PCAD could easily be used to investigate surface coatings, biological membranes, bio-fouling, anti-corrosive paints, protective films, polymer

coatings and any other flat surface where the dissolution kinetics are of interest. Further work for this technique should include supporting the topographic data with AFM measurements and testing on a wider array of substrates, include materials with higher and lower densities and surface hardness to test whether the method could be used to investigate metal corrosion and other relevant dissolution processes.

Chapter 4 takes the platform of SICM-SCM, conceptualised and established at Warwick and utilises it to investigate dental substrates. Initially imaging the enamel and dentine microstructure and revealing the complex network of inter-locking prisms present in dental enamel. Surface charge heterogeneities over the inter-rod enamel regions were visualised in mature enamel for the first time. The ability of the technique to interrogate the subtle changes imparted by crystal structure and composition (specifically organic content) on the observed surface charge is a powerful tool going forward, opening the door for the analysis of a multitude of substrates.

Analysis of dentine revealed unexpected surface charge heterogeneities corresponding to the dental tubules, indicating a change in morphology over those regions. This demonstrates the techniques potential to investigate subtle surface chemistry that may be missed with conventional topographic methods. Displaying areas of high and low surface charge density can help understand the purpose of substructures and provides a new insight to interface interactions at the nanoscale.

Experiments were designed to utilise the measured surface charge of an enamel sample pre and post dietary acid exposure, attempting to visualise any change in surface charge imparted by the acid wash. Exposure to a weak citric acid solution left the surface considerably more negative, particularly at the enamel prism junctions. This was contrasted with phosphoric acid which did not appear to modify the surface charge to any significant degree. This shows that mechanistic differences in the mode of acid attack for dietary acids can be investigated and points of vulnerability to acid dissolution in the surface can be visualised. This was compared to HCl, a more aggressive mineral acid which etched the central rod regions more aggressively and lead to a blanket shift in the surface charge to the negative. This allows conclusions to be drawn about the dominant pathway in early stage erosion for the acids and it may be that calcium chelation is playing a larger role in the initial stages of enamel dissolution in the case of citric acid. Whilst more experiments are needed to

conclusively say if this is the case, SICM-SCM provides a platform for investigating such subtle surface chemistry. Again, the technique provides information not obtainable through other methodologies. The difficulty of these experiments is not to be underestimated and larger scale studies would be time consuming, particular difficulties being establishing a firm baseline with enamel and other biological materials due to their heterogeneous nature and developing a method to standardise the surface charge calculation between different nanopipettes.

Finally, remineralisation processes were investigated by first exposing the surface to citric acid and then replenishing it via application of a calcium and phosphate rich remineralisation solution, designed to mimic the mouths natural enamel restoration process. Although a complete return to the baseline surface charge was not seen, the surface did appear to repair to some extent and the quantification and visualisation of this process with such a mild acid challenge is, to the extent of our knowledge, the first time this has been documented. Further supporting data for this process, such as AFM or SEM images would be of benefit in future studies.

SICM SCM has a place in answering fundamental questions with regards to dissolution processes and has shown its ability to investigate very subtle interfacial changes and is able to give a visualisation of points of increased vulnerability of a surface. This may prove indispensable as we seek to further our knowledge of nano and microstructures and develop enhanced methods of protecting and repairing surfaces susceptible to acid attack. However the method does not yet suit a screening style application due to the difficulty in reproducing results and the large time investment required to obtain the data and then convert the normalised current values through FEM modelling, both specialised tasks that require training and specific knowhow.

In the final results chapter, SICM-SCM is used to visualise the surface charge discrepancies on gram-negative and gram-positive bacteria. To achieve this, new methods of live bacterial imaging are implemented, leading to protocols for analysing viable, live bacteria for the first time. The methods implemented will translate well to analysing other living substrates (such as cells) and opens the door to exciting research on antibiotic resistant bacteria and other increasingly important fields.

The differences in the normalized currents observed between the bacterial strains are large and consistent. The cell wall structure leads to variation in the observed surface charge. The more insulating gram-negative bacteria produced surface charge values within the range predicted by current models of SICM surface charge. Gram-positive bacteria did not, which lead to a revamping of the FEM methods used with the hope of developing a more comprehensive model that accounted for such high normalized currents. Whilst the model developed did not account for the high charges seen, this raises interesting questions with regards to the nature of the bacterial cell. Even with conditions and biological parameters pushed to their feasible limits, the charge observed remained unaccounted for. This points to factors not incorporated into the model having an unexpectedly large effect. This may be metabolic process or excretions by the cell producing much higher charge densities than previously recorded. The model developed will go some way to explaining the nature of the bacterial cell wall and is a good baseline for investigating further highly complex biological structures.

The work presented here achieves advances in the fields it sets out to investigate and provides a platform for exciting future research with SICM. What is detailed here will further the viability of SICM as a choice for serious materials science studies of dissolution processes and as a premier biological imaging technique now capable of live bacterial cell imaging. The potential for furthering knowledge of dissolution processes is a benefit to the field of dental science, particularly early stage acid erosion and provides and exciting toolbox for use on other complex substrates.

7 Appendix

7.1 SICM-PCAD Appendix

7.1.1 Example Raw Data *Z* Profiles for SICM-PCAD

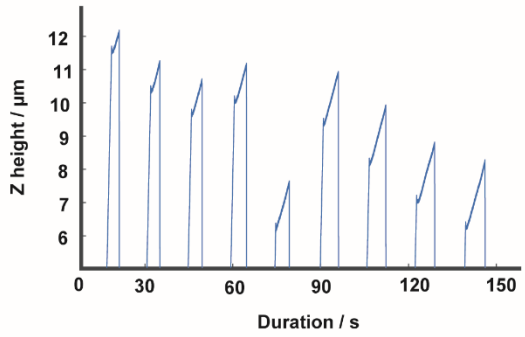

Figure 7.1 Z Trace Increasing Potential Example

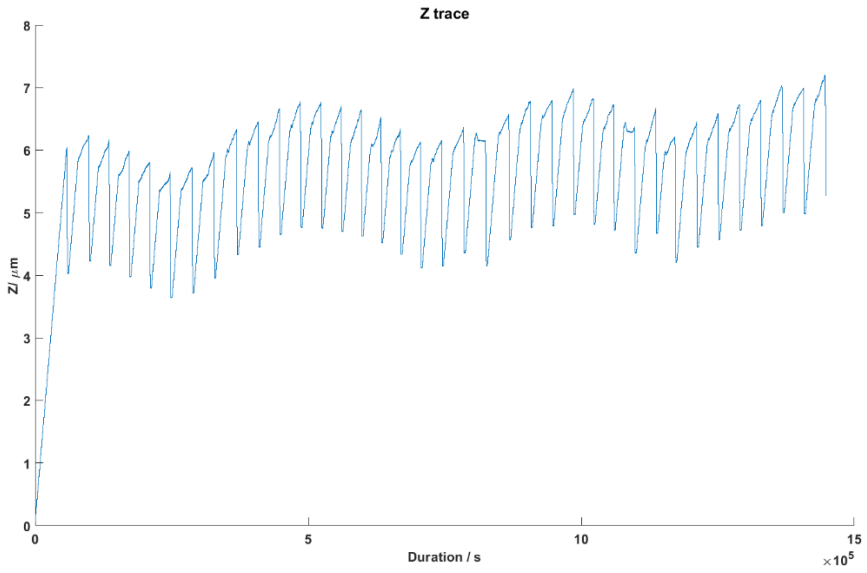

Figure 7.2 Z Trace Full Sound Enamel

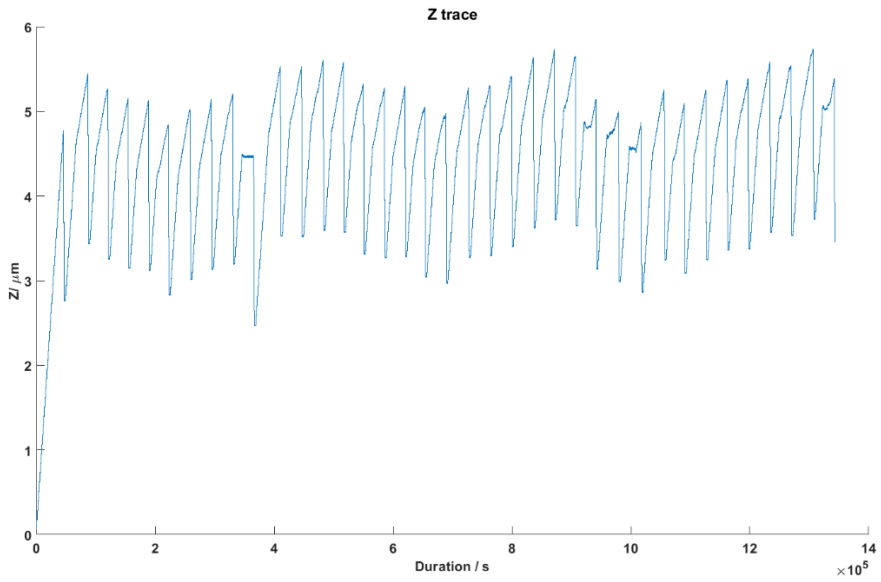

Figure 7.3 Z Trace Full Citric Acid Treated Enamel

Figures 7.1, 7.2 and 7.3 give some example raw data that the etch pit depths are calculated from. 7.1 shows the z traces as the delivery time is increased by 1 second on each approach. 7.2 shows 36 etch pits on untreated enamel. 7.3 shows 36 etches on citric acid treated enamel. The false engagements are obvious in 7.3.

7.2 SICM Dental Surface Charge Mapping Appendix

7.2.1 Current Potential Plots for Nanopipette Viability

CPP taken before and after SICM mapping and surface treatments in section 4.2.3. The lack of change in the voltammogram is a good sign the nanopipette is still intact after the respective maps. This process was used to check the viability of the nanopipette in all the charge mapping data containing a surface treatment that required the removal of electrolyte to administer.

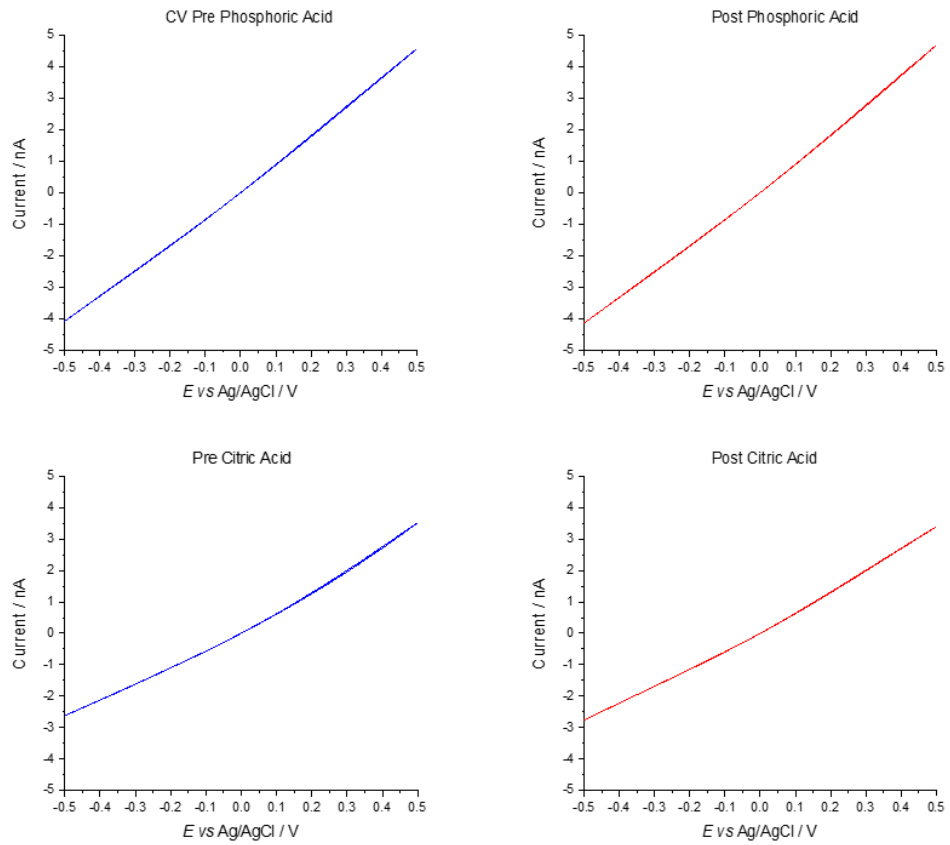

Figure 7.4 Nanopipette CPP for Citric and Phosphoric Acid Studies

Nanopipette voltammetry taken after each successful SICM map. The minimal changes to the magnitude of the current passed and the retention of the curve shape gives a good indication that the nanopipette has not been damaged during the coarse retract and approach required between treatments. It should be noted that the change in current magnitude between the phosphoric and the citric nanopipettes is due to change in pore size, the larger diameter nanopipette (phosphoric) passing more current. The scan rate was 100 mV/s and the supporting electrolyte was 50 mM KCl.

7.2.2 Inter Rod Enamel Surface Charge Calibration Graph

The data presented in Figure 4.2 uses the phosphoric acid experiment calibration presented in the main text in section 4.3 to convert the normalized currents to surface charge. These data were taken with the same nanopipette. The data in Figure 4.3 uses the calibration given below in Figure 7.5.

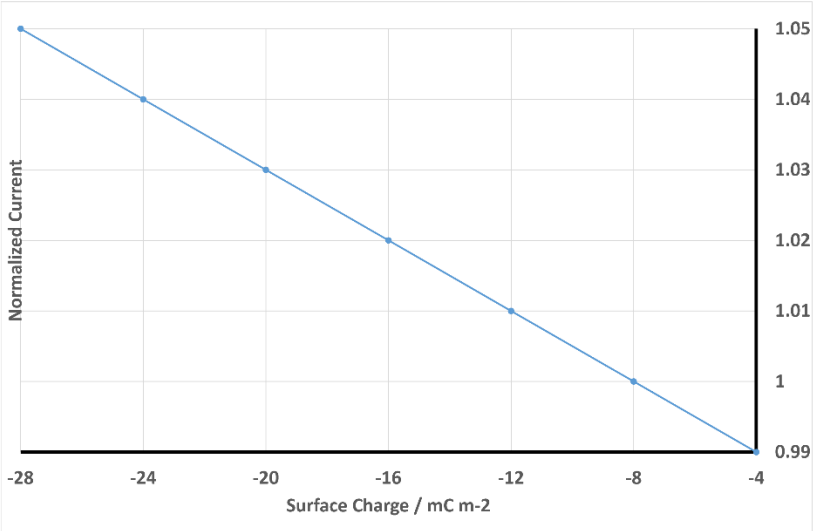

Figure 7.5 Inter-Rod Enamel Calibration

The calibration used to convert the surface charge in figure 4.4. The approach distance used was 35 nm, calculated with an FEM modelled approach curve.

7.2.3 Dentine Surface Charge Map Calibration Graphs

FEM calculated approach curve and normalized current to surface charge calibration plot for the dentine surface charge maps in section 4.2.2.

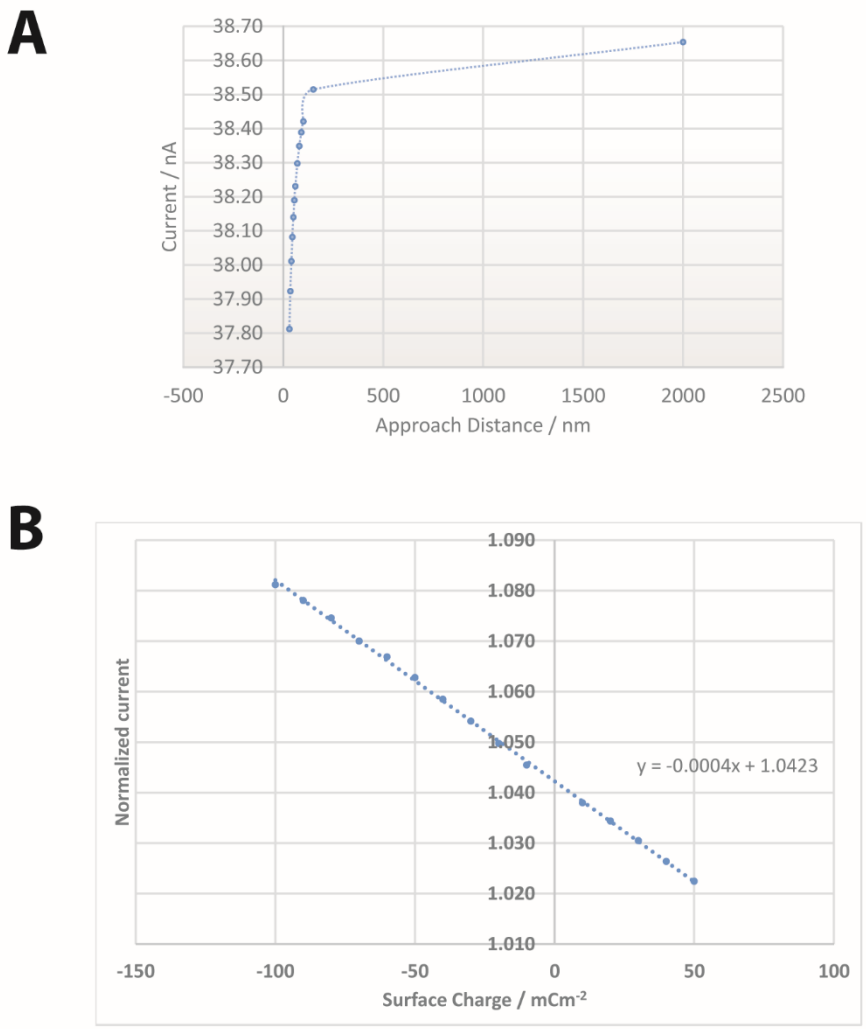

Figure 7.6 Approach Curve and Surface Charge Calibration – Dentine

Approach curve (A) and normalized current to surface charge calibration (B) used to calculate the dentine surface charge values. The 2% threshold was met at 30 nm so this value was used as the approach distance d.

7.2.4 Citric Acid Normalized Current Data

Normalized current data used to calculate surface charge maps in for the citric acid experiment in section 4.2.3.1. The phosphoric acid normalized current maps are in the main text in section 4.4.

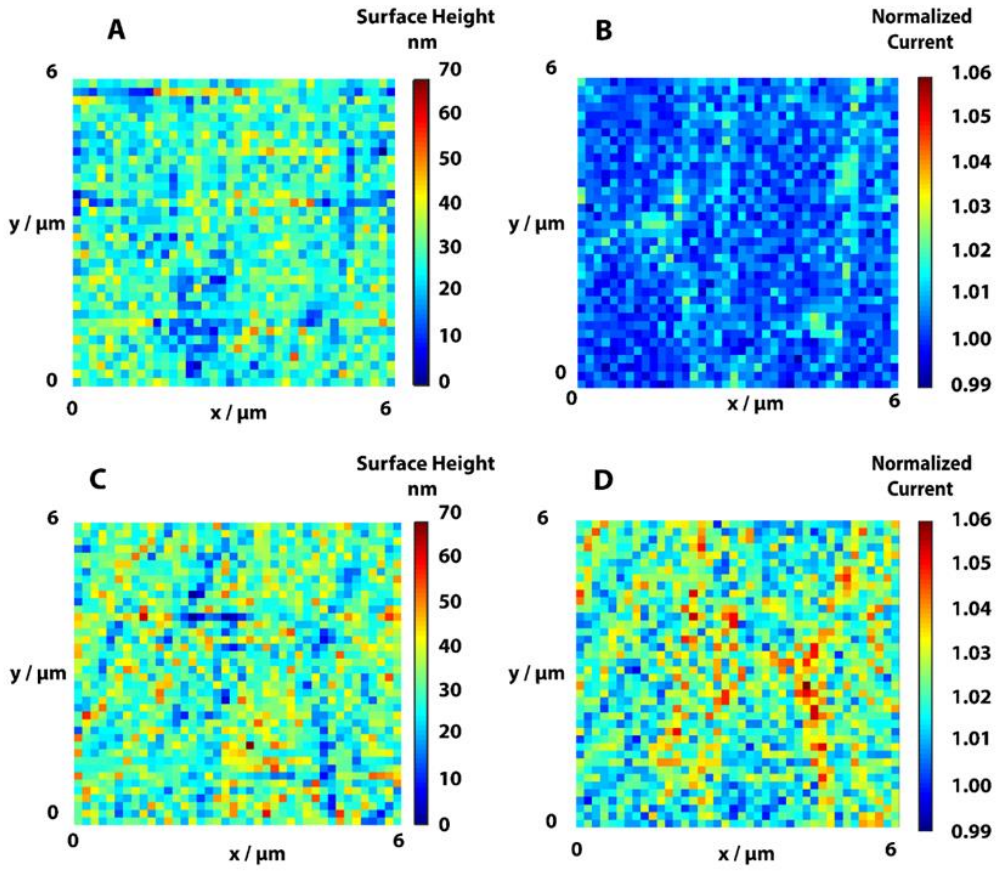

Figure 7.7 Normalized Current Data for Citric Acid SICM Maps

SICM topography (A) and normalized current (B) before citric acid treatment. SICM topography (C) and normalized current (D) after citric acid treatment. SICM conditions: 50 mM KCl, 150 nm borosilicate nanopipette, -50 mV approach bias, +500 mV pulse bias, displayed data calculated 100 ms after pulse applied.

7.2.5 HCl Enamel Surface Charge Map Calibration Graphs

Calibration curve for surface of enamel surface charge pre and post HCl exposure. Used to calculate Figure 4.10.

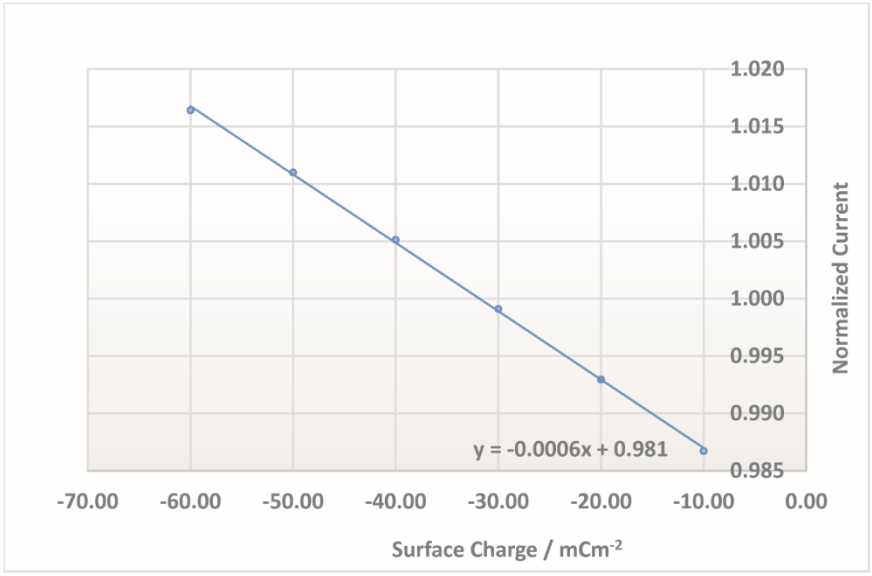

Figure 7.8 HCl FEM Surface Charge Calibration Plot

Surface charge calibration plot calculated at approach distance of 40 nm.

7.2.6 Remineralisation surface charge data and calibrations

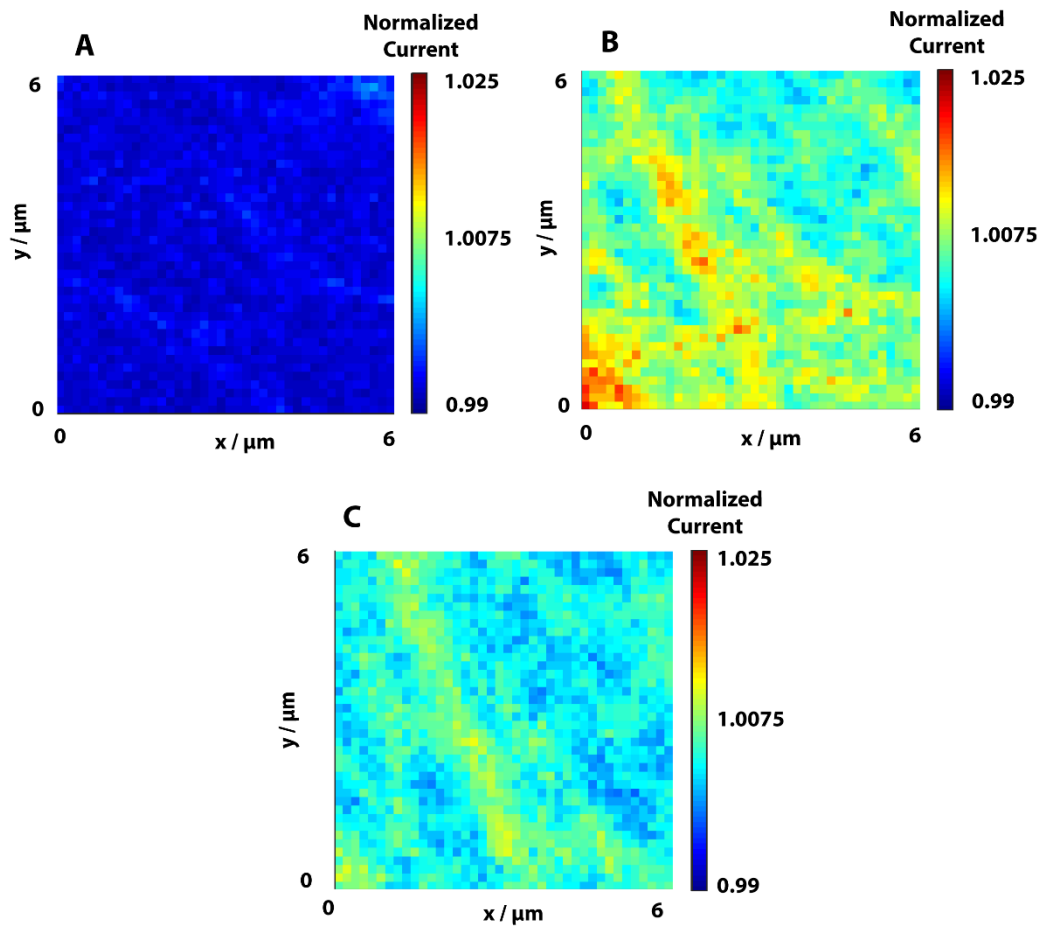

Figure 7.9 Normalized Current Remineralisation 1

SICM normalized current before treatment (**A**) and normalized current after citric acid exposure (**B**) and normalized current after 30 minute remineralisation (**C**). SICM conditions: 50 mM KCl, 150 nm borosilicate nanopipette, -50 mV approach bias, +500 mV pulse bias, displayed data calculated 100 ms after pulse applied.

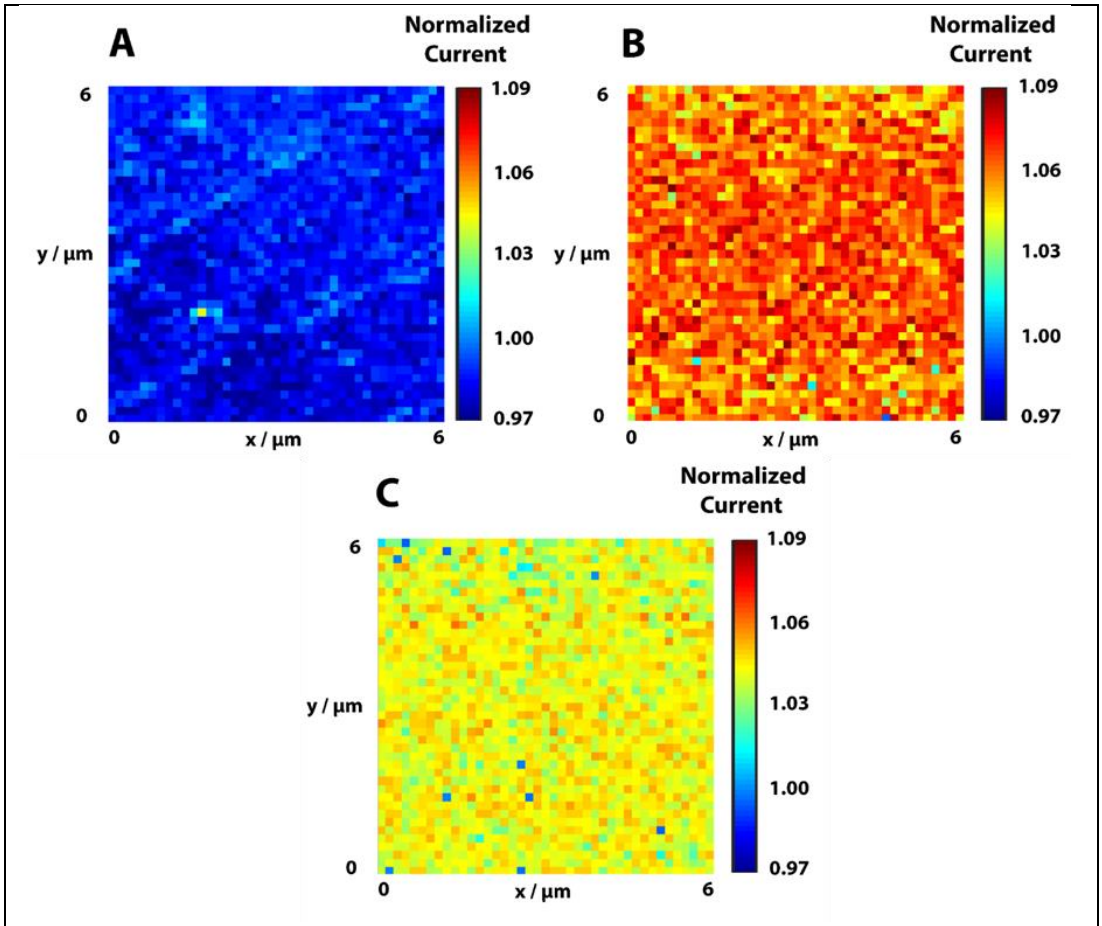

Figure 7.10 Normalized Current Remineralisation 2

SICM normalized current before treatment (**A**) and normalized current after citric acid exposure (**B**) and normalized current after 30 minute remineralisation (**C**). SICM conditions: 50 mM KCl, 150 nm borosilicate nanopipette, -50 mV approach bias, +500 mV pulse bias, displayed data calculated 100 ms after pulse applied.

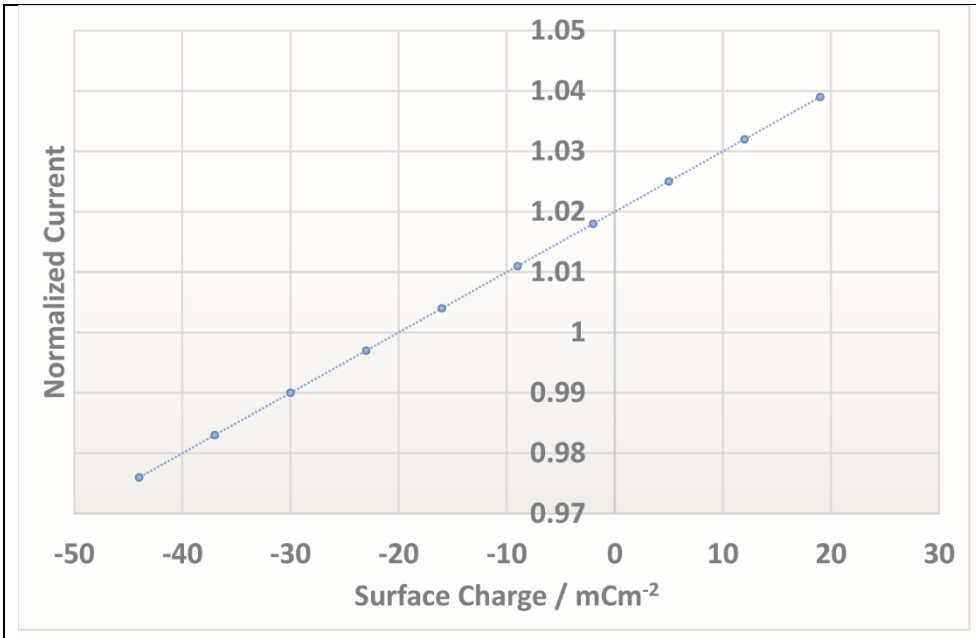

Figure 7.11 Remineralisation 1 Calibration Curve

Surface charge calibration plot calculated at approach distance of 35 nm

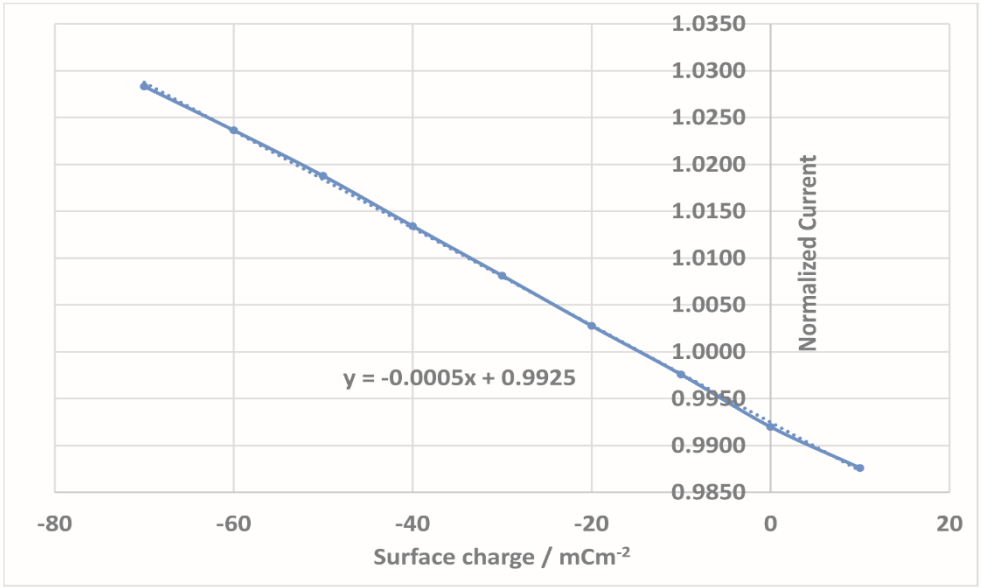

Figure 7.12 Remineralisation 2 Calibration Curve.

Surface charge calibration plot calculated at approach distance of 30 nm.

7.3 SICM Bacterial Surface Charge Mapping Appendix

7.3.1 Bacterial Cultures

A wildtype *Eschericia coli* K12 strains was used in this study, originally obtained DSMZ.

Due to issues in the mobility of the *Bacillus subtilis* avoiding the SICM scans, a *B.subtilis* NCIB 3610 mutant strain deplete in the *hag* genes was used instead. The strain (denoted as DS1677)) was obtained from Munehiro Asally, University of Warwick, and is referenced in Mukherjee *et al.* (2013).[1]

The Δ*hag* mutant prevents production of flagellin (termed as Hag), which is a key subunit for the polymerisation that forms bacterial flagella. Therefore, species deplete in Hag have limited flagella, resulting in reduced motility. For the application of SICM, the limited motility enabled the adhesives to hold the bacteria stationary across the SICM scan.

7.3.2 Bacterial Growth Media

Modified M9 media (M9m) used for bacterial culturing was based on established minimal media and adapted for growing a range of bacteria of interest, including the *E. coli* and *B. subtilis* used in this work.[2] The media is also adapted to render it suitable for use as an electrolyte for SICM scanning. Listed in Table 7.1 are the final components included in 1L of the full M9 media with glucose as a carbon source. Tables 7.2-4 provide the composition of each individual component, used as purchased from Fisher Scientific. All media were adjusted to pH 7, autoclaved, and used within a week of formation.

Table 7.1 Full M9m Media Components

	Details explained in	Components added to 1L
5x M9 minimal salts	Table 2	200 mL
1 M $MgSO_4 \bullet 7H_2O$	-	2 mL
Carbon source (0.4% w/v)	-	20 mL
1 M $CaCl_2$	-	100 μL
10 mM $FeCl_3 \bullet 6H_2O$	-	1 mL
1000x Trace metal solution	Table 3	1 mL
5-vitamin solution	Table 4	1 mL

Table 7.2 Quantities and Concentrations for M9m Minimal Salts

	Components added for stock soluton 1L	**Concentration in 1L stock (mM)**	**Concentration in 1L final full M9 media (mM)**
$Na_2HPO_4 \bullet 7H_2O$	64 g	238 mM	47.6 mM
KH_2PO_4	15 g	110 mM	22 mM
NaCl	2.5 g	43 mM	8.6 mM
NH_4Cl	5 g	93 mM	18.6 mM

Table 7.3 Quantities and Concentrations for 1000x Trace Metal Solution

	Components added to 1L stock solution	**Concentration in 1L stock (mM)**	**Concentration in 1L final full M9 media (μM)**
$CuCl_2 \bullet 2H_2O$	5.455 mg	0.032 mM	0.032 μM
$ZnSO_4 \bullet 7H_2O$	219.968 mg	0.765 mM	0.765 μM
$CoCl_2$	21.436 mg	0.169 mM	0.169 μM
$Na_2MoO_4 \bullet 2H_2O$	399.218 mg	1.650 mM	1.650 μM
H_3BO_3	2862.729 mg	46.300 mM	46.300 μM
$NiCl_2 \bullet 6H_2O$	998.382 mg	4.200 mM	4.200 μM
$Na_2WO4 \bullet 4H_2O$	80.154 mg	0.243 mM	0.243 μM
$Na_2SeO_3 \bullet 5H_2O$	59.966 mg	0.228 mM	0.228 μM

Table 7.4 Quantities and Concentrations for 5-Vitamin Solution

	Components added to 100 mL stock solution	**Concentration in 100mL stock (mM)**	**Concentration in 1L final full M9 media (μM)**
Biotin	2 mg	0.082 mM	0.082 μM
Pyridoxine hydrochloride	10 mg	0.486 mM	0.486 μM
Thiamin hydrochloride	5 mg	0.148 mM	0.148 μM
Riboflavin	5 mg	0.133 mM	0.133 μM
Nicotonic acid	5 mg	0.406 mM	0.406 μM

7.3.3 Growth and Viability of Bacterial Strains

After the SICM experiment, bacteria were streaked from the experimental substrate onto LB-agarose plates and aliquots from the bath were also plated onto LB-agarose, with blank media and seed cultures as controls.

Growth studies were performed to ensure that the cells were in a healthy growth stage during the SICM experiment. Growth was measured in a 96 well plate (Falcon 96 Well Cell Culture plate, sterile (Corning, UK, #353072)) where the absorbance at 600 nm over time was used to examine the growth of culture, where increased absorbance is indicative of bacterial growth, as is standard procedure for growth studies. The optical density at 600 nm (OD_{600}) was measured using a BMG Clariostar plate, set at 37°C with a double orbital shaking at 150 rpm, measurements of growth were recorded once every 10 minutes for 2000 minutes.

200 μL of M9m was added to each well, to which 2 μL from a dense bacterial culture was added at the start of measurement. Along with replicates of each bacterial strains (*B.subtilis* ΔhAg, *B.subtilis* Δ*eps*, *E.coli* WT), a control series of M9m was included for background subtraction.

The growth curves for the three bacterial strains are shown before (Figure 7.13), included is the M9m control to demonstrate the stability across the course of the experiment. Cultures are grown overnight from freezer stocks, therefore using the growth curve at approximately 15 hours (900 minutes), the *E.coli* would be in an early stationary phase, and the *B.subtilis* strains would both have passed the exponential growth phase and entered a lagging stationary phase.

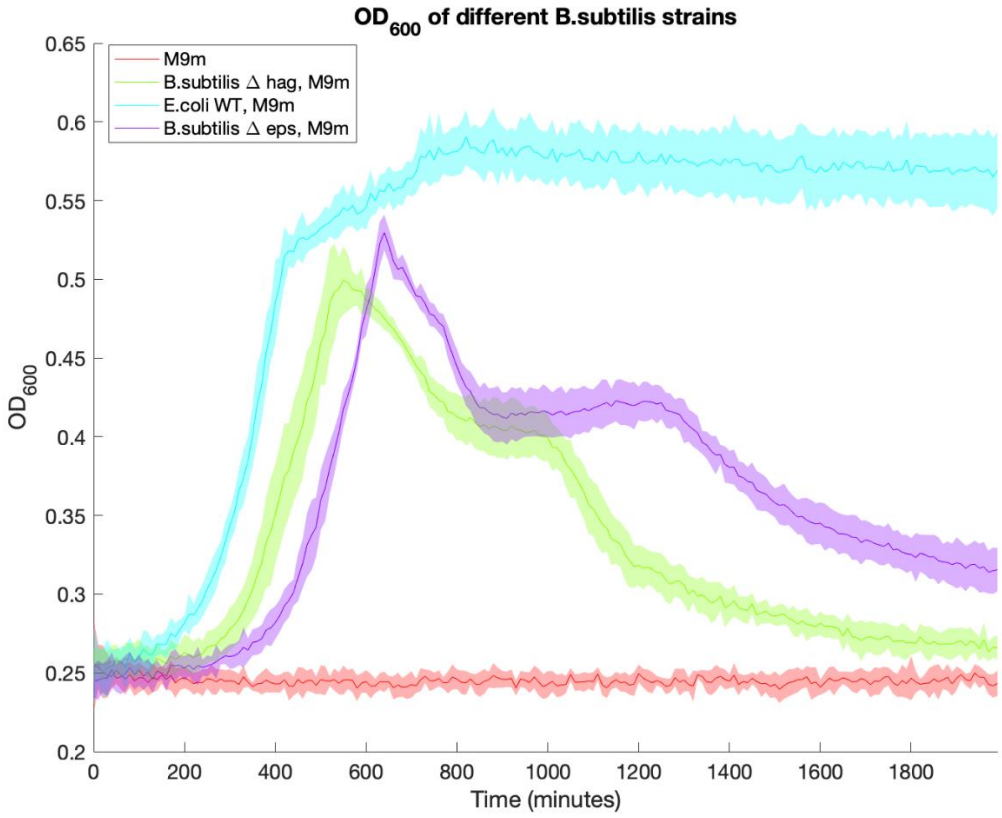

Figure 7.13 OD 600 Curve for Bacterial Growth Rate in M9

Mean optical density at 600 nm (OD_{600}) of different bacterial strains as grown in M9m media, and measured by a plate reader. Standard deviation is shown by the shading, measured across 2000 minutes, one measurement every 10 minutes.

In order to determine if there are viable cells left in the sample dishes of bacteria samples following a day of SICM experiments, surface swabs and liquid aliquots from SICM samples were spread on Lysogeny broth (LB) agar plates and left for 36 hours at 37°C. This was initially performed to allow colony counting of viable cells between different strains and electrolytes (i.e. 50 mM KCl or M9m). However, what was found that all the samples grew to a density where colony counting was not possible, and whilst this showed growth of bacteria in KCl samples, it was not a quantitative assessment of the differences in viability between the SICM samples with KCl and M9m media in the place of electrolyte. These samples were compared to equivalently treated samples of cell free media to serve as a control, in thee samples there was no observed bacterial growth as expected, demonstrating the bacterial growth was not caused by a lab or experiment contamination.

Whilst the LB plate show that there are viable cells following the SICM experiment using KCl and M9m as an electrolyte, it does not indicate the percentage of cell death or survival.

To try to obtain some quantitative observations of the growth of bacteria exposed to KCl, a plate reader experiment was set up where bacteria samples were exposed to 50 mM KCl for 8 hours (the total standard length of SICM experiments), where recovery growth when bacteria was placed back in M9m was recorded over time and compared to cultures not incubated in KCl.

Cultures of *B.subtilis Δhag*, *B.subtilis Δeps*, and *E.coli* WT were grown overnight in M9m at 37°C. 1 mL samples of each culture were centrifuged for 5 minutes at 5000 rpm to sediment the cells, where the supernatant was then removed and replaced with 1 mL of a 50 mM KCl solution buffed to pH 7 with Tris. The cells were resuspended and left in the microbial flow hood at room temperature for 8 hours, a similar maximum length of time to a day of SICM experiments. A control condition was included where sedimented cells were instead suspended in fresh M9m, in attempts to determine if the centrifugation process affected the cell viability following incubation.

After incubating for 8 hours, the cultures were again centrifuged for 5 minutes at 5000 pm and resuspended in 10 mL of fresh M9m. The 10-fold dilution of cells in media, instead of an 100-fold dilution such as in SI-4, was used to ensure that a representative proportion of the incubated cells enter to growth plates, therefore more clearly highlighting difference between KCl-incubated and M9m-incubated cells.

8 replicates of 200 μL samples from each condition were added to a transparent 96 well plate (Falcon 96 Well Cell Culture plate, sterile (Corning, UK, #353072)), along with a condition of M9m for background subtraction. The optical density at 600 nm (OD_{600}) was measured using a BMG Clariostar plate, set at 37°C with a double orbital shaking at 150 rpm, measurements of growth were recorded once every 10 minutes for 2000 minutes. The results of the growth study are shown in Figure SI.2.

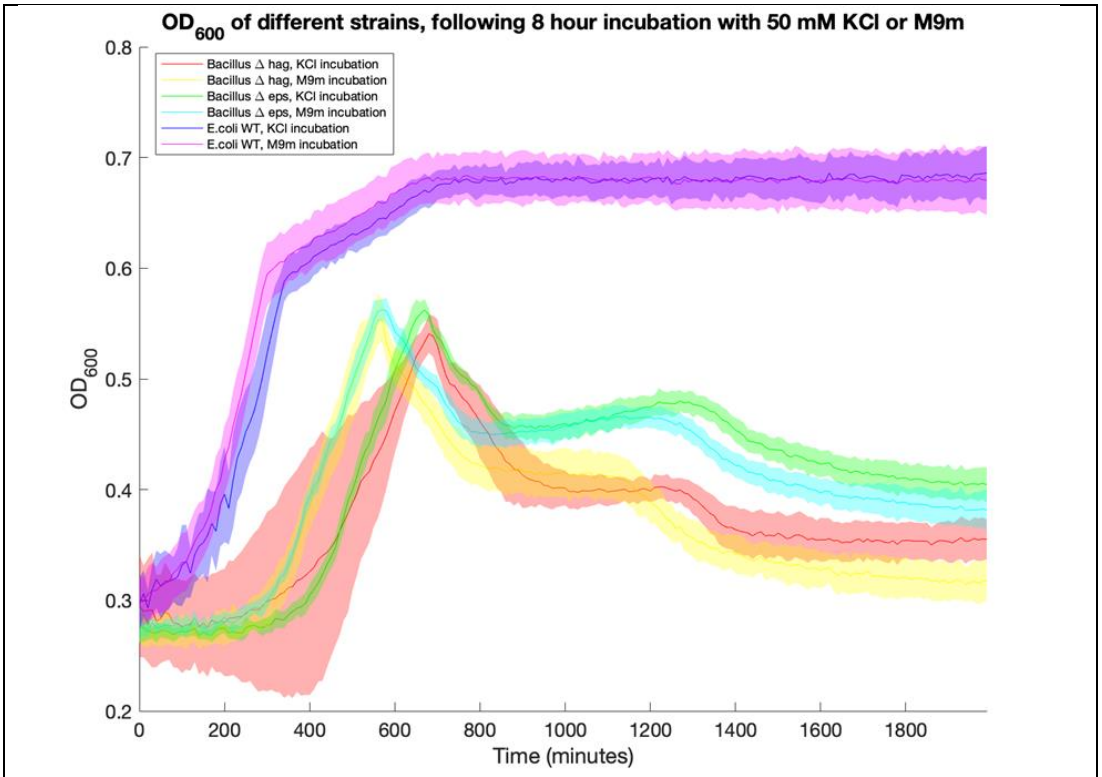

Figure 7.14 OD 600 Curve for Bacterial Growth Rate in M9 with KCl

Mean optical density at 600 nm (OD_{600}) of different bacterial strains as grown in M9m media, following incubation of either KCl or M9m. Standard deviation is shown by the shading, measured across 2000 minutes, one measurement every 10 minutes (mean of 8 repeats with standard deviation at each time point).

The *B.subtilis* strains incubated in KCl show a delayed exponential growth curve until they reach maximum absorbance. This would imply that either the initial viable cell concentration is lower in the KCl condition at the initiation of the plate reader recording, which could indicate cell death in KCl, or a delay in recovery into exponential growth following KCl incubation. It is noted that the cells in 50 mM KCl are expected not to grow as the solution lacks carbon source or other nutrients, therefore the incubation in M9m could have increased cell growth going into the plate reader, even at room temperature. If the M9m-incubated condition has a higher initial viable cell concentration, then it would be expected that the peak of the exponential growth stage would be reached sooner.

There is also a slight delay in the exponential growth in *E. coli*, however as the bacteria species is faster growing the delay is less prominent.

In conclusion, these results do show a difference in growth between the KCl- and M9m- incubated condition also all strains, however exponential growth still peaks within a reasonable time frame following inoculation which implies that a considerable number of cells are still viable following KCl incubation. Whilst this does not indicate if the cells studied in the SICM are alive, it would suggest that the cells are not completely unviable and are recoverable following the SICM experiment.

7.4 Matlab Code

7.4.1 Surface Charge Mapping Script

```
%A=load('Filename.tsv');%load data in as A, comment out after already loaded to save
time on future runs
%%
%CV at surface only
set(0,'DefaultFigureColormap',feval('jet'))
close all
movie=0;
Extract_data=0;%1 if running for first time, 0 if data already loaded
time_to_plot=50000;%what part of IT curve to plot in us
hopping_distance=0.15;%in um
average=0;%frames to average
plot_movie=0;%plot IT as a movie with settings chosen later
channel_to_plot=3;
channel_line_number=7;
channel_voltage=5;
channel_dc=4;
channel_xdata=1;
channel_ydata=2;
channel_zdata=3;
channel_phase=13;
channel_amp=12;
frame_to_plot=0;%0 whole movie, or individual frame if not 0.
remove_topog_drift=1;%1 or 0
startpoint=1;
endpoint=6500;
correctstart=1;
correctend=6561;
datapointtime=4*128;
pulsetime=45000;
normalise=2;%0 no normalise, 1 normalise to bulk subtraction,2 normalise to bulk
division, 3 plot bulk
fixcbar=2;
%1. Fix between maximum and minimum over whole scan
%2. Colourbar for each frame
labelsize=20;
%Shouldnt need to change anything below here
last_line = max(A(channel_line_number,:));
lines_in_hop=7;%number of lines between each approach
first_approach=2;%9 normally, 2 if small hopping distance <=150nm
first_surface_IT=first_approach+1;%line number for first part of first cv
first_bulk_IT=first_surface_IT+3;
%If you want to crop
if Extract_data==0
XMIN=1;%line number you want to crop from and to
XMAX=90;
YMIN=1;
YMAX=90;
end
if Extract_data==1
    %%
    %Make X, Y Grid for plots
    %Extract topography
    count1=1;
    count2=1;
```

```
    h1 = waitbar(0,'Initializing Topography waitbar...');
    for i=[first_approach:lines_in_hop:last_line]
        %if(mod(count2,x+1)~=1)
            b=A(:,A(channel_line_number,:)==i);%picks out approaches by line number
            XMapreal(count1)=mean(b(channel_xdata,:));
            YMapreal(count1)=mean(b(channel_ydata,:));
            appcurrent(count1)=mean(b(channel_dc));
            Applinecheck(count1)=b(channel_line_number,1);
            zdata=b(channel_zdata,:);
            if numel(zdata)==0
                ZMap(count1)=ZMap(count1-1);%if empty approach, topography same as
last
            else
                ZMap(count1)=zdata(end);
            end
            count1=count1+1;
        %end
        count2=count2+1;
        waitbar(i/last_line,h1,'Topography Progress')
    end
    close(h1)
    zr2=ZMap;
    appcurrentraw=appcurrent;
    XMapraw=XMapreal;
    YMapraw=YMapreal;

    %ZMap(end)=[];
    %Next section of code reshapes to grid and checks right number of hops

    %Map_b = zeros(floor((last_line-first_approach)/lines_in_hop)+1,no_frames);

    %Now extract CV data
        count1=1;
        count2=1;
        h2 = waitbar(0,'Initializing Functional waitbar...');
        for i=first_surface_IT:lines_in_hop:last_line%forward part of cv V0 to V1
            %if(mod(count2,x+1)~=1)
                ibulk=i+(first_bulk_IT-first_surface_IT);
                b=A(:,A(channel_line_number,:)==i);%extracts data of these line
numbers
                bbulk=A(:,A(channel_line_number,:)==ibulk);
                if(numel(b)>0&&numel(bbulk)>0)
                    currenttimesurf(count1,1:length(b))=b(channel_dc,:);
                    currenttimebulk(count1,1:length(bbulk))=bbulk(channel_dc,:);
                else
                    currenttimesurf(count1,:)=currenttimesurf(count1-1,:);
                    currenttimebulk(count1,:)=currenttimebulk(count1-1,:);
                end
                count1=count1+1;
            %end
            count2=count2+1;
            waitbar(i/last_line,h2,'Functional Progress')

        end
        close(h2)
end
if Extract_data==0
%%
%%
ZMap=zr2;
XMapreal=XMapraw;
YMapreal=YMapraw;
currenttimebulkreal=currenttimebulk;
currenttimesurfreal=currenttimesurf;
tol=hopping_distance/5;
countsame=1;
for i=2:length(XMapreal)
    if(abs(XMapreal(i)-XMapreal(i-1))<tol && abs(YMapreal(i)-YMapreal(i-1))<tol)
        list_same(countsame)=i-1;
        countsame=countsame+1;
    end
end
for j=length(list_same):-1:1
    XMapreal(list_same(j))=[];
    YMapreal(list_same(j))=[];
    ZMap(list_same(j))=[];
    currenttimebulkreal(list_same(j),:)=[];
```

```
    currenttimesurfreal(list_same(j),:)=[];
end
countx=1;
county=1;
listx=XMapreal(1);
listy=YMapreal(1);
for k=2:length(XMapreal)
    if(XMapreal(k)>max(listx)+tol)
        listx(length(listx)+1)=XMapreal(k);
        countx=countx+1;
    end
    if(YMapreal(k)>max(listy)+tol)
        listy(length(listy)+1)=YMapreal(k);
        county=county+1;
    end
end
listtoremovex=[];
countxremove=1;
for o=1:length(listx)
    countox=0;
    for i=1:length(XMapreal)
        if(abs(XMapreal(i)-listx(o))<tol)
            countox=countox+1;
        end
    end
    if(countox==1)
        listtoremovex(countxremove)=listx(o);
        countxremove=countxremove+1;
        countx=countx-1;
    end
end
listtoremovey=[];
countyremove=1;
for o=1:length(listy)
    countoy=0;
    for i=1:length(YMapreal)
        if(abs(YMapreal(i)-listy(o))<tol)
            countoy=countoy+1;
        end
    end
    if(countoy==1)
        listtoremovey(countyremove)=listy(o);
        countyremove=countyremove+1;
        county=county-1;
    end
end
listtoremovefinal=[];
countfinal=0;
for p=1:length(XMapreal)
    for q=1:length(listtoremovex)
        if(abs(XMapreal(p)-listtoremovex(q))<tol)
            countfinal=countfinal+1;
            listtoremovefinal(countfinal)=p;
        end
    end
    for q=1:length(listtoremovey)
        if(abs(YMapreal(p)-listtoremovey(q))<tol)
            countfinal=countfinal+1;
            listtoremovefinal(countfinal)=p;
        end
    end
end
if(isempty(listtoremovefinal)~=1)
    for j=length(listtoremovefinal):-1:1
        XMapreal(listtoremovefinal(j))=[];
        YMapreal(listtoremovefinal(j))=[];
        ZMap(listtoremovefinal(j))=[];
        currenttimebulkreal(listtoremovefinal(j),:)=[];
        currenttimesurfreal(listtoremovefinal(j),:)=[];
    end
end
x=countx;
y=county;
if(XMAX>x)
    XMAX=x;
end
if(YMAX>y)
```

```
    YMAX=y;
end

ZMap=max(ZMap)-ZMap;
    ZMap=ZMap';
    XMapreal=XMapreal';
    YMapreal=YMapreal';
    ZMap=reshape(ZMap,x,y);
    XMapreal=reshape(XMapreal,x,y);
    YMapreal=reshape(YMapreal,x,y);
    ZMap=ZMap';
    XMapreal=XMapreal';
    YMapreal=YMapreal';
    flipstart=2;
    for i=flipstart:2:y
        ZMap(i,:)=fliplr(ZMap(i,:));
        XMapreal(i,:)=fliplr(XMapreal(i,:));
        YMapreal(i,:)=fliplr(YMapreal(i,:));
    end
    ZMap=ZMap-min(min(ZMap));
    if remove_topog_drift==1
            %ZMap=test2;
            ZMap3=ZMap;
        for i=1:y
            datap=[1,x];
            [xData, yData] = prepareCurveData( datap, ZMap(i,[1,end])) ;
            ft = fittype( 'poly1' );
            opts = fitoptions( ft );
            opts.Lower = [-Inf -Inf];
            opts.Upper = [Inf Inf];
            driftfit2 = fit( xData, yData, ft, opts );
            MyCoeffs3=coeffvalues(driftfit2);
            ZMap3(i,:)=ZMap(i,:)-MyCoeffs3(1)*[1:x]-MyCoeffs3(2);
            ZMap(i,:)=ZMap3(i,:);
        end
    end
set(0,'defaultfigurecolor',[1 1 1])
minlength_IT=min([size(currenttimebulkreal,2),size(currenttimesurfreal,2)]);
timelist=0:datapointtime:datapointtime*(minlength_IT-1);
if(normalise==2)
    Map=currenttimesurfreal(:,1:minlength_IT)./currenttimebulkreal(:,1:minlength_IT);
elseif(normalise==0)
    Map=currenttimesurfreal(:,1:minlength_IT);
elseif(normalise==3)
    Map=currenttimebulkreal(:,1:minlength_IT);
elseif(normalise==1)
    Map=currenttimesurfreal(:,1:minlength_IT)-currenttimebulkreal(1:minlength_IT);
end
%next section plots topography
if channel_to_plot==3
    zcorrected=ZMap;
    zcorrected=zcorrected-min(min(zcorrected));
    figure( 'Name', 'Topography' );
    imagesc(zcorrected(YMIN:YMAX,XMIN:XMAX))
    view( [0, 90] );
    caxis([nanmin(nanmin(zcorrected)) nanmax(nanmax(zcorrected))])
    figset_9channel
    set(gca,'XTick',[XMIN,XMAX])
    set(gca,'XTickLabel',[0,hopping_distance*(XMAX-XMIN)])
    set(gca,'YTick',[YMIN,YMAX])
    set(gca,'YTickLabel',[hopping_distance*(YMAX-YMIN),0])
else%plot the chosen variable
       if(plot_movie==1)
        frames_that_will_be_plotted=1:1:minlength_IT;%all data
        movie=1;
    else
        difference=abs(time_to_plot-timelist);
        [idx2 idx2] = min(difference);
        frames_that_will_be_plotted=idx2;
        movie=0;
    end
    count=0;
    frame_count=1;
    for i=frames_that_will_be_plotted
        str = num2str(round(timelist(i)));
        comb=strcat(str,' \mus');
        if(average==0)
```

```
            toplot_s=Map(:,i);
        else
            toplot_2=Map(:,i-average:i);
            toplot_s=Map(:,i);
            for j=1:length(toplot_s)
                toplot_s(j)=mean(toplot_2(j,:));
            end
        end
        toplot_s=toplot_s';
        toplot_s=reshape(toplot_s,x,y);
        toplot_s=toplot_s';
        for i=flipstart:2:y
            toplot_s(i,:)=fliplr(toplot_s(i,:));
        end
            h4 = imagesc(toplot_s(YMIN:YMAX,XMIN:XMAX));
            cbar=colorbar;
            caxis([nanmin(nanmin(toplot_s)) nanmax(nanmax(toplot_s))]);
            if fixcbar==1
                if channel_to_plot==channel_dc
                    caxis([nanmin(nanmin(Map(:,find(v_list==min(v_list)))))
nanmax(nanmax(Map(:,find(v_list==max(v_list)))))]);
                else
                    caxis([nanmin(nanmin(Map)) nanmax(nanmax(Map))]);
                end
            end
            if fixcbar==3
                caxis([cbarmin,cbarmax])
            end
        title(comb,'fontsize',labelsize,'fontweight','bold' )
        figset_9channel
        %axis off
        set(gca,'XTick',[XMIN,XMAX])
        set(gca,'XTickLabel',[0,hopping_distance*(XMAX-XMIN)])
        set(gca,'YTick',[YMIN,YMAX])
        set(gca,'YTickLabel',[hopping_distance*(YMAX-YMIN),0])
        pause(0.1)
        gcf
    end
end
end
```

7.4.2 SICM Topography Only Script

```
%A=load('Filename.tsv');%load data in as A, comment out after already loaded to save
time on future runs
%%
%CV at surface only
set(0,'DefaultFigureColormap',feval('jet'))
close all
movie=0;
Extract_data=0;%1 if running for first time, 0 if data already loaded
hopping_distance=0.2;%in um
channel_to_plot=3;
channel_line_number=11;
channel_voltage=8;
channel_dc=4;
channel_xdata=1;
channel_ydata=2;
channel_zdata=3;
channel_phase=13;
channel_amp=12;
frame_to_plot=0;%0 whole movie, or individual frame if not 0.
remove_topog_drift=1;%1 or 0
startpoint=1;
endpoint=6500;
correctstart=1;
correctend=6561;
datapointtime=4*128;
fixcbar=2;
%1. Fix between maximum and minimum over whole scan
%2. Colourbar for each frame
labelsize=20;
%Shouldnt need to change anything below here
last_line = max(A(channel_line_number,:));
```

```
lines_in_hop=3;%number of lines between each approach
first_approach=2;%9 normally, 2 if small hopping distance <=150nm
%If you want to crop
if Extract_data==0
XMIN=1;%line number you want to crop from and to
XMAX=90;
YMIN=1;
YMAX=90;
end
if Extract_data==1
    %%
    %Make X, Y Grid for plots
    %Extract topography
    count1=1;
    count2=1;
    h1 = waitbar(0,'Initializing Topography waitbar...');
    for i=[first_approach:lines_in_hop:last_line]
        %if(mod(count2,x+1)~=1)
            b=A(:,A(channel_line_number,:)==i);%picks out approaches by line number
            XMapreal(count1)=mean(b(channel_xdata,:));
            YMapreal(count1)=mean(b(channel_ydata,:));
            appcurrent(count1)=mean(b(channel_dc));
            Applinecheck(count1)=b(channel_line_number,1);
            zdata=b(channel_zdata,:);
            if numel(zdata)==0
                ZMap(count1)=ZMap(count1-1);%if empty approach, topography same as
last
            else
                ZMap(count1)=zdata(end);
            end
            count1=count1+1;
        %end
        count2=count2+1;
        waitbar(i/last_line,h1,'Topography Progress')
    end
    close(h1)

    appcurrentraw=appcurrent;
    XMapraw=XMapreal;
    YMapraw=YMapreal;

    %ZMap(end)=[];
    %Next section of code reshapes to grid and checks right number of hops


    %Map_b = zeros(floor((last_line-first_approach)/lines_in_hop)+1,no_frames);

    %Now extract CV data
end
if Extract_data==0
%%
%%

XMapreal=XMapraw;
YMapreal=YMapraw;
tol=hopping_distance/3;
countsame=1;
for i=2:length(XMapreal)
    if(abs(XMapreal(i)-XMapreal(i-1))<tol && abs(YMapreal(i)-YMapreal(i-1))<tol)
        list_same(countsame)=i-1;
        countsame=countsame+1;
    end
end
if(countsame>1)
for j=length(list_same):-1:1
    XMapreal(list_same(j))=[];
    YMapreal(list_same(j))=[];
    ZMap(list_same(j))=[];
end
end
countx=1;
county=1;
listx=XMapreal(1);
listy=YMapreal(1);
for k=2:length(XMapreal)
    if(XMapreal(k)>max(listx)+tol)
        listx(length(listx)+1)=XMapreal(k);
```

```
        countx=countx+1;
    end
    if(YMapreal(k)>max(listy)+tol)
        listy(length(listy)+1)=YMapreal(k);
        county=county+1;
    end
end
listtoremovex=[];
countxremove=1;
for o=1:length(listx)
    countox=0;
    for i=1:length(XMapreal)
        if(abs(XMapreal(i)-listx(o))<tol)
            countox=countox+1;
        end
    end
    if(countox==1)
        listtoremovex(countxremove)=listx(o);
        countxremove=countxremove+1;
        countx=countx-1;
    end
end
listtoremovey=[];
countyremove=1;
for o=1:length(listy)
    countoy=0;
    for i=1:length(YMapreal)
        if(abs(YMapreal(i)-listy(o))<tol)
            countoy=countoy+1;
        end
    end
    if(countoy==1)
        listtoremovey(countyremove)=listy(o);
        countyremove=countyremove+1;
        county=county-1;
    end
end
listtoremovefinal=[];
countfinal=0;
for p=1:length(XMapreal)
    for q=1:length(listtoremovex)
        if(abs(XMapreal(p)-listtoremovex(q))<tol)
            countfinal=countfinal+1;
            listtoremovefinal(countfinal)=p;
        end
    end
    for q=1:length(listtoremovey)
        if(abs(YMapreal(p)-listtoremovey(q))<tol)
            countfinal=countfinal+1;
            listtoremovefinal(countfinal)=p;
        end
    end
end
if(isempty(listtoremovefinal)~=1)
    for j=length(listtoremovefinal):-1:1
        XMapreal(listtoremovefinal(j))=[];
        YMapreal(listtoremovefinal(j))=[];
        ZMap(listtoremovefinal(j))=[];
    end
end
x=countx;
y=county;
if(XMAX>x)
    XMAX=x;
end
if(YMAX>y)
    YMAX=y;
end

ZMap=max(ZMap)-ZMap;
    ZMap=ZMap';
    XMapreal=XMapreal';
    YMapreal=YMapreal';
    ZMap=reshape(ZMap,x,y);
    XMapreal=reshape(XMapreal,x,y);
    YMapreal=reshape(YMapreal,x,y);
    ZMap=ZMap';
```

```
    XMapreal=XMapreal';
    YMapreal=YMapreal';
    flipstart=2;
    for i=flipstart:2:y
        ZMap(i,:)=fliplr(ZMap(i,:));
        XMapreal(i,:)=fliplr(XMapreal(i,:));
        YMapreal(i,:)=fliplr(YMapreal(i,:));
    end
    ZMap=ZMap-min(min(ZMap));
     if remove_topog_drift==1
            %ZMap=test2;
            ZMap3=ZMap;
        for i=1:y
            datap=[1,x];
            [xData, yData] = prepareCurveData( datap, ZMap(i,[1,end])) ;
            ft = fittype( 'poly1' );
            opts = fitoptions( ft );
            opts.Lower = [-Inf -Inf];
            opts.Upper = [Inf Inf];
            driftfit2 = fit( xData, yData, ft, opts );
            MyCoeffs3=coeffvalues(driftfit2);
            ZMap3(i,:)=ZMap(i,:)-MyCoeffs3(1)*[1:x]-MyCoeffs3(2);
            ZMap(i,:)=ZMap3(i,:);
        end
    end
set(0,'defaultfigurecolor',[1 1 1])
%next section plots topography
if channel_to_plot==3
    zcorrected=ZMap;
    zcorrected=zcorrected-min(min(zcorrected));
    figure( 'Name', 'Topography' );
    imagesc(zcorrected(YMIN:YMAX,XMIN:XMAX))
    view( [0, 90] );
    caxis([nanmin(nanmin(zcorrected)) nanmax(nanmax(zcorrected))])
    figset_9channel
    set(gca,'XTick',[XMIN,XMAX])
    set(gca,'XTickLabel',[0,hopping_distance*(XMAX-XMIN)])
    set(gca,'YTick',[YMIN,YMAX])
    set(gca,'YTickLabel',[hopping_distance*(YMAX-YMIN),0])
end
end
```

7.4.3 Etch Pit Array Script

```
array_min=zeros(6,6);
array_max=zeros(6,6);
i_approach=1;

for i_deliver=[6:4:max(A(11,:))];
channel_z=3;
channel_DC=4;
channel_AC=12;
channel_phase=13;
channel_line_number=11;
line_number_at_surface=i_deliver;
time_per_point=4*128;
time_units=2;%0=us,1=ms,2=s,3=min
crop_percentage=5;
while_at_surface_z=A(channel_z,A(channel_line_number,:)==line_number_at_surface);
while_at_surface_DC=A(channel_DC,A(channel_line_number,:)==line_number_at_surface);
%while_at_surface_AC=A(channel_AC,A(channel_line_number,:)==line_number_at_surface);
%while_at_surface_phase=A(channel_phase,A(channel_line_number,:)==line_number_at_surf
ace);
raw_time_at_surface=time_per_point*[0:1:length(while_at_surface_z)-1];
no_timepoints=length(raw_time_at_surface);
first_time_include=floor(no_timepoints*crop_percentage/100);
if time_units==0
    converted_time=raw_time_at_surface;
elseif time_units==1
    converted_time=raw_time_at_surface/1000;
elseif time_units==2
    converted_time=raw_time_at_surface/1E6;
```

```
elseif time_units==3
    converted_time=raw_time_at_surface/(60*1E6);
else
    display('Units selected wrongly')
    exit
end
array_min(i_approach)=min(while_at_surface_z);
array_max(i_approach)=max(while_at_surface_z);
figure(1)
hold all
plot(converted_time(first_time_include:end)-
converted_time(first_time_include),while_at_surface_z(first_time_include:end)-
while_at_surface_z(first_time_include))
set(gca,'FontSize',16,'fontweight','bold')
title('Cummulative Etch Pit Tip 3 Array 2','fontweight','bold','fontsize',18)
xlabel('Pulse Time / s','fontweight','bold','fontsize',16)
ylabel('Z Depth / \mum','fontweight','bold','fontsize',16)

figure(2)
hold all
plot(converted_time(first_time_include:end)-
converted_time(first_time_include),while_at_surface_DC(first_time_include:end))
%figure(3)
%hold all
%plot(converted_time(first_time_include:end)-
converted_time(first_time_include),while_at_surface_AC(first_time_include:end))
%figure(4)
%hold all
%plot(converted_time(first_time_include:end)-
converted_time(first_time_include),while_at_surface_phase(first_time_include:end))
i_approach= i_approach+1;
end
array_magnitude = array_max-array_min;
data=reshape(array_magnitude,[36,1])
array_average = mean(mean(array_magnitude))
deviation= std(array_magnitude(1:36))
figure (5)
hold all
plot(A(3,:));
set(gca,'FontSize',16,'fontweight','bold')
title('Z trace','fontweight','bold','fontsize',18)
xlabel('Duration / s','fontweight','bold','fontsize',16)
ylabel('Z/ \mum','fontweight','bold','fontsize',16)
figure (6)
plot(A(4,:));
set(gca,'FontSize',16,'fontweight','bold')
title('Current trace','fontweight','bold','fontsize',18)
xlabel('Duration / s','fontweight','bold','fontsize',16)
ylabel('Current / A','fontweight','bold','fontsize',16)
```

7.5 References

1 S. Mukherjee, P. Babitzke and D. B. Kearns, *J. Bacteriol.*, 2013, **195**, 297–306.

2 M. Ehrenberg, H. Bremer and P. P. Dennis, *Biochimie*, 2013, **95**, 643–658.